Department of Chemical Engineering
Curtin University Malaysia

Development of Blend Cellulose Acetate Butyrate/Multi-Walled Carbon Nanotubes Mixed Matrix Membrane for CO_2/N_2 Separation

Lee Ren Jie

This thesis is presented for the Degree of
Doctor of Philosophy
of
Curtin University

September 2019

To the best of my knowledge and belief, this thesis contains no material previously published by any other person except where due acknowledgement has been made.

This thesis contains no material which has been accepted for the award of any other degree or diploma in any university.

Signature	:	
Name	:	Lee Ren Jie
Date	:	18/09/2019

ACKNOWLEDGEMENT

First and foremost, I am grateful for what God have blessed me till today. For all the up and down situation, I encountered in my life, He has always been there for me. Comforting and encouraging me whenever I confronted difficulties in life. I am mostly grateful for His undivided mercy and love and made all things possible with His multifarious wisdom.

I would like to take this opportunity also, to express my utmost gratitude to Dr. Zeinab Abbas Jawad whom had given her full commitment by providing all the necessary facilities and sharing her knowledge in the membrane technology field. Her endless help and support had made the journey of my postgraduate study to be smooth. It is an honour to be able to work with Dr. Zeinab, not only her patient amazed me, she also consistently guides me towards the right path whenever I am off track from my objectives. Not to forget Prof. Abdul Latif Ahmad from Universiti Sains Malaysia (USM) who is the associate supervisor for this project. Honestly, I appreciate him for allowing me to utilize the equipment in USM whenever I need to characterize my samples. Same goes to Associate Prof. Dr. Chua Han Bing, who is the co-supervisor of this project, for his sincere encouraging words. Finally, I am grateful to Dr. Hisham Khaled Ben Mahmud who is the chairman of my thesis committee for his generous opinions and advice.

Apart from that, a special thanks to the lab technicians, Ms. Magdalene Bangkang Anak Joing and Ms. Michelle Martin, for providing the research equipment and chemical materials on time, who were also friendly and helpful. I would also like to express my sincere thanks to lab manager Ms. Helda Puyang Jau and technician Mr. Marconi Anak Janggu for their provision and assistance for allowing me to conduct the experiments in a safe and sound environment. Lastly, I would like to thank my family for their love and support throughout the journey of my postgraduate study.

I would like to appreciate Ministry of Higher Education Malaysia (MOHE) for providing Fundamental Research Grant Scheme (FRGS) (MOHE Ref. No: FRGS/1/2015/TK02/CURTIN/03/1) and Cost Centre: 001048. Also, I would like to thank LRGS USM (Account No: 304/PJKIMIA/6050296/U124), and Curtin Cost Centre: 001047.

LIST OF PUBLICATIONS FROM THE THESIS

Patent Submission

1. Cellulose Acetate Butyrate/Multi-Walled Carbon Nanotubes Blending Mixed Matrix Membrane with enhanced CO_2 capture properties

The research described in the thesis had resulted in the following publications:

International Publication

1. Lee, R.J., Jawad, Z.A., Ahmad, A.L., Ngo, J.Q. and Chua, H.B. 2017. Improvement of CO_2/N_2 separation performance by polymer matrix cellulose acetate butyrate. Materials Science and Engineering Conference Series (Vol. 206, No. 1. 012072). **(Best Paper Award)**
2. Lee, R.J., Jawad, Z.A., Ahmad, A.L. and Chua, H.B., 2018. Incorporation of functionalized multi-walled carbon nanotubes (MWCNTs) into cellulose acetate butyrate (CAB) polymeric matrix to improve the CO_2/N_2 separation. Process Safety and Environmental Protection, 117, pp.159-167.
3. Lee, R.J., Jawad, Z.A., Ahmad, A.L. and Chua, H.B., 2018. Synthesis of Cellulose Acetate Butyrate (CAB)/multi-walled carbon nanotubes (MWCNTs) mixed matrix membrane (MMM) to ameliorate CO_2/N_2 separation. Materials Science and Engineering Conference Series.

Book Chapter

1. R. J. Lee, Z. A. Jawad, A. L. Ahmad, H. B. Chua, H. P. Ngang, S. H. S. Zein. 2017. Rheological evaluation of the fabrication parameters of cellulose acetate butyrate membrane on the CO_2/N_2 separation performance. Book of Membrane Technology for CO_2 Sequestration. CRC Press/Taylor & Francis Group.

International and National Conferences

1. R.J. Lee, Z.A. Jawad, A.L. Ahmad, J.Q. Ngo, H.B. Chua (2016) Improvement of CO_2/N_2 separation performance by cellulose acetate butyrate polymer matrix. The 29th Symposium of Malaysia Chemical Engineers (SOMChE 2016), 1st-3rd December, Miri, Sarawak, Malaysia

2. R. J. Lee, Z. A. Jawad, A. L. Ahmad, H. B. Chua. 2017. A novel mixed matrix membrane of Cellulose Acetate Butyrate/functionalized multi-walled carbon nanotubes for CO_2/N_2 separation. The 30th Symposium of Malaysia Chemical Engineers (SOMChE 2017), 6-7th December, Kuala Lumpur, Malaysia.
3. R. J. Lee, Z. A. Jawad, A. L. Ahmad, H. B. Chua. 2017. Incorporation of functionalized MWCNTs into cellulose acetate butyrate polymeric matrix to enhance CO_2/N_2 separation. One Curtin International Postgraduate Conference (OCPC 2017), 10-12th December, Miri, Sarawak, Malaysia.
4. R. J. Lee, Z. A. Jawad, A. L. Ahmad, H. B. Chua. 2017. Synthesis of Cellulose Acetate Butyrate (CAB)/multi-walled carbon nanotubes (MWCNTs) mixed matrix membrane (MMM) to ameliorate CO_2/N_2 separation. One Curtin International Postgraduate Conference (OCPC 2018), 26-28th November, Miri, Sarawak, Malaysia.

ABSTRACT

The increase in emission of greenhouse gases (GHGs) specifically, carbon dioxide (CO_2) in recent years due to rapid development of modern civilisation, has been identified as the main contributor to global warming. Existing membrane technology has been applied in gas separation application extensively to limit the emission of GHGs. Due to its superior performance in terms of efficiency and cost effectiveness, membrane technology has undergone intensive development to address related global issues. The aim of this study is to synthesise and develop a new blended mixed matrix membrane (MMM) to enhance gas separation, specifically to improve the CO_2 permeance and selectivity towards separation of CO_2/N_2. Cellulose Acetate Butyrate (CAB) polymer was selected as the polymer matrix material in this study due to the functional groups it comprises which has the capability of achieving high CO_2 permeability. Firstly, the neat membranes were fabricated through the wet phase inversion technique based on different casting conditions. The casting conditions include the studied range for polymer concentration from 3 to 5 wt%, casting thickness range from 200 to 300 µm, solvent evaporation time from 4 to 6 minutes and solvent exchange time for isopropyl alcohol and n-hexane from 15 to 60 minutes with different molecular weight (*Mn*) CAB polymers (*Mn* of 12000, 65000 and 70000). The synthesised membranes under different fabrication conditions were then characterised with scanning electron micrograph (SEM) to determine the morphology of the CAB membrane for CO_2/N_2 separation. The results showed that neat membrane (CAB-70000) fabricated with 4 wt% CAB (Mn of 70000) polymer concentration, 250 µm casting thickness, 5 minutes solvent evaporation time and solvent exchange time of 30 minutes for isopropyl alcohol and n-hexane, achieved the best CO_2/N_2 separation. CAB-70000 showed an average selectivity of 6.12 ± 0.09 and CO_2 permeance up to 227.95 ± 0.39 GPU. Based on the performance of CAB-70000, the multi-walled carbon nanotubes (MWCNTs) were incorporated into the CAB matrix to produce MMM for the enhancement of CO_2/N_2 separation performance. The functionalised-MWCNTs (MWCNTs-F) were produced by mixing Beta-cyclodextrin (β-CD) with MWCNTs. This was to prevent the MWCNTs agglomeration issue caused by Van der Waals attraction forces attributed by the pristine-MWCNTs. Based on the effects of MWCNTs-F loadings, the MMM-0.8F demonstrated the best CO_2 permeance (377.62 ± 1.20 GPU) and selectivity performance (13.17 ± 1.39) at 0.8 wt% MWCNTs-F loadings. The significant increment of separation performance for MMM-0.8F was consequently attributed to the high solubility of CO_2 in nano-channel, which originated from MWCNTs and optimal

loadings of MWCNTs-F incorporated into the MMM. Thus, ensuring the smooth transport of CO_2 gas molecules. In addition, in order to ensure the competitiveness of the membrane, the blend MMM was developed and fabricated by blending different molecular weight (*Mn*) CAB polymers. The study revealed that M2 with *Mn* combination of 70000:30000 at the ratio of 2:1 wt% demonstrated a CO_2/N_2 separation increment of 29.76% as compared to MMM-0.8F. Furthermore, based on the kinetic sorption study, M2 also presented the highest solubility coefficient of $7.58\times10^{12} \pm 1.01 cm^3(STP)/cm^4 cmHg$ due to the high carboxyl (C=O) functional group composition, which improved and expanded the capacity of CAB chains leading to high CO_2 permeance. The CO_2/N_2 binary gas permeation study was conducted on the blend MMMs based on different industrial feed compositions. At the feed composition of 50:50 vol%, the M2 exhibited highest composition selectivity of 7.85 ± 1.48. The reduction of composition selectivity as compared with ideal selectivity was due to the sorption competitive of coupling effect that existed within the mixed gas phase. In summary, this study outlined a detailed direction for the development of blend MMM technology in gas separation process application. The perspective of the newly fabricated blend MMM highlighted in this study is expected to benefit researchers and manufacturers in terms of fabricating a cost effective and high energy savvy membrane with improved gas separation properties for best blend MMM performances.

Keywords: Cellulose Acetate Butyrate; Mixed Matrix Membrane; Blend Mixed Matrix Membrane; Gas Separation; Membrane technology

TABLE OF CONTENTS

LIST OF FIGURES

LIST OF TABLES

NOMENCLATURES

ATR-FTIR	Attenuated Total Reflectance Fourier Transform Infrared Spectroscopy
β-CD	Beta cyclodextrin
CA	Cellulose Acetate
C-O	Ether
C=O	Carbonyl
CAB	Cellulose Acetate Butyrate
CCS	Carbon Capture and Storage
CH_4	Methane
CMS	Carbon molecular sieve
CNTs	Carbon Nanotubes
CO	Carbon monoxide
CO_2	Carbon dioxide
DSC	Differential Scanning Calorimetry
GHG	Greenhouse gases
GPU	Gas permeation unit
hr	hour
IP	Inorganic phase
M_n	Molecular weight
MMM	Mixed matrix membrane
MMMs	Mixed matrix membranes
Min	Minute
MWCNTs	Multi-walled carbon nanotubes
MWCNTs-P	Pristine-multi-walled carbon nanotubes
MWCNTs-F	Functionalized-multi-walled carbon nanotubes
N_2	Nitrogen
-OH	Hydroxyl
O_2	Oxygen
PES	Polyethersulfone
PEG	Poly (ethylene glycol)
PI	Polyimide
PVA	polyvinylalcohol

SEM	Scanning electron microscopy
SWCNTs	Single-walled carbon nanotubes
TCD	Thermal conduction detector
vol %	Volume percentage
wt%	Weight percentage
XPS	X-ray Photoelectron Spectroscopy
XRD	X-ray Diffraction

LIST OF SYMBOLS

Å	Angstrom
A	Effective membrane area (m^2)
a	Ideal separation factor
D	Coefficient of Diffusivity
F	Wetting force
G	Molar flux
l	Membrane thickness (μm)
Mw	Molecular weight (g/mol)
p	Pressure (cmHg)
ΔP	Pressure difference (Pa)
P	Permeance
P_{CO2}	Permeability of carbon dioxide (mol/ m^2s Pa)
P_{N2}	Permeability of nitrogen (mol/ m^2s Pa)
Q	Volumetric flow rate
r	Pore radius (cm)
R	Gas constant (Pa.m^3/mol/K)
S	Coefficient of Solubility
T	Transmittance
T	Temperature (K)

GREEK LETTERS

α	Selectivity
μ	micro
λ	Molecule mean free path
η	Gas Viscosity
γ_L	surface tension of liquid

CHAPTER ONE

INTRODUCTION

1.1 Background

1.1.1 Carbon dioxide and its Global Warming Issue

By 2050 the world population is estimated to reach 10 billion due to rapid urbanisation in developing countries (Tripathi et al., 2019). According to the Population Reference Bureau 2018, an increase of 2.3 billion or 29 % from the 7.6 billion people of the world was expected (Banuri et al., 2019, Toshiko et al., 2018). In this regard, demand for more energy will be required in the 21st century to meet urgent needs of earth's industrialization development. It is predicted that energy demand will increase by 57% in the year 2050 (EIA 2018, Khanna et al., 2019). Fossil fuels being the major contributor to the world energy supply due to abundant and cheap fossil energy supplies, itself has contributed around 65 % of the total carbon dioxide (CO_2) emission to the environment (Andrew 2018, Pan et al., 2019). Consequently, the continuous CO_2 emission has led to global warming, which is due to the excessive discharge of pollutants emitted from the combustion activities in the primary industries (Hashimoto 2019).

The control of anthropogenic CO_2 emissions is one of the most challenging environmental issues faced by industrialised countries due to the large amounts of CO_2 emitted annually into the atmosphere (Carapellucci and Milazzo 2003). Burning of fossil fuels is responsible for the majority of these CO_2 emissions and therefore, there is an urgent need in developing technologies to reduce the CO_2 emissions (Hashimoto 2019, Kentish et al., 2008). The conventional process for CO_2 separation includes absorptions, adsorptions, cryogenic distillations, and membrane technologies. The advantages and disadvantages of each technology are summarised in **Table 1.1**. According to this **Table 1.1**, membrane technology

is amongst the best technologies for CO_2 separation. The membrane technology offers high-energy efficiency and process simplicity with only one major disadvantage which is low selectivity thus, making membrane gas separation extremely attractive and promising for CO_2 separation (Abertz et al., 2006). The ability to selectively pass one component in a mixture while rejecting others is described as the perfect separation device (Wang et al., 2014).

Table 1.1 Conventional CO_2 separation technologies

Processes	Advantages	Disadvantages	Reference
Absorption	• High efficiencies of absorption (>90 %). • Sorbents are able to be regenerated through depressurisations and heating. • Most developed technology for CO_2 separations.	• Efficiencies of absorption highly dependent on CO_2 concentrations. • Large amount of heats essential for the regeneration of sorbents. • Have to fully understand the degradations of sorbents impacts on the environment.	(Bhown and Freeman. 2011, Leung et al., 2014)
Adsorption	• Reversible process and recyclable absorbents. • High efficiencies of adsorptions (>85%)	• High temperature adsorbents are needed. • Require high energy for desorption of CO_2.	(Takamura et al., 2001)
Membrane Separations	• Technology implemented for many years for other gases separations. • High efficiencies of separations (>80%).	• Several problems on operations which include the fouling and low fluxes.	(Aaron and Tsouris. 2005)
Cryogenic Distillation	• Matured process. • Technology implemented for many years for CO_2 recoveries.	• Feasible only for high concentration of CO_2 (>90%). • Have to be applied extremely low temperatures. • Highly energy ntensive technology.	(Gottlicher and Pruschek. 1997)

1.1.2 Membrane gas separation technology

In the past few decades, researchers have contributed much effort in combating this global issue to limit and minimise the impact of greenhouse gases (GHGs). According to Graham in 1866 with Loeb and Sourirajan (Loeb et al., 1997, Kentish et al, 2008), the concept of membrane separation was proposed by developing the first anisotropic membrane in 1961. Gas separation membranes were first commercialised in 1977 when Monsanto/Perma released their hydrogen recovery system (Kentish et al., 2008). The success in implementing membrane technology and other gas membrane systems by Cynara et al. (1990) led to substantial innovation during the 1980s and 1990s into membrane materials (Koros W. 1993). These innovations have improved the gas separation efficiency by 57% and membrane durability, making membrane gas separation commercially competitive with existing separation technologies (Baker 2002, Kentish et al., 2008).

In the past few years, membrane separation technology has been utilised extensively for gas separation purpose and is currently applied to a wide range of industrial processes (Yang et al., 2008, Kappel et al., 2014, Barnes et al., 2014, Zhu et al., 2014, Rezakazemi et al., 2018). This is because membrane gas separation consumes relatively lower energies, and ease of scale-up without the need of any additives due to its simplicity in concept and operation (Rezakazemi et al., 2014, Dinda 2013). Moreover, the membrane gas separation technology can operate under mild conditions and can function well when it is combined with other processes as it can be easily integrated into simple automation, thus, making the operation simple (Baker 2012). Even though the membrane life span can be rather short due to aging effects, the overall cost of fabrication is still lower than other processes (Mulder 2012). Hence, it can be concluded that the membrane technology offers the most favourable approach for CO_2 separation due to its

advantages such as cost effectiveness, environmentally friendly, simplicity and versatility (Chen 2002).

In membrane gas separation, the selection of the polymer matrix material plays an important role because each polymer consists of different polymer compositions and it can affect the interaction between permeant and membrane. Hence, the diffusion characteristics and separation performance of the membrane synthesised (Lalia et al., 2013, Zha et al., 2015, Feng et al., 2015, Rezakazemi et al., 2018, Shekhawat 2003). Meanwhile, the membrane separation performance is indicated by two main parameters, which are selectivity and gas permeance. In an ideal situation, both high selectivity and permeance are preferred as this induces less capital costs and operating expenses for the industries (Paradise and Goswami, 2007, Low et al., 2013). Therefore, in order to achieve high permeance and selectivity performance membrane, the polymer matrix material selection of the membrane is a crucial factor (Friess et al., 2011).

1.1.3 Polymeric membrane

Cellulose is amongst the best of all polymeric materials for membrane fabrication as it is abundantly available, able to degrade naturally, has high fouling resistance and it is compatible biologically (Asgarkhani et al., 2013). There are numerous types of cellulose derivatives, such as cellulose acetate (CA), cellulose butyrate (CB), cellulose propionate (CP), and cellulose acetate butyrate (CAB). CAB was first investigated and studied by Sourirajan (1980) back in 1958, then followed by Manjikian and others in reverse osmosis (RO) separation (Wang et al., 1994). According to Wang et al. (1994) and Ohya et al. (1980), it was reported that the CAB membrane possessed high solute separation with high membrane permeability, and that CAB provided ease of fabrication as some pre-treatment was negligible (Ohya et al., 1980, Wang et al., 1994).

Among all the cellulose derivatives, CAB possess some interesting characteristics including, well film forming properties, acetyl and butyryl functional groups, which can effectively improve and further expand the capacity of the cellulose chain giving high sorption characteristic, as well as high impact, weather and chemical resistance (Feng et al., 2015, Basu et al., 2010b, Kunthadong et al., 2015). In addition, CAB, which is fabricated mainly by fibrous cellulose and pre-treated with acetic, butyric, sulphuric and anhydrides acids, presents a relatively higher permeability of CO_2 than other cellulose derivatives (Chen et al., 2014). Therefore, CAB is an excellent polymer to synthesise high efficiency CO_2/N_2 separation membrane. However, the major drawback of all polymeric membranes is having low selectivity (Liu et al., 2013, Wang et al., 1994). In this regard, to improve the selectivity performance of the polymeric membrane, the mixed matrix membrane (MMM) is proposed with the incorporation of inorganic fillers into the polymer matrix.

1.1.4 Mixed matrix membrane (MMM)

The membrane separation properties of the polymeric membrane can be improved with the development of MMMs. The MMM is a heterogeneous membrane consisting of inorganic fillers embedded in a polymer matrix, which can be fabricated into hollow fibre or a flat sheet membrane, as shown in **Figure 1.1** (Kang et al., 2015, Aroon, 2010b). The MMMs are well known for its capability to enhance the properties of polymeric membranes (Bernardo et al., 2009). With the inorganic fillers embedded in the form of nanoparticles incorporated into the polymeric matrix, the fabrication of MMM with the combination of polymer matrix and inorganic fillers generally provide greater gas separation performance due to the enhance permeance of the MMM (Jawad et al., 2015).

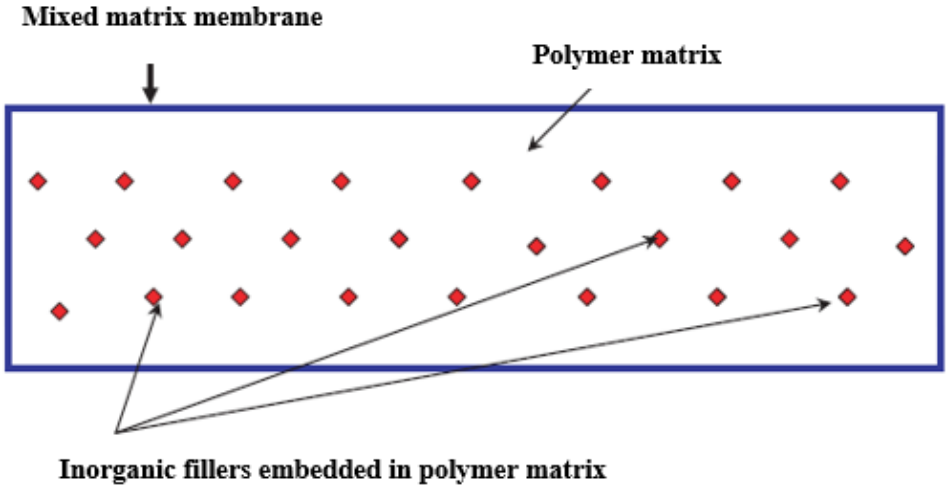

Figure 1.1 Schematic diagram of the inorganic dispersed phase embedded in the polymer matrix (Aroon, 2010b)

Technically, the mixing of the inorganic component in MMMs is a feasible approach for modification of the membrane, to enhance the selectivity for a given gas, mixture by increasing the, sorption of the desired, gas component within, the MMM (Ismail et al., 2011). Moreover, the MMMs are proven to have better physical, thermal and mechanical properties towards inorganic chemical due to their excellent durability properties inherited from inorganic fillers (Hu et al., 1997). Consequently, this makes the MMM better in stability, high resistance and tougher against the change in perm-selectivity with pressure and temperature (Zhao et al., 2014). Subsequently, the membrane is often evaluated based on Robeson's upper bound curve to indicate the membrane separation effectiveness and efficiencies. Membranes, with separation performances above this curve are attractive to the industrial applications. As a result, there is an urgent need to advance the membrane performance, such as permeability and selectivity with the integration of second phase polymer to fabricate blend MMM (Isanejad and Mohammadi 2018).

1.1.5 Blend mixed matrix membrane

Recently, the development of membrane technology has focused on fabricating blend MMM that combine the advantages of blending two or more polymeric polymers approaches to create a new material with different physical properties (Visakh et al., 2016). The polymers used in the blending can be between glassy-glassy, glassy-rubbery and rubbery-rubbery polymers at different ratios of polymer concentration or molecular weight (*Mn*) (Abdul Mannan et al., 2019, Joseph et al., 2018, Ali et al., 2018). Subsequently, the blending of polymeric polymers at different *Mn* to fabricate blend MMM is an efficient method to modify polymer chain packing and improve the polymer chain packing characteristic size. As a result, the fraction of amorphous region for gas transport is enhanced (Wang et al., 2014). Moreover, the strong interaction between the polymer blending can significantly enhance gas transport behaviour due to higher polymer chain mobility, which can expand the permeability capacity within the blend MMM (Zhao et al., 2012, Shan et al., 2012). In addition, with the incorporation of inorganic fillers such as MWCNTs into the blend MMM, the selectivity is enhanced due to the affinity of quadra- nonpolar gas such as CO_2, compared to inert gases for example N_2, H_2, or O_2 (Murali et al., 2010).

According to Wang et al. (2014), the poly-ethylene glycol (PEG) based polymers at different *Mn* were utilised to fabricate blend MMMs to investigate the *Mn* dependence. They reported that blending low *Mn* of PEG-based polymers enhanced CO_2/N_2 separation. This is because the incorporation of low *Mn* of PEGs tends to inhibit crystallisation of Pebax, resulting in the increase of CO_2 diffusivity and solubility (Wang et al., 2014). Meanwhile, Dai et al. (2018) also stated that blending *Mn* of 250 PEG dimethyl ether (DME) with *Mn* of 500 PEGDME into Nafion membrane will further enhance the CO_2 permeability from 57.4 to 446

Barrer and CO_2/N_2 selectivity from 3.3 to 37 (Dai et al., 2018). The Nafion/PEGDME blend MMM is able to demonstrate higher CO_2 permeation properties by incorporating low *Mn* of PEGDME due to the hydrophilic PEGDME chains that enhanced the CO_2 transport (Dai et al., 2018). As a result, blending polymer at different *Mn* is a vital factor for blend MMM, as it has significant impact on the CO_2/N_2 separation performance (Dilshad et al., 2019).

1.2 Problem Statement

For the past decades, human activities have contributed to the major release of greenhouse gases (GHGs) such as CO_2 to the environment, and the anthropogenic CO_2 are mainly from fossil fuel combustion related to activities (Ziyarati et al., 2019, Songolzadeh et al., 2014). The cumulative effects of GHGs has led to ozone depletion, which allows more heat to enter and trap within the earth causing global warming and climate change (Deng et al., 2019, Li et al., 2018). To address the climate change issue, GHGs specifically the CO_2 are required to be separated from the industrial gases to avoid emitting into the atmosphere as a mitigation measure to protect the ozone layer (Awasti et al., 2019). In order to achieve this goal, membrane technology has been recognised as a highly promising technology for the separation of bulk acidic gases.

As a result, membrane technology has been developed to address the global warming issue. For instance, through the membrane technology it had successfully separate the CO_2 using membrane that demonstrated high CO_2 permeance, high selectivity, and defect free membrane-based gas separation process (Toshiko et al., 2018). In the past decades, polymeric membranes have been widely used in the development of gas separation membranes due to their rigid and selective nature that offer decent mechanical stability under high pressure, easy formability and excellent scalability (Kentish et al., 2008). However, for membrane to achieve

high permeability and selectivity it has to rely closely on the membrane preparation parameters such as, membrane casting thickness, polymer concentration and solvent evaporating time (Adewole et al., 2015, Jawad et al., 2015a, Ong et al., 2008, Ngang et al., 2012).

Apart from the polymeric membrane, advantages and fabrication parameters discussed above, the trade-off between permeability and selectivity is the major challenge confronted by the polymeric membrane (Bozorg et al., 2019). Therefore, to address the limitation of polymeric membranes to achieve high CO_2/N_2 separation performance. The membrane development has focused on combining polymer matrix with inorganic fillers to fabricate mixed matrix membrane (MMM) to enhance the membrane structure that allows more flexible transportation of gas, hence, greater CO_2 separation efficiency (Ghadimi et al., 2014).

The MMM has gained great attention as an excellent candidate in membrane technology in the development of CO_2 separation, given its compatible features and properties required for effective gas separation. The MMM provides the opportunity to overcome the limitations specifically, low selectivity in polymeric membrane, and achieve higher CO_2 separation performances (Chung et al., 2007). Nevertheless, to fabricate a MMM with high CO_2 permeance and selectivity, the loadings of functionalised multi-walled carbon nanotubes (MWCNTs-F) incorporated into the polymer matrix need to be optimised to reduce the agglomeration issue caused by the Van der Waals attraction forces within the membrane structure, which can hinder the permeance of gas due to the formation of clusters that lead to poor interfacial interaction between CAB matrix and MWNCTs-F. Although MMM have demonstrated outstanding separation performance, there is still an urgent need to further

improve the permeance and selectivity performance of the MMM to ensure higher efficiencies in separation towards CO_2/N_2.

In this regard, to enhance the separation performance of MMM, the development of membrane technology has focused on blending polymers to produce blend MMM (Feng et al., 2019). According to Shahid and Nijmeijer (2017), polymer blending is an effective method to modify polymer properties, because polymer blending is a simple, reproducible and easy processing method. The blend MMM is generally fabricated with different compositions of polymers and functional groups as this can enhance the permeability and separation performance of the membrane due to the combine benefit effects in terms of mechanical strength and rigidity, and also good flexibility and high permeability by blending the polymers (Moghadassi et al., 2013). According to Shirvani et al. (2019), they investigated the influence of blending polyurethane/poly(vinyl alcohol) (PU/PVA) with silica nanoparticles. They concluded that by blending low *Mn* of PVA (200) with PU, the CO_2 solubility increased from 15.9 ± 0.8 to 38.3 ± 1.9 Barrer. This was attributed to strong interactions with the non-polar group C-O-C in the soft segments of PU and the high intensity –OH groups present in low *Mn* of PVA (Shirvani et al., 2019). Thus, the effect of blending polymers at different *Mn* is a significant factor to fabricate high CO_2 permeance membrane due to the membrane composition blend, which can promote higher CO_2 solubility (Shan et al., 2012). Therefore, the challenge of the current work is to synthesise a CAB blend MMM with high CO_2 permeance and CO_2/N_2 separation performance based on the combination of CAB *Mn*, together with the incorporation of optimal MWCNTs-F loadings into the CAB polymer matrix. In particular, the role of functional groups present in CAB blend MMMs was investigated with the aim to achieve high CO_2/N_2 separation and improving the membrane gas permeance.

1.3 Research questions

The research questions of this study are:

1. What are the fabrication effects of membrane fabrication parameters in developing a good performance neat membrane for CO_2/N_2 separation?
2. What is the fundamental interaction between CAB and MWCNTs on the membrane permeance and selectivity performance of the fabricated MMM?
3. What is the effects of MWCNTs loadings on MMM (CAB/MWCNTs-F) in term of membrane morphology, gas permeance, and CO_2/N_2 separation performance?
4. How the blending of different *Mn* CAB polymers with MWCNTs-F to fabricate blend MMM can enhance the gas permeance and CO_2/N_2 separation performance?
5. What is the kinetic sorption coefficient of different *Mn* CAB polymers? What is the binary gas separation performance of the blend MMM synthesised as compared to ideal selectivity?

1.4 Objectives

The main goal of this research study is to fabricate neat CAB membranes, MMMs and blend MMMs to achieve high efficiencies and separation performance towards CO_2/N_2. In particular, to investigate the relation associated between the fabrication parameters and gas permeation properties of CAB polymer. Henceforth, the research objectives are:

1. To optimise the CAB membrane CO_2 permeance and CO_2/N_2 selectivity based on fabrication parameters, such as, effect of polymer concentration, casting thickness, solvent evaporation time, solvent exchange time for isopropyl alcohol and n-hexane, and *Mn* of CAB polymers that is associated with dense structure and smooth membrane surface morphology.

2. To determine the interaction between CAB and MWCNTs in developing a defect-free MMM towards high CO_2/N_2 separation, supported with the characterisation results including SEM, ATR-FTIR, contact angle analysis, XRD, DSC and EDX-mapping analysis.
3. To study the enhancement of CO_2 permeance and CO_2/N_2 separation performance by optimising the MWCNTs-F loadings incorporated into CAB matrix.
4. To develop blend MMMs (CAB-MWCNTs-F) at different *Mn* CAB polymer combinations to enhance the CO_2 permeance based on the combined composition of functional groups contributed by the CAB polymers and to optimise its selectivity performance further towards high CO_2/N_2 separation.
5. To evaluate diffusivity and solubility coefficients correlated to the blend MMMs in CO_2/N_2 gas separation performance using the kinetic sorption study.

1.5 Significance

The membrane technology is being considered as a highly promising method for efficient CO_2 separations. As a result, there are many ongoing researches synthesising membrane with different types of polymers targeted for high separation performance. The CAB especially, has high tolerance to solvent and is chemically stable as well as suitable to be used as a polymer matrix to develop the blend MMM. In addition, among the cellulose materials, CAB has the functional groups such as carboxyl, acetyl and hydroxyl, which can expand the capacity of chain spacing and improve the CO_2 permeance in the gas separation performance. However, no research has reported performing synthesise of blend MMM from CAB and MWCNTs. Thus, the fabrication of blend MMM was intensively studied in this research to enhance the permeance and selectivity of CO_2/N_2 separation.

Initially, the CAB polymeric membrane fabrication parameters is to optimise in terms of casting thickness, polymer concentration, solvent evaporation time and solvent exchange time for isopropyl alcohol and n-hexane to improve CO_2 permeance within the CAB polymer matrix. All the above-mentioned parameters are important key factors in demonstrating that the effects of fabrication parameters have direct influence on the membrane morphology and CO_2/N_2 separation performance of the membrane. In the meantime, studies had found that the incorporation of MWCNTs into the membrane matrix can enhanced the membrane's hydrophilicity, permeate flux, anti-fouling property and mechanical strength (Ho et al., 2017). However, the preparation of MMM based on MWCNTs is still a great challenge, specifically the formation of large bundle when high quantity amount of CNTs were incorporated to the polymer matrix, due to the Van der Waals attraction. Agglomeration of MWCNTs results in heterogeneity in membrane surface and unwanted membrane properties such as low permeance and membrane selectivity (Jawad et al., 2015a). For this reason, the incorporation of MWCNTs-P and MWCNTs-F into CAB polymer matrix has been studied along with the optimum loadings of MWCNTs-F to enhance the selectivity performance of the synthesised MMM. Therefore, through this optimisation study of MWCNTs-F, the agglomeration issue is overcome.

Meanwhile, the enhancement of membrane selectivity towards higher efficiencies is favourable for the industries, as it can improve the overall separation performance of the membrane application. At the moment, limited study has been carried out to improve the CO_2/N_2 separation performance for blend MMM that is based on CAB polymer matrix. For this reason, blend MMM is synthesised with different molecular weight (*Mn*) of CAB polymers to enhance the CO_2 permeance of the blend MMM. The increment in CO_2 permeance for the blend MMM is associated with the highly hydrophilic groups, such as C=O and O-H, which are able

to increase the hydrophilicity of the blend MMM. Consequently, as the hydrophilicity of the blend MMM increases, this leads to stronger dipole-quadrupole interaction between the non-polar CO_2 molecules with polar O-H group, thus, causing the blend MMM to have higher affinity towards CO_2 molecules and subsequently the CO_2 permeance for blend MMM increases.

Additionally, the kinetic gas sorption study was conducted to determine the diffusivity and solubility coefficients based on the fabricated blend MMMs. Up to date, limited literatures have studied the sorption thermodynamics and kinetics related to CAB based blend MMMs. Hence, by evaluating the kinetic coefficients of the blend MMMs, the motion of interaction between the inter-chain hydrogen bonding, which leads to increase of membrane chain packing associated with the penetrant gas molecules are determined based on the solution diffusion mechanism. Besides, no literatures of CO_2/N_2 binary gas permeation study have been conducted on CAB blend MMM. The binary gas permeation study of the blend MMM is essential in improving CO_2 separation performance, as it is a material performance evaluation under conditions that mimic post-combustion CO_2 separation, which is utilised to study the ideal conditions and chemical interactions that could potentially enhance gas separation performance. Therefore, from this study the newly fabricated blend MMM is expected to increase both permeance and selectivity towards CO_2/N_2. Subsequently, due to the enhance separation performance of the newly synthesised blend MMM, it can highly reduce the operational costs and energy requirements of the membrane application and industries.

1.6 Scope of study

In this present study, the effects of the preparation properties of the CAB membrane were investigated. This includes CAB polymer concentration (3 wt% to 5 wt%), membrane casting thickness (200 µm to 300 µm), solvent evaporation time (4 minutes to 6 minutes), solvent exchange time for isopropyl alcohol and n-hexane (15 minutes to 60 minutes), and evaluation of CAB molecular weight (*Mn*) from 12000 to 70000. The synthesised membranes were characterised using scanning electron microscopy (SEM) to determine the membrane surface and cross-sectional morphology. The X-ray photoelectron spectroscopy (XPS) characterisation was conducted to determine the element composition of CAB-12000, CAB-65000 and CAB-70000. Meanwhile, for the membrane performance, the CO_2 and N_2 permeance was obtained to evaluate the ideal selectivity of CO_2/N_2 separation. The optimal CAB membrane parameters determined was then utilised to prepare the MMM. The MMM was synthesised according to the optimal parameters from CAB membrane as a continuous study to further enhance the selectivity performance of the CAB membrane.

In the MMM synthesis, the pristine-MMM (MMM-1.0P) incorporated with MWCNTs-P and functionalised-MMM (MMM-1.0F) integrated with MWCNTs-F, were characterised first using SEM, Attenuated Total Reflectance Fourier Transform Infrared spectroscopy (ATR-FTIR), Differential Scanning Calorimetry (DSC), and X-ray Diffraction (XRD) to evaluate the compatibility of incorporating functionalisation of MWCNTs-F into the CAB matrix. In addition, the effects of loadings of MWCNTs-F incorporated into CAB polymers was evaluated based on the membrane morphology and separation performance yield to determine the optimal loadings of MWCNTs-F for the MMM. Furthermore, the separation performance of the MMM-1.0P and MMM-1.0F were then compared with the optimal CAB membrane (CAB-70000) to

evaluate the best permeance and selectivity towards the separation of CO_2 from CO_2/N_2. The best MMM (MMM-1.0F) determined was then used to synthesise the blend MMM due to the fact that the blend MMM can enhance the CO_2 permeance and lead to high separation efficiency based on the intermolecular interaction, which can modify the chain packing.

In this regard, it is highly essential to find the optimum blend combination of CAB polymers at different molecular weights (*Mn*) for the fabrication of blend MMM incorporated with optimised loadings of MWCNTs-F, as this is a promising method to enhance the selectivity performance of the blend MMM by modifying the intermolecular polymer chain packing. Thus, all the blend MMMs synthesised were compared in terms of the membrane morphologies and gas separation performance supported by various characterisation results. With regards to the membrane separation performance, the CO_2/N_2 permeance and selectivity were supported with the characterisation results of SEM, ATR-FTIR, XRD, DSC and Contact angle. Moreover, the kinetic sorption of the synthesised blend-MMMs at different CAB polymer combinations was further studied. The CO_2 diffusion coefficients and CO_2 solubility coefficients were evaluated to identify the mass transport for CO_2 through the prepared blend MMMs. Finally, the best blend MMM in terms of CO_2/N_2 selectivity performance was tested using CO_2/N_2 binary gas mixture to evaluate the blend MMM actual performance based on the industrial post-combustion conditions. Consequently, the CO_2/N_2 feed composition percentage of 20/80 vol%, 40/60 vol%, 50/50 vol%, 60/40 vol% and 80/20 vol% were utilised to evaluate the permeation and separation performances of the blend MMMs.

1.7 Layout of Thesis

This thesis is focused on the fabrication and characterisation of CAB neat membrane, MMM, and blend MMM towards high CO_2/N_2 separation performance. Thus, it is outlined in

five chapters as exemplified in **Figure 1.2**. Each chapter is summarised and addressed as below:

In Chapter 1, a general background on the global issue of greenhouse gases specifically CO_2 was addressed and conventional technologies to mitigate the CO_2 was highlighted. In addition, the overview of gas separation by membrane technology was also presented followed by the overview of polymeric membrane and the development of MMM and properties introduced in this chapter. This was followed by the problem statement and objectives. The significance of this research study was defined in the next section. Then, it was supported by the scope of study and thesis organisation to conclude Chapter 1.

In Chapter 2, a review on the post combustion CO_2 capture methods that was commercialised in the industry was presented. Moreover, the application of membrane technology for CO_2 separation was presented followed by the definition of polymeric membrane, inorganic membrane, MMM and blend MMM. Meanwhile, for the membrane synthesise preparation parameters, which include effects of polymer concentrations, casting thicknesses, solvent evaporation times, solvent exchange times and polymer molecular weights were discussed in this section. The inorganic fillers (CNTs) were then introduced together with the challenges to incorporate the inorganic fillers with the polymer matrix was presented later in this chapter. The polymer blend MMM in gas separation was then explored based on the effect of molecular weight. Additionally, the transport mechanisms for membrane gas separation was presented in the last part of this chapter.

In Chapter 3, the details of the materials utilised, and experimental procedures were discussed explicitly. This included the fabrication of neat membrane, CNTs functionalisation with Chen's soft cutting method, and the development of MMM between CAB and MWCNTs. Besides, the characterisation methods used in this thesis were introduced in this chapter to support the permeance and selectivity performance obtained from the membrane throughout the discussion parts. On the other hand, the operation of test rig for CO_2/N_2 permeance was highlighted in this chapter. The kinetic sorption model derived in this chapter, explained the mathematical derivation for the gas permeation model of solution-diffusion mechanism.

Chapter 4 covers all the results of the experiments and explanations according to each objective. Experimental results on the effects of CAB fabrication parameters on the surface morphology, cross-sectional structure and gas separation performance were studied in detail supported by the characterisation results to explain the phenomenon. Then, the optimised preparation parameters for CAB membrane were further utilised to incorporate with MWCNTs for the synthesis of MMM with the purpose of enhancing the membrane selectivity. Furthermore, the loadings of MWCNTs on MMM were evaluated in this chapter. Moreover, blend MMM, which was fabricated using two CAB polymer combination was also discussed in this chapter. Besides that, both the kinetic sorption and binary gas permeation were studied for the blend MMMs, which were synthesised to determine the diffusion and solubility coefficients and the actual separation performance in real world application.

Lastly, in Chapter 5, the results of the findings in this research study were summarised according to each of the research objectives, which were primarily focused towards the synthesised high-performance blend MMM with good CO_2 permeance and CO_2/N_2 separation.

This was followed by concluding remarks and some proposed recommendations for future outlook of this research work.

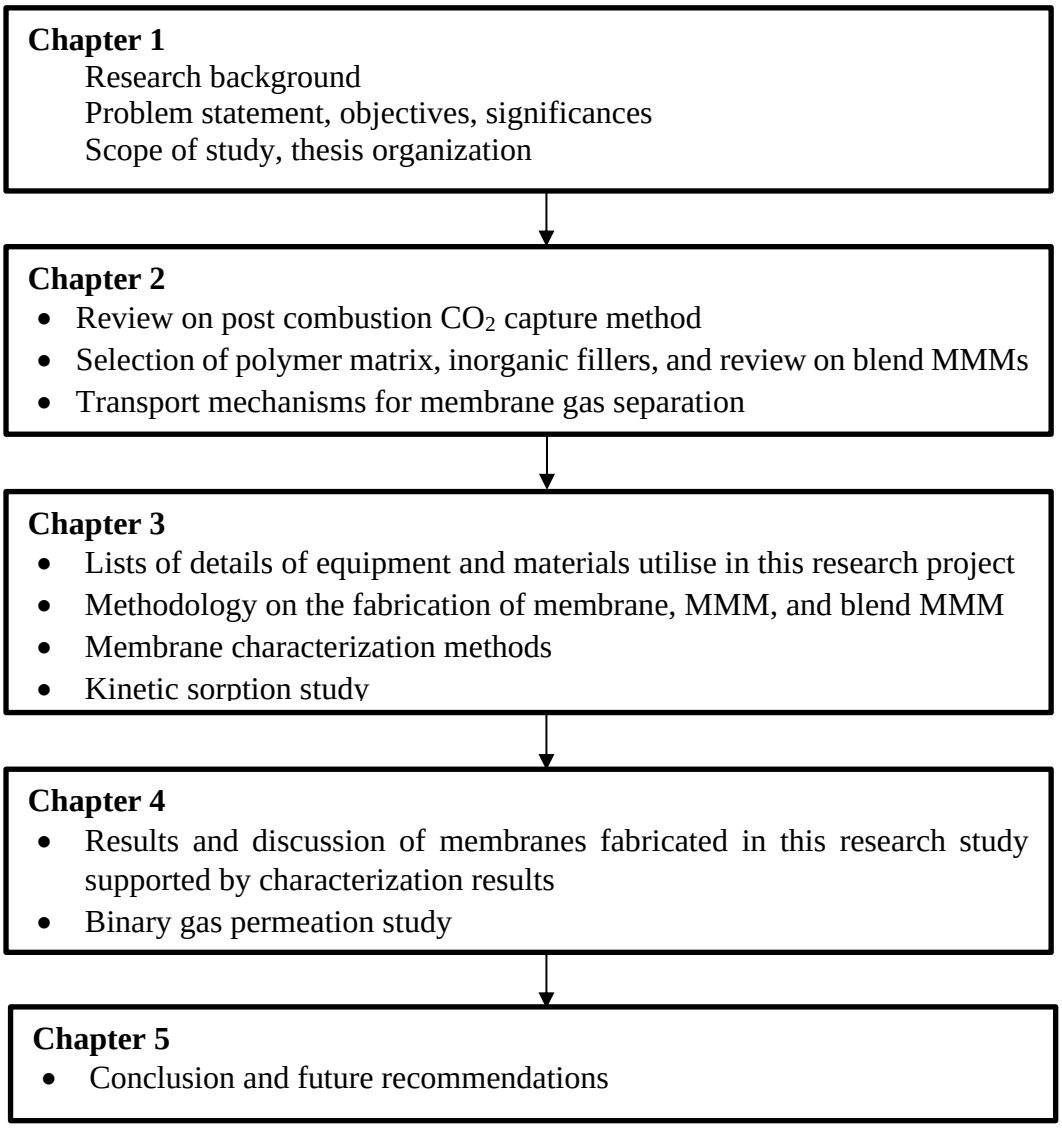

Figure 1.2 Overall thesis layout flowchart

CHAPTER TWO

LITERATURE REVIEW

2.1 Global issue of carbon dioxide as Greenhouse Gases (GHGs)

Carbon dioxide (CO_2) has been identified as the main constituent of greenhouse gases (GHGs), causing temperature changes that are irreversible by natural processes on timescales relevant to human societies (Venturi et al., 2019). Halting climate change therefore requires that CO_2 emissions from all sources need to be either eliminated or matched by an equal amount of anthropogenic CO_2 removal from the atmosphere (Matthews et al., 2018). According to Zhang and Tremblay (2019), the major sources of CO_2 (20%) and N_2 (50%) emissions originate from the natural gas streams, biogas and flue gas from fossil fuel combustion, and they are still the main source of energy output throughout the world (Zhang and Trembly 2019, Hake et al., 2019). The substantial growth of CO_2 emissions over the past 150 years has resulted in a significant increase of the atmospheric CO_2 concentration by approximately 60%, which favours the depletion of ozone layer, thus, causing the increase of the Earth's average temperature (Zhang et al., 2015). The increasing upward trend of the Earth's average temperature can affect human health, lives and industries associated with temperature ascension (Pearce et al., 2019, Mavrotas et al., 2000).

In this regard, Carbon Capture and Storage (CSS) system and low-emission fossil fuel technologies have been introduced to limit the emission of GHGs, particularly CO_2, to address the problems associated with climate change (Zhang et al., 2014). Gas separation can be accomplished either through chemical solvent technology or membrane technology (Pan et al., 2012). The membrane technology, in contrast, is more suitable as compared to chemical solvent

technology due to several advantages such as energy efficiency, eco-friendly and cheaper operational costs (Shelley, 2009, Takht Ravanchi et al., 2009, Bernardo et al., 2009).

2.2 Membrane technology

The application of membrane technology in separating CO_2 has shown a huge increase since its first invention in 1981, which focused on applications with high amounts of CO_2 emission (Zhao et al., 2008). The membrane gas separation technology has been built up with the purpose of separating the individual gas components based on the different permeation rates of each gas component through a thin membrane barrier (Powell and Qiao, 2006). Various conditions from the outer environment can affect the membrane transportation, which include convection and diffusion of individual molecules, induced by an electric field or concentration, pressure or temperature gradient (Baker and Lokhandwala 2008). As for the membrane technology, the gas separation process is mainly driven by differences in concentration whereby, the feed stream has higher gas pressure and the permeate stream is at atmospheric pressure by default. As a result, due to the concentration differences on each side, the gas component flows from the high-pressure side to the lower side.

As depicted in **Figure 2.1**, this is the basic concept of membrane separation technology, whereby the separating driving force is initiated by the different concentration gradients across the membrane (Dortmundt and Doshi, 1999). The membrane separation performance characteristics are commonly indicated by permeation and selectivity. Permeability is defined as the ability of the permeants to pass through a membrane. While, selectivity is defined as the ratio of permeability of the more permeable component to that of the less permeable (Kohl and Nielsen, 1997). In an ideal situation, high permeability is preferable while maintaining high

selectivity, therefore smaller membrane area and lower driving force are required. Thus, such ideal conditions require less operating costs and hence, lower capital costs.

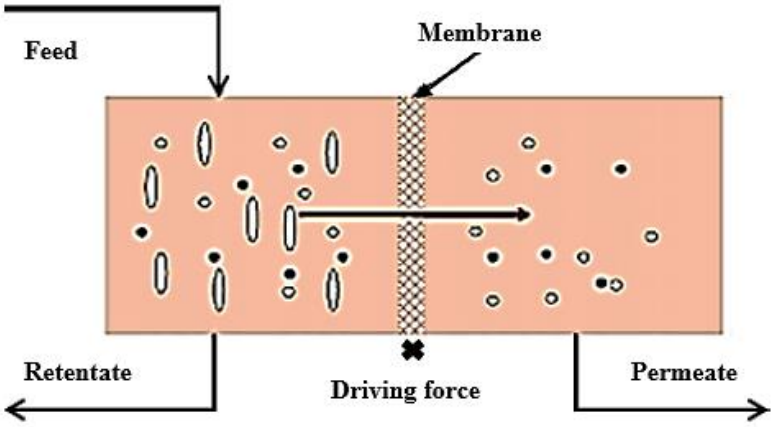

Figure 2.1 Principle concept of membrane separation process (Ismail et al. 2009)

Consequently, it is highly important to consider both the parameters to ensure high efficient separation in all commercial gas separation applications (Ismail et al., 2009, Zhang et al., 2013). In addition, Paradise and Goswami (2007) further highlighted that in order to manufacture standard membrane modules, permeability and selectivity are not the only important factors (Low et al., 2013). The ideal membrane should be thermally and chemically robust, plasticisation resistant to guarantee the continual performance throughout the long time periods of usage (Kentish et al., 2008).

Specifically, the membrane can then be further classified into symmetrical membranes or anisotropic membranes, as illustrated in **Figure 2.2** (Takht Ravanchi et al., 2009). Besides, the membranes are typically categorised based on the synthesised material used in the fabrication process into three main types, which are the polymeric membranes, inorganic membranes and mixed matrix membranes (MMMs) (Kentish et al., 2008). The polymeric membrane especially, has received great attention in the early stage of membrane development because of its superior

thermal, chemical and plasticisation resilience, as well as substantial mechanical strength, which makes it attractive in membrane gas separation (Chung 1996).

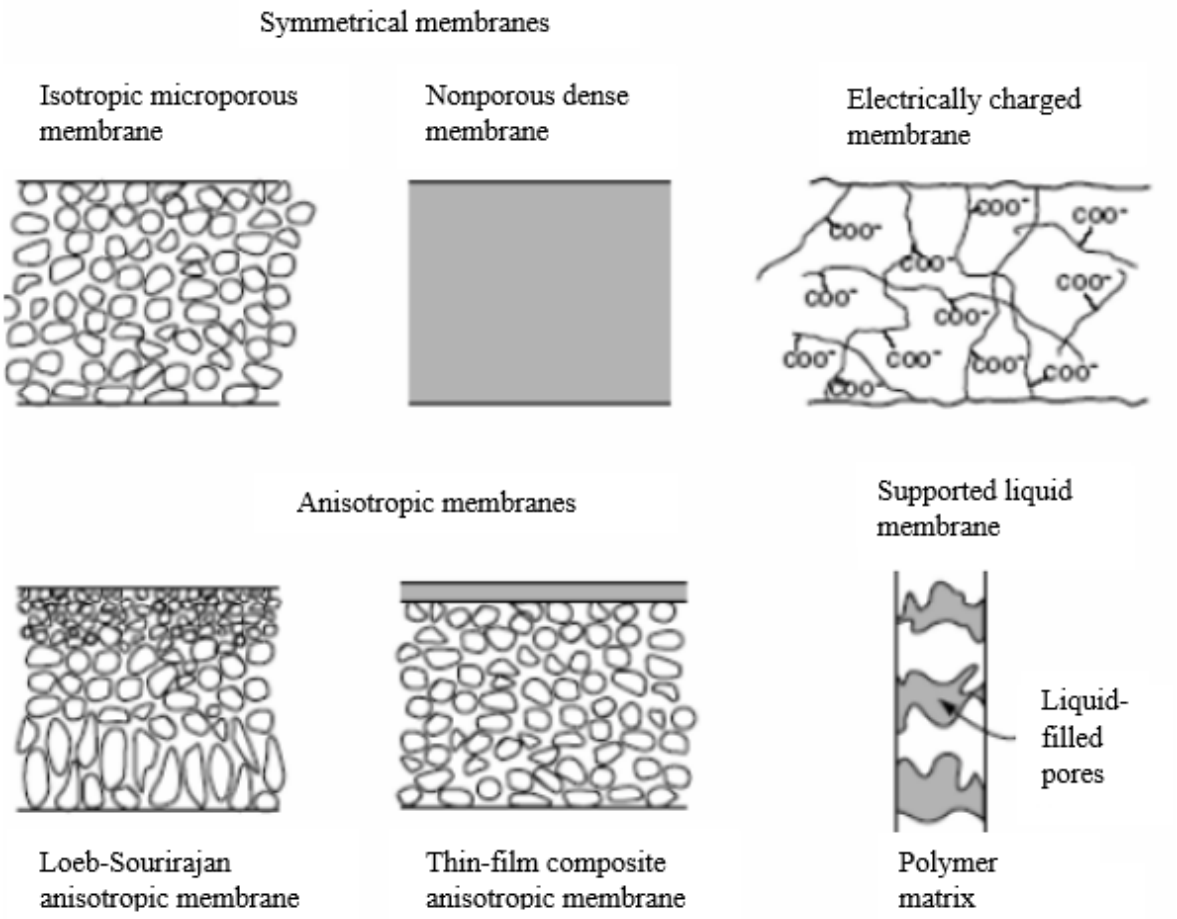

Figure 2.2 Diverse types of principle membrane (Takht Ravanchi et al., 2009)

2.3 Polymeric membrane

The polymeric membranes are normally dense or porous, which can be further categorised into rubbery and glassy polymers (Kentish et al., 2008). Both the rubbery and glassy polymers are distinguished by the operating temperature relative to the glass transition temperature of the polymer (Adewole et al., 2013). Rubbery membranes usually operate above the glass transition temperature, while glassy membranes operate below the glass transition temperature, as depicted in **Figure 2.3**. As the temperature increases, the rubbery polymer will have more free

volume within the membrane due to the increase in polymer volume. However, because of temperature constraint, the glassy polymer will show a decline in the fractional free volume, which correlates with the increase in temperature (Sanyal et al., 2018, Kentish et al., 2008).

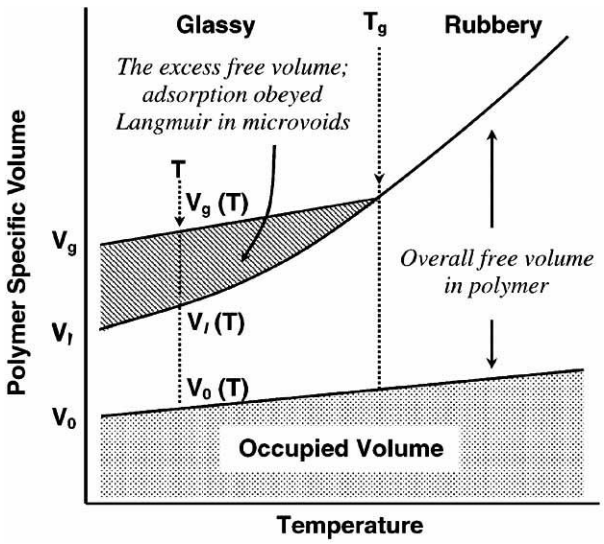

Figure 2.3 Relationship between the polymer specific volume and temperature in polymer (Kanehashi and Nagai, 2005)

The characteristics of the rubbery polymer are soft and elastic. Due to its elasticity the polymer can rotate around its axis from the polymer backbone segments, while the glassy polymer is rigid and tough due to its steric hindrance along the polymer backbone, which limits the rotation of the polymer segments (Bernardo et al., 2009). This allows the rubbery polymer to withstand the high elevated temperature, although it has low selectivity due to big pore volume. On the other hand, the glassy polymer has high selectivity but unable to withstand the elevated temperature. Both the rubbery and glassy polymers are the main membranes that have received attention from the industry due to their good separation properties and chemical stability, which have been applied to CO_2 gas separation (Takht Ravanchi et al., 2009).

The selection of membrane material in membrane fabrication is one of the crucial factors to ensure that the membrane produced can meet the targeted gas separation and operating conditions. The cellulose-based material is commonly utilised in gas separation due to its attractive properties including good flexibility and moderate rigid chains (Podall 1971). Amongst all the cellulose esters, cellulose acetate butyrate (CAB) has good chlorine tolerance, solubility and chemical stability, thus, making it an ideal candidate in membrane gas separation field (Abetz et al., 2006, Chen et al., 2008). However, for the majority of the polymeric membranes, there is a trade-off relationship between permeability and selectivity whereby, a high selectivity polymeric membrane tends to have low permeance and vice versa (Kentish et al., 2008). According to Robeson (1991), this trade-off between permeability and selectivity can be represented as an upper bound membrane performance (Robeson 1991).

2.3.1 Robeson's Chart

The trade-off between permeability and selectivity has been a serious issue faced by the polymeric membrane over the years. For this reason, the relationship between permeability and selectivity is always inversely proportional to each other. Consequently, membrane with high gas permeability is always accompanied by low selectivity performance and this is the well-known trade-off connection between permeability and selectivity (Zhang et al., 2013). In this regard, an empirical formula was proposed by Robeson (1991) to illustrate the upper bound curve between these two parameters, as presented in **Equation 2.1**. It represents the benchmark for the membrane separation performance (Robeson 1991).

$$P_i = k \propto_{ij^n} \quad \textbf{(2.1)}$$

The P_i represents the permeability and $\propto_{ij}$ is the selectivity, while k and n are the calculated coefficients for the upper bound linear relationship for each feed gas used (Robeson 1991).

Subsequently, Freeman (1999) studied further on the upper bound curve and generated a summarised membrane performance chart based on the previous studies, as illustrated in **Figure 2.4**, whereby the data are plotted according to the function of $\propto_{ij}$ against P_i. From this study, Freeman et al. (1999) stated that the increment of selectivity through inter-chain spacing and chain stiffness plays an important role in order for the membrane performance to exceed the upper bound, as high chain packing membrane often yields low permeance results due to the stacking of polymer chains that inhibit the efficient mass transport of gas molecules (Freeman et al., 1999).

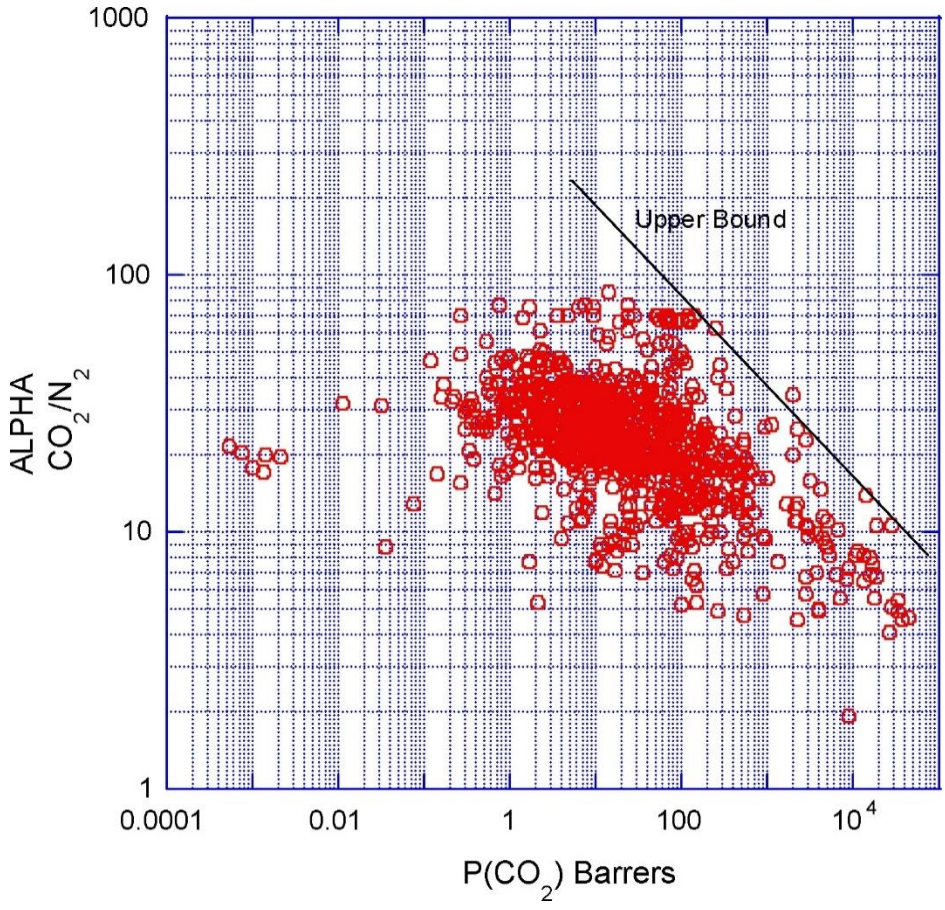

Figure 2.4 Robeson's upper bound correlation chart for CO_2/N_2 separation (Robeson 2008)

2.3.2 CAB membrane in gas separation application

The most common and widely utilised membranes in the manufacturing process include cellulose acetate (CA), cellulose propionate, cellulose acetate propionate and CAB (Asgarkhani et al., 2013). As mentioned by Shanbhag et al. (2007), the CAB exhibits excellent film-forming properties and the butyryl group in CAB can effectively improve and expand the capacity of cellulose chain membrane material volume through enlarging the free volume (Cheng et al., 2006). Moreover, Basu et al. (2010b) reported that the CAB has multi-chiral carbon atoms in its molecular structure unit that has been used in membrane preparation due to the decent membrane characteristics present (Basu et al., 2010b). The CAB polymer possesses several prominent characteristics including high impact resistance, well maintained weather resistance, notable chemical resistance with excellent film forming characteristics inherited from the acetyl and hydroxyl groups (Xie et al., 2008). The molecular structure of CAB is presented in **Figure 2.5**, which is a physical thermoplastic polymer composed of esterified cellulose and includes both acetyl and butyryl groups (Xie et al., 2008)

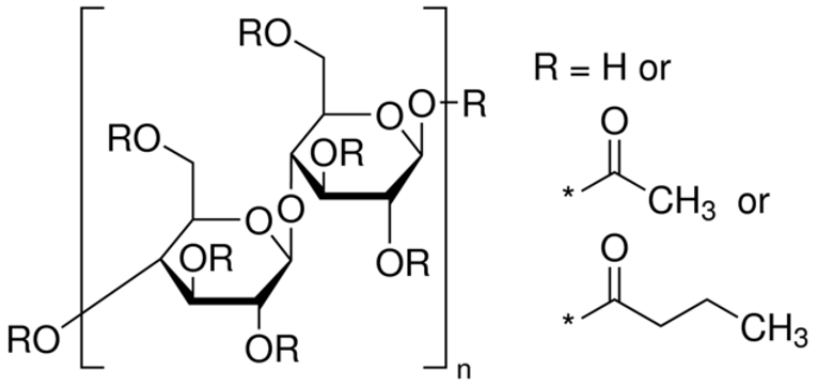

Figure 2.5 CAB molecular structure (Kunthadong et al., 2015)

Kunthadong et al. (2015) studied four types of cellulose aliphatate esters, which include CA, cellulose butyrate (CB), cellulose propionate and CAB towards gases such as oxygen (O_2),

nitrogen (N_2), methane (CH_4), carbon monoxide (CO) and CO_2. These results found that the CAB with short acetyl groups appear to have better selectivity and higher gas permeability as compared to others due to the presence of short acetyl groups and relatively long butyl groups (Kunthadong et al., 2015).

Although the CAB membranes offer advantages in terms of higher level of mechanical stability, cost-effectiveness, easy formability and excellent scalability properties (Chen et al., 2014), the structure of the polymeric membranes usually have difficulties in maintaining good performance for both permeability and selectivity. This is due to the trade-off relationship between permeability and selectivity (Ismail et al., 2009, Kentish et al., 2008). The polymeric membranes suffer swelling phenomena, which subsequently alter the chemical properties of the membrane and affect the separating performance (Bahukudumbi and Ford, 2006).

2.3.2.1 Effect of polymer concentration

The membrane gas separation performance can be affected by various membrane preparation conditions. One of the key factors which influence the performance of membrane is the polymer concentration (Wang et al., 2007). This is because of the significant effect of polymer concentration on the solution's viscosity. In fact, increasing the polymer concentration increases the overall viscosity of the dope solution and therefore, affecting the membrane gas separation (Goh et al., 2011). Based on Jawad et al. (2015), the morphology and separation performance of the membrane is also closely related to the effect of polymer concentration. From the author's discussion, when the polymer concentration is increased from 15 wt% to 17 wt% the surface morphology of the membrane changes from smooth to porous due to rapid diffusion of the coagulant in the casting solution (Jawad et al., 2015). As high polymer concentration solution usually has less solvent in the mixture, this allows the limited non-

solvent to exchange with the solvent within membrane during the membrane immersion process, therefore preventing the formation of porous membrane (Ngang et al., 2012). In short, different polymer concentrations can have various effects on the membrane gas separation performance (Jawad et al., 2015b).

2.3.2.2 Effect of membrane casting thickness

The membrane casting thickness is also another important factor that critically affects the structure of the membrane and separation performance. A thick membrane above 300 μm usually exerts undesirable effect towards gas permeation by hindering the full potential of the membrane with more resistance pathway (Xing et al., 2010). Moreover, increasing the membrane casting thickness from 200 to 400 μm causes the membrane structure transition from finger to sponge-like membrane morphology (Jansen et al., 2005, Ngang et al., 2012). Therefore, in order to attain superior gas separation performance, the membrane should be thin in thickness and casting thickness is one of the factors that influences the morphology of the membrane thickness (Ahmad et al., 2017, Vogrin et al., 2002).

2.3.2.3 Effect of solvent evaporation time

The solvent evaporation time is crucial for membrane formation, as the structure of the membrane determines the separation ability of the membrane (Khorshidi et al., 2015). After synthesis, the as-spun membrane undergoes solvent evaporation. Based on Young et al. (2000) work, a membrane that is subjected to longer solvent evaporation time above 6 minutes is most likely to produce macro voids membrane due to different diffusion kinetics involved during the formation of the membrane (Chung 2007). However, a membrane subjected to direct phase inversion with short solvent evaporation time of less than 5 minutes favours the formation of tight morphology on the surface with finger-like macro voids on cross-sectional (Fang et al.,

1994). In addition, these morphologies affect the gas separation performance. As a result, the solvent evaporation time for the membrane has to be optimised in order to obtain thin and high selective membrane for gas separation (Young et al., 2000).

2.3.2.4 Effect of solvent exchange drying method

In recent years, the solvent exchange drying technique has been found to play a critical role in altering the membrane structure and gas permeability of the membrane. During the membrane fabrication process, the membrane is usually immersed in water to eliminate the remaining solvent within the membrane structure. However, due to the large amount of solvent within the membrane being replaced by water throughout the immersion process, this causes enormous capillary forces to take place, which can significantly damage the membrane structure (Aroon et al., 2010d). In this regard, to slow down the drastic changes of the capillary forces occurring during the immersion process, the solvent exchange method is utilised. In this method, the water molecules within the membrane is first replaced with volatile fluids to reduce the surface tension prior to the final stage of complete drying. The process of this method is usually to immerse the membrane first with a water-soluble alcohol, and then replacing the alcohol with a volatile organic compound of low surface tension (Wang et al., 2000).

Jie et al. (2005) reported that when the membrane was prepared through the solvent exchange method, the selectivity performance for H_2/CH_4 and H_2/N_2 improved from 2.92 to 4.14 for the cellulose hollow fibre membrane. In this case study, Jie et al. (2005) indicated that the ethanol-hexane used during the solvent exchange method was one of the most feasible methods due to simplicity of procedure and satisfying results. Liu et al. (2004) concluded that when using isopropanol and n-butanol with a weight ratio of 3:1for the solvent exchange method, the selectivity performance of the poly(ether block amide) (PEBA) increased from 32.7

to 44.1 (Liu et al., 2004). Further, it was also concluded that the formation of a uniform and defect-free PEBA membrane was due to the solvent exchange system used whereby, the surface thermodynamic properties and miscibility of the solvents used helped to minimise the surface tension during the drying procedure (Liu et al., 2004).

2.4 Inorganic membrane

In addressing the problem of the trade-off between selectivity and permeability for the polymeric membrane, the inorganic membranes that are fabricated from metallic, ceramic and pyrolyzed carbon gained global interest due to the advantages they offered (Strathmann and Kock, 1977, Young et al., 2000, Aroon et al., 2010). The inorganic membrane is favourable due to its high solvent-resistant properties, thermal and pore structure stability (Yang et al., 2008, Zhang et al., 2014, Pietraß, 2006). In addition, the inorganic membrane is not affected by the swelling-induced plasticisation issue that occurs in polymeric membrane due to its ability of operating at high pressure (Li et al., 2007). Besides, Li et al. (2007) highlighted that the inorganic membrane is able to overcome the normal trade-off relationship between permeability and selectivity present in the polymeric membrane due to the integration of size exclusion properties of the molecular sieve within the pores, thus, providing selective gas separation (Caro and Noack, 2008, Kentish et al., 2008).

Despite the excellent selectivity demonstrated by the inorganic membrane, the full potential of the inorganic membrane is still partially hindered by the high capital cost of membrane fabrication as well as the complexity in its handling due to lack of technology to produce a defect-free membrane (Zimmerman et al., 1997). With the present deficiency of the polymeric materials and comparative disadvantages of the inorganic membrane, this prompted

the development of the MMM that offers more advantages over polymeric and inorganic membranes (Ciobanu et al., 2008, Caro et al., 2000, Ismail et al., 2009, Noble, 2011).

2.5 Mixed Matrix Membrane (MMM)

The MMM has emerged as a new candidate with favourable properties required in the membrane separation process, as tabulated in **Table 2.1**. However, the challenge of synthesising MMM relies greatly on the compatibility between the polymer matrix used and the inorganic fillers incorporated. In this regard, numerous researches have been carried out to determine the compatibility between the polymer matrix with the selection of inorganic filler used for the fabrication of MMM. Besides, the MMM has demonstrated promising permeance and selectivity performance based on the use of selected inorganic fillers. (Sanip et al., 2011, Aroon et al., 2010, Ahn et al., 2008). Hence, excellent gas separation can be achieved through the MMM, provided that appropriate materials between the polymeric matrix and inorganic fillers with good compatibility are selected (Mahajan and Koros, 2002, Sanip et al., 2011, Chung et al., 2007).

The excellent separation performance of MMM has been justified through incorporation of inorganic fillers such as porous zeolites (Cong et al., 2007), non-porous silica (Goh et al., 2011), metal oxides (Husain and Koros, 2007), carbon molecular sieve (CMS) and carbon nanotubes (CNTs) (Kim et al., 2006, Basu et al., 2010a). Goh et al. (2011) explained that the embedding of inorganic fillers into polymeric matrix causes the alteration in packing of polymer chains and creates cavities around its surface that facilitates transportation of gas molecules through the membrane (Chung et al., 2007).

Table 2.1 Membrane properties comparison (Ismail et al. 2009)

Properties	Polymeric membrane	Inorganic membrane	Mixed matrix membrane
Cost	Economical to fabricate	High fabrication cost	Moderate
Chemical and thermal stability	Moderate	High	High
Mechanical strength	Good	Poor	Excellent
Compatibility to solvent	Limited	Wide range	Limited
Swelling	Frequently occurs	Free of swelling	Free of swelling
Separation performance	Moderate	Moderate	High
Handling	Robust	Brittle	Robust

Figure 2.6 illustrates the schematic of the inorganic fillers that are being embedded in the polymer phase of the MMM. The inorganic fillers are commonly used to enhance the efficiency of the gas molecules mass transport through the membrane by increasing the membrane diffusion surface area and yield higher permeability and selectivity membrane than pure organic and inorganic membrane (Zhang et al., 2013, Goh et al., 2011). The size and shape of the fillers plays an important role in MMM, in terms of determining its capability to discriminate penetration of different molecules (Zeng et al., 2008). Recently, the CNTs inorganic fillers demonstrated excellent permeability in the membrane gas separation field due to their promising mass transport behaviour contributed by the CNTs nano-channel, which is greater than other porous fillers. Thus, this make CNTs an ideal inorganic filler to incorporate with other polymer matrixes (Widjojo et al., 2008, Pal, 2008).

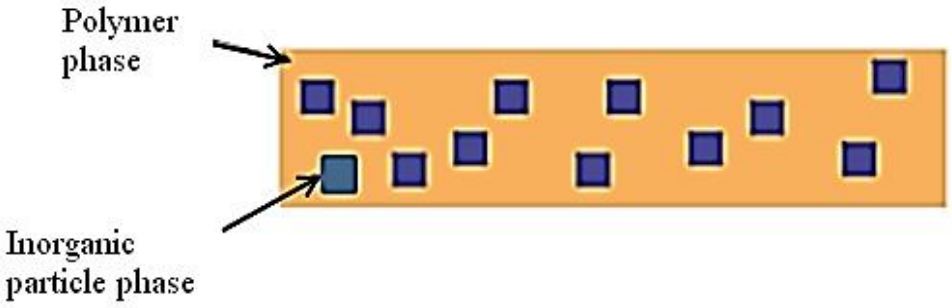

Figure 2.6 Schematic of incorporating fillers into polymer (Chung et al. 2007)

2.5.1 CNTs in MMM fabrication

The CNT belongs to the fullerene structural family, which consists of six carbon rings and are arranged in a hexagonal lattice (Sanip et al., 2011). The CNTs are similar to graphite. Both exhibit the strongest chemical bond in nature, which is the carbon-carbon bond (Ismail et al., 2009). This provides CNTs with high mechanical strength. Incorporating CNTs filler therefore, enhances the mechanical strength of the inorganic disperse phase in MMM (Ismail et al., 2011).

In addition, the CNTs can be classified into single-walled CNTs (SWCNTs) and multi-walled CNTs (MWCNTs) (Ruoff and Lorents, 1995). As presented in **Figure 2.7**, the SWCNTs has a single graphene layer, whereas the MWCNTs has two or more concentric cylindrical shells of graphene sheets coaxially arranged around a hollow core (Paradise and Goswami, 2007, Bikiaris et al., 2008). With the recent development of the fabrication techniques of the CNTs with the membrane, researchers reported that to achieve well dispersed CNTs within the MMM is challenging due to the agglomeration issues caused by Van der Waals forces within the CNTs itself (Iijima, 1991).

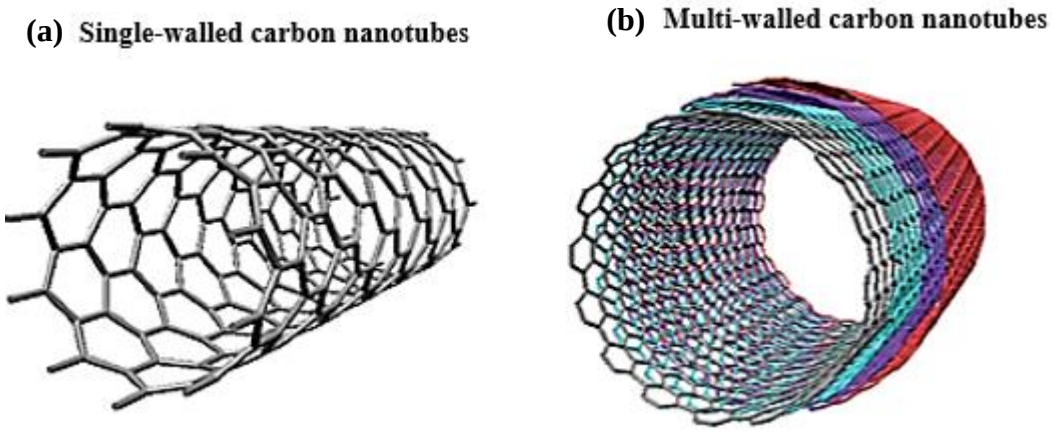

Figure 2.7 Structure of carbon nanotubes (a) SWCNTs and (b) MWCNTs (Ismail et al. 2009)

The separation performances of some MMMs with different polymer matrix and CNTs are tabulated in **Table 2.2**.

Table 2.2 Summary of CNTs gas separation performance (CO_2/N_2) from previous work

Ref(s)	Polymer matrix	Inorganic phase (IP)	IP, wt%	P_{CO2}	P_{N2}	Selectivity, α	Conditions
(Sun et al., 2017)	PI	MWCNTs	0.00	2.31[b]	0.15[b]	15.40	15-20 μm
			1.00	3.32[b]	0.18[b]	18.44	
			2.00	4.58[b]	0.22[b]	20.82	
			3.00	5.44[b]	0.24[b]	22.67	
			4.00	4.05[b]	0.20[b]	20.25	
(Ahmad et al., 2014)	CA	MWCNTs-F	0.00	400.93[a]	12.18[a]	32.92	$3x10^5$ Pa, 250μm
			0.05	511.56[a]	16.03[a]	31.92	
			0.10	741.67[a]	18.46[a]	40.17	
			0.20	138.37[a]	16.01[a]	8.39	
(Aroon et al. 2010)	PI	MWCNTs-P	0.0	16.83*	-	10.9	15 bar gauge, 25 °C
			1.0	10.47*	-	17.5	
		MWCNTs-F	1.0	37.31*	-	16.5	
(Sanip et al. 2011)	PI	MWCNTs-F	0.0	~0.5 [#]	-	~2	3-10 bar, 35°C
			0.7	~4-10 [#]	-	~7-8	
(Ismail et al. 2011)	PES	MWCNTs	0.0	10.98 [#]	0.80 [#]	13.73	4 bar for CO_2, 3 bar for N_2, 25 °C
			0.5	6.79 [#]	0.29 [#]	23.41	
			1.0	2.79 [#]	0.51 [#]	5.47	
			2.0	11.60 [#]	0.67 [#]	17.31	
			3.0	13.56 [#]	1.18 [#]	11.49	
(Bethune et al., 1993)	-	CNTs	0.1	$0.01x10^{-3}$ [+]	-	0.0	1 bar, 27 °C
			1.0	$0.05x10^{-3}$ [+]	-	2.5	
(Ma and Kim, 2011)	PVA	MWCNTs	1.0	3294*	-	-	0.2 MPa, 380.15 K
			2.0	3391*	-	-	

				3.0	3415*	-	-	
				4.0	3405*	-	-	
				8.0	3436*	-	-	
(Ban and Huang, 2012)		Matrimid	CNTs	0.0	6.46*	0.10*	64.6	1 bar, 27 °C
				2.0	20.53*	0.40*	51.4	
				5.0	38.07*	0.47*	81.0	
				8.0	29.89*	0.43*	70.1	
				10.0	10.29*	0.39*	26.4	

PI= polyimide; PES= polyethersulfone; PVA= polyvinylalcohol; CA= cellulose acetate
*Barrer; #GPU; +mol.cm^{-2}.s^{-1}

The effective use of CNTs in MMM depends greatly on the structure, which includes the length, diameter and the ability to disperse uniformly throughout the matrix. The physical properties of SWCNTs and MWCNTs are shown in **Table 2.3**. One problem associated with CNTs is the presence of Van der Waals attraction force that causes the CNTs to agglomerate together into crystalline ropes or bundles (Li et al., 2015). This highly entangled network is typically formed by 100-500 tubes due to the poor interfacial interaction between CNTs and the polymeric matrix. The inherent feature of CNTs is the thin diameter in nano-scale with high aspect ratio (>1000), which creates a large surface area resulting in poor mechanical and electrical properties, thus, making CNTs inefficient throughout the separation process (Jawad et al., 2015a, Sanip et al., 2011). Therefore, in order to address this issue, functionalisation has been developed to effectively prevent the agglomeration problem in CNTs (Coleman et al., 2006).

Table 2.3 SWCNTs and MWCNTs physical properties (Ma et al. 2010)

Properties	**SWCNTs**	**MWCNTs**
Specific gravity (g/cm^3)	0.8	1.8
Electrical conductivity (S/cm)	10^2-10^6	10^3-10^5
Electron mobility (cm^2/V.s)	~10^5	10^4-10^5
Thermal conductivity (W/m.K)	6000	2000
Coefficient of thermal expansion (K^{-1})	Negligible	Negligible
Thermal stability in air (°C)	>600	>600

2.5.1.1 Functionalisation of CNTs

Functionalisation methods are being classified into two main groups, namely the covalent and non-covalent functionalisation (Kim and Mai 1998). The covalent functionalisation method is commonly employed to increase the solubility of inorganic fillers and eventually leads to better dispersion within the membrane matrix (Sahoo et al., 2010). On the other hand, the non-covalent functionalisation has been recognised as the most promising approach for the MMM. This is because the non-covalent functionalisation method has the ability to scale up to the desired plant level while maintaining the structural integrity of CNTs. Most importantly, this method avoids the usage of strong oxidant or chemicals, thus, making it environmental friendly (Sanip et al., 2011, Sahoo et al., 2010, Samal and Geckeler 2000).

The non-covalent functionalisation can be further classified into surfactant adsorption, endohedral method and polymer wrapping (Peng et al., 2007). The polymer wrapping is preferred among all methods as it is an effective technique to wrap the functionalisation agents around the CNTs forming the super molecular complex that provides strong binding between the polymer backbone and CNTs through the Van der Waals interactions (Liu et al., 2008, Ma and Kim, 2011). In addition, polymer wrapping is favourable as it causes the polymer to lie along the parallel axis instead of mapping onto the chirality of the underlying tube. This in return creates a homogeneous structure of CNTs, as shown in **Figure 2.8** (Panhuis et al., 2003).

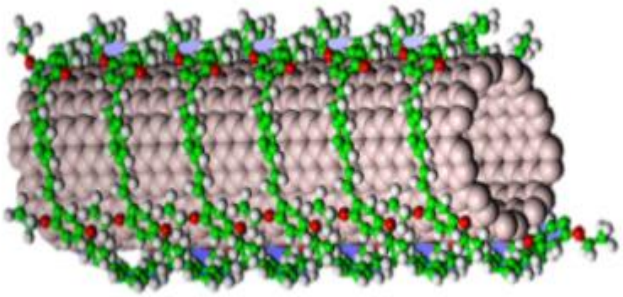

Figure 2.8 Schematic of CNT functionalization using polymer wrapping (Ma et al. 2010)

Chen's soft-cutting technique is one of the approaches for non-covalent functionalisation that avoids the usage of strong chemicals and oxidants, which can prompt damage to the CNTs (Chen et al., 2001). As a result, it protects the CNTs from external damage as well as the laborious method of sonication in solvent, which makes scaling-up difficult (Panhuis et al., 2003). Jansen et al. (2005) observed that the binding of SWCNTs within the organic matrix was distributed homogeneously among the suspended solution and had significantly improved the CNTs' distribution (Jansen et al., 2005).

The functionalisation of MWCNTs with Beta-Cyclodextrin (β-CD) is an effective way to prevent agglomeration and nanotubes aggregation that yield better dispersion and homogeneous CNTs within the polymer matrix (Jawad et al., 2015a). The CDs are derived from cyclic oligosaccharide of 6-8 glucopyranoside units, which can be represented as toroid with an inner diameter cavity (Del Valle 2004). The β-CD is a bottomless bowl-shaped macro-ring derived from the cyclic oligosaccharide's family, as shown in **Figure 2.9** (Del Valle 2004).

The β-CD is selected because of its hydroxyl functional group that can enhance the permeability of MMM due to its strong interaction between the non-polar hydroxyl group and non-polar CO_2 molecules (Sanip et al., 2011). Moreover, the MWCNTs-F functionalised with

β-CD has the characteristics of hydrophobic inner cavity and hydrophilic surface. Hence, it is suitable for various gas molecules that are polar, non-polar, amphiphilic and bola-amphiphilic (Jiang and Chung, 2009, Ismail et al., 2009, Kim et al., 2007).

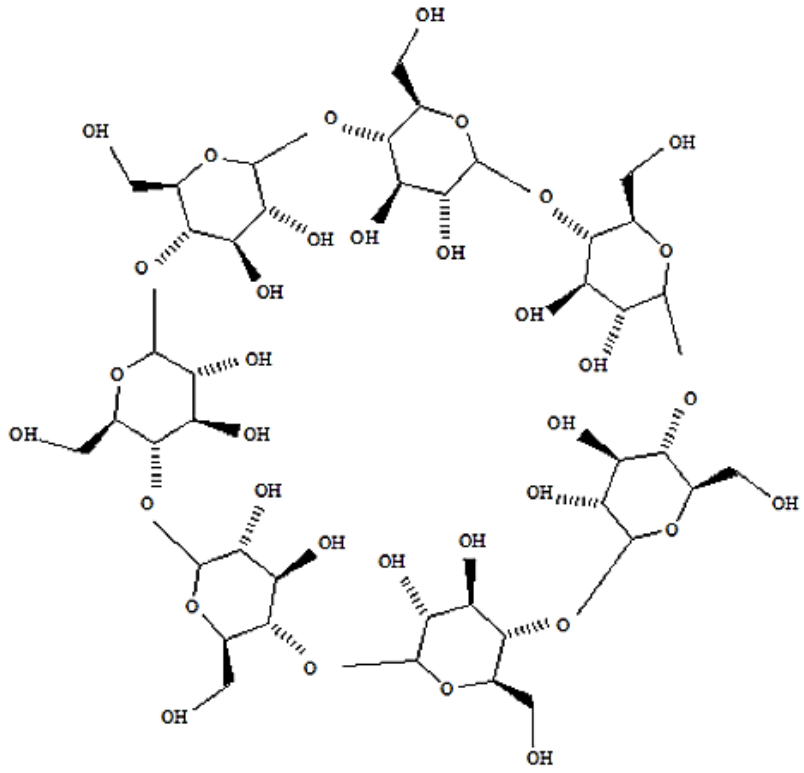

Figure 2.9 Schematic diagram of β-CD (Jawad et al. 2015a, Del Valle 2004)

The functionalisation of MWCNTs with β-CD has been studied by Sanip et al. (2011) and Jawad et al. (2015a). They highlighted that through the integration of β-CD as the functionalisation agent of MWCNTs, the MMM gained significant increment in separation performance. However, the existing MMM development is not fully exploited yet, due to the enhancement of permeability with the expense of selectivity and vice versa. In this regard, the development of membrane has focused on combining two or more polymers with inorganic materials to fabricate the blend MMM with high permeability and selectivity performance to meet the demand of high-energy industries.

2.6 Blend mixed matrix membrane (MMM)

Based on the limitation of MMM, the blend MMM is a promising alternative to enhance the permeance properties of MMM. The breakthrough technique of fabricating blend MMM has gained much attention recently due to its high potential of developing high performance membrane in gas separation applications (Safarpour et al., 2016). Moreover, as compared to the traditional MMM, the blend MMM demonstrates great potential for remarkable savings in membrane costs through substituting the functional material with inexpensive alternatives in the membrane structure (Hosseini et al., 2010). In addition, Chen and Ho (2016) reported that the blend MMM provides greater flexibility in tailoring the membrane morphology and gas permeance, which leads to high CO_2 permeance due to the compatible functional groups in the blend MMM structure (Estahbanati et al., 2017, Chen and Ho 2016).

Furthermore, the fabrication of blend MMM with desirable characteristics is not a small task and requires great amount of careful consideration from the physicochemical properties of materials throughout the entire chain of dope formulation, membrane fabrication and phase inversion process. Moreover, complexity often arises in blending both polymers with different functional groups and properties due to the compatibility of two distinct materials used. An ideal blend MMM should demonstrate characteristics such as thin dense membrane morphology with high gas permeance but at the same time having the mechanical strength to withstand high feed gas pressure (Hosseini et al., 2010).

Besides, one of the main benefits of blend MMM lies in the great prospect of utilising wide range high performance materials for membrane-based separation applications. Li et al. (2019) developed blend MMMs with low molecular weights (*Mn*) poly (ethylene glycol)

(PEGDME-500). They stated that the blend MMM demonstrated highest permeability of 1566.8 Barrer with a CO_2/N_2 selectivity of 35.1. The separation performance of blend MMM indicates that the usage of low *Mn* PEG with low hydroxyl end groups significantly influences the gas permeability and selectivity of the blend MMM. This is because the hydroxyl group content within the PEG polymer can prompt the formation of hydrogen bond within the membrane to block the gas transportation (Patel and Spontak 2004). Consequently, when low *Mn* PEG with lower hydroxyl content is used, the impeding effect of hydrogen bonding lessened, resulting in the increment of gas permeability (Li t al., 2019). In this aspect, the study of the effect of various *Mn* blends of polymer combination to synthesise blend MMM is essential for the development of high-performance CO_2/N_2 gas separation blend MMM (Hosseini et al., 2010).

2.7 Transport mechanisms for membrane gas separation

The motion of transport for gas separation through membrane is generically referred to as diffusion mechanisms. Diffusion mechanisms are defined as gas species that move through a material or medium at a rate or in a direction that differs from the medium as a whole (Ho and Sirkar 2012). There are several types of mechanisms that has been established according to theories that explained the fundamentals of the gas separation transport mechanisms. The most well-known transport mechanisms include Knudsen diffusion, molecular sieving, capillary condensation, surface diffusion and solution diffusion (Kentish et al., 2008). Since the transport of gas separation process rely mainly on the membrane's properties and operating conditions, the fundamentals of gas separation mechanisms should be well justified (Freeman et al., 2006).

2.7.1 Knudsen diffusion

Generally, Knudsen diffusion normally occurs in microporous membrane through the pinholes of dense membrane whereby, the component molecules collide frequently with the walls (Lewis 2018). The motion of collision for Knudsen diffusion is illustrated in **Figure 2.10**. For Knudsen diffusion, when the λ value is smaller than 0.05, more collisions occur against the wall than the collisions between the gas molecules Hence, the molecules move more independently. Since all collisions happen in according to the gas molecular weight and kinetic diameter, thus, the gas molecules that are smaller in molecular weight and lighter in kinetic diameter are more likely to diffuse faster through the membrane.

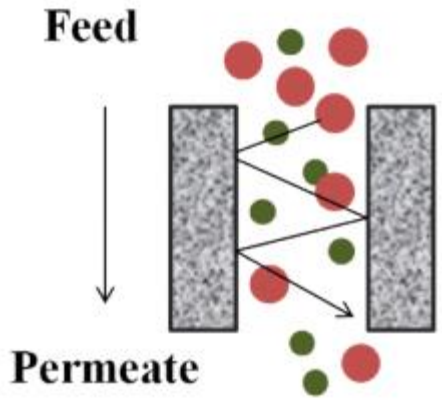

Figure 2.10 Schematic diagram of Knudsen diffusion mechanism (Ren et al., 2015)

2.7.2 Molecular sieving

The molecular sieving model is another transport mechanism used in gas separation and only limited to situations when the pore sizes of the membrane are less than 7Å. In order for molecular sieving to take place, the membrane pore size needs to be strictly between the gas molecules that are targeted to be separated. For this reason, molecular sieving only allows specific component molecules to pass through, while retaining those larger than the membrane

pore size (Sridhar et al., 2014). The schematic diagram of molecular sieving is depicted in **Figure 2.11**.

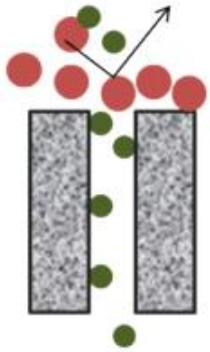

Figure 2.11 Schematic diagram of molecular sieving mechanism (Ren et al., 2015)

2.7.3 Capillary condensation

On the other hand, the capillary condensation transport mechanism only occurs when the condensed gas has fully filled the pores within the membrane. When a certain critical pressure is reached, the capillary condensation mechanism prevents other gas components from entering the pores, as illustrated in **Figure 2.12**. Henceforth, the capillary condensation mechanism only occurs by partial condensation of any one component from the gas mixtures. This mechanism normally happens when there is meso-porous pore present (pore diameter > 3.0 nm) (Pengilley 2016). Eventually, due to the nature of this mechanism, which selectively allows non-condensable to pass through by blocking out the condensable one, it leads to high selectivity performance of the membrane (Lewis 2018).

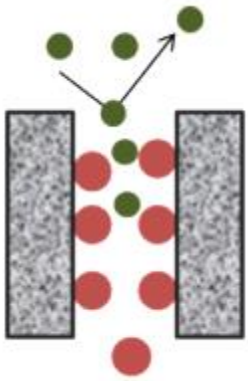

Figure 2.12 Schematic diagram of capillary condensation mechanism (Ren et al., 2015)

2.7.4 Surface diffusion

In addition, surface diffusion mechanism only occurs in porous membrane and usually takes place when the gas molecules have strong affinity with the membrane's surface (Lewis 2018). Consequently, the schematic diagram of surface diffusion is portrayed in **Figure 2.13**. According to this **Figure 2.13**, the molecules attach closely with the membrane pores wall during surface diffusion. Through this mechanism, the driving force of surface diffusion is mainly driven by the differences in adsorption affinity (Lewis 2018).

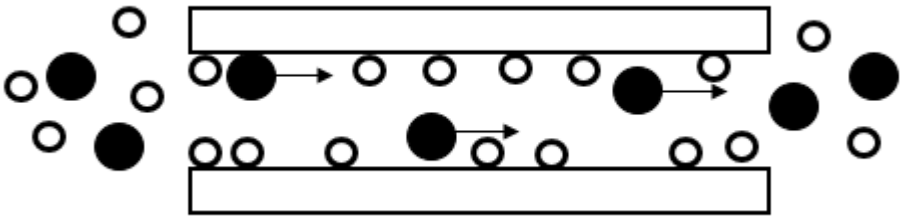

Figure 2.13 Schematic representation of surface-diffusion mechanism (Afzali et al., 2018)

The membrane pores are theoretically considered to be the integration of capillaries as the nano-pores within membrane are assumed to be the capillaries. Moreover, gas adsorption on nano-pore walls of the membrane is regarded as Langmuir monolayer adsorption and the

height of the adsorption monolayer is set to be equivalent to the diameter of a gas molecule (Wu et al., 2015).

2.7.5 Poiseuille flow

The Poiseuille flow mechanism occurs when the membrane pore sizes (r) are greater than the mean free path (λ) by a coefficient of 3 (r/λ >3), or when the membrane pore sizes are between 200 nm to 3000 nm. The driving force of this mechanism mainly depends on the different pressure gradients between the feed and permeate sides. The Poiseuille flow also commonly known as the convective diffusion operates in an inverse manner to Knudsen diffusion. The Poiseuille flow is different from Knudsen diffusion because Poiseuille flow operates through the collisions between gas components instead of the pore walls, as portrayed in Knudsen diffusion. This led to the gas components to pass through the pores by drift velocity, as illustrated in **Figure 2.14** (Bitter 2012). The molar flux (G_{Poi}) of this diffusion is described in **Equation 2.9** (Lewis 2018, Pengilley 2016).

$$G_{Poi} = \frac{r_2(p_1 - p_2)}{16L\mu RT} \qquad \textbf{(2.9)}$$

Where, r is the radius of membrane, P_1 and P_2 represent the pressures at feed and permeate sides, respectively, L is the length of the membrane, μ is the viscosity of gas, R is the universal gas constant and T is the temperature (Lewis 2018).

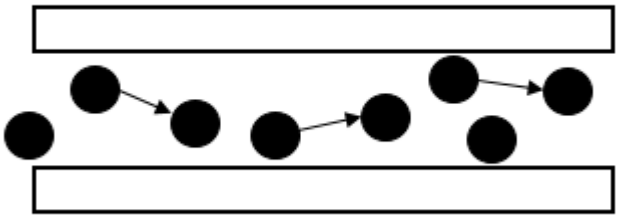

Figure 2.14 Schematic representation for Poiseuille flow (Shindo and Nagai 2013)

2.7.6 Solution-diffusion

In contrast to the porous membrane transport mechanism, the gas transport through dense membrane can only be described with the solution-diffusion mechanism. The highlighted feature of solution-diffusion mechanism is the ability to control different gas molecules permeation within the membrane during the gas separation process (Pandey and Chauhan 2001). This mechanism does not solely rely on the diffusivity coefficients only but also depends on the physical-chemical interaction between the gas molecules with the polymer matrix, which eventually determines the gas permeation efficiency (Kentish et al., 2008). Furthermore, the solution diffusion works according to the principle of selective permeation through the polymer matrix which highly dependent on the gas solubility of the molecules through the membrane (Kinoshita et al., 2017). Meanwhile, less soluble gas takes more time to permeate the membrane (Zarshenas et al., 2016).

The solution-diffusion mechanism can subsequently be divided into three diffusion steps. Firstly, the gas molecules from the feed stream get in contact with the membrane surfaces, which are absorbed into these surfaces, as defined in the sorption phase (Sridhar et al., 2014). Then, the second phase is the diffusion of molecules through the polymer matrix (Sridhar et al., 2014). Finally, the last step is referred to as the evaporation phase whereby, desorption of gas molecules takes place at the permeate streamside and exits the polymer matrix (Sridhar et al., 2014). For this mechanism, the thermodynamic activities such as pressure or concentration differences along the membrane are the main driving force for solution-diffusion. The schematic diagram of solution-diffusion is illustrated in **Figure 2.15**, where due to different concentration profiles on the feed and permeate sides, the concentration gradient appears in the path (Ren et al., 2015).

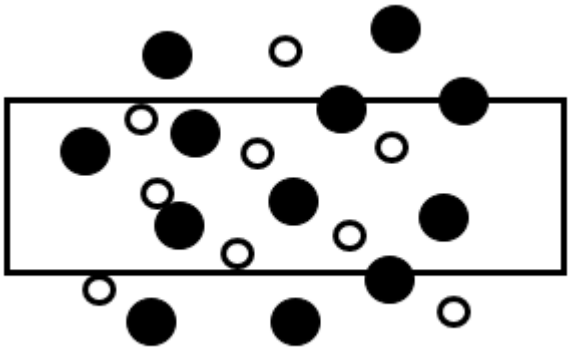

Figure 2.15 Schematic illustration of solution-diffusion mechanism (Ren et al., 2015)

Regarding the membrane separation efficiency for this mechanism, it actually relies on the permeability of gas across the membrane, where the permeability (*P*) can be obtained in **Equation 2.10** (Kobayashi and Müllen 2015).

$$P = D \times S \tag{2.10}$$

Where, the coefficient of diffusivity is represented as *D* and solubility coefficient as *S*. Additionally, the selectivity (α) of the membrane can be expressed with the ratio of permeability of each gas component, as demonstrated in **Equation 2.11** (Kobayashi and Müllen 2015).

$$\alpha_{a/b} = \frac{P_a}{P_b} \tag{2.11}$$

Besides, the gas flow rates (*Q*) can be calculated using the well-known **Equation 2.12** (Kobayashi and Müllen 2015).

$$Q = \frac{PA(p_1 - p_2)}{l} \tag{2.12}$$

Where, P_1 and P_2 represent the pressures at feed and permeate sides, respectively, the membrane area is denoted as *A* and thickness of membrane as *l* (Kobayashi and Müllen 2015).

MATERIALS AND METHOD

3.1 Overview

Firstly, the overall research flowchart of this present research study is illustrated in **Figure 3.1**. Thereafter, followed by discussion involving the chemicals, materials and analytical equipment employed throughout this research work. Initially, the methodology of preparing cellulose acetate butyrate (CAB) membrane is discussed. This is followed by the preparation conditions of each parameter including polymer concentration, casting thickness, solvent evaporation time, solvent exchange duration for Isopropyl alcohol and n-Hexane and CAB membranes fabricated at different molecular weights. Then, the experimental procedure to functionalise multi-walled carbon nanotubes (MWCNTs), mixed matrix membranes (MMM) and blend MMMs are outlined in detail. The preparation method of MMM and blend MMMs are evaluated based on the single gas permeation studies of CO_2 and N_2, in terms of the loadings of MWCNTs and molecular weight (*Mn*) combinations used to prepare the blend MMMs, respectively.

In addition, the fundamental theory of the characterisation works and gas permeation model for gas separation are described in detail. Furthermore, the model of kinetic sorption study is derived with all the equations expressed based on the assumptions made and presented in this chapter to evaluate the solubility coefficient of the membrane synthesised. Lastly, the binary gas permeation study is evaluated based on the CO_2/N_2 gas mixture.

3.4 Overall research experimental flowchart

The general experiment procedures carried out in this research is depicted in **Figure 3.1**.

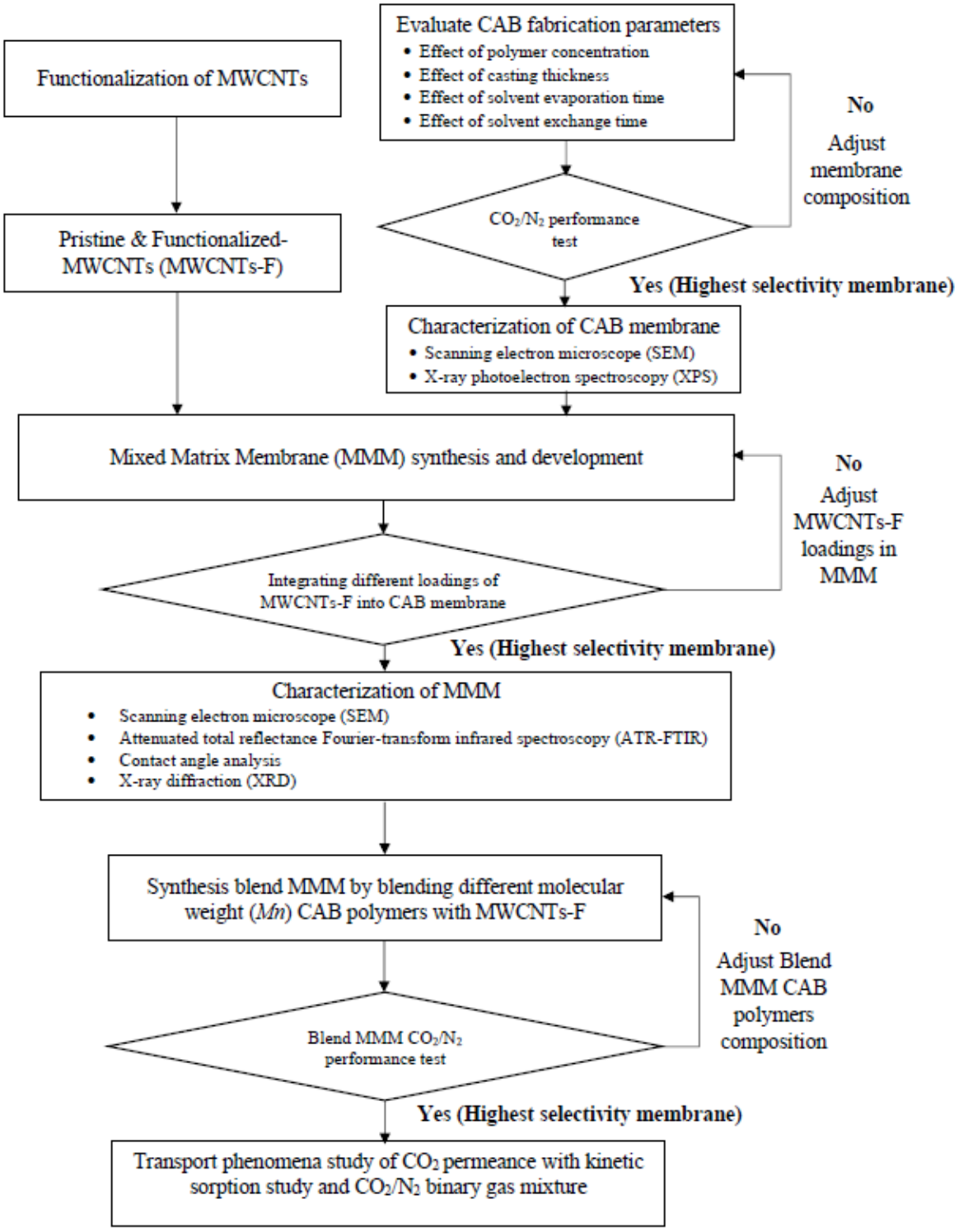

Figure 3.1 Flowchart of overall experimental works

3.3 Materials and chemicals

The list of materials and chemicals used for the membrane fabrication, characterization and permeation studies is shown in **Table 3.1**.

Table 3.1 List of chemicals and materials involved

Chemicals/ Brand	Specification/ Assay	Supplier	Purpose
Cellulose Acetate Butyrate (CAB), Sigma Aldrich	*Mn*= 12000 (Acetyl= 16-19 wt %) (Butyryl= 30-35 wt%) *Mn*= 30000 (Acetyl= 12-15 wt %) (Butyryl= 36-40 wt%) *Mn*= 65000 (Acetyl= 28-31 wt %) (Butyryl= 16.5-19 wt%) (Hydroxyl= 0.9-1.3 wt%) *Mn*= 70000 (Acetyl= 12-15 wt %) (Butyryl= 35-39 wt%) (Hydroxyl= 1.2-2.2 wt%)	Sigma Aldrich, Malaysia	Membrane polymer
Chloroform, Merck	>96%	Merck Chemical, Malaysia	Chemical used to dissolve CAB polymer
Multi-walled carbon nanotubes (MWCNTs)	>95% (length ranging from 5 to 50μm)	Shenzhen Nanotech Port Co. Ltd, China	Inorganic fillers for mixed matrix membrane
Beta-Cyclodextrin (β-CD), Merck	98.3%	Merck Chemical, Malaysia	Powder used for MWCNTs functionalization
Acetone, Merck	ACS reagent ≥ 99.9%	Merck Chemical, Malaysia	Chemical used for cleaning purpose
Ethanol, Merck	ACS reagent ≥ 99.9%	Merck Chemical, Malaysia	Chemical used for mixing β-CD and MWCNTs
Isopropyl alcohol, Merck	99.8%	Merck Chemical, Malaysia	Solvent to dry membrane
n-hexane, Merck	99.8%	Merck Chemical, Malaysia	Solvent to dry membrane
Carbon dioxide (CO_2)	99.99%	Eastern Oxygen Industries Sdn Bhd, Malaysia	Gas permeation test
Nitrogen (N_2)	99.99%	Eastern Oxygen Industries Sdn Bhd, Malaysia	Gas permeation test

3.4 Apparatus and equipment

The apparatus and equipment involved in this research are shown in **Table 3.2**.

Table 3.2 List of apparatus and equipment

Apparatus/ Equipment	Quantity	Function
Testing Rig	1	Membrane gas permeation test
Mortar and Pestle	1	Grinding of β-CD and MWCNTs
Weighing dish	1	MWCNTs functionalization
Electronic top-pan balance	1	MWCNTs functionalization
Fume hood	1	Membrane fabrication and MWCNTs functionalization
Oven	1	Drying of apparatus and filter papers
Casting machine	1	Membrane fabrication
Magnetic stirrer bar	2	Membrane fabrication
Magnetic stirrer	2	Membrane fabrication
Ultrasonic Degasser	1	To eliminate bubble in solution
Glass plates	8	Membrane fabrication
500ml Borosilicate Glass	1	Container for solution mixing
100ml Duran Bottle	4	Container for solution mixing
250ml Beakers	2	Membrane fabrication
Filter funnel	1	Membrane fabrication
10 ml Measuring Cylinder	2	Membrane fabrication
50 ml Measuring Cylinder	2	Membrane fabrication
Spatula	1	Membrane fabrication
Dropper	1	Membrane fabrication

3.5 Cellulose Acetate Butyrate (CAB) polymer dope preparation

The CAB membrane was prepared via wet phase inversion method, followed by solvent exchange to dry the membrane. A dope solution consisting of 4 wt% CAB (*Mn* of 70000) powders and 96 wt% chloroform was prepared following the conditions of each parameter. The solution was stirred for 24 hours and sonicated for 20 minutes to eliminate the gas bubbles in the solution (Lai et al., 2008, Coltelli et al., 2008). The solution was then poured into space within casting bar with glass plate underneath. The automatic film applicator (Elcometer 4340, E.U.) was used for the casting of the membrane. A 5 minutes of solvent evaporation time was allowed following each parameter's condition before immersion of the membrane in distilled water (27 °C) for a 24 hours duration (Feng et al., 2015). The solvent exchange was performed on the as-spun membrane first with 60 minutes immersion period in isopropyl alcohol and continued with another 60 minutes immersion period in n-hexane. The resultant membrane was then dried at ambient temperature to eliminate remaining volatile liquid in between two glass plates filled with filter paper for 24 hours before use (S.Minhas, 1992).

3.5.1 Polymer concentration parameter

The solution of the neat membrane was prepared following the fabrication method as described in section 2.2. The studied range for this parameter was from 3 to 5 weight percentage (wt%). The synthesis condition of the membrane is illustrated in **Table 3.3**. The sample description is arrange following the fabrication parameters used for polymer concentration, casting thickness, and solvent evaporation time for the membrane synthesise (i.e. CAB-3/250/5: 3 wt % polymer concentration/ 250 µm casting thickness/ 5 minutes solvent evaporation time).

Table 3.3 Composition of membrane prepared at different CAB polymer concentration

Sample Description	CAB (wt%)	Chloroform (wt%)	Casting Thickness (µm)	Evaporation time (min)
CAB-3/250/5	3	97	250	5
CAB-4/250/5	4	96	250	5
CAB-5/250/5	5	95	250	5

3.5.2 Casting thickness parameter

The membranes were prepared at different casting thickness following the fabrication method, as described in section 2.2. The studied range for this parameter was 200 to 300 µm. The synthesise condition of the membrane is shown in **Table 3.4**.

Table 3.4 The composition of membrane prepared at different casting thickness

Sample Description	CAB (wt%)	Chloroform (wt%)	Casting Thickness (µm)	Evaporation time (min)
CAB-4/200/5	4	96	200	5
CAB-4/250/5	4	96	250	5
CAB-4/300/5	4	96	300	5

3.5.3 Solvent evaporation time parameter

The solution of the neat membrane was prepared following the fabrication method, as described in section 2.2. The studied range for this parameter was from 4 to 6 minutes. The synthesise condition of the membrane is presented in **Table 3.5**.

Table 3.5 Composition of membrane prepared at different solvent evaporation time

Sample Description	CAB (wt%)	Chloroform (wt%)	Casting Thickness (μm)	Evaporation time (min)
CAB-4/250/4	4	96	250	4
CAB-4/250/5	4	96	250	5
CAB-4/250/6	4	96	250	6

3.5.4 Effect of solvent exchange time with isopropyl alcohol

Meanwhile, for the effect of solvent exchange time, the membranes were prepared following the fabrication method, as described in section 2.2. The solvent exchange duration studied is tabulated in **Table 3.6** with 15 minutes (CAB-15Iso), 30 minutes (CAB-30Iso) and 60 minutes (CAB-60Iso) for isopropyl alcohol, followed by 60 minutes of n-hexane.

Table 3.6 Composition of membrane prepared at different solvent exchange time for isopropyl alcohol

Sample Description	CAB (wt%)	Chloroform (wt%)	Casting Thickness (μm)	Evaporation time (min)	Solvent exchange time Isopropyl/n-Hexane (min)
CAB-15Iso	4	96	250	5	15/60
CAB-30Iso	4	96	250	5	30/60
CAB-60Iso	4	96	250	5	60/60

3.5.5 Effect of solvent exchange time with n-hexane

In addition, the solution of the solvent exchange time with n-hexane was prepared following the fabrication method, as described in section 2.2. The resultant membranes were first solvent exchanged with isopropyl alcohol for 30 minutes followed by solvent exchange times ranging from 15 minutes (CAB-15H), 30 minutes (CAB-30H) to 60 minutes (CAB-60H) for n-hexane, as tabulated in **Table 3.7**.

Table 3.7 Composition of membrane prepared at different solvent exchange time with n-hexane

Sample Description	CAB (wt%)	Chloroform (wt%)	Casting Thickness (μm)	Evaporation time (min)	Solvent exchange time Isopropyl/n-Hexane (min)
CAB-15H	4	96	250	5	30/15
CAB-30H	4	96	250	5	30/30
CAB-60H	4	96	250	5	30/60

3.5.6 Effect of CAB at different molecular weight (M_n)

The membranes were prepared with different CAB M_n of 12000 (CAB-12000), 65000 (CAB-65000) and 70000 (CAB-70000) for the preparation of the dope solution. Thereafter, following the fabrication method as mentioned in section 2.2, the solvent exchange time for isopropyl alcohol and n-hexane were set for 30 minutes each, as depicted in **Table 3.8**.

Table 3.8 Composition of membrane prepared at different *Mn* polymer

Sample Description	CAB (wt%)	Chloroform (wt%)	Casting Thickness (μm)	Evaporation time (min)	Solvent exchange time Isopropyl/n-Hexane (min)
CAB-12000	4	96	250	5	30/30
CAB-65000	4	96	250	5	30/30
CAB-70000	4	96	250	5	30/30

3.6 MWCNTs functionalisation

The functionalisation of MWCNTs was carried out by drying the MWCNTs first in an oven for 24 hours at 120°C to remove moisture. The dried MWCNTs were then functionalised using Chen's soft cutting method (Chen et al., 2001). Based on this functionalisation technique, pristine-MWCNTs (MWCNTs-P) were grounded with mortar and pestle at a concentration ratio of 1:30 wt% (MWCNTs: β-CD). Ethanol was added in the first 10 minutes of grinding to form a greyish sticky mixture. Another 2.5 hours grinding was continued to obtain the semi-solid MWCNTs-F, which were then heated in the oven at a temperature of 80°C for 24 hours to obtain the powdered MWCNTs-F (Aroon et al., 2010b).

3.7 Fabrication of mixed matrix membrane (MMM)

The MMMs were prepared via wet phase inversion method, followed by solvent exchange approach to eliminate the moisture on the membrane. For MMM-1.0P, a specific amount of the solid base pristine-MWCNTs (MWCNTs-P) were added to the solvent chloroform ($CHCl_3$) and sonicated for 20 minutes. The mixture was stirred for another 4 hours

with magnetic stirrer to ensure well-dispersed particle distribution (Aroon et al., 2010c). The CAB polymer was then added into the mixture of MWCNTs-P with chloroform, and stirred for 24 hours until the CAB polymer was completely dissolved in the mixture. The casting procedure was similar to the fabrication steps of CAB membrane in section 3.5. Meanwhile, MMM-1.0F was prepared by incorporating functionalised-MWCNTs (MWCNTs-F) using the same method as mentioned for MMM-1.0P. Through this study, the phenomenon of incorporating MWCNTs-F as compared to MWCNTs-P into the CAB polymer matrix was investigated (Ahmad et al., 2014). The composition of the MMM prepared is illustrated in **Table 3.9**. Meanwhile, for the effects of MWCNTs-F loadings the MMM composition is tabulated in **Table 3.10**.

Table 3.9 MMM composition with the incorporation of MWCNTs-P and MWCNTs-F

Sample	Polymer	Solvent	MWCNTS		
	CAB (wt %)	$CHCl_3$ (wt %)	Total filler[a] (wt%)	Solid base MWCNTs[b] (wt%)	Solid base β-CD[c] (wt%)
MMM-1.0P	4	95	1.00	0.01	0.00
MMM-1.0F	4	95	1.00	0.01	0.30

[a] Total filler = amount MWCNTs embedded into CAB polymer
[b] Solid base MWCNTs = (amount of filler x CAB)/(1- total base filler (1 + 30))
[c] Solid base β-CD = 30 x solid base MWCNTs

Table 3.10 MMM composition with different loadings of MWCNTs-F

Sample	Polymer	Solvent	MWCNTS		
	CAB (wt %)	$CHCl_3$ (wt %)	Total filler[a] (wt%)	Solid base MWCNTs[b] (wt%)	Solid base β-CD[c] (wt%)
MMM-0.7F	4	95.3	0.70	0.023	0.677
MMM-0.8F	4	95.2	0.80	0.025	0.774
MMM-0.9F	4	95.1	0.90	0.029	0.871

[a] Total filler = amount MWCNTs embedded into CAB polymer
[b] Solid base MWCNTs = (amount of filler x CAB)/(1- total base filler (1 + 30))
[c] Solid base β-CD = 30 x solid base MWCNTs

3.8 Synthesise of blend MMM

The blend MMMs were prepared via wet phase inversion method and subsequently solvent exchanged with isopropyl alcohol as the first drying solvent and n-hexane as the second drying solvent, to eliminate the moisture on the membrane. A total amount of 0.8 wt % solid base MWCNTs-F was added into the solvent chloroform and sonicated for 20 minutes. The mixture was subsequently stirred for another 4 hours with magnetic stirrer to ensure well-dispersed MWCNTs particle distribution (Aroon et al., 2010c). A predetermined amount of two different molecular weights of CAB polymers were then added into the dope solution of MWCNTs-F with chloroform and stirred for 24 hours until the CAB polymer was completely dissolved in the mixture. The membrane casting procedure was similar to the procedure as mentioned in section 3.5. The composition of the membrane prepared is illustrated in **Table 3.11**.

Table 3.11 Composition of the blend MMM

Sample	Polymer		Solvent	MWCNTS		
	CAB1 (wt %)	CAB2 (wt %)	$CHCl_3$ (wt %)	Total filler[a] (wt%)	Solid base MWCNTs[b] (wt%)	Solid base β-CD[c] (wt%)
M1	2.67 (70000)	1.33 (12000)	96	0.8	0.03	0.77
M2	2.67 (70000)	1.33 (30000)	96	0.8	0.03	0.77
M3	2.67 (70000)	1.33 (65000)	96	0.8	0.03	0.77

[a] Total filler = amount MWCNTs embedded into CAB polymer
[b] Solid base MWCNTs = (amount of filler x CAB)/(1- total base filler (1 + 30))
[c] Solid base β-CD = 30 x solid base MWCNTs

3.6 Membrane gas permeation studies

3.6.1 Experimental rig setup (single gas permeation)

A list of equipment used in the gas permeation rig setup along with the specifications and function of the equipment are presented in **Table 3.12**.

Table 3.12 List of components of experimental rig setup

Component	Unit	Specification	Function
Mass flow controller	3	Aalborg AFC 26, 0-200ml/min	To control the flow rate of feed gas (CO_2 and N_2)
Mass flow controller command unit	1	Aalborg brand	To manipulate the value of feed gas flow rate
Pressure gauge	1	Unijin brand	To measure the pressure in feed stream and permeate stream
Pressure relieve valve	1	Swagelok brand	To adjust the pressure in retentate stream
Needle valve	3	Swagelok brand	To open and close the feed gas stream
Gas permeation cell	1		To analyze the membrane gas permeation test
Bubble flow meter	1	0-100 ml	To determine the amount of gas flow from permeate stream

The testing for single gas permeation was conducted using purified CO_2 and N_2 gas at ambient temperature. A schematic diagram and actual experimental rig setup are illustrated in **Figures 3.2** and **3.3**, respectively. The feed rate of each gas supplied from compressed gas cylinder tank was controlled at 100ml/min using the mass flow controller (Aalborg AFC26, USA). The mass flow controller was connected to a two-channel digital set point readout unit (Aalborg 0-200 ml, USA) to display and further control the output flow of the feed gas (S.Minhas, 1992). Gas leak detection test was conducted before starting the permeability test on the connecting pipes (Jawad et al., 2015a). Pure N_2 gas was used to flush and purge out any gases that remained in the gas pipes for duration of 15 minutes. After that, the prepared membrane was cut into a round disc shape with an effective diameter of 7.07 cm^2 and placed

in the membrane permeation cell (Jawad et al., 2015a). The permeance of the membrane was obtained and measured through the volume displacement of the soap bubble flow meter with the use of a stopwatch to calculate the displacement time (Ahmad et al., 2014).

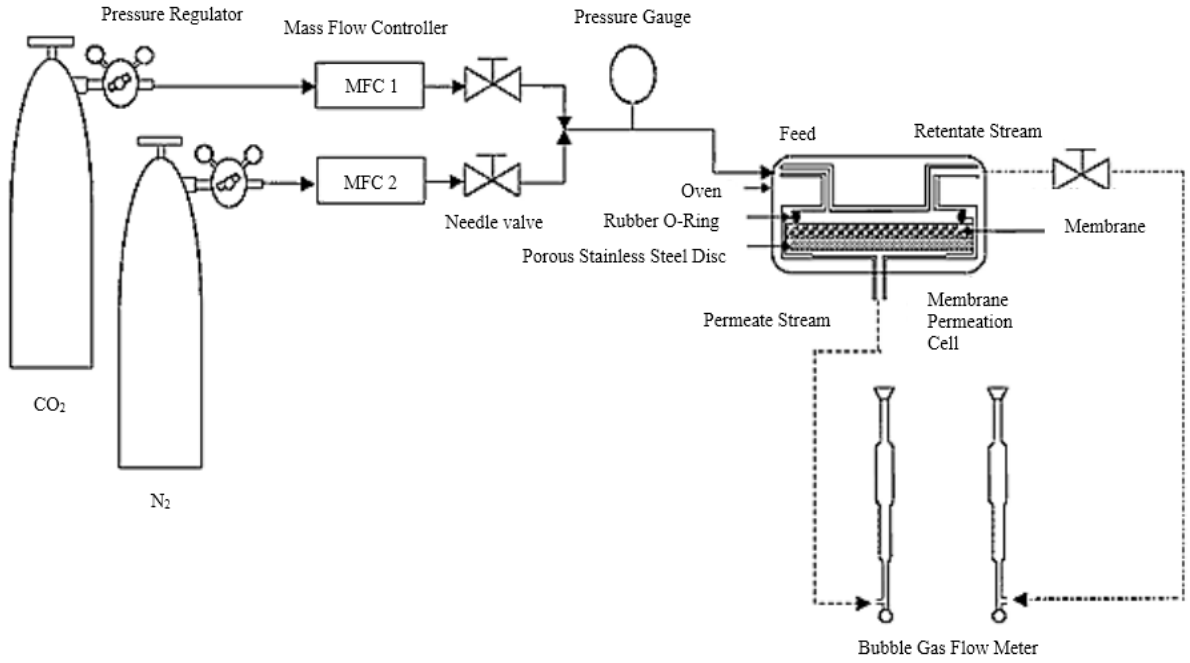

Figure 3.2 Schematic diagram of permeability test rig

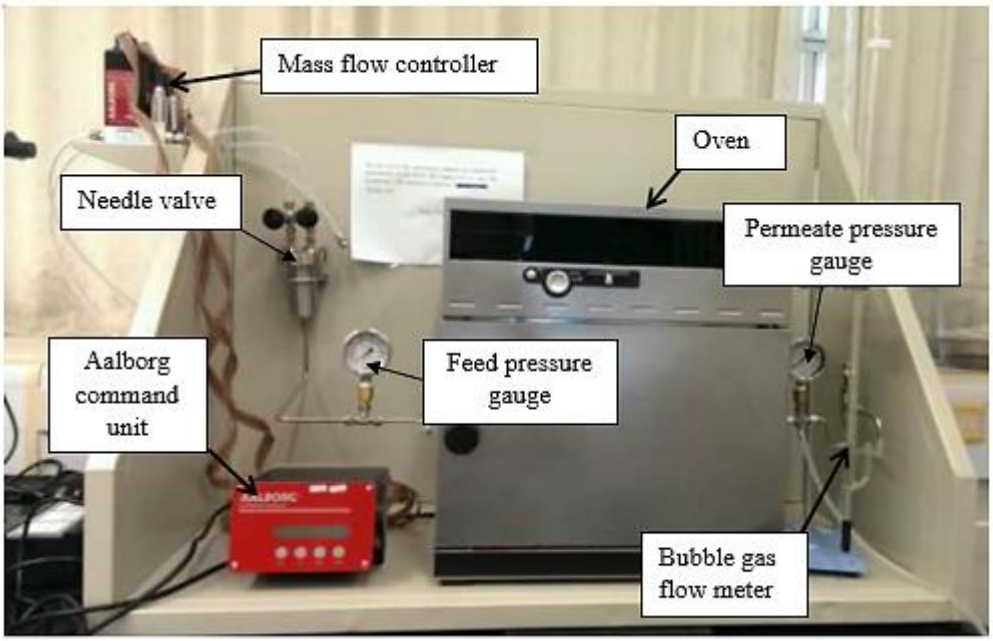

Figure 3.3 Actual gas permeation test rig setup

The details of actual internal design of the gas permeation cell are depicted in **Figure 3.4a** (Jawad et al., 2015b). The top part of the membrane gas permeation cell has the rubber O-ring to secure the feed gas from escalating from the permeation cell, as displayed in **Figure 3.4b**. Meanwhile, **Figure 3.4c** illustrates the bottom permeation cell that consists of a porous stainless steel disc to allow the permeant gas to pass through the permeation cell and flow to the bubble flow meter. In addition, the membrane permeation cell was tightened with 6 nuts arranged opposite to one another with an effective permeation area of 7.065 cm^2.

The gas permeation coefficient and separation performance of the membrane was determined in terms of gas permeance and ideal selectivity. First, the single gas flow rate (F_a) was calculated based on **Equation 3.1** (Jawad et al., 2015b).

$$F_a = \frac{PV}{RT} \tag{3.1}$$

Where, the absolute pressure of gas is expressed as P, the mean velocity of gas component is V, the gas constant is R, and T is the absolute temperature of gas. With the flow rate (F_a) of gas obtained, the flux of the gas component (N_a) can be determined using **Equation 3.2** (Jawad et al., 2015b).

$$N_a = \frac{mol\ of\ gas\ component}{t \cdot A_m} \tag{3.2}$$

Where, t represents the time in seconds, while A_m is the effective area of membrane in m^2. Hence, the permeability (P_a) (mol/m^2.s.Pa) of the membrane can be calculated using **Equation 3.3** (Jawad et al., 2015b).

$$P_a = \frac{N_a}{\Delta p} \tag{3.3}$$

Where, p represents the total pressure difference across the membrane in Pa. In this research study the gas permeation unit is indicated by (P_a/l), where, l is the thickness of the membrane in µm. Therefore, the unit conversion is required to convert the permeability (mol/m^2.s.Pa) to permeance (GPU). The GPU unit is expressed in **Equation 3.4** (Jami'an et al., 2015).

$$GPU = \frac{10^{-6} mol}{m^2 \cdot s \cdot 3000 Pa} \quad \textbf{(3.4)}$$

Meanwhile, the ideal selectivity factor (α_{ab}) of the gas components, which are CO_2 and N_2 can be determined using **Equation 3.5** (Jawad et al., 2015a). Each specimen of the membrane was tested at least 4 times to ensure precision of the results generated. The average values together with the standard errors were also included in the calculation.

$$\alpha_{ab} = \frac{P_a}{P_b} = [(P/l)_a/(P/l)_b] \quad \textbf{(3.5)}$$

The calculation samples for the membranes are presented in **Appendix A**.

3.6.2 Binary gas permeation

The binary gas permeation study for CO_2/N_2 gas mixture was conducted to evaluate the membrane performance when under binary gases phase. The flow rates of the gas mixture (CO_2/N_2) was monitored using 2 units of mass flow controller, which were mass flow controller 1 and mass flow controller 2, respectively. The pressure relieve valve was used to adjust the retentate stream pressure to ensure that the pressure within the permeation cell did not exceed the required pressure (Basu et al., 2011). Consequently, bubble flow meters were connected with the retentate and permeate streams to determine the flow rate of CO_2 and N_2. Finally, the gas composition from retentate and permeate gas streams were directed towards the GC stream and analysed using Agilent GC (model 7890A, GC system).

With reference to binary gas permeation analysis, the gas component was directed from permeate and retentate streams into the Agilent GC system (model 7890A) through a 0.125 inches copper tube. The Agilent GC system was equipped with thermal conduction detector (TCD) for gas component detection purpose. A Molsieve 5A 80/100 (3 Ft x 2 mm) and Porapak Q 80/100 (6 Ft x 2mm) stainless steel packed column was used in GC for gas components analysing purpose (Basu et al., 2011). The helium gas was used as the carrier gas in GC. During the gas components analysis, a temperature of 80°C was set for the oven temperature. While the TCD temperature was set to 150°C with a reference and makeup flow of 50 ml/min and 5 ml/min, respectively. With these predetermined operating conditions, the GC was calibrated with a run time of 10 minutes. The gas components were analysed using the calibration curve, as illustrated in **Appendix B**.

The permeability (*P*) coefficient for binary gas permeation analysis can be calculated using **Equation 3.6** (Khan et al., 2010).

$$P_i = \frac{N_i y_i}{\Delta p_i x_i} \quad \textbf{(3.6)}$$

Where, *Ni* is the molar flow rate in mol/m^2.sec, p_i represents the pressure difference across the membrane, y_i and x_i are the mole fraction of the gas component *i* in upstream and downstream, respectively. The permeability obtained is then converted into GPU based on **Equation 3.4** mentioned previously.

Meanwhile, the composition selectivity for binary gas mixture is defined as the ratio of the permeability coefficients for each gas component. The composition selectivity can be determined using **Equation 3.7** (Adhikari and Lin 2016).

$$\alpha_{ij} = \frac{y_i/y_j}{x_i/x_j} \quad \textbf{(3.7)}$$

Where, y_i and y_j represent the mole fraction of gas components in the permeate stream, and x_i and x_j are the mole fraction of gas components in feed stream. The binary gas analysis was conducted for at least 3 times for each sample to ensure the consistency of the results. A sample calculation of the binary gas permeation is demonstrated in **Appendix C**.

3.7 Membrane characterization

3.7.1 Scanning Electron Microscopy (SEM)

Scanning electron microscopy (SEM) was utilised to determine the microstructural features of the membrane, which was in the range of 2-20 nm and suitable for membrane morphology investigations (Tong et al., 2010). The CAB membranes, MMMs and blend MMMs morphology, including surface and cross-sectional were observed using SEM (Hitachi

TM3000, Tokyo, Japan) with high-sensitive semiconductor detector at 5Kv. Each membrane sample was cut into small pieces and then kept in the cryogenic freezer with plastic petri dish up to -80°C for 24 hours to give a consistent and clean cut by freezing. The samples were coated with a platinum layer to prevent high energy beam damage before the characterisation works. Furthermore, every sample average membrane thickness was calculated based on the frequency count as measured using the Image-J software. Approximately, 100 measurements were taken to confirm the average membrane thickness.

3.7.2 Attenuated Total Reflectance Fourier-transform Infrared Spectroscopy (ATR-FTIR)

The Attenuated total reflectance Fourier-transform infrared spectroscopy (ATR-FTIR) technique was applied to identify the functional groups within the membrane through the identification of various bonds based on the compound wavenumber (Ruysschaert and Raussens 2018). The ATR-FTIR analysis was performed with Nicolet IS10 (USA) spectrometer with a wavenumber range of 3800-700 cm^{-1}. The settings of this ATR-FTIR characterisation was performed according to the Fourier transform principle. The chemistry functionality in terms of sinusoidal basis was expressed in the Fourier principle (Ruysschaert and Raussens 2018). The single-beam absorption spectrum was applied and normalised by comparing it with the background spectrum prior to the sample measurement. The absorption data was expressed in transmittance ($T=I/I_o$), whereby I is the sample intensity and I_o is the background intensity. All data were collected with 32 scans and resolution of 4 cm^{-1} setting through the diamond crystal. Prior to collecting the samples spectra wavenumber, the background information of the room condition was obtained first and was repeated three times for each sample.

3.7.3 Contact angle analysis

The contact angle analysis was conducted with the purpose of identifying the quantifying surface energetics and using the results to predict wetting, spreading and adhesion on the polymers' surfaces. These measurements were an effective way to predict the thermodynamic work of adhesion from constants that characterise each independent material (Tong et al., 2010). The attractive forces available in polymers can be generally summarised into two types: London-Lifshitz attractive energies (dispersion energy) and Lewis acid-base (electron donor acceptor force). Hence, to predict the effects of interphase modifications it was necessary to characterise the surface chemistry quantitatively to enhance the membrane adsorption (Tong et al., 2010). The contact angle is determined by using **Equation 3.8** (Tong et al., 2010).

$$\cos\theta = \frac{F}{p\gamma_L} \qquad \textbf{(3.8)}$$

Where, F represent wetting force, γ_L is the surface tension of liquid, and p is the perimeter. Rame-Hart Model 300 Advanced Goniometer was used to measure the wettability of the membrane. On flat surfaces, the contact angle was measured with a single sessile drop using a telescope with adjustable cross hairs (Tong et al., 2010). The angles obtained were used to analyse the properties of membrane in terms of hydrophilicity and the repulsion forces between the interfacial properties. In order to assure the reproducibility and preciseness of the experimental data taken, at least 10 measurements were taken for each sample.

3.7.4 X-ray Photoelectron Spectroscopy (XPS)

X-ray Photoelectron Spectroscopy (XPS) is the most widely used surface analysis technique because it can be applied to a broad range of materials and provides valuable quantitative and chemical state information from the surface of the material being studied (Nour et al., 2013). XPS is well known as a standard tool for surface material characterisation (Hilal

et al., 2017). The average depth of XPS measurement analysis is about 5nm. The spatial distribution information can be acquired by scanning the micro-focused X-ray beam unto the membrane surface (Nour et al., 2013). The combination of XPS and ion milling (sputtering) is commonly used for the characterisation of thin film morphology to obtain the depth distribution information (Hilal et al., 2017).

The membranes fabricated were characterised with the High Resolution Multi-Technique X-Ray Spectrometer (Axis Ultra DLD XPS, Kratos, Shimadzu Corporation, Japan). The analysis was carried out using a PHI 1600 spectrometer with hybrid lens mode, 150 W (Anode: Mono), 1000 meV step and 5 sweeps for each membrane at room temperature.

3.7.5 Thermogravimetric Analysis (TGA)

Thermogravimetric analysis (TGA) is a thermal analysis method to inspect the changes of sample mass over time as the temperature changes. This measurement provides information about physical phenomena, such as phase transitions, adsorption and desorption, thermal decomposition and solid-gas reactions (Madzarevic et al., 2019). The degradation curve of the membrane samples were obtained through TGA using Mettler Toledo (Switzerland) to analyse the membrane weight lost with respect to temperature. 5.0 grams of membrane sample was allocated in the alumina pan for each characterisation. The temperature was increased from 27°C to a final temperature of 600°C with a heating rate of 10°C /min with nitrogen gas.

3.7.6 Differential Scanning Calorimetry (DSC)

Differential scanning calorimetry was used to determine the prepared MMMs thermal properties (Molki et al., 2018). The purpose of this characterisation is to study the effect of MWCNTs loadings along with the blend MMMs content on the membrane glass transition

temperature (T_g). The T_g of the membrane samples were obtained using the DSC (model 823e, Mettler Toledo, Switzerland) instrument. The membrane samples were cut into 5mg each and were heated from 25 to 900 °C at a rate of 10 °C/min under nitrogen feed gas. The data obtained were analysed with STAR analysis software. The DSC thermograms of MMMs and blend MMMs were illustrated in **Appendix D**.

3.7.7 X-Ray Diffraction (XRD)

The X-ray and neutron reflectivity measurement were utilised to identify the density or concentration profile of thin films and adsorbed layers (Tong et al., 2010). The X-rays were initially dispersed throughout the samples by the electron, and classical electrodynamics applied to determine the scattered electron (Tong et al., 2010). In order to obtain the intensity data, the XRD equipment was used based on the diffracted X-ray beam reflection according to Bragg's law **Equation 3.9** (Erinosho et al., 2016):

$$n\lambda = 2d\ sin\theta \qquad \textbf{(3.9)}$$

Where, n denotes the integer, λ represents the wavelength of the X-rays, d is the inter-planer spacing, and 2θ signifies the diffraction angle between the diffracted X-ray beam and the beam of transmittance (Erinosho et al., 2016). All the XRD data were collected under room temperature with X'Pert PRO diffractometer (PANanalytical) using Cu Kα radiation (λ = 1.5418 Å, U = 40 kV, I = 30 mA) in para-focusing Bragg-Brentano geometry. A counting time of 20.32s step-1, step size of 0.034° and angular range of 10-70° were used for all the scanned data with X'Celerator detector. Data evaluation was performed using the software HighScore Plus (Bugoi et al., 2008).

3.7.8 Kinetic gas sorption study

The carbon dioxide (CO_2) sorption study was conducted using Mettler Toledo TGA (Switzerland) for all the synthesised blend MMMs. The condition of the overall kinetic sorption study profile is depicted in **Figure 3.4** (Jawad et al., 2015b). First of all, the experiment was carried out by placing 2.10 mg of sample into the alumina pan of TGA. The impurities of gas or moisture retained inside TGA was purged by flowing purified N_2 at rate of 50 ml/min into the chamber (Jawad et al., 2015b). Then, the sample was subjected to a heating rate of 10°C/min until it reached the temperature of 130°C. This temperature was maintained for 10 minutes. After that, the sample was allowed to cool down to room temperature with a rate of 10°C/min. Once the sample chamber reached the room temperature, CO_2 was released into the chamber at a constant flow rate of 50ml/min (Jawad et al., 2015b). Meanwhile, the adsorption isotherms reading were recorded with a step size of 1.2 sec. The sample was then subjected to 3 hours of CO_2 gas exposure until it reached the equilibrium state with the final temperature of 130°C (Jawad et al., 2015b). Where, the C_o signify there is no CO_2 in the chamber after purging using the N_2 gas, C_t describe the absorption phase for the membrane with the increase of temperature, and C_∞ denote the concentration of CO_2 reach at the equilibrium state for the membrane. The degradation data of the membrane was collected and tabulated in STAR analysis software to obtain the degradation curve of the samples.

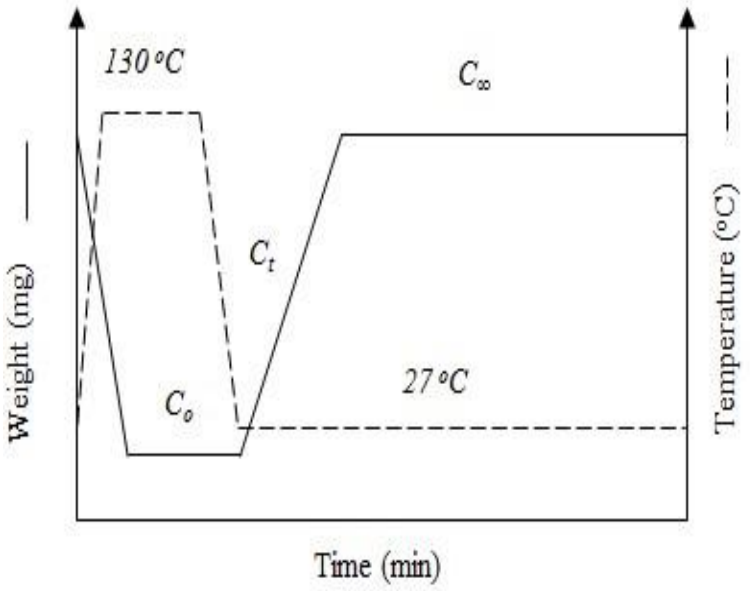

Figure 3.4 Kinetic sorption study profile (Jawad et al., 2015b)

3.7.8.1 Kinetic study assumptions

In this kinetic sorption study, the following assumptions were made for the gas permeation and CO_2/N_2 separation performance, which are listed below:

1. The diffusion and solubility coefficients were independent of pressure. Both of the coefficients were obtained by assuming the pressure was constant across the membrane cell.
2. Ideal gas behaviour was assumed throughout the case study of kinetic sorption.
3. Isothermal temperature was assumed and constant throughout the kinetic study for both CO_2/N_2 gas molecules.
4. The mass transport of the gas is unidirectional, occurring only in the perpendicular direction towards the membrane surface.
5. Pure CO_2 gas with no impurities was used during the single permeation test.
6. No plasticisation occurred within the membrane structure.

3.7.8.2 Transient sorption modelling

The transient sorption modelling was further discussed to explain the fundamental of the kinetic sorption study. In this section, unsteady-state diffusion was assumed in which the diffusing species were diluted and the concentration of gas species (c) and diffusion rate (D) were uniform, so the diffusion equation was applicable in this case. A schematic diagram of flat dense membrane with thickness (L) and a stagnant boundary layer (BL) adjacent to the membrane is illustrated in **Figure 3.5**. Initially, the membrane was exposed to uniform concentration of gas species A with a bulk concentration of A (C_A). External mass transfer of gas species A (C_{Af}) took place on the surface of the membrane and the gas species was governed by convection with a fluid-phase mass transfer coefficient (k_c).

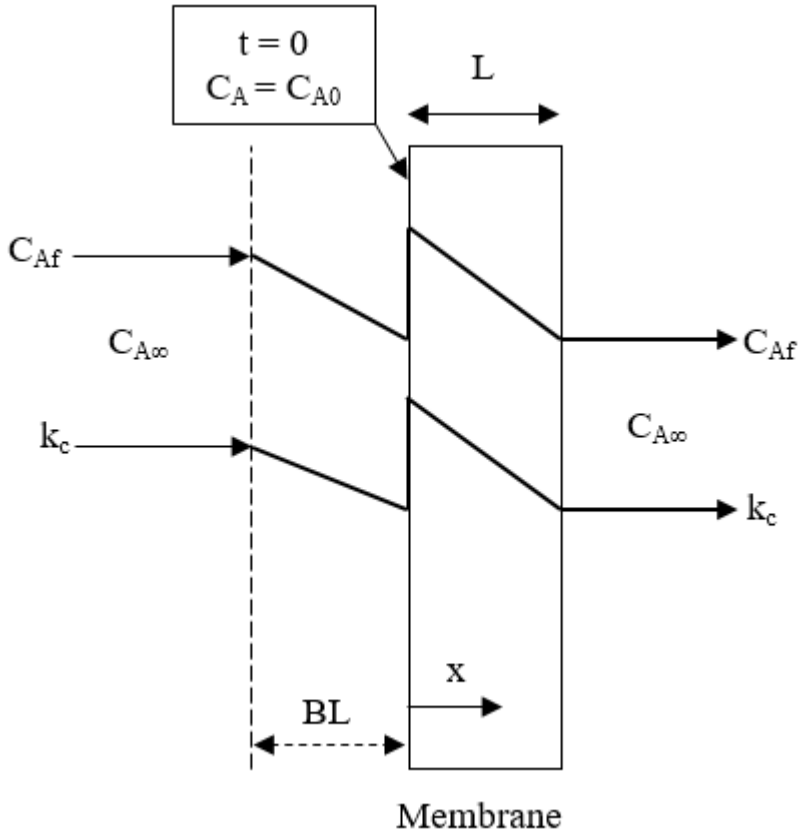

Figure 3.5 Schematic diagram of transient mass transfer in a flat membrane surrounded by gas species A diffuses through the membrane

The transient sorption equation in rectangular coordinates in this experiment of CO_2 at 25.0 °C was conducted with dense membrane. This can be described using Fick's second law **Equation 3.10** (B. Satilmis et al., 2018).

$$\frac{\partial c}{\partial \tau} = D\frac{\partial^2 c}{\partial x^2} \quad \textbf{(3.10)}$$

Where, c is the molar concentration of the diffusing compound and D is the sorption coefficient. The initial condition is shown in **Equation 3.11** (B. Satilmis et al., 2018).

$$C_A = C_{A0}, t = 0 \quad \textbf{(3.11)}$$

Where, C_{A0} represents the initial concentration profile when time (t) is 0 seconds. The first boundary condition is made based on the symmetry of the concentration profile as expressed in **Equation 3.12** (B. Satilmis et al., 2018).

$$\frac{\partial c_A}{\partial x} = 0, x = 0 \quad \textbf{(3.12)}$$

Where, x at 0 is the starting position of the membrane. Due to membrane symmetry, the membrane thickness is taken into consideration ($0 < x < L$). This condition is similar to stating that the molar flux of gas specimen A on the plane x = 0 is zero. The following condition of molar flux (N_A) can be described by **Equation 3.13** (B. Satilmis et al., 2018).

$$N_A = -D_{AB}\frac{\partial c_A}{\partial x} \quad \textbf{(3.13)}$$

A second boundary condition comes from the mole balance of A at the surface of the membrane ($x = L$). The total N_A of species A, which diffuse into the membrane through solution-

diffusion is equal to N_A transferred by convection to the bulk of the fluid. This is described by **Equation 3.14** (B. Satilmis et al., 2018).

$$-D_{AB}\frac{\partial c_A}{\partial x} = k_c\left(c_{Af} - c_{A\infty}\right) \quad \textbf{(3.14)}$$

The fluid concentration of gas component A when in contact with the surface of membrane (c_{Af}) is at an equilibrium concentration within the membrane. Hence, **Equation 3.15** is expressed to assume the linear partitioning (B. Satilmis et al., 2018).

$$c_{Af} = Kc_A \quad \textbf{(3.15)}$$

Subsequently, by substituting **Equation 3.15** with **Equation 3.14**, the boundary condition in **Equation 3.14** can now be expressed as **Equation 3.16** (B. Satilmis et al., 2018).

$$-D_{AB}\frac{\partial c_A}{\partial x} = k_c K\left(c_A - \frac{c_{A\infty}}{K}\right), x = L \quad \textbf{(3.16)}$$

Equation 3.16 consists of 6 parameters: D_{AB}, c_{A0}, L, k_c, K and $c_{A\infty}$ where, any changes made on these constants would affect the concentration field. To simplify the number of parameters in **Equation 3.16**, the equation can be redefined in dimensionless form. The following variables are defined in **Equation 3.17** (B. Satilmis et al., 2018).

$$\Theta = \frac{c_A - c_{A\infty}/K}{c_{A0} - c_{A\infty}/K}, \eta = \frac{x}{L}, \tau = \frac{D_{AB}t}{L^2} \quad \textbf{(3.17)}$$

Where, ɵ represents the dimensionless concentration difference, η is the dimensionless position and τ is the dimensionless time. By substituting all the variables in **Equation 3.17** into **Equation 3.10**, the initial and boundary conditions for **Equations 3.11**, **3.12** and **3.16** leads to the derivation of **Equations 3.18**, **3.19**, **3.20** and **3.21**, after manipulation.

$$\frac{\partial \Theta}{\partial \tau} = \frac{\partial^2 \Theta}{\partial \eta^2} \quad \textbf{(3.18)}$$

$$\Theta = 1\,, \tau = 0 \quad \textbf{(3.19)}$$

$$\frac{\partial \Theta}{\partial \eta} = 0, \eta = 0 \quad \textbf{(3.20)}$$

$$\frac{\partial \Theta}{\partial \eta} = -Bi\Theta, \eta = 1 \quad \textbf{(3.21)}$$

Where, the mass transfer in Biot number (*Bi*) is a unit-less parameter defined by **Equation 3.22** (B. Satilmis et al., 2018).

$$Bi = \frac{k_c KL}{D_{AB}} \quad \textbf{(3.22)}$$

Thus, the dimensionless formulation now has only one parameter, which is *Bi* instead of the 6 parameters present earlier. Therefore, the *Bi* number is the remaining physical parameter that affects the dimensionless concentration field ($\Theta\ (\tau, \eta)$). The *Bi* number can be interpreted as a comparative ratio between the external mass transfer process (k_c) and internal diffusion (D_{AB}). According to Sáez and Baygents (2014), the dimensionless **Equation 3.21** can be solved using **Equation 3.23**.

$$\Theta(\tau, \eta) = f(\eta) g(\tau) \quad \textbf{(3.23)}$$

By substituting the differential equation and separation, **Equation 3.23** can now be expressed in **Equation 3.24** (Sáez and Baygents 2014).

$$\frac{1}{g}\frac{dg}{d\tau} = \frac{1}{f}\frac{d^2f}{d\eta^2} = -\lambda^2 \quad \textbf{(3.24)}$$

Where, the left-hand side equation depends on dimensionless time unit (τ), while the right-hand side equation depends on the dimensionless position (η) (Sáez and Baygents 2014). Hence, an equilibrium must be achieved on both sides to be equal to a constant of sample mass (λ), with the sign of negative to indicate the exponential decay with time. Furthermore, the differential **Equation 3.24** of *g* and *f* can be directly integrated to be expressed as **Equations 3.25** and **3.26** (Sáez and Baygents 2014).

$$g\text{: } \frac{dg}{g} = -\lambda^2 d\tau \Longrightarrow g = Ae^{-\lambda^2\tau} \quad \textbf{(3.25)}$$

$$f\text{: } \frac{d^2f}{d\eta^2} + \lambda^2 f = 0 \quad \textbf{(3.26)}$$

Where, the solution is described in **Equation 3.27** and together with the boundary conditions for **Equation 3.27**, is presented in **Equations 3.28** and **3.29**, respectively (Sáez and Baygents 2014).

$$f = C_1 \sin(\lambda\eta) + C_2 cos(\lambda\eta) \quad \textbf{(3.27)}$$

$$g\frac{df}{d\eta} = 0 \Longrightarrow = \frac{df}{d\eta} = 0, \eta = 0 \quad \textbf{(3.28)}$$

$$g\frac{df}{d\eta} = -Bifg \Longrightarrow = \frac{df}{d\eta} = -Bif, \eta = 1 \quad \textbf{(3.29)}$$

By substituting **Equation 3.27** with the boundary conditions, Equation **3.30** results (Sáez and Baygents 2014).

$$-C_2\lambda \sin\lambda = -C_2 Bi \cos\lambda \quad \textbf{(3.30)}$$

Since the bulk concentration (C_2) cannot be zero (or else this would lead to trivial solution $\Theta \equiv 0$), by rearranging **Equation 3.30**, **Equation 3.31** is formed (Sáez and Baygents 2014).

$$\lambda \tan\lambda = Bi \quad \textbf{(3.31)}$$

According to Sáez and Baygents (2014), it was concluded that the **Equation 3.31** had infinite solution, because **Equation 3.31** is the eigenvalue condition. Therefore, **Equation 3.27** has infinite solution when the boundary condition of bulk concentration is C_1=0. Until this point, the problem formulation that have not been used yet is the initial condition as mentioned in **Equation 3.19**. According to Kreyszig (2008), the theory of separation of variables can be indicated using the linear combination of all the solutions given in **Equation 3.23** whereby, **Equation 3.32** is derived **(**Kreyszig 2008).

$$\Theta(\tau,\eta) = \sum_{n=1}^{\infty} a_n \cos(\lambda_n \eta) e^{-\lambda_n^2 \tau} \quad \textbf{(3.32)}$$

Where, a_n is the series coefficient. The a_n integral is expressed in **Equation 3.33 (**Kreyszig 2008).

$$a_n = \frac{2sin\lambda_n}{\lambda_n + sin\lambda_n cos\lambda_n} \quad \textbf{(3.33)}$$

By substituting **Equation 3.33** by **Equation 3.32**, the final solution is presented as **Equation 3.34 (**Kreyszig 2008).

$$\Theta(\tau,\eta)=\sum_{n=1}^{\infty}\frac{2sin\lambda_n}{\lambda_n+sin\lambda_n cos\lambda_n}\cos(\lambda_n\eta)e^{-\lambda_n^2\tau} \quad \textbf{(3.34)}$$

Based on **Equation 3.34**, Sáez and Baygents (2014) stated that the larger the value of τ, more rapid the decay rate with the increased series of coefficient *n*. The detailed calculation of **Equation 3.34** demonstrated that if *Bi* > 0.01, and τ > 0.1, the approximate solution can be redefined as **Equation 3.35** (Sáez and Baygents 2014).

$$\Theta(\tau,\eta)\cong\sum_{n=1}^{\infty}\frac{2sin\lambda_1}{\lambda_1+sin\lambda_1 cos\lambda_1}\cos(\lambda_1\eta)\,e^{-\lambda_1^2\tau}\ ,Bi>0.01,\tau>0.1 \quad \textbf{(3.35)}$$

In the meantime, the molar flux of gas component A at the surface of the membrane can be determined by taking the average differential **Equation 3.10** over the membrane volume, as illustrated in **Equation 3.36** (Sáez and Baygents 2014).

$$\frac{1}{L}\int_0^L\frac{\partial c_A}{\partial t}dx=\frac{1}{L}\int_0^L D_{AB}\frac{\partial^2 c_A}{\partial x^2}dx \quad \textbf{(3.36)}$$

After integrating the right-hand side, the average molar concentration of A in the membrane can now be expressed as **Equation 3.37** (Sáez and Baygents 2014).

$$\frac{d\langle c_A\rangle}{dt}=\frac{D_{AB}}{L}\frac{\partial c_A}{\partial x} \quad \textbf{(3.37)}$$

By referring to the **Equation 3.13** and applying it to **Equation 3.37**, the **Equation 3.38** is formed (Sáez and Baygents 2014).

$$N_{Ax}=-L\frac{d\langle c_A\rangle}{dt} \quad \textbf{(3.38)}$$

The average dimensionless concentration can now be determined, using the dimensionless version of **Equation 3.37**. The equation is now expressed as **Equation 3.39** (Sáez and Baygents 2014).

$$\langle \Theta \rangle = \int_0^1 \Theta d\eta \tag{3.39}$$

By substituting the solution from **Equation 3.34** into **Equation 3.39** and integrating it leads to the formation of **Equation 3.40** (Sáez and Baygents 2014).

$$\langle \Theta \rangle = \sum_{n=1}^{\infty} \frac{2sin^2\lambda_n}{(\lambda_n + sin\lambda_n cos\lambda_n)\lambda_n} e^{-\lambda_n^2 \tau} \tag{3.40}$$

The flux can now be calculated by combining the **Equations 3.17**, **3.38** and **3.40**, which yield **Equation 3.41** (Sáez and Baygents 2014).

$$N_{Ax} = \frac{D_{AB}}{L}(C_{A0} - C_{A\infty}/K) \sum_{n=1}^{\infty} \frac{2sin^2\lambda_n}{(\lambda_n + sin\lambda_n cos\lambda_n)\lambda_n} e^{-\lambda_n^2 \tau} \tag{3.41}$$

The solution as expressed in **Equation 3.41**, corresponds to a flat film membrane that is exposed to fluid on all sides (**Figure 3.6**). However, due to the boundary condition taken at the centreline also implies that N_{Ax} = 0 when x = 0. This means that the **Equation 3.41** is applicable to a plate thickness of L only, when in contact with the surface of the membrane. Therefore, this creates a limiting case whereby, the **Equation 3.41** is only applicable when the convective mass transfer to the surroundings is faster than the diffusion within the polymer matrix i.e., when Bi >1. This means that the concentration of gas component A at the surface is equal to the concentration at equilibrium with the fluid bulk, which is, $C_A = C_{A\infty}/K$. The dimensionless

concentration on the film membrane can then be derived, as shown in **Equation 3.42** (Sáez and Baygents 2014).

$$\Theta(\tau,\eta) = \frac{4}{\pi}\sum_{n=1}^{\infty}\frac{(-1)^{n-1}}{(2n-1)}\cos\left[\frac{(2n-1)\pi\eta}{2}\right] e^{-((2n-1)^2\pi^2\tau/4)} \qquad \textbf{(3.42)}$$

Equation 3.42 results when using the separation variables replacing the convective boundary condition by substituting $\Theta = 0$ and $\eta = 1$. However, this equation is not applicable when $\tau <$ 0.04, because the perturbation imposed by exposing the surface of the film membrane to the fluid does not have enough time to permeate into the centre of the polymer matrix (Sáez and Baygents 2014).

In this regard, due to the applicability of **Equation 3.42** that restricts fluid systems that have $\tau = 1$, this assumption often mitigates the occurrence of more complicated mechanisms, such as concentration dependency of the solubility coefficient (O. Vopicka et al., 2013). Therefore, another approach is utilised here to describe the transient transport of a low-molecular weight compound in an infinite medium that can be classified by the time dependence of the variance of the concentration distribution, as shown in **Equation 3.43** (Ebneyamini et al., 2017).

$$\sigma_\alpha^2(\tau) = 2D_\alpha\tau^\alpha \qquad \textbf{(3.43)}$$

Where, σ represents the concentration profile of gas component A. If the sorption process obeys Fick's law (following **Equation (3.10)**) then α equals one. The slow sorption occurs if $0<\alpha<1$ and fast sorption occurs if $1<\alpha<2$ where, the process of super sorption in systems is without chemical reaction, whose two basic mechanisms were reported in the literature (O.

Vopicka et al., 2013). The mechanism of super sorption is referred to as the sorption in disordered media. The sorption in disordered media is described as the nature of random diffusing pattern. This type of transport can be parameterised as the sorption is factually structured media or with the fractional sorption equations (O. Vopicka et al., 2013). Hence, the model based on fractional sorption equation is applied in this work.

Fast sorption is usually observed in MMM, where the sorption rate is generally faster than desorption rate. At the molecular-level mechanism, the movement of the species changed from typical Brownian diffusion to Lévy walk on the surface mediated by the bulk. This super sorption mechanism is expected in MMM because of its strong diffusivity behaviour according to the solution diffusion mechanism and where the concentration gradient acts as the main driving force of the gas transport (Ebneyamini et al., 2017). This process can be described phenomenologically with the convective–sorption equation, as suggested according to the description of transient sorption in strong swelling glassy polymers, and particularly for sorption in MMM.

The transient convective–diffusive transport of a compound in a one-dimensional medium can be described with **Equation 3.44** (Ebneyamini et al., 2017).

$$\frac{\partial c}{\partial \tau} = D\frac{\partial^2 c}{\partial x^2} - v\frac{\partial c}{\partial x} \qquad \textbf{(3.44)}$$

Where, D is the sorption coefficient and v is the convective velocity of the sorbate in the matrix. Solution of **Equation 3.44** for sorption of a compound into the polymer matrix can be obtained under initial and boundary conditions of $c(0,\tau)=c(\tau)$, $c(x,0)=0$ for $0 \leq x \leq l/2$ and

$(\partial c(x,\tau)\big/\partial x)_{x=l/2}=0$, where $\tau \geq 0$ and $c(\tau) \in <0,1>$. Various solutions of **Equation 3.44** for dense media are found in the literature (B. Satilmis 2018). An equation capable of describing anomalous diffusion in the stretched-time standard sorption is demonstrated in **Equation 3.45** (O. Vopicka et al., 2013).

$$\frac{\partial c}{\partial(\tau^{\alpha})} = D_{\alpha}\frac{\partial^2 c}{\partial x^2} \qquad \textbf{(3.45)}$$

Where, α ($0<\alpha<2$) is the time-stretching factor and D_{α} ($m^2\ s^{-\alpha}$) is the generalised sorption coefficient. The **Equation 3.45** is a stochastic model of diffusion, which depends on the generalised time of Brownian mechanism (O. Vopicka et al., 2013). Consequently, **Equation 3.46** is one of the simplest fractional sorption equations (O. Vopicka et al., 2013).

$$\frac{\partial_c}{\partial_{\tau}} = \propto \cdot\, \tau^{\propto -1} D_{\alpha}\frac{\partial^2 c}{\partial x^2} \qquad \textbf{(3.46)}$$

This implies the time-dependency on the overall sorption coefficient ($\alpha \cdot \tau^{\alpha-1} \cdot D\alpha$). However, the function $\tau^{\alpha-1}$ limits at infinity as time approaches zero (for $0<\alpha<1$) or when time becomes infinite (for $1>\alpha>2$). The implication of the infinite overall sorption coefficient in **Equation 3.46** restricts the applicability of the model for the purpose of qualitative classification. **Equation 3.46** can be solved analytically for the case of sorption of a compound according to the polymer matrix. Thus, the relative amount of the sorbate, expressed for initial and boundary conditions $c(0,\tau)=c(l,\tau)=1$ and $c(x,0)=0$ for $0 \leq x \leq l$ for $\tau \geq 0$, has the form of **Equation 3.47**,

$$\frac{Q_{(\tau)}}{Q_{\infty}} = 1 - \frac{8}{\pi^2}\sum_{i=0}^{i=\infty}\frac{1}{(2i+1)^2}\,exp\left[-\frac{\pi^2 D_{\propto}\tau^{\propto}\cdot(2i+1)^2}{l^2}\right] \qquad \textbf{(3.47)}$$

Where, $Q(\tau)$ is the amount of sorbate in the slab of polymer in time τ and Q_∞ is the amount of sorbate in the slab of polymer at sorption equilibrium. The above **Equation 3.47** is a generalisation of the equation, which was originally derived for α=1 (O. Vopicka et al., 2013).

CHAPTER THREE

RESULTS AND DISCUSSIONS

4.0 Overview

The main goal of this work is to synthesise a mixed matrix membrane (MMM) from cellulose acetate butyrate (CAB) and multi-walled carbon nanotubes (MWCNTs) that are excellent for carbon dioxide and nitrogen (CO_2/N_2) separation. The first section 4.1 presents the results of different parametric studies performed with the CAB membrane in terms of polymer concentration, casting thickness, solvent evaporation time, solvent exchange time of isopropyl alcohol and n-hexane, and effect of different CAB molecular weight (M_n) used to obtain the optimal neat CAB membrane. Subsequently, the optimised neat CAB membrane preparation method attained from section 4.1 was further used to fabricate MMM by incorporating functionalised MWCNTs into the CAB polymer matrix (section 4.2). In section 4.2, the discussion focused on the synthesised pristine and functionalised MMM, followed by the effect of different loading concentrations of MWCNTs-F in CAB polymer matrix in section 4.3. In addition, section 4.4 discusses the blend MMM fabricated by blending two CAB polymers at different *Mn* and were compared based on the membrane morphologies and separation performances. Further, the CO_2 kinetic sorption study was evaluated together with the diffusivity and solubility coefficients for the blend MMMs that were kinetically determined in section 4.5. Consequently, the CO_2 permeance and CO_2/N_2 separation performance achieved for the blend MMMs were compared with Robeson's curve in section 4.7. Lastly, section 4.8 highlights the permeation and separation performances of the CO_2/N_2 binary gas mixture for the best-synthesised blend MMM, in terms of the permeance for CO_2 and N_2 as well as the evaluation of the composition selectivity.

4.1 Cellulose Acetate Butyrate (CAB) membrane fabrication

In this research study, CAB was chosen as the main polymeric matrix composition. This is because the CAB polymer exhibits few prominent characteristics, which can effectively improve and further expand the cellulose chain, hence, giving high CO_2 sorption characteristic (Kunthadong et al., 2015). Nevertheless, the optimal fabrication conditions need to be considered when synthesising high performance CAB membrane for CO_2/N_2 separation. As a result, experimental works were carried out to evaluate the fabrication condition and to study their influences in terms of membrane morphologies and separation performance.

4.1.1 Effect of CAB polymer concentration

The surface morphology of the membrane can be affected by various parameters. One of the dominant parameters is the polymer concentration. The SEM characterisations are represented in **Figure 4.1** with CAB polymer concentration of 3 wt% (CAB-3/250/5), 4 wt% (CAB-4/250/5) and 5 wt% (CAB-5/250/5), respectively. From **Figure 4.1a**, a porous surface was observed for CAB-3/250/5. Gradually with the increase of polymer concentration to 4 wt%, a smooth structure was formed (**Figure 4.1c**). Then, at 5 wt% the surface structure of CAB membrane changed to rough (**Figure 4.1e**). This was a result of the transition from liquid-liquid demixing to solid-liquid demixing at higher polymer concentration, due to higher kinetic aspect contributed by higher polymer concentration in the coagulant bath that reduce the rate of demixing (Baker et al., 2010, Sadeghi et al., 2009). When the rate of demixing is reduced during the membrane formation process, it can hinder the synthesising rate for the membrane which lead to the rough surface formation due to the delay polymer matrix coagulation. Based on **Figure 4.1b**, the thickness of CAB-3/250/5 is 7.23 ± 0.50 μm, which is relatively thinner than CAB-4/250/5 (11.32 ± 0.70 μm) and CAB-5/250/5 (11.52 ± 0.02 μm) (**Figures 4.1d** and **f**). As the CAB polymer concentration reduced, a rapid diffusion occurred, exchanging the non-

solvent in the film of the polymer membrane while the solvent diffused out from the film (Han and Nam, 2002). Consequently, a thin dense membrane was formed for CAB-3.

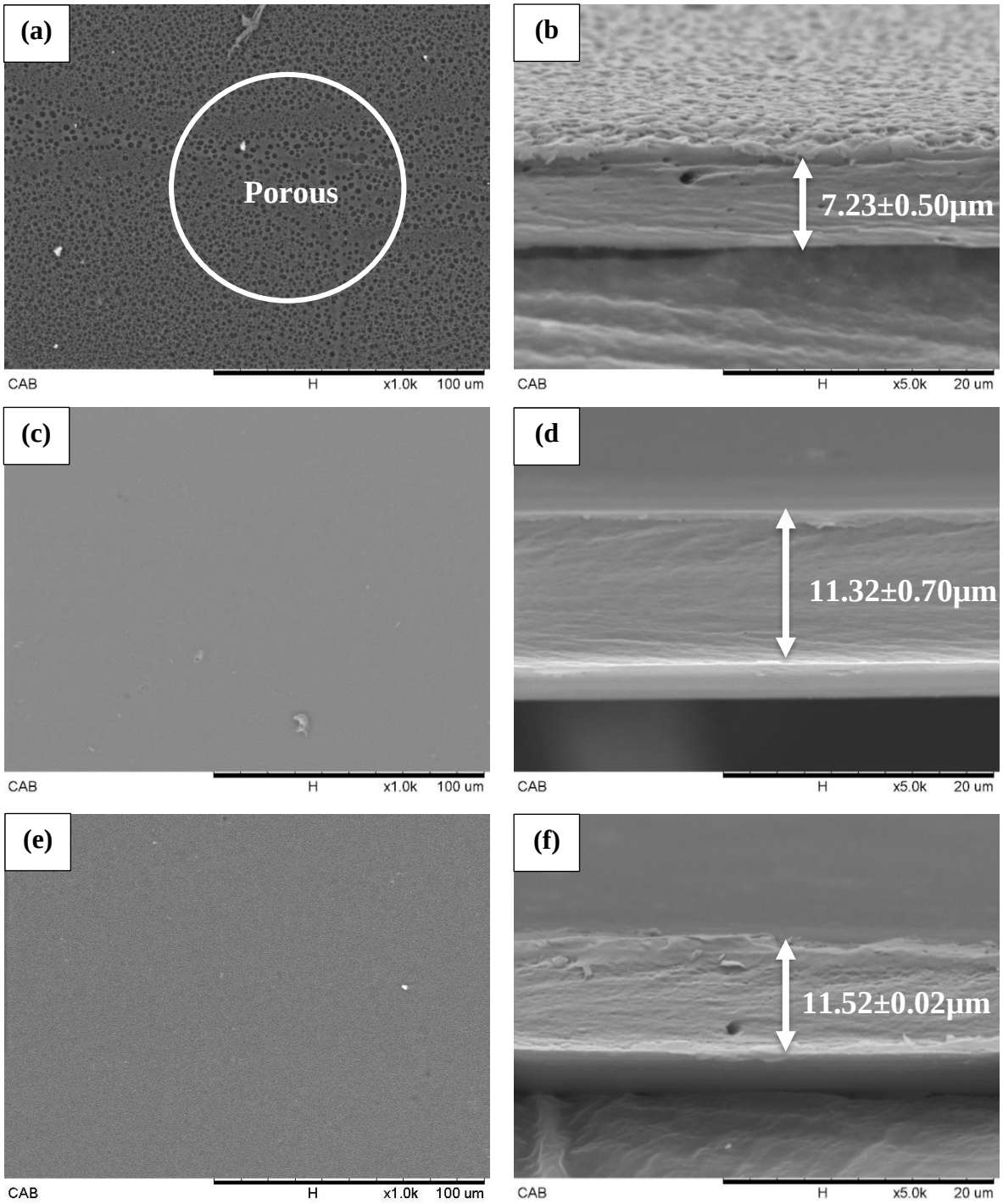

Figure 4.1 Surface and cross-sectional SEM of CAB membranes (*Mn* of 70000) at polymer concentrations of (a-b) 3 wt% (CAB-3/250/5), (c-d) 4 wt% (CAB-4/250/5), and (e-f) 5 wt% (CAB-5/250/5), with a casting thickness of 250 µm and 5 min solvent evaporation time

The CO_2 permeances for CAB-3/250/5, CAB-4/250/5 and CAB-5/250/5 are shown in **Figure 4.2**. The permeance of CO_2 increased from 41.70 ± 0.70 GPU to 398.46 ± 1.43 GPU when the polymer concentration increased from 3 wt% to 4 wt%, respectively. When 4 wt% of the CAB polymer was used, the resultant membrane (CAB-4/250/5) was able to achieve the highest CO_2 permeance. The reason was due to the formation of a smooth and selective dense membrane which has lower mass transport resistance that allow the fast transport of CO_2 permeate, as depicted in **Figures 4.1c** and **d** (Luo et al., 2016). However, when the CAB polymer concentration was increased to 5 wt%, the permeance of CO_2 reduced to 91.54 ± 1.05 GPU. This could be related to the rough surface of CAB-5/250/5 and the thick membrane formation (11.52 ± 0.02 µm) displayed in **Figures 4.1e** and **f**, which can subsequently suppress the CO_2 diffusion efficiency within the membrane due to the increase of overall mass transport resistance caused by the closely packed polymer that aggregates and precipitate during the membrane formation, due to the increased of polymer concentration (Hamad et al., 2005).

Meanwhile, the N_2 permeance for CAB-3/250/5, CAB-4/250/5 and CAB-5/250/5 are 31.68 ± 0.50, 121.55 ± 1.30 and 42.73 ± 0.57 GPU, respectively, as shown in **Figure 4.3**. CAB-4/250/5 demonstrated the highest N_2 permeance. The possible explanation for the rising trend was the smooth structure of CAB-4/250/5, which enhanced the gas separation performance (Duan et al., 2014, Freeman, 1999). Subsequently, the N_2 permeance of CAB-5/250/5 reduced because of the highly viscous casting solution, which slowed down the membrane precipitation process and produced a denser membrane (Khulbe et al., 2007). Hence, this induces more resistant to the gas diffusion process. However, contradict results was exemplified when increasing the polymer concentration from CAB-3/250/5 to CAB-4/250/5. This is subsequently attributed to the poor adhesion between polymers revealed by CAB-3/250/5 (**Figure 4.1b**), which leads to the low N_2 permeance (Dorosti et al., 2011).

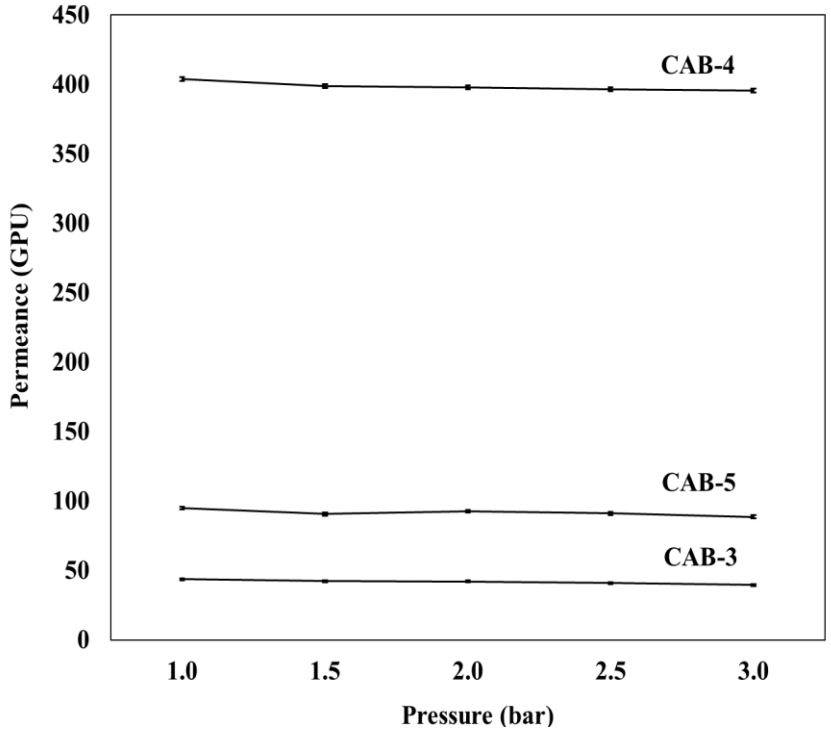

Figure 4.2 CO_2 permeance for membranes synthesised with 3 wt% (CAB-3/250/5), 4 wt% (CAB-4/250/5), and 5 wt% (CAB-5/250/5) of CAB polymer (*Mn* of 70000), and a casting thickness of 250 µm and 5 min solvent evaporation time

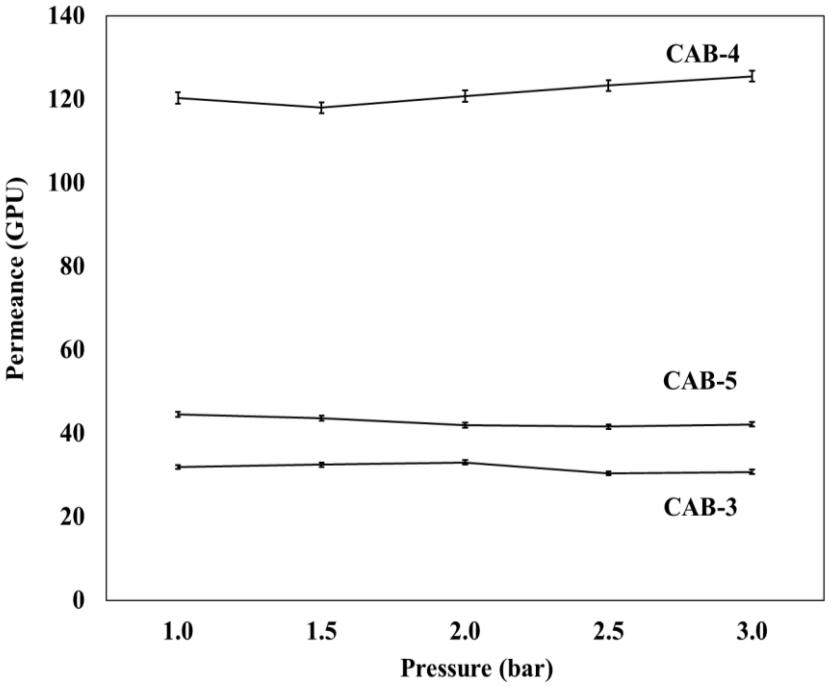

Figure 4.3 N_2 permeance for membranes synthesised at 3 wt% (CAB-3/250/5), 4 wt% (CAB-4/250/5), and 5 wt% (CAB-5/250/5) of CAB polymer (*Mn* of 70000), with a casting thickness of 250 µm and 5 min solvent evaporation time

The ideal selectivity of CO_2/N_2 gas separation performance for membranes CAB-3/250/5, CAB-4/250/5 and CAB-5/250/5 are demonstrated in **Figure 4.4**. Amongst the membranes, CAB-4/250/5 exhibited the best selectivity results, which was 3.28 ± 0.04. This was due to the smooth and thinner membrane structure (11.32 ± 0.70 µm), as depicted in **Figures 4.1c** and **d**, respectively, even though CAB-3/250/5 demonstrated thinner membrane thickness (7.23 ± 0.50 µm) than CAB-4/250/5 (11.32 ± 0.70 µm). However, CAB-3/250/5 had low selectivity of 1.32 ± 0.02 due to its porous surface (**Figure 4.1a)** that could disrupt the CO_2 selectivity. Hence, the permeance results (Khulbe et al., 1997).

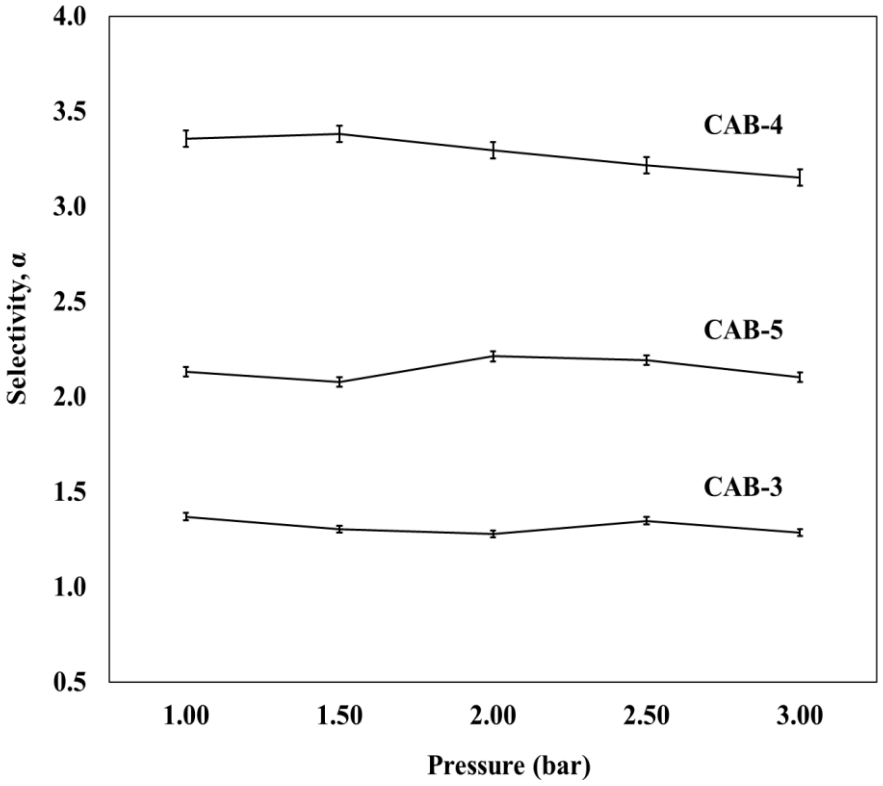

Figure 4.4 Ideal selectivity of CO_2/N_2 for CAB membranes (*Mn* of 70000) synthesised at different polymer concentration 3 wt% (CAB-3/250/5), 4 wt% (CAB-4/250/5), and 5 wt% (CAB-5/250/5), with a casting thickness of 250 µm and 5 min solvent evaporation time

4.1.2 Effect of casting thickness

The effect of casting thickness on the structure and performance of the CAB membrane is depicted in **Figure 4.5**. Based on **Figure 4.5**, a porous structure of CAB-4/200/5 (200 µm) was illustrated. As the casting thickness of the membranes increased, a smooth surface was observed for CAB-4/250/5 (250 µm), as demonstrated in **Figure 4.5c**. Alternatively, a rough surface was formed for CAB-4/300/5 (250 µm) as seen in **Figure 4.5e.** The change in the structure was due to the different rates of demixing that occurred as the phase precipitation proceeded when high casting thickness was applied, causing the deposition speed of the membrane to reduce during the membrane formation phase. The slow deposition rate avoids rapid exchange of non-solvent and solvent within the membrane. As a result, the surface structure of the CAB membrane was built up based on the sufficient phase precipitation period given (Yeow et al., 2005, Jawad et al., 2015a).

The cross-sectional micrographs of the fabricated CAB membranes at casting thickness of 200 µm (CAB-4/200/5), 250 µm (CAB-4/250/5) and 300 µm (CAB-4/300/5) are revealed in **Figures 4.5b**, **d**, and **f**, respectively. From the micrographs, dense structures were depicted from all the cross-sectional figures (**Figure 4.5a, c, and e**). The dense structure formation was based on the casting thickness used for the preparation of membrane. Whereby the solvent volume imbedded in the polymer matrix is different, due to the varying membrane thickness of each membrane, and the solvent was gradually replaced by distilled water in the coagulation bath. As the volatility of the solvent (chloroform =159 mmHg) is generally higher than distilled water (27 mmHg), as a result the solvent is gradually dissolved in distilled water and causing the reduction of membrane thickness from 12.89 ± 0.10 µm to 11.32 ± 0.06 µm for CAB-4/200/5 and CAB-4/250/5, respectively. Meanwhile, due to the limitation of membrane immersion period the amount of chloroform replaced by distilled water is also limited to certain volume.

Therefore, the increase in membrane thickness for CAB-300 (12.42 ± 0.05 µm) was mainly attributed by the increase of initial casting thickness applied (Moaddeb and Koros 1997).

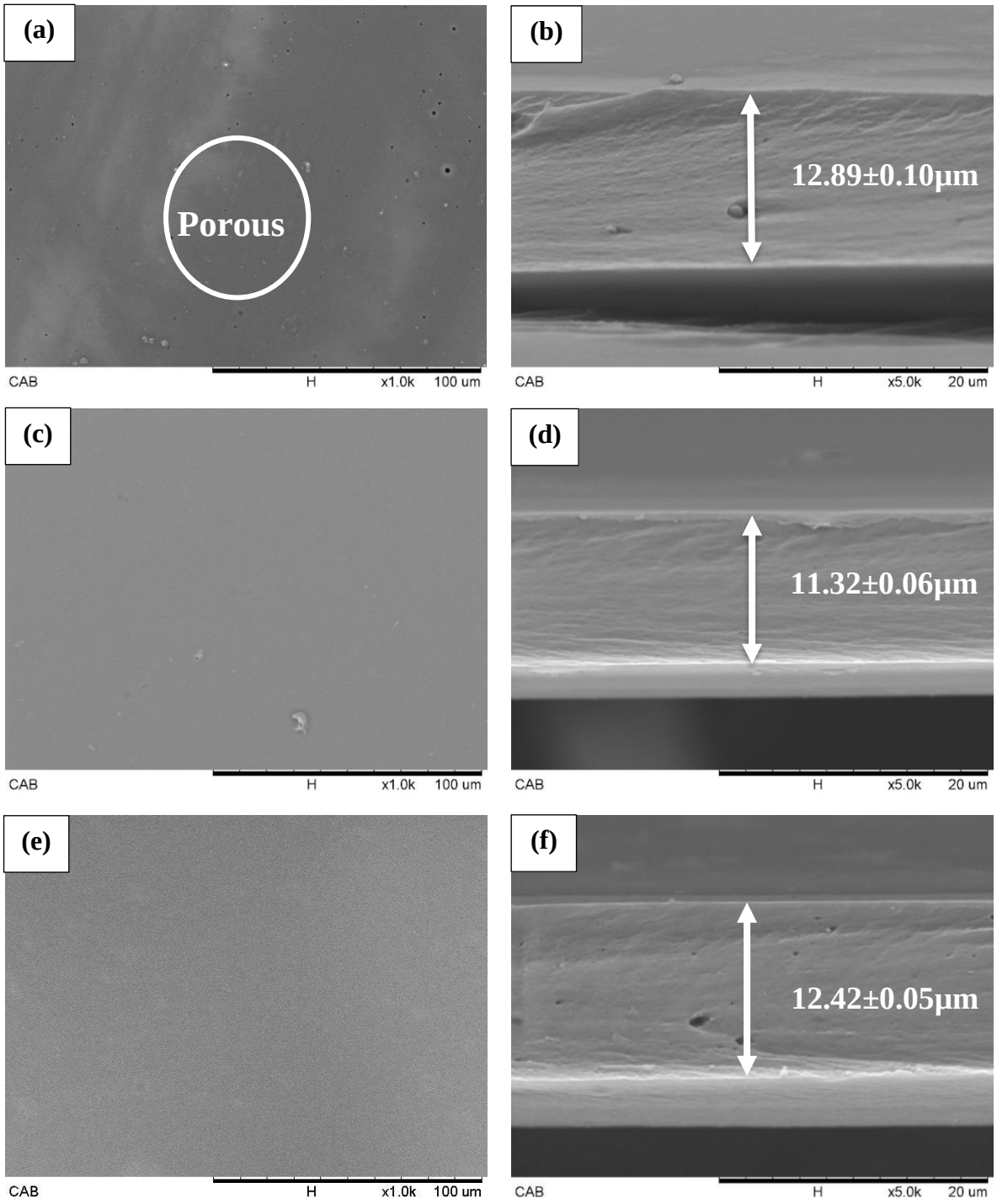

Figure 4.5 Top and cross-sectional SEM of CAB membranes at casting thickness (a-b) 200 µm (CAB-4/200/5), (c-d) 250 µm (CAB-4/250/5), and (e-f) 300 µm (CAB-4/300/5), with 4 wt% CAB polymer concentration and 5 min solvent evaporation time

The CO_2 permeance of CAB-4/200/5, CAB-4/250/5 and CAB-4/300/5 are illustrated in **Figure 4.6**. Notably, CAB-4/250/5 demonstrated a higher permeance results of 398.46 ± 1.43 GPU, as compared with CAB-4/200/5 (143.03 ± 0.62 GPU) and CAB-4/300/5 (12.93 ± 0.34 GPU). This was due to the selective smooth surface structure of CAB-4/250/5, which allowed the solution diffusion mechanism to occur efficiently, which subsequently increased the CO_2 permeance diffusion process (Ahmad et al., 2013). Meanwhile, the CO_2 permeance of CAB-4/300/5 reduced to 12.93 ± 0.34 GPU. This indicated that a higher casting thickness beyond 250 µm could exert extra resistance towards gas diffusion within the membrane and can affect the efficiency of gas permeation due to the thick dense membrane synthesised (**Figure 4.5f)**.

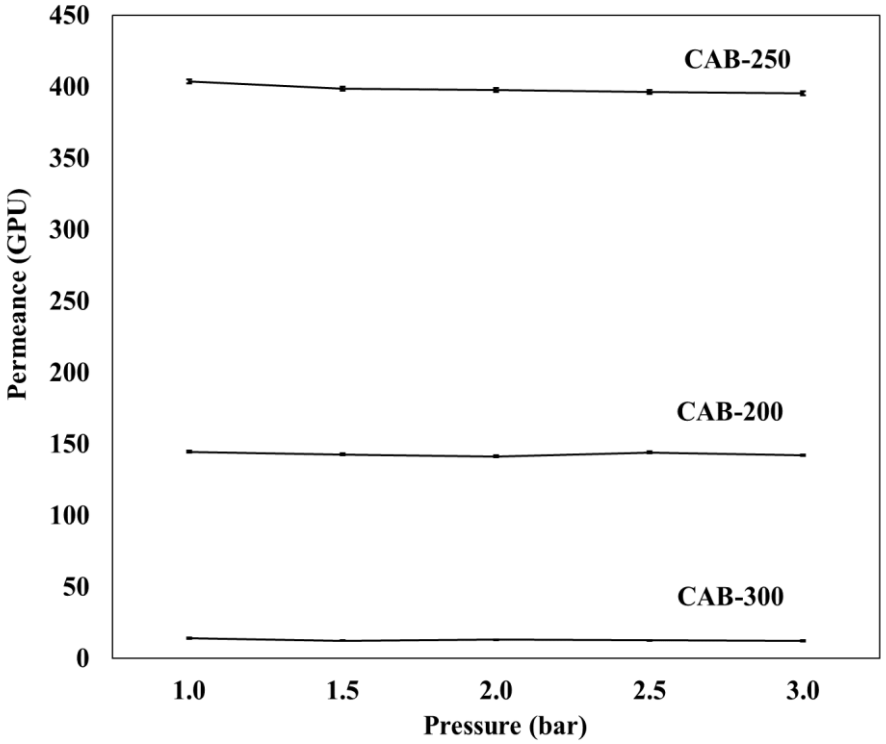

Figure 4.6 CO_2 permeance for membranes fabricated at 200 µm (CAB-4/200/5), 250 µm (CAB-4/250/5), and 300 µm (CAB-4/300/5), with 4 wt% CAB polymer concentration (*Mn* of 70000) and 5 min solvent evaporation time

On the other hand, the N_2 permeance for CAB-4/200/5, CAB-4/250/5 and CAB-4/300/5 are 112.83 ± 0.85, 121.55 ± 1.30, and 11.26 ± 0.31 GPU, respectively as illustrated in **Figure 4.7**. The CAB-4/250/5 exhibited higher N_2 permeance results. This was due to the initial casting thickness used, resulting in a smooth membrane structure, which created less resistance towards the diffusion of N_2 gas within the membrane and generally favoured the solution diffusion process (Thomas et al., 2014). The low N_2 permeance result yield for CAB-4/300/5 (11.26 ± 0.31 GPU) was mainly attributed to the thick dense membrane structure (12.42 ± 0.05 µm), which ultimately governed the solution diffusion rate of the membrane, as thicker membrane usually induces more resistant to gas diffusion (Jawad et al., 2015a).

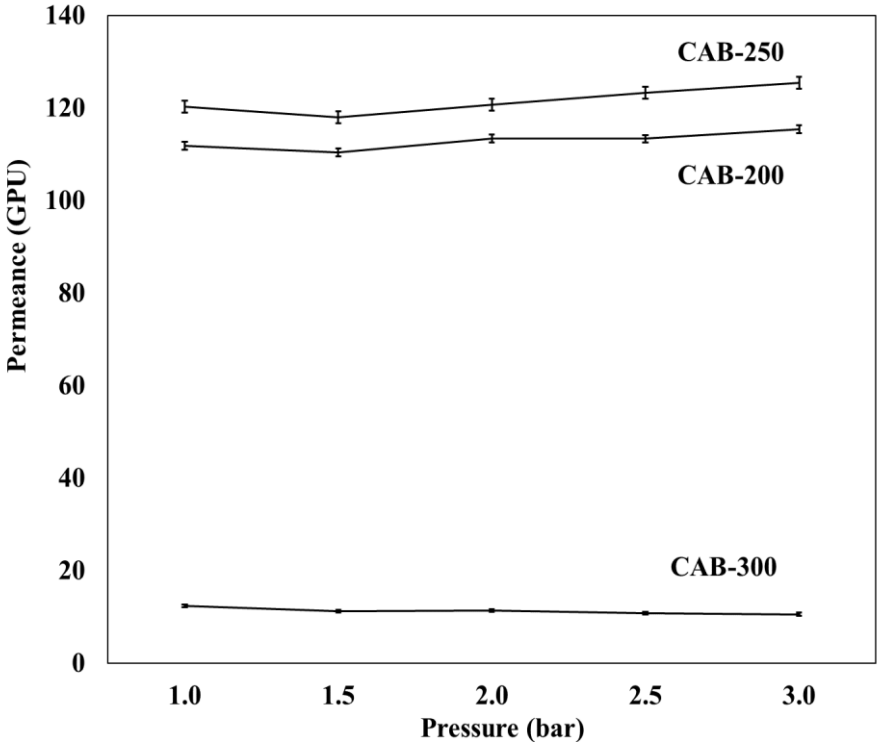

Figure 4.7 N_2 permeance for membranes fabricated at 200 µm (CAB-4/200/5), 250 µm (CAB-4/250/5), and 300 µm (CAB-4/300/5), with 4 wt% CAB polymer concentration (*Mn* of 70000) and 5 min solvent evaporation time

The ideal selectivity of CO_2/N_2 separation performance for CAB-4/200/5, CAB-4/250/5 and CAB-4/300/5 are seen in **Figure 4.8**. It can be observed from the results that by increasing the casting thickness from 200 µm to 250 µm the selectivity increased from 1.27 ± 0.01 GPU (CAB-4/200/5) to 3.28 ± 0.04 GPU (CAB-4/250/5). The acceptable results obtained for CAB-4/250/5 was due to the membrane structure formation of the polymer matrix, which eventually increased the CO_2 permeance against the N_2 permeance attained. However, the selectivity reduced to 1.15 ± 0.01 GPU when a higher casting thickness (300 µm) was implemented for CAB-4/300/5. Even though the thickness of a membrane is essential for effective gas separation, however excessive membrane thickness can restrict the gas flow within the membrane (Li et al., 2013).

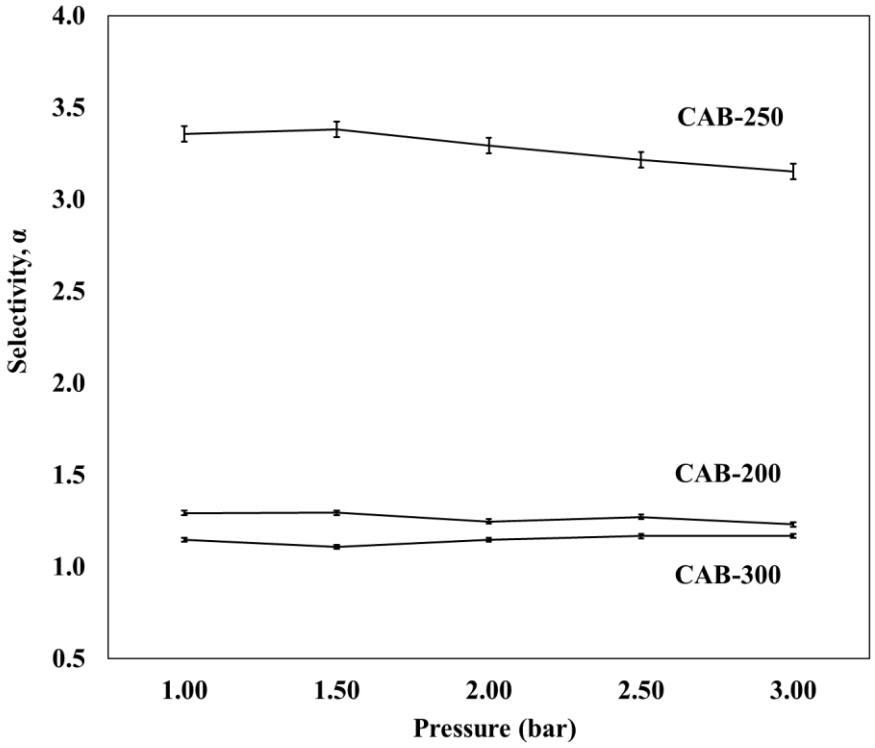

Figure 4.8 Ideal selectivity of CO_2/N_2 for membranes fabricated at different casting thickness with 200 µm (CAB-4/200/5), 250 µm (CAB-4/250/5), and 300 µm (CAB-4/300/5), with 4 wt% CAB polymer concentration (*Mn* of 70000) and 5 min solvent evaporation time

4.1.3 Effect of solvent evaporation time

One of the crucial parameters in membrane morphology is related to solvent evaporation duration (Freeman, 1999). From the SEM images illustrated in **Figures 4.9a** and **4.9c**, a smooth surface was observed for CAB-4/250/4 (4 min) and CAB-4/250/5 (5 min), respectively. Conversely, CAB-4/250/6 (6 min) underwent a transitional phase from smooth to porous surface structure. The possible explanation for this behaviour was due to the evaporation of the solvent (chloroform) occurring within the as-spun membrane. Provided that sufficient evaporation time was given before the immersion precipitation step, it would otherwise promote the formation of porous and dense membrane structures (Koros et al., 1988).

With reference to **Figures 4.9b**, **d**, and **f**, the cross-sectional thickness for membranes CAB-4/250/4, CAB-4/250/5 and CAB-4/250/6 are 13.19 ± 2.72, 11.32 ± 0.06, and 11.48 ± 1.70 µm, respectively. This was a result of the densification phenomenon of the membrane as the solvent evaporated from the as spun membrane (Fang et al., 1994). Based on **Figure 4.9**, as the solvent evaporation time increased from 4 minutes to 6 minutes, the thickness of the membrane decreased from 13.19 ± 2.72 to 11.48 ± 1.70 µm. The possible explanation for this phenomenon could be related to the evaporation time allocated for the exchange between solvent outflow with the humid air inflow from the environment within the as-spun membrane (Young et al., 2000). As regards the CAB-4/250/4, with shorter evaporation time assigned, most of the solvent retained within the membrane, thus, generating a thick dense membrane. While increasing the solvent exchange time to 6 minutes, more solvent was allowed to exchange with the humid air from the atmosphere and the water molecules from humid air merged with the membrane, hence, causing the formation of a thick dense membrane (Sabde et al., 1997).

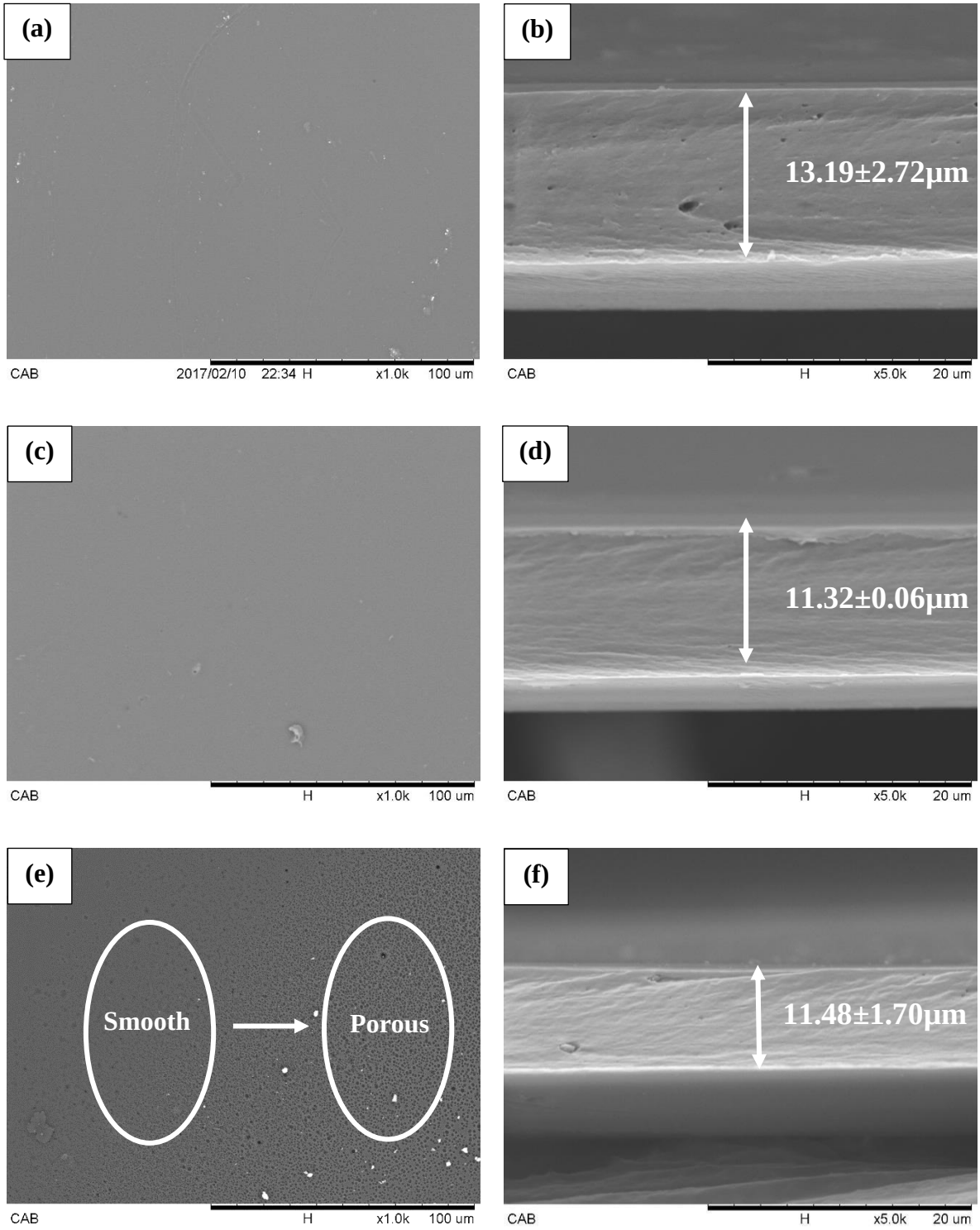

Figure 4.9 Surface and cross-sectional SEM of CAB membranes (*Mn* of 70000) at different solvent evaporation time (a-b) 4 min (CAB-4M), (c-d) 5 min (CAB-5M), and (e-f) 6 min (CAB-6M), with a casting thickness of 250 µm and 4 wt% CAB polymer concentration

As seen from **Figure 4.10**, the CO_2 permeance for membrane CAB-4/250/5 (398.46 ± 1.43 GPU) is generally higher than CAB-4/250/4 (47.71 ± 1.14 GPU) and CAB-4/250/6 (122.65 ± 1.64 GPU). The possible explanation for this result outcome was because of the thinner dense membrane formed with 5 minutes solvent evaporation time utilised. For this reason the membrane was able to achieve good CO_2 permeance for CAB-4/250/5. However, the CO_2 permeance reduced for both CAB-4/250/4 and CAB-4/250/6. This might be the result of the thick dense membrane for CAB-4/250/4 (13.19 ± 2.72 µm, **Figure 4.9b**) and CAB-4/250/6 (11.48 ± 1.70 µm, **Figure 4.9f**), which hindered the diffusivity efficiency of the membrane by implementing extra flow resistance towards the membrane itself (Menut et al., 2002). Above all, to achieve a high CO_2 permeance within the membrane, a thin membrane thickness is crucial to attain high CO_2 permeance.

In **Figure 4.11**, CAB-4/250/5 (121.55 ± 1.30 GPU) with 5 minutes solvent evaporation time demonstrated highest N_2 permeance as compared to CAB-4/250/4 (55.83 ± 0.49 GPU) and CAB-4/250/6 (101.92 ± 0.76 GPU). The low N_2 permeance for CAB-4/250/4 (4 min) was closely related to the thick dense morphology of the membrane, which suppressed the permeance rate of N_2. With reference to CAB-4/250/4, where a short evaporation period applied, it caused a lesser volume of solvent evaporation outflow from the membrane during the solvent evaporation period (Mi et al., 2003). This eventually restricted the higher quantity of solvent to retain within the polymer matrix and consequently producing a thicker dense membrane structure, as depicted in **Figure 4.9f** (Stern et al., 1989). However, for CAB-4/250/6 (6 min) extra solvent evaporation time was allocated, causing more solvent to outflow and replaced with air (Kim et al., 2018). Hence, a thinner dense membrane resulted for CAB-4/250/6 as compared with CAB-4/250/4. However, the thickness of CAB-4/250/6 eventually limited the gas diffusion rate of the feed gas (Oyama et al., 2002).

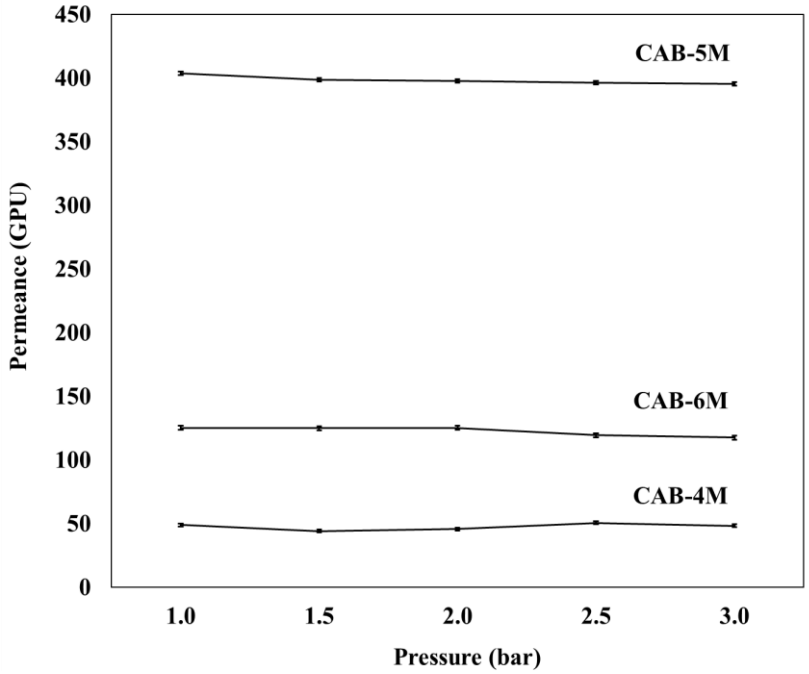

Figure 4.10 CO_2 permeance for membranes synthesised by 4 min (CAB-4/250/4), 5 min (CAB-4/250/5), and 6 min (CAB-4/250/6) solvent evaporation time, with a casting thickness of 250 µm and 4 wt% CAB polymer concentration (*Mn* of 70000)

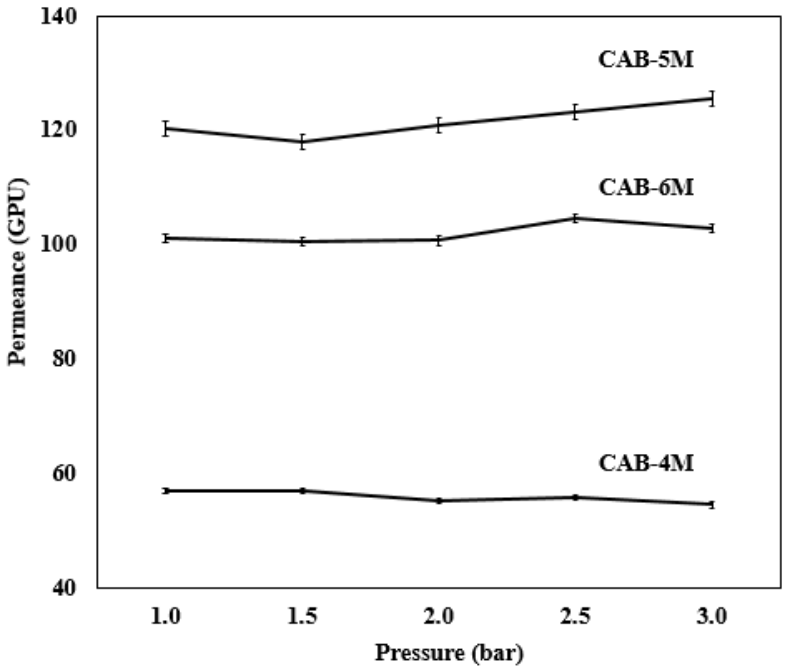

Figure 4.11 N_2 permeance for membranes synthesised by 4 min (CAB-4/250/4), 5 min (CAB-4/250/5), and 6 min (CAB-4/250/6) solvent evaporation time, with a casting thickness of 250 µm and 4 wt% CAB polymer concentration (*Mn* of 70000)

Based on **Figure 4.12**, CAB-5M proved the highest CO_2/N_2 separation performance with a selectivity of 3.28 ± 0.04 as compared to CAB-4/250/4 (0.85 ± 0.02) and CAB-4/250/6 (1.20 ± 0.02). The possible reason was that the smooth surface and thinner thickness of CAB-5M (**Figures 4.9c** and **d**) selectively allowed a predetermined amount of CO_2 to pass through the dense membrane according to the solution-diffusion mechanism (Fadzillah et al., 2017).

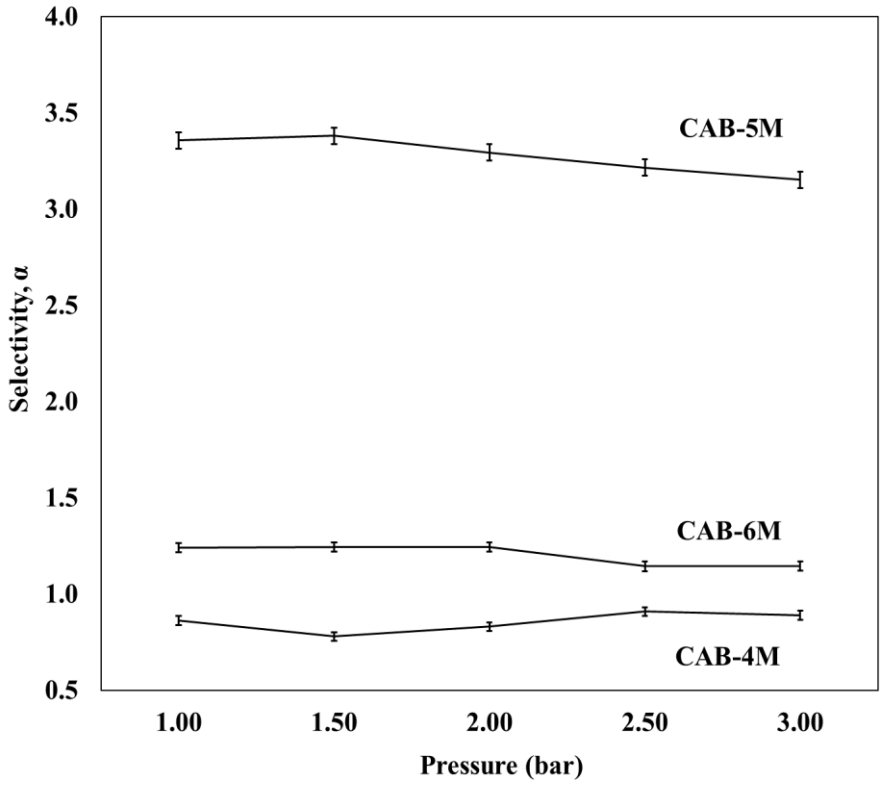

Figure 4.12 Ideal selectivity of CO_2/N_2 by CAB membranes at different solvent evaporation time 4 min (CAB-4/250/4), 5 min (CAB-4/250/5), and 6 min (CAB-4/250/6), with a casting thickness of 250 µm and 4 wt% CAB polymer concentration (*Mn* of 70000)

4.1.4 Effect of exchange time with isopropyl alcohol

The solvent exchange was performed after the precipitation immersion processes of the CAB membrane for the purpose of drying or removing any remaining volatile liquid in the membrane. **Figures 4.13a** and **b**, exhibits a porous surface and irregular dense cross-sectional

structure for CAB-15Iso (15 min) with a membrane thickness of 13.87 ± 0.23 µm. This porous structure surface was caused by the rapid solvent exchange between the water molecules available within the CAB structure and the first solvent (isopropyl alcohol) (Lui et al., 1988). During the first step of the solvent exchange process, an enormous amount of water molecules embedded in the membrane were generally replaced by isopropyl alcohol. As a result, due to the short 15 minutes solvent exchange immersion period allocated, vigorous pore formation appeared throughout the film membrane (Lui et al., 1988). The CAB-15Iso demonstrated higher membrane thickness because of the short solvent exchange time applied, resulting in more water molecules retained inside the membrane (Zinadini et al., 2014).

Meanwhile, when increasing the isopropyl alcohol solvent exchange time to 30 minutes (CAB-30Iso) and then subsequently to 60 minutes (CAB-60Iso), both CAB-30Iso (30 min) and CAB-60Iso (60 min) revealed a smooth surface (**Figures 4.13c** and **e**) with 9.45 ± 0.06 µm and 9.30 ± 0.05 µm thin dense membrane thickness, as demonstrated in **Figures 4.13d** and **f**, respectively. The formation of the smooth surface and thin membrane was because of the longer immersion period allocated. Therefore, providing a longer period for the non-solvent (H_2O) in the film membrane to exchange with the isopropyl alcohol (Radjabian et al., 2014) resulted in the formation of a thin dense membrane with homogeneous smooth surface structure as revealed from CAB-30Iso and CAB-60Iso.

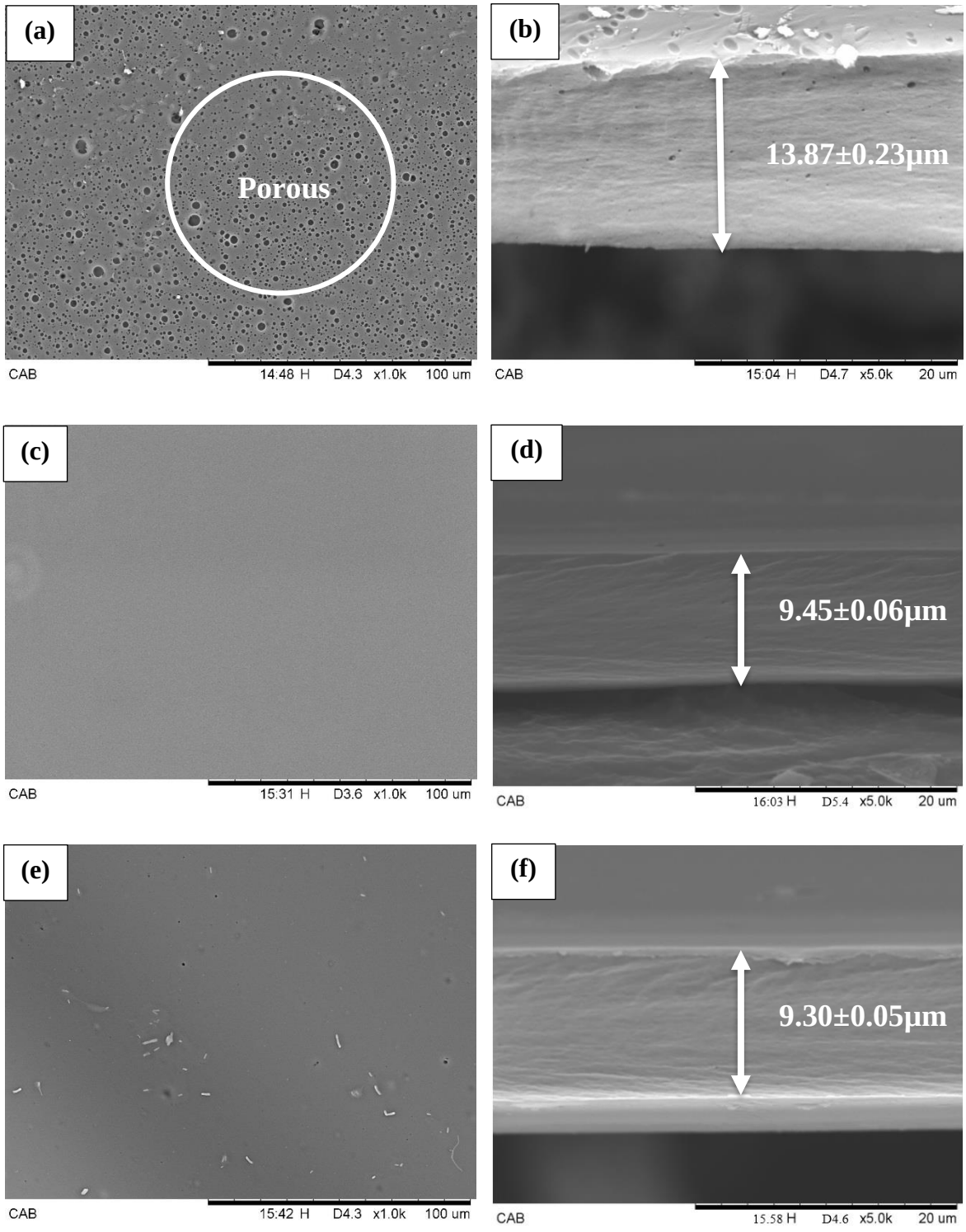

Figure 4.13 Surface and cross-sectional SEM of CAB membranes (*Mn* of 70000) dried with isopropyl alcohol first for a solvent exchange duration of (a-b) 15 min (CAB-15Iso), (c-d) 30 min (CAB-30Iso), and (e-f) 60 min (CAB-60Iso); then subsequently solvent exchanged with 60 min of n-hexane as the final solvent, at casting thickness of 250 µm and 5 min solvent evaporation time

As seen in **Figure 4.14**, the CO_2 permeance rates increased from 65.53 ± 0.34 GPU (CAB-15Iso) to 262.29 ± 0.16 GPU (CAB-30Iso) and further increased to 398.82 ± 0.94 GPU (CAB-60Iso) when the solvent exchange duration of isopropyl alcohol changed from 15 to 30 and 60 minutes, respectively. This was mainly due to the extensive water content reduction within the membrane structure because of the longer immersion period allocated. The steady exchange rate of water with isopropyl alcohol within the CAB polymer matrix caused less CO_2 molecules to interact with the water, thus, allowing more CO_2 gas to permeate through the membrane (Jawad et al., 2015b). In the meantime, the high CO_2 permeance rate for CAB-60Iso (60 min) was subsequently due to extended immersion period up to 60 min. Therefore, this allow sufficient time for the water molecules embedded within CAB-60Iso to be replaced with isopropyl alcohol, as a result CAB-60Iso yielded the highest CO_2 permeance rate amongst other membranes (CAB-15Iso and CAB-30Iso).

The N_2 permeance rates for CAB-15Iso, CAB-30Iso and CAB-60Iso are depicted in **Figure 4.15**. The results of the N_2 permeance obtained were 64.59 ± 0.41 GPU (CAB-15Iso), 70.49 ± 0.33 GPU (CAB-30Iso) and 121.76 ± 0.83 GPU (CAB-60Iso), respectively. The possible explanation was the reduction in the membrane thickness from 13.87 µm to 9.3 µm (**Figure 5**). In addition, as isopropyl alcohol is mainly made up from non-polar molecules, the remaining molecules within the CAB structure can easily attract light gas molecules (Katayama and Nitta, 1976). Thus, with longer solvent exchange duration, more isopropyl alcohol was retained within the polymer matrix and thus, attracting more N_2 gas molecules and resulting in high N_2 permeance rate for CAB-60Iso (60 min). Eventually as the solvent exchange duration decreased, the N_2 permeance rate for the CAB-15Iso and CAB-30Iso reduced as well.

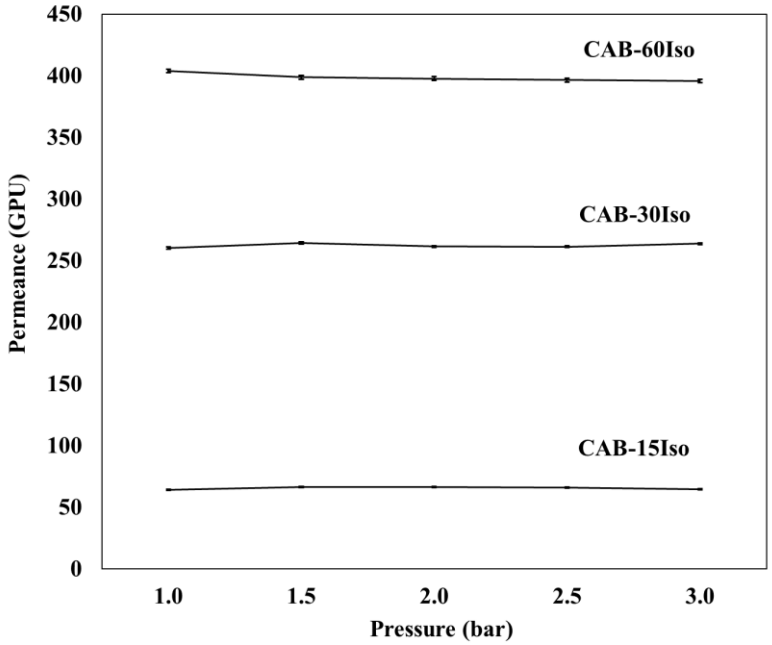

Figure 4.14 CO_2 permeance for CAB membranes (*Mn* of 70000) dried with 15 min (CAB-15Iso), 30 min (CAB-30Iso), and 60 min (CAB-60Iso) of isopropyl alcohol; then subsequently solvent exchanged with 60 min of n-hexane as the final solvent, at casting thickness of 250 µm and 5 min solvent evaporation time

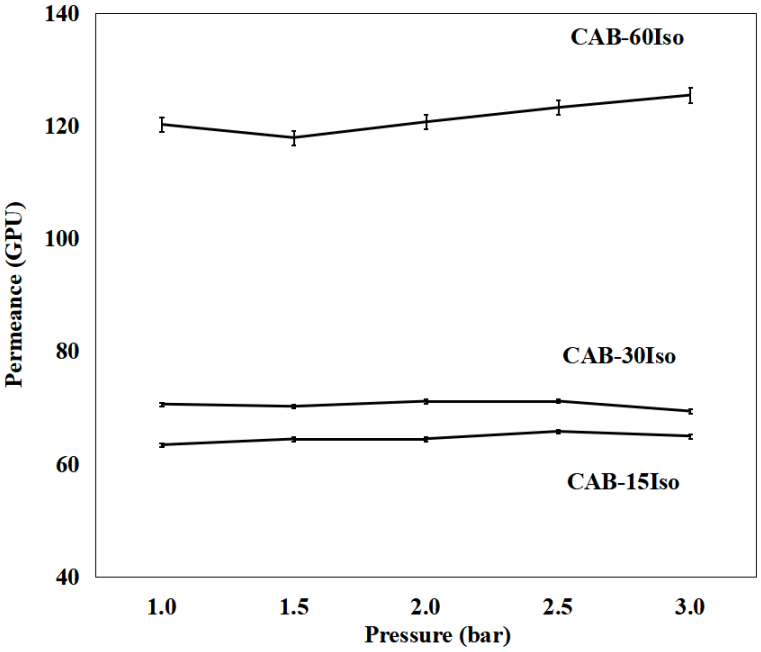

Figure 4.15 N_2 permeance for CAB membranes (Mn of 70000) dried with 15 min (CAB-15Iso), 30 min (CAB-30Iso), and 60 min (CAB-60Iso) of isopropyl alcohol; then subsequently solvent exchanged with 60 min of n-hexane as the final solvent, at casting thickness of 250 µm and 5 min solvent evaporation time

As discussed previously, CAB-60Iso (60 min) showed a thin dense membrane formation with high CO_2 and N_2 permeance rates. However, based on **Figure 4.16** CAB-30Iso (30 min) yielded the best selectivity performance. This was due to the smooth homogeneous surface and superior cross-sectional morphology, which selectively allowed a predetermined amount of CO_2 and N_2 to pass through the dense membrane. On the contrary, the CAB-15Iso (15 min) demonstrated low selectivity as shown in **Figure 4.16**. This was due to the thick membrane structure present (**Figures 4.13a** and **b**), which imposed an undesirable effect on the membrane permeance performance due to extra resistance pathway generated (Rahimpour et al., 2008, Yang and Wang, 2006). As a result, CAB-30Iso (30 min) was preferable as compared to CAB-15Iso (15 min) and CAB-60Iso (60 min) because of the excellent morphology present with good selectivity performance.

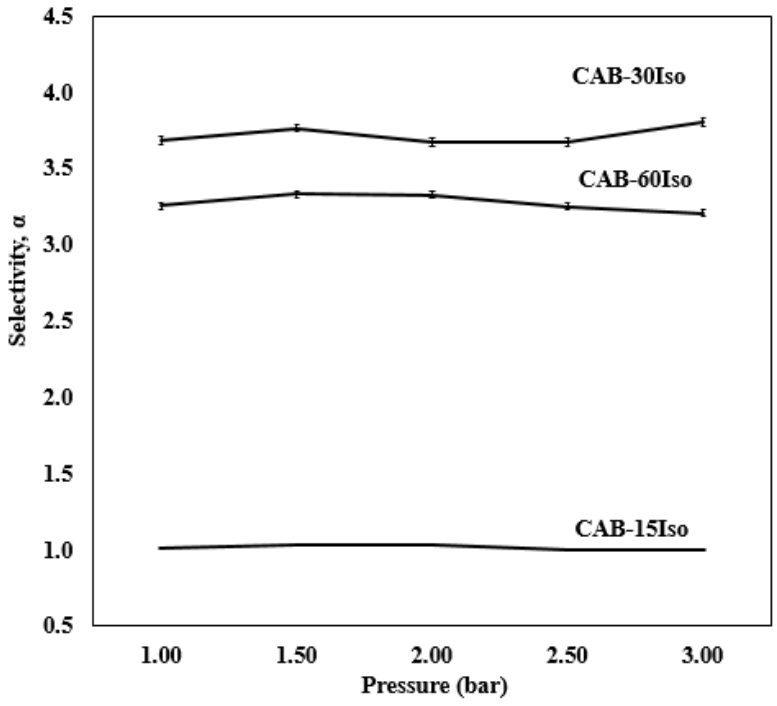

Figure 4.16 Ideal selectivity of CO_2/N_2 for CAB membranes (*Mn* of 70000) synthesised with a solvent exchange duration of 15 min (CAB-15Iso), 30 min (CAB-30Iso), and 60 min (CAB-60Iso); then subsequently exchanged with 60 min of n-hexane as the final solvent, at casting thickness of 250 µm and 5 min solvent evaporation time

4.1.5 Effect of exchange time with n-hexane

As discussed in the previous **section 4.1.4**, the best solvent exchange time for isopropyl alcohol was 30 minutes (CAB-30Iso). For this reason, the CAB membrane was subjected to further optimisation with the drying time of n-hexane. The main reason why solvent exchange had been conducted in two consecutive way is because the first step is to eliminate the water molecules from the polymer matrix, and the second steps is to reduce the non-solvent isopropyl alcohol from the membrane. Since isopropyl alcohol (100 mg L^{-1}) is completely miscible (form a homogenous mixture when added) in water, while n-hexane is semi-miscibility (9.5 mg L^{-1}) with water, therefore isopropyl alcohol was used first since it can efficiently remove the water molecules, then followed by n-hexane to remove isopropyl alcohol. Additionally, the n-hexane is a non-polar solvent (Ngadiran et al., 2019). It can enhance the sorption of non-polar gas such as CO_2 due to the net electric dipole moment, since non-polar gas tends to be attracted to and are more soluble in non-polar solvent (n-hexane) (Son et al., 2019).

In this study, the CAB membranes were dried with solvent exchange time of 15 minutes (CAB-15H), 30 minutes (CAB-30H) and 60 minutes (CAB-60H) using n-hexane. As seen from the SEM image revealed in **Figure 4.17**, the surface of CAB-15H (15 min) exhibited a porous structure, while both CAB-30H (30 min) and CAB-60H (60 min) showed smooth surfaces. The main reason for the porous structure shown in CAB-15H was due to the rapid evaporation of the volatile solvent from the membrane structure itself when a short duration of immersion period was implemented (Chung and Kafchinski, 1997). When the solvent exchange immersion period was gradually increased, it provided the membrane sufficient time for the solvent exchange to occur between isopropyl alcohol and n-hexane at a consistent and steady rate. Subsequently, when the solvent exchange process within the polymer was suppressed

vigorously, it resulted a smooth homogeneous surface for CAB-30H (30 min) and CAB-60H (60 min) (Choi et al., 2006).

As presented in **Figure 4.17**, the membrane thickness is 11.79 ± 0.18, 9.50 ± 0.10 and 9.45 ± 0.06 µm for CAB-15H (15 min), CAB-30H (30 min) and CAB-60H (60 min), respectively. These results showed that the increased exchange time of n-hexane caused the CAB membrane to become more compact due to membrane densification as time passed (Sabde et al., 1997). In addition, the main reason for this reduction of the membrane thickness was due to the isopropyl alcohol within the membrane slowly being replaced by n-hexane with time. The replacement of isopropyl alcohol with n-hexane occurred when the molecular affinity of n-hexane was greater than isopropyl alcohol (Hansen, 2007). With reference to the Hansen solubility chart, the solubility for isopropyl alcohol, n-hexane and water were 23.6, 14.9 and 47.9 $MPa^{1/2}$, respectively (Egan and Dufresne, 2008, Hansen, 2007). Principally, the molecular affinity is in the order of CAB-water>CAB-isopropyl alcohol>CAB-n-hexane and this order represents the attraction force between the polymer and the solvent and non-solvent used (Kim and Oh, 2001).

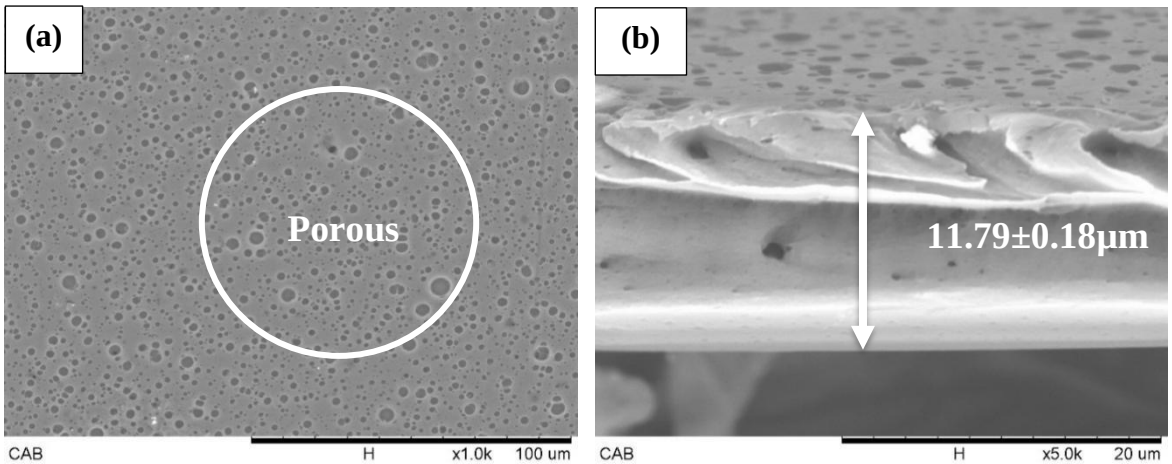

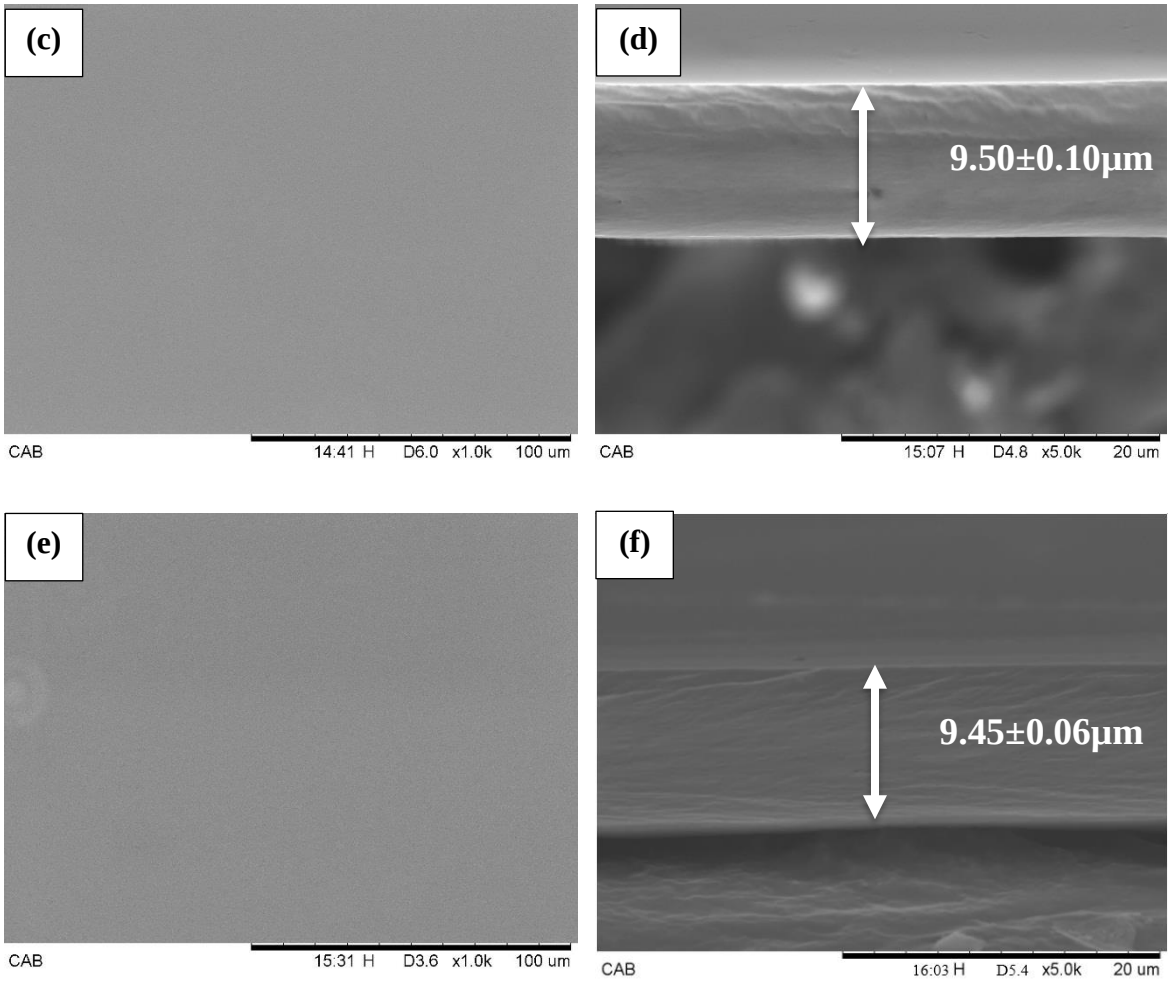

Figure 4.17 Surface and cross-sectional SEM of CAB membranes dried with 30 min of isopropyl alcohol first then followed by; (a-b) 15 min (CAB-15H), (c-d) 30 min (CAB-30H), and (e-f) 60 min (CAB-60H) of solvent exchange time using n-hexane, at casting thickness of 250 µm and 5 min solvent evaporation time

According to the CO_2 permeance results displayed in **Figure 4.18**, the CAB-60H clearly indicated the highest CO_2 permeance rate followed by CAB-30H and CAB-15H. As observed from **Figure 4.18**, the CO_2 permeance increased significantly from 21.55 ± 0.03 GPU to 227.95 ± 0.39 GPU due to the increased solvent exchange time from 15 minutes (CAB-15H) to 30 minutes (CAB-30H). This was because when the exchange time increased, it provided sufficient time for the exchange of isopropyl alcohol content with n-hexane and therefore, generated a relatively thinner and compact cross-sectional membrane, which favoured CO_2 permeation

through the membrane (Jawad et al., 2015b). In addition, the CO_2 permeance increased further when the solvent exchange duration increased from 30 to 60 minutes for CAB-30H (227.95 ± 0.39 GPU) to CAB-60H (262.29 ± 0.16 GPU), respectively. The increase in CO_2 permeance could be related to the increase in the number of the remaining polar n-hexane molecules within the membrane structure, resulting in a more active interaction with the CO_2 molecules as well as resulting in a higher CO_2 permeance yield (Jawad et al., 2015b).

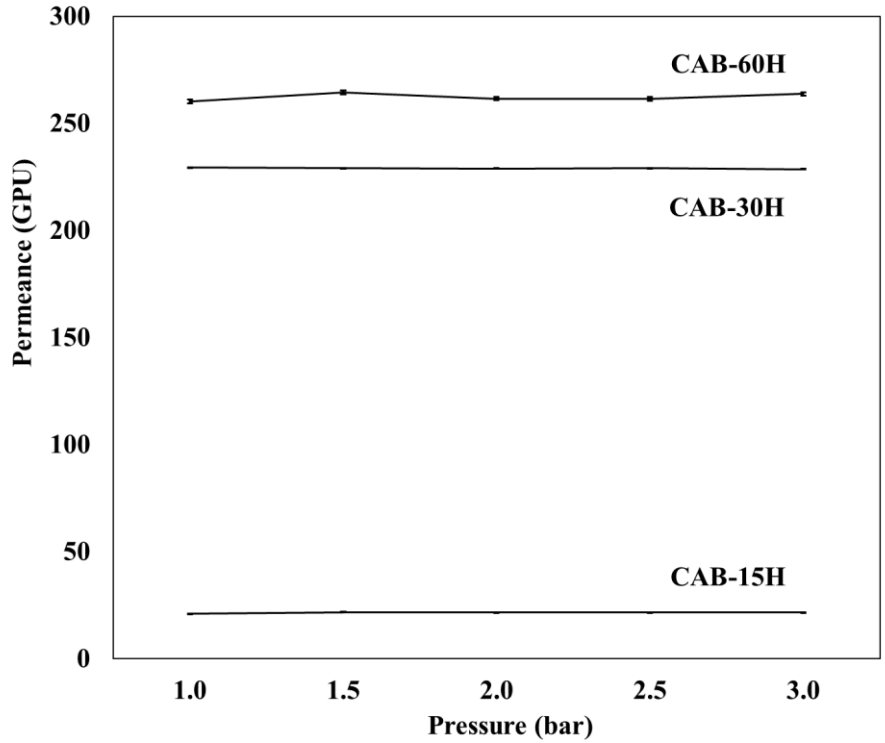

Figure 4.18 CO_2 permeance for CAB membranes (*Mn* of 70000) dried with 15 min (CAB-15H), 30 min (CAB-30H), and 60 min (CAB-60H) of n-hexane, at casting thickness of 250 µm and 5 min solvent evaporation time

Meanwhile, **Figure 4.19** illustrates the drastic increase of N_2 permeance from 10.03 ± 0.02 GPU to 37.28 ± 0.54 GPU when the solvent exchange time of n-hexane increased from 15 minutes (CAB-15H) to 30 minutes (CAB-30H). The reason for this increment was attributed to the thin dense membrane structure of CAB-30H (9.50 ± 0.10 µm, **Figure 4.17d**), which allowed the feed N_2 gas to pass through the least resistance pathway. However, the high N_2 permeance for CAB-60H (70.49 ± 0.33 GPU, **Figure 4.17f**) was due to stress of surface tension caused by

high capillary forces due to the evaporation of residual n-hexane within the membrane when it is expose to the ambient air, which led to the shrinkage in the membrane structure (Matsuyama et al., 2002).

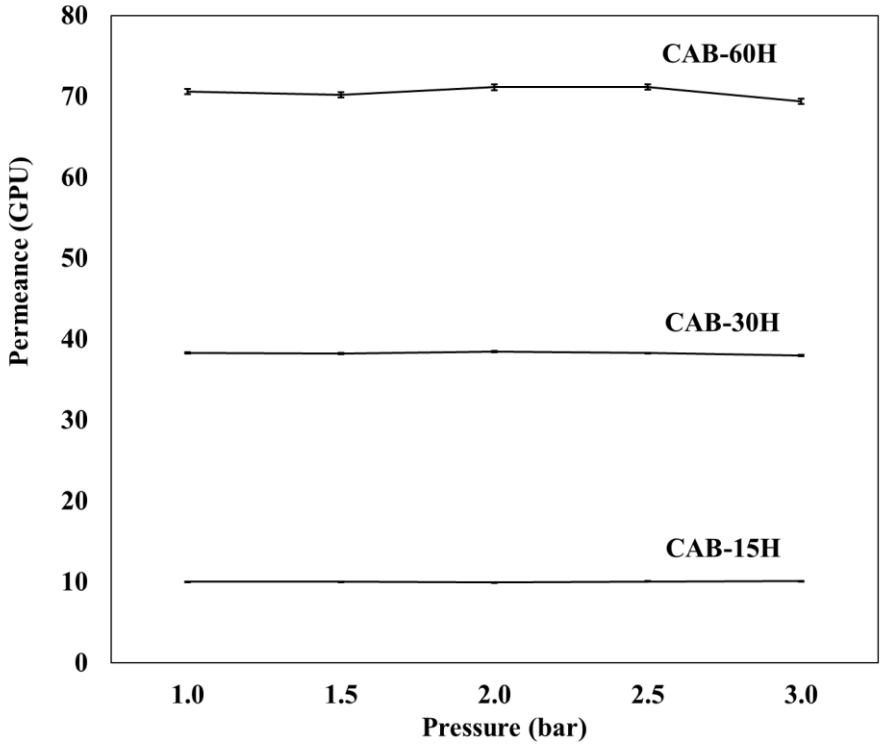

Figure 4.19 N_2 permeance for CAB membranes (*Mn* of 70000) dried with 15 min (CAB-15H), 30 min (CAB-30H), and 60 min (CAB-60H) of n-hexane, at casting thickness of 250 µm and 5 min solvent evaporation time

As displayed in **Figure 4.20**, the CAB-30H membrane showed the highest gas selectivity achieved at 6.12 ± 0.09. This result further proved that to have a high gas separation performance, a smooth surface with regular thin dense membrane morphology was preferable (**Figures 4.17c** and **d**) (Huang and Feng, 1995, Jansen et al., 2005, Matsuyama et al., 2002, Lui et al., 1988). On the other hand, CAB-15H showed a lower separation performance of 2.15 ± 0.17. This was due to the collapse in the membrane structure caused by the short solvent immersion time, generating an uneven porous surface and thick dense membrane structure, as presented in **Figures 4.17a** and **b**. In addition, the CAB-60H exhibited a smooth surface and

thinner dense membrane morphology (9.45 ± 0.06 µm), as depicted in **Figures 4.17e** and **f**. However, the low selectivity performance for CAB-60H (3.72 ± 0.03) was a result of excessive exchange time with n-hexane, which deformed the functionality of the membrane and hence, generating moderate selectivity performance (Budd et al., 2005).

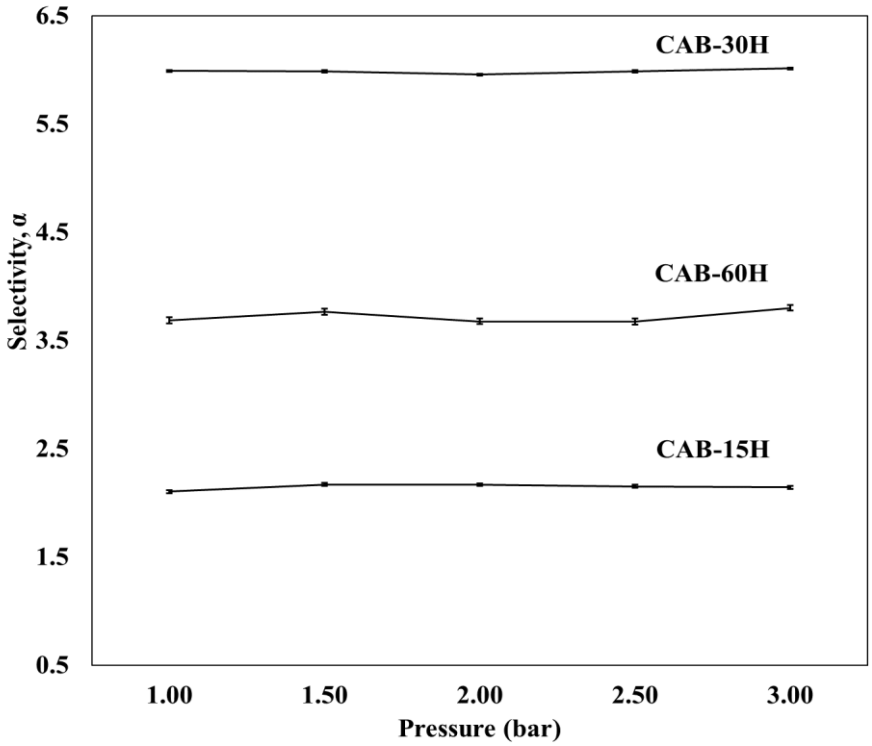

Figure 4.20 Ideal selectivity of CO_2/N_2 for CAB membranes (*Mn* of 70000) dried with 30 min of isopropyl alcohol first then followed by; 15 min (CAB-15H), 30 min (CAB-30H), and 60 min (CAB-60H) of solvent exchange with n-hexane, at casting thickness of 250 µm and 5 min solvent evaporation time

4.1.6 Effect of CAB at different molecular weight (M_n)

According to Wang et al. (2014), the *Mn* is deduced to have prominent effect on the membrane gas separation performance, as the transport of gas through polymer matrix mainly depends on chain packing or transient gaps generated by the thermally induced chain segment rearrangement (Merkel et al., 2002, Wang et al., 2014). Moreover, the high chain packing efficiency and low chain mobility in polymer matrix are usually regarded as the restricting factor towards the polymer's permeability (Wang et al., 2014). Thus, different *Mn* CAB (12000,

65000, 70000) with different acetyl (16-19, 28-31, 12-15 wt %), butyryl (30-35, 16.5-19, 35-39 wt%) and hydroxyl (-,0.9-1.3, 1.2-2.2 wt%) groups were investigated, as demonstrated in **Figure 4.21**.

As depicted in **Figures 4.21a** and **c**, a porous structure was observed for the membranes synthesised with *Mn* of 12000 (CAB-12000) and 65000 (CAB-65000), while the membrane fabricated with *Mn* 70000 (CAB-70000) showed a smooth surface, as depicted in **Figure. 4.21e**. The reason for the transition of membrane surface from porous to smooth was due to the high molecular weight of CAB, which caused the increased number of chain packing between the macromolecular chains in the solution (Jansen et al., 2006). Thus, the high molecular weight of CAB favoured the gelation of the polymer rich phase after the phase inversion occurred and consequently suppressing the formation of porous structure during the early stage (Jansen et al., 2005).

As shown in **Figures 4.21b**, **d**, and **f**, the thickness of CAB-12000, CAB-65000 and CAB-70000 are 10.96 ± 0.10, 16.05 ± 0.17 and 9.50 ± 0.10 µm, respectively. The increment in the CAB molecular weight further influenced the membrane thickness through the rheological properties of the casting solution (Jansen et al., 2005). This was due to the high molecular weight of the CAB polymer being utilised for the membrane fabrication, which gives more rapid gelation (Jansen et al., 2005). After rapid gelation, the porous structure was greatly suppressed and further evaporation of solvent and non-solvent from the polymer matrix resulted in a gradual shrinkage of the structure (**Figure 4.21f**) (Jansen et al., 2005). Consequently, the thickness of CAB-70000 (9.50 ± 0.10 µm) was thinner than CAB-12000 (10.96 ± 0.10 µm) and CAB-65000 (16.05 ± 0.17 µm).

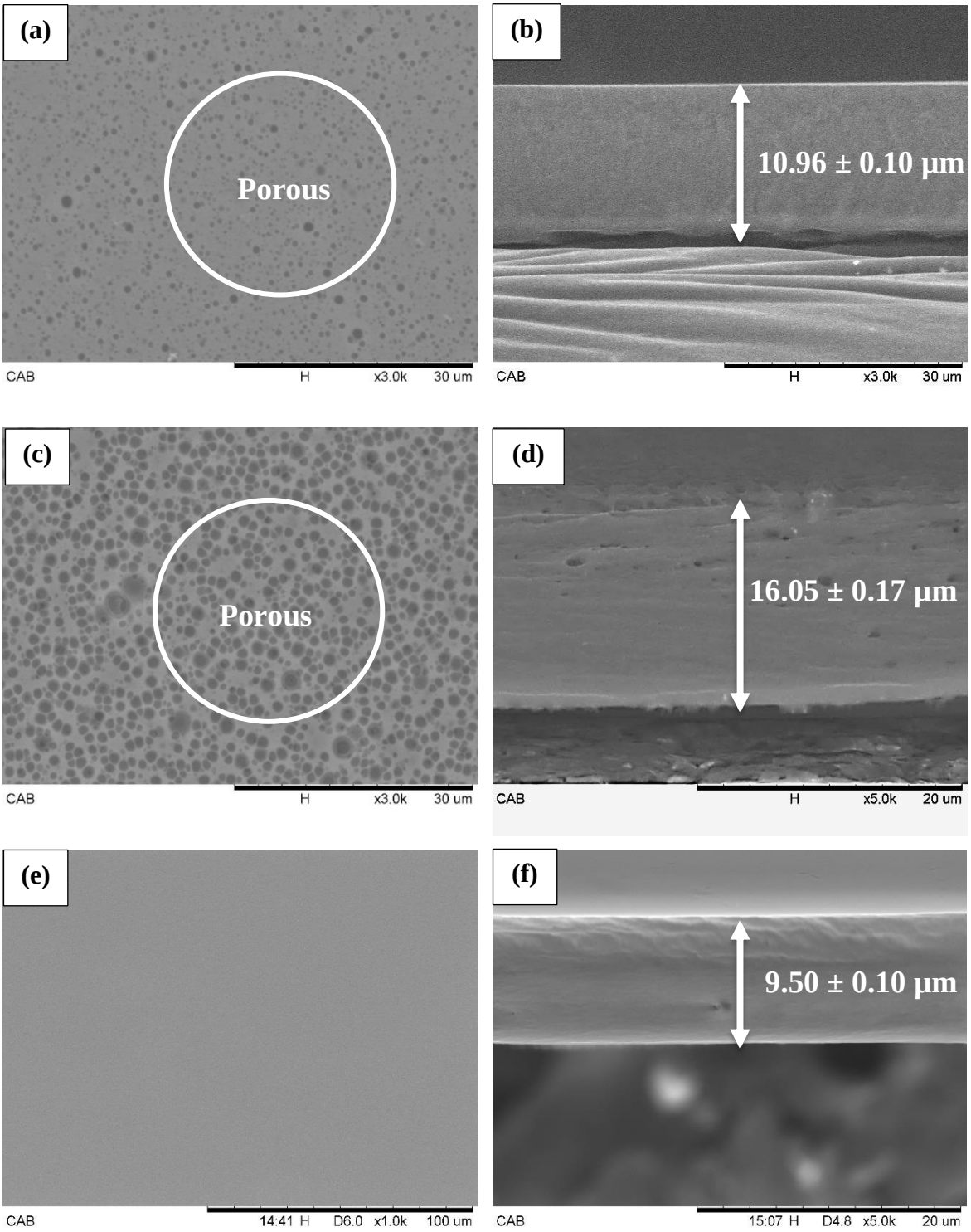

Figure 4.21 Surface and cross-sectional SEM of CAB membranes prepared with polymer concentration of 4 wt% and molecular weight (Mn) of (a-b) 12000 (CAB-12000), (c-d) 65000 (CAB-65000), and (e-f) 70000 (CAB-70000), at casting thickness of 250 µm and 5 min solvent evaporation time

The performance of CO_2 permeance attained for different M_n of CAB-12000, CAB-65000 and CAB-70000 are 101.42 ± 0.97, 74.37 ± 1.25 and 227.95 ± 0.39 GPU, respectively, as shown in **Figure 4.22**. The decreased CO_2 permeance rates observed from CAB-12000 (acetyl 28-31 wt%) to CAB-65000 (acetyl 16-19 wt%) are due to the rough membrane morphology, as presented in **Figure 4.21d**. Meanwhile, CAB-65000 with greater membrane thickness of 16.05 ± 0.17 µm shows low CO_2 permeance in **Figure 4.22**. The possible explanation for the decrease in CO_2 permeance was caused by the rigidity and steric effects of the acetyl groups (Wan et al., 2003). Consequently, this decreased the higher intrinsic solubility of CO_2 due to the existence of greater number of acetyl–acetyl interactions (Koros et al., 1988b, Scholes et al., 2012). The significant increase of CO_2 permeance from CAB-65000 (74.37 ± 1.25 GPU) to CAB-70000 (227.95 ± 0.39 GPU) was due to the low acetyl content of CAB-70000 (acetyl 12-15 wt%), with less acetyl-acetyl interactions that caused rigidity and steric effects within the membrane (Scholes et al., 2012).

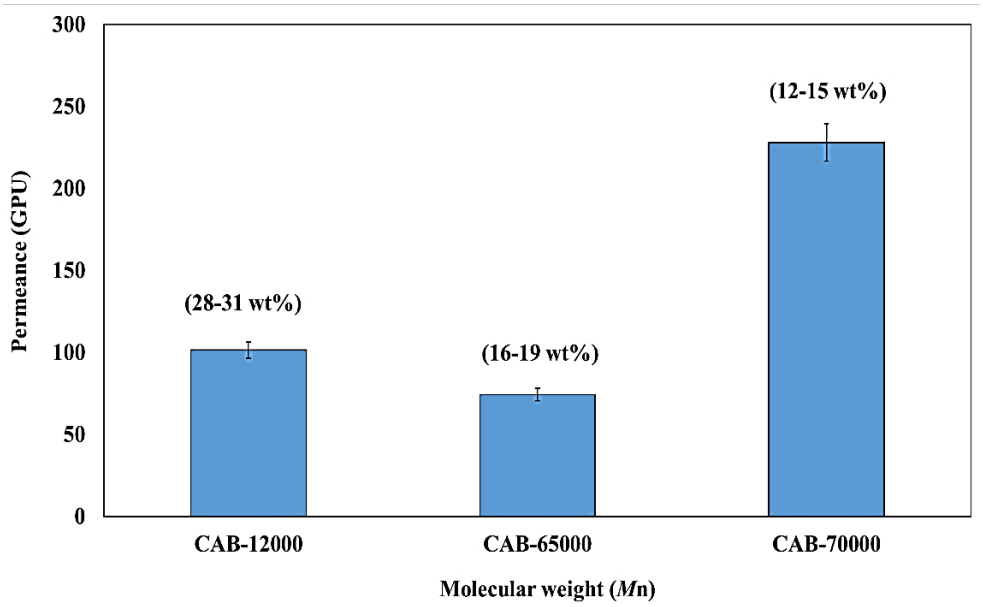

Figure 4.22 CO_2 permeance results for CAB membranes fabricated at different molecular weight (*Mn*) comprising CAB-12000, CAB-65000, and CAB-70000 acetyl content of 28-31 wt%, 16-19 wt%, and 12-15wt%, respectively

Figure 4.23 shows that the N_2 permeance rate attained for CAB-12000, CAB-65000 and CAB-70000 are 95.26 ± 1.06, 48.94 ± 0.89 and 37.28 ± 0.54 GPU, respectively. The reduction in N_2 permeance was due to the high presence of the hydroxyl group (1.2-2.2 wt%) content within the CAB-70000 polymer. The intermolecular attraction between the hydroxyl (-OH) and carbonyl (C=O) group of the CAB polymer could prompt the formation of hydrogen bonds, which could delay the de-mixing between the coagulant with the non-solvent causing the smooth homogeneous formation of the membrane surface. This could influence the N_2 permeance rate (Childress and Elimelech, 1996). Thus it can be concluded that the increment of the -OH group within the membrane composition, favoured the formation of homogeneous surface morphology. The -OH group could also further increase the preferential restrictions on membrane pore formation thus, enhancing the selectivity performance of the membrane (Yave et al., 2009).

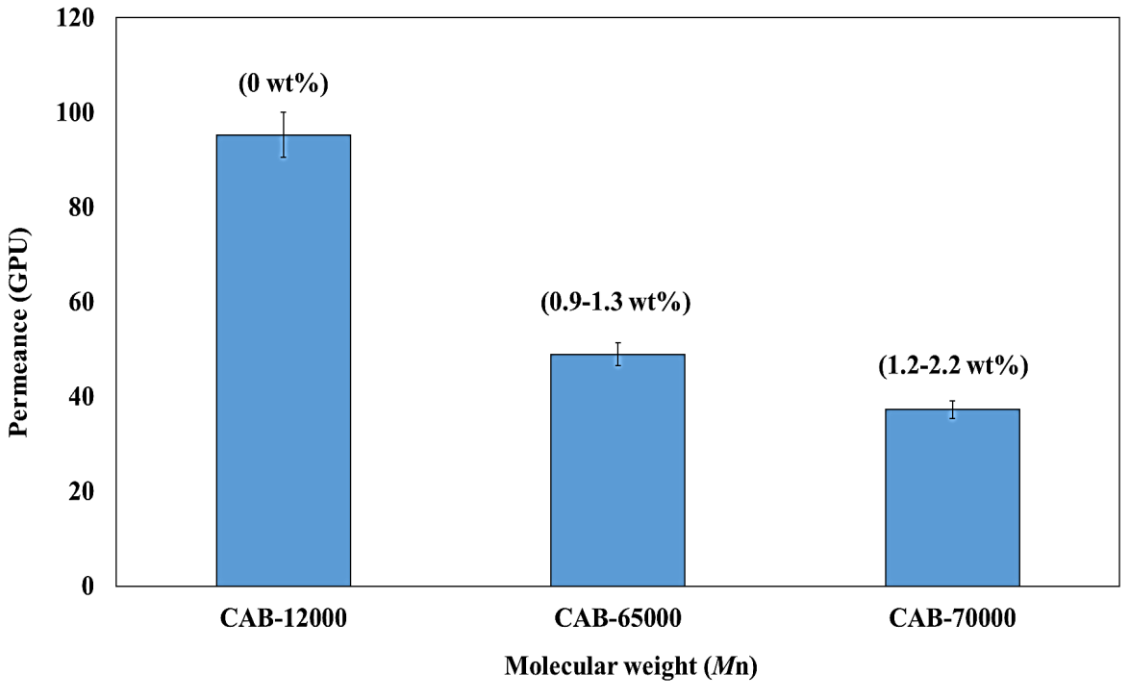

Figure 4.23 N_2 permeance results for CAB membranes synthesised at different molecular weight (*Mn*) comprising CAB-12000, CAB-65000, and CAB-70000 hydroxyl content of 0 wt%, 0.9-1.3 wt%, and 1.2-2.2 wt%, respectively

Figure 4.24 reveals the selectivity results for different CAB *Mn* of 12000 (CAB-12000), 65000 (CAB-65000) and 70000 (CAB-70000), respectively. From the selectivity performance portrayed in **Figure 4.24**, CAB-70000 achieved the highest selectivity of 6.12 ± 0.09, followed by CAB-65000 with a moderate selectivity of 1.52 ± 0.04 and CAB-12000 with the lowest selectivity of 1.06 ± 0.01. The high selectivity performance of CAB-70000 was due to the high presence of the butyryl group content (35-39 wt%), which can promote better CO_2 diffusion due to the increase of non-polar butyryl chain within the structure of the membrane, thus, making the membrane more hydrophobic in nature (Wan et al., 2004, Ong et al., 2012).

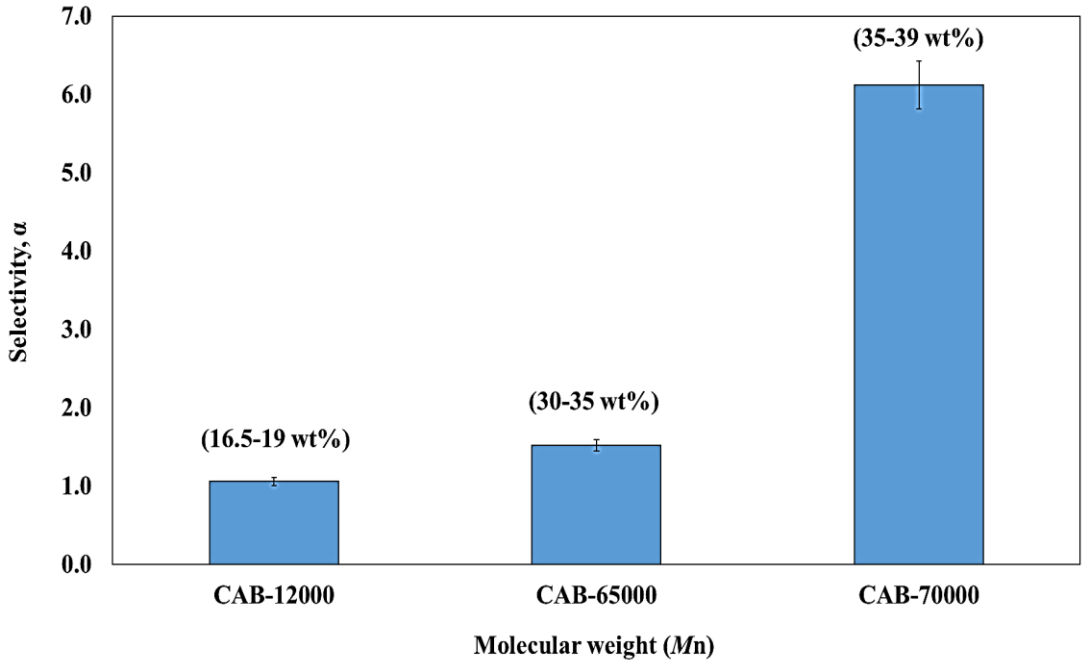

Figure 4.24 CO_2/N_2 selectivity results for CAB membranes at different molecular weight (*Mn*) comprising CAB-12000, CAB-65000, and CAB-70000 butyryl content of 16.5-19 wt%, 30-35 wt%, and 35-39 wt%, respectively

4.1.7 X-ray Photoelectron Spectroscopy (XPS) Analysis

The XPS characterisation was adopted in this study to analyse the quantitative element composition of the CAB membrane fabricated. The quantitative element composition of the membrane surface was determined from the spectrum obtained. Consequently, CAB-12000, CAB-65000 and CAB-70000 were analysed through XPS analysis. The surface chemical quantitative compositions are depicted in **Table 4.1** and **Figure 4.25**, respectively.

Observing the results tabulated in **Table 4.1**, both the atomic and mass concentration of the oxygen (O) atom decreased with the increase in the CAB membrane molecular weights. The decreasing trend of atomic concentration from 34.02>30.88>27.30% and mass concentration from 40.72>37.31>33.35% of the O atom was due to the decrease of the acetyl group derived from each CAB polymer (Suttiwijitpukdee et al., 2011). As indicated clearly in **Figure 4.22**, the acetyl group affected the permeance of CO_2 within the membrane. Hence, this further proved that increasing the acetyl group or O atom presence within the membrane subsequently, decreased the permeance of CO_2. The increase in the O element was mainly funded by the breaking of the carbonyl (C=O) group and prompted the formation of a new carboxyl group (-COOH) (Liu et al., 2014). The increase in the carboxyl group made the membrane more hydrophilic, resulting in the decline of the CO_2 permeance flux (Xia and Ni, 2015, Xu et al., 2014).

Table 4.1 Element composition of the CAB membrane synthesised at different molecular weight

Peak	CAB-12000		CAB-65000		CAB-70000	
	Atomic Conc %	Mass Conc %	Atomic Conc %	Mass Conc %	Atomic Conc %	Mass Conc %
O 1s	34.02	40.72	30.88	37.31	27.30	33.35
C 1s	65.98	59.28	69.12	62.69	72.70	66.65

On the other hand, when observing the carbon (C) element present within CAB-12000, CAB-65000 and CAB-70000 in **Figure 4.25**, the C atoms increased with increase in the polymer molecular weights. The atomic concentration increased from 65.98>69.12>72.70 and the mass concentration increased from 59.28>62.69>66.65 for CAB-12000, CAB-65000 and CAB-70000, respectively. The increase in the C element within the membrane was because of the increase in the butyryl group within the CAB polymer. As indicated in **Figure 4.24**, the butyryl group played a crucial role in manipulating the selectivity performance of the membrane because it could increase the CO_2 diffusion due to the increase of the non-polar butyryl chain within the structure of the membrane (Wan et al., 2004). As a result the membrane became more hydrophobic in nature, and hence, promoted better CO_2 permeance flux (Ong et al., 2012).

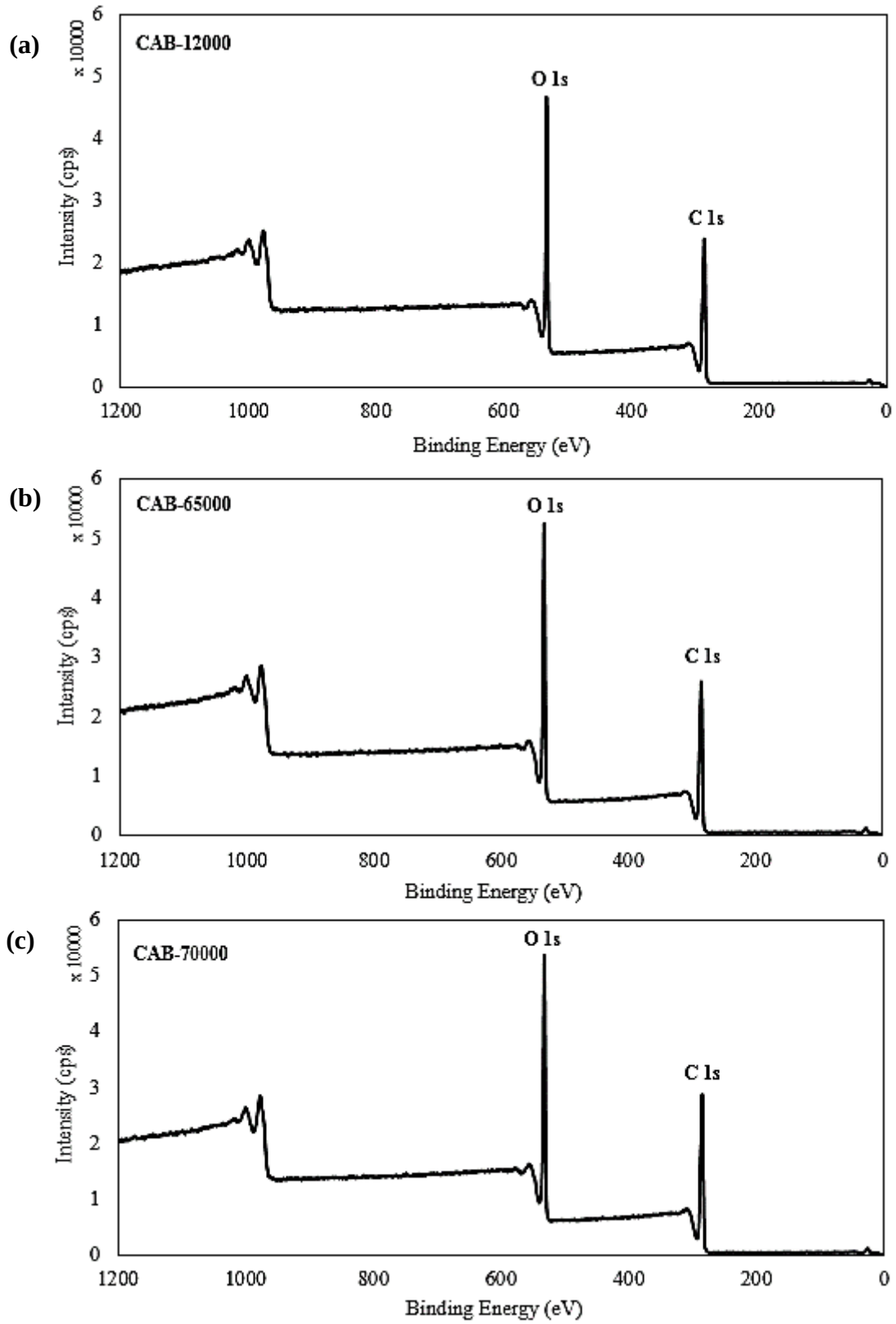

Figure 4.25 Element composition of XPS spectrum for (a) CAB-12000, (b) CAB-65000, and (c) CAB-70000

4.2 Development of Mixed Matrix Membrane (MMM)

Based on the previous discussion made, CAB-70000 has demonstrated the best CO_2 permeance and CO_2/N_2 selectivity; thus, it was further utilized to develop the mixed matrix membrane (MMM) by integrating MWCNTs into the CAB polymer matrix. MWCNTs was selected as the inorganic fillers among all the others inorganic fillers due to their superior gas separation and mechanical properties (Aroon et al., 2010). All the MMMs fabricated were dried with the optimal solvent exchange duration (30 min of isopropyl alcohol and 30 min of n-Hexane).

4.2.1 Incorporation of MWCNTs-P into CAB polymer matrix

According to **Figure 4.26d**, pristine-MMM (MMM-0.1P) was found to be a relatively thick membrane (9.77 ± 2.43 μm), as compared to the neat CAB membrane **(Figure 4.26b)** with a membrane thickness of 9.50 ± 2.12 μm. The MMM-0.1P exhibited high membrane thickness was corresponding to the aggregated clusters of MWCNTs found within membrane morphology, as represented in **Figure 4.26c**. The agglomeration of MWCNTs within the MMM-0.1P was mainly due to Van der-Waals forces and their hydrophobic nature, which entangled together into bundle and caused agglomeration within the MMM (Sahoo et al., 2010). On the other hand, the neat membrane (CAB-70000) revealed a smooth surface in **Figure 4.26a**. For this reason, it can be determined that the MWCNTs-P had stronger fundamental interaction than the interaction with the CAB polymer matrix (Kim et al., 2007; Ma et al., 2007; Ismail et al., 2011). Thus, MWCNTs-P were unwell distributed within the MMM-1.0P as described in **Figure 4.26c** and **d**.

Based on the previous discussion, the selectivity of MMM-1.0P is low due to the agglomeration problem mentioned earlier. Thus, to address the agglomeration issue, functionalisation of MWCNTs-P with β-CD was utilized to produce MWCNTs-F. Contrasting to MWCNTs-P, when MWNCTs-F were embedded into the CAB polymer matrix, the functionalized-MMM (MMM-0.1F) displayed a smoother surface with less clusters observed **(Figure 4.26e)**. Moreover, MMM-0.1F showed a thinner (9.71 ± 0.62 μm) dense membrane **(Figure 4.26f)**. This was due to the better distributed of MWCNTs-F within MMM-1.0F after functionalisation of MWCNTs that overcame the build-up of agglomerated clusters, as mentioned by Aroon et al. (2010b). The integration of MWCNTs-F into the solution dope improved the polymer-particle interactions due to the hydrophobic outer layer of β-CD which induced better polymer-particle interaction. Consequently, with the incorporation of MWCNTs-F, it suppressed the formation of clusters within the polymeric matrix. As a result, a membrane with less clusters surface was presented for MMM-1.0F (Aroon et al., 2010b).

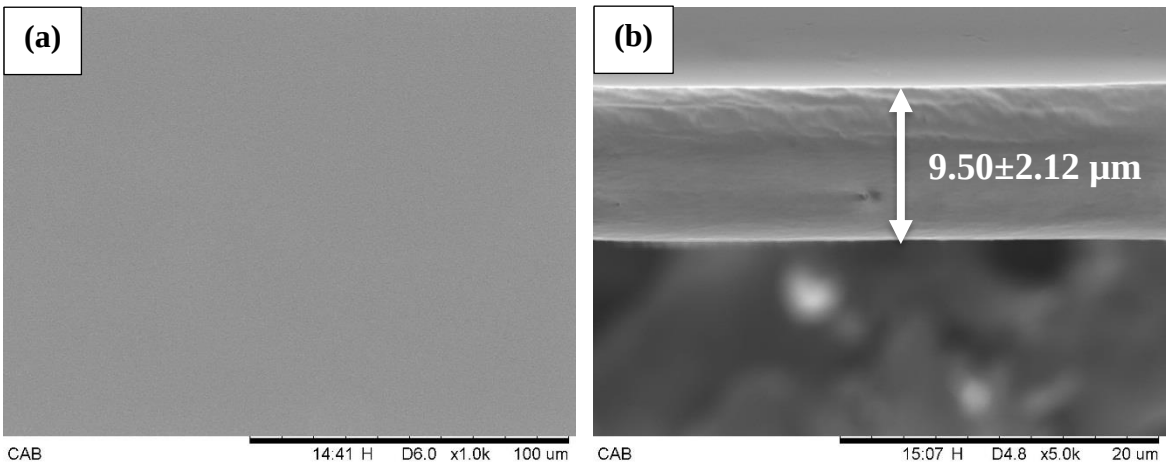

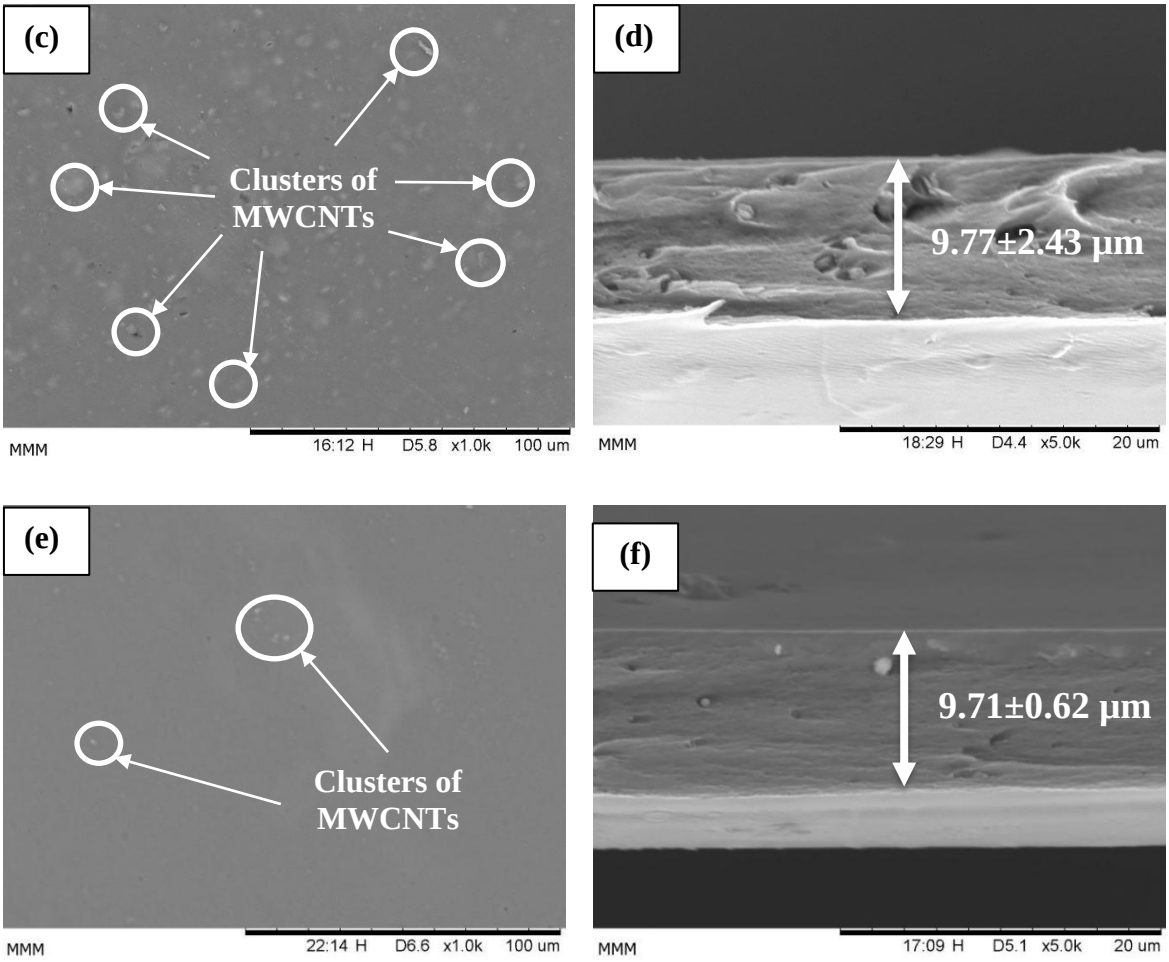

Figure 4.26 Surface and cross-sectional SEM of (a-b) neat membrane (CAB-70000), (c-d) pristine mixed matrix membrane (MMM-1.0P), and (e-f) functionalized mixed matrix membrane (MMM-1.0F) at casting thickness of 250 µm and 5 min solvent evaporation time

As shown in **Figure 4.27**, CAB-70000, MMM-1.0P, and MMM-1.0F were evaluated based on the CO_2 separation performance. According to **Figure 4.27**, the CO_2 permeance decreased significantly from 227.95 ± 0.39 GPU to 150.54 ± 0.32 GPU for CAB-70000 and MMM-1.0P, respectively. The CO_2 permeance of MMM-1.0P decreased, was subsequently due to the highly entangled bundle or clusters present within the membrane (**Figure 4.26c**). The clusters can disturb the inherent smoothness of the potential-energy surface of MWCNTs, which were distributed within the MMM and consequently resulting in poor gas permeance (Ahmad et al., 2014, Goh et al., 2011). As displayed in **Figure 4.27**, the MMM-1.0F (291.64 ±

1.02 GPU) shown to have good CO_2 permeance rate over the MMM-1.0P (150.54 ± 0.32 GPU). This is subsequently due to the well dispersed MWCNTs-F within the CAB matrix, after the functionalization treatment of MWCNTs to reduce the agglomeration issue. As a result, the MMM-1.0F integrated with MWCNTs-F, possess more interstitial channel sites with high binding energy, and nano-channel with large surface area which in turn help MMM-1.0F to yield high selectivity (Ismail et al., 2011). In fact, based on the extremely high aspect ratio (>1000) of MWCNTs-F, intrinsic smoothness of hydrophobic graphite walls and nano-scale inner diameters of MWCNTs-F also contribute to the high selectivity performance of MMM-1.0F (Noy et al., 2007).

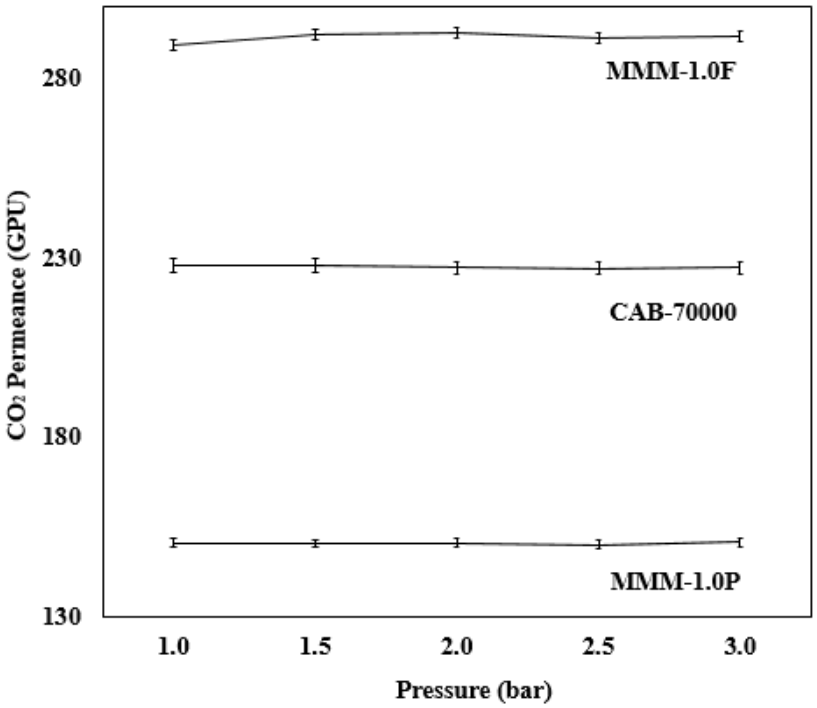

Figure 4.27 CO_2 permeance comparison between neat (CAB-70000), pristine mixed matrix membrane (MMM-1.0P), and functionalized mixed matrix membrane (MMM-1.0F) at 1.0 wt% loadings membrane fabricated at casting thickness of 250 µm and 5 min solvent evaporation time

In addition, the Attenuated Total Reflectance Fourier-transform Infrared (ATR-FTIR) spectroscopy was used to describe the results of CO_2 permeance, based on the successful incorporation of MWCNTs-F into CAB polymer matrix. With regards to the ATR-FTIR spectra, the neat membrane (CAB-70000), MMM-1.0P, and MMM-1.0F functional groups are presented in **Figure 4.28**.

The transmittance peak at around 2965 cm^{-1} is attributed by C-H stretching (Lavorgna et al., 2013). Meanwhile, the peak at around 1736 cm^{-1} is assigned to the carbonyl group vibration of carboxylic acid (C=O) groups, and the peak at 1159 cm^{-1} represents the stretching of acrylate groups (acrylic C-O bond) (Suttiwijitpukdee et al., 2011). Further, the peak at 1038 cm^{-1} is referred to as the C-O-C stretching (Lou et al., 2014). In addition, the peak at 1366 cm^{-1} is contributed by the -OH group (Del Valle. 2004). Based on **Figure 4.28**, the increment in the transmittance of the functional groups of MMM-1.0P and MMM-1.0F in comparison to CAB-70000 is due to the aromatic carbon-rings found in MWCNTs and the -OH group available in beta-cyclodextrin (β-CD), which is the functionalisation dispersant of MWCNTs (Lavorgna et al., 2013, Del Valle. 2004). This phenomenon is further schematically described in **Figure 4.29**.

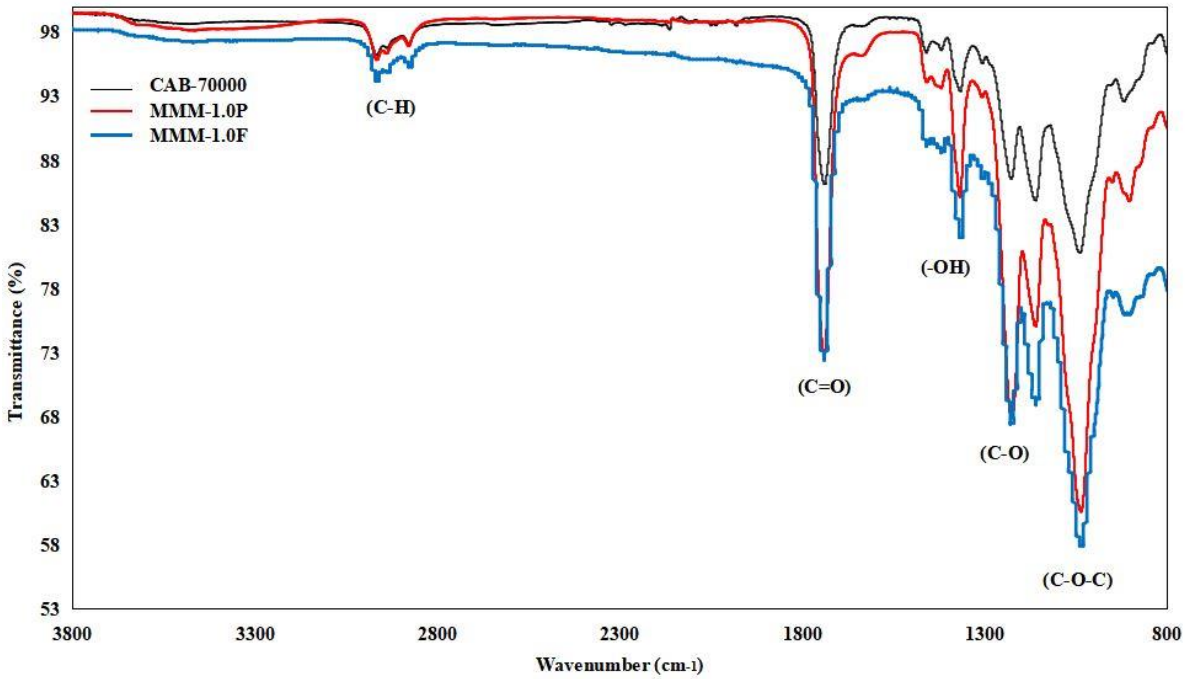

Figure 4.28 ATR-FTIR of neat (CAB-70000), pristine mixed matrix membrane (MMM-1.0P), and functionalized mixed matrix membrane (MMM-1.0F) at 1.0 wt% loadings membrane fabricated at casting thickness of 250 µm and 5 min solvent evaporation time

Based on **Figure 4.29a**, the MWCNTs with C=O and -OH groups were functionalised using the dispersant (β-CD) with -OH group and non-aqueous media (ethanol) with C-H group. In this functionalisation method, the C-O-C functional group that formed on the surface of MWCNTs-F was due to the oxidation-reduction reaction (Tsai et al., 2018) and the C-H functional group attached on the surface of MWCNTs was due to the non-aqueous media (ethanol) (Feller et al., 2002). Thus, the C-O-C and C-H functional groups were added to the original groups (C=O and –OH) of MWCNTs-F (Ahmad et al., 2013).

Based on the justification in **Figure 4.29a**, the functional groups of CAB-M consists of C-H, C=O, –OH, C-O and C-O-C. Thus, by incorporating the MWCNTs-F (C-H, C=O, –OH and C-O-C) within the polymeric structure of CAB-M, the transmittance peaks of C-H, C=O, –OH and C-O-C increased in the final structure of MMM, as schematically described in **Figure**

4.29b. Meanwhile, the intensity of C-O functional group increased. This might be because of the reaction between the C atoms from MWCNTs with the O atoms from CAB polymer matrix (Li et al., 2018). Based on Shan et al. (2012) and Bae and Snurr (2011), the highly polar functional groups that can affect the gas separation performances are carboxyl (C=O) and hydroxyl (O-H) (Shan et al., 2012, Bae and Snurr, 2011). In this case, these polar functional groups (C=O and O-H) interact with the non-polar CO_2. As a result, the CO_2 permeance and CO_2/N_2 selectivity of the MMM can be improved.

(a)

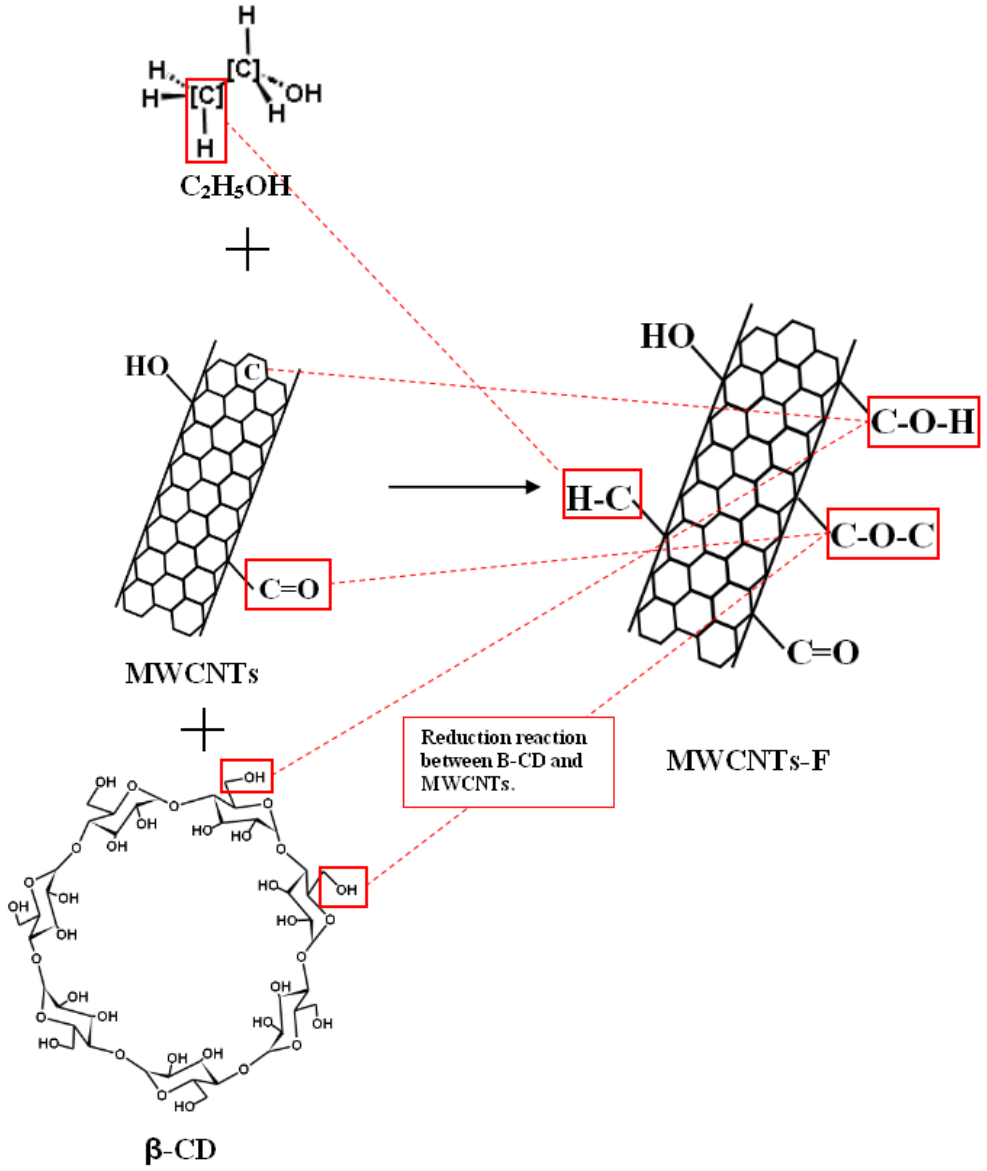

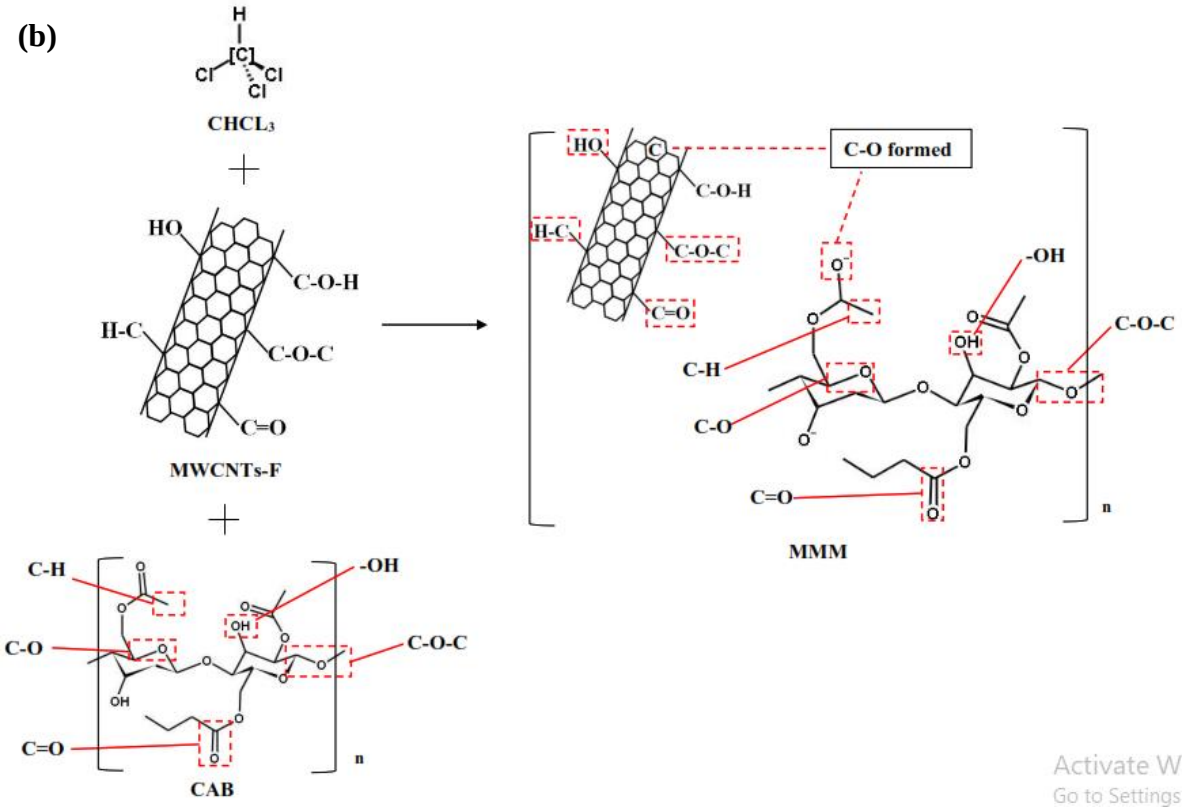

Figure 4.29 Schematic diagram on interaction between (a) MWCNTs and β-CD, (b) MWCNTs-F and CAB

Meanwhile, the N_2 permeance for CAB-70000 and MMM-1.0P were illustrated in **Figure 4.30**. From **Figure 4.30**, the N_2 permeance demonstrated closed results (37.28 ± 2.54 GPU (CAB-70000) to 35.12 ± 0.06 GPU (MMM-1.0P)), when MWCNTs-P were incorporated into the CAB polymer matrix. The minor reduction in the N_2 permeance correlates to the incorporation of MWCNTs-P into the CAB polymer matrix, which is consider as inert filler prior the functionalization of MWCNTs. When the inert fillers (MWCNTs-P) were integrated with the polymer matrix, it can affect the membrane phase separation kinetics and dope stability. As a result, the N_2 permeance for MMM-1.0P reduce, which was attributed by the incorporation of impermeable MWCNTs-P (Aroon et al., 2010c). Subsequently, when MWCNTs-F were integrated into CAB polymer matrix, the N_2 permeance decreased further from 35.12 ± 0.06 GPU (MMM-1.0P) to 23.22 ± 0.17 GPU (MMM-1.0F), respectively. The decrement of N_2 permeance for MMM-1.0F was because of the incorporation of MWCNTs-F,

which improved interfacial wetting and bonding of MWCNTs with CAB matrix through the functionalization with β-CD, and thus, creating strong MWCNTs array polymer interface adhesion between the surrounding of CAB chains that can hold high amount of N_2 gas (Ismail et al., 2011, Yang et al., 2005). Hence, the N_2 permeance of MMM-1.0F is significantly lower than MMM-1.0P. Moreover, low N_2 permeance also promote better membrane selectivity with high CO_2 permeance yield from MMM-1.0F, because the selectivity coefficient of membrane is based on the permeance of CO_2 against the permeance of N_2. Therefore, the combination between high permeance CO_2 with low permeance N_2 is ideal for MMM-1.0F, in order to achieve high separation efficiency (Xiang et al., 2016).

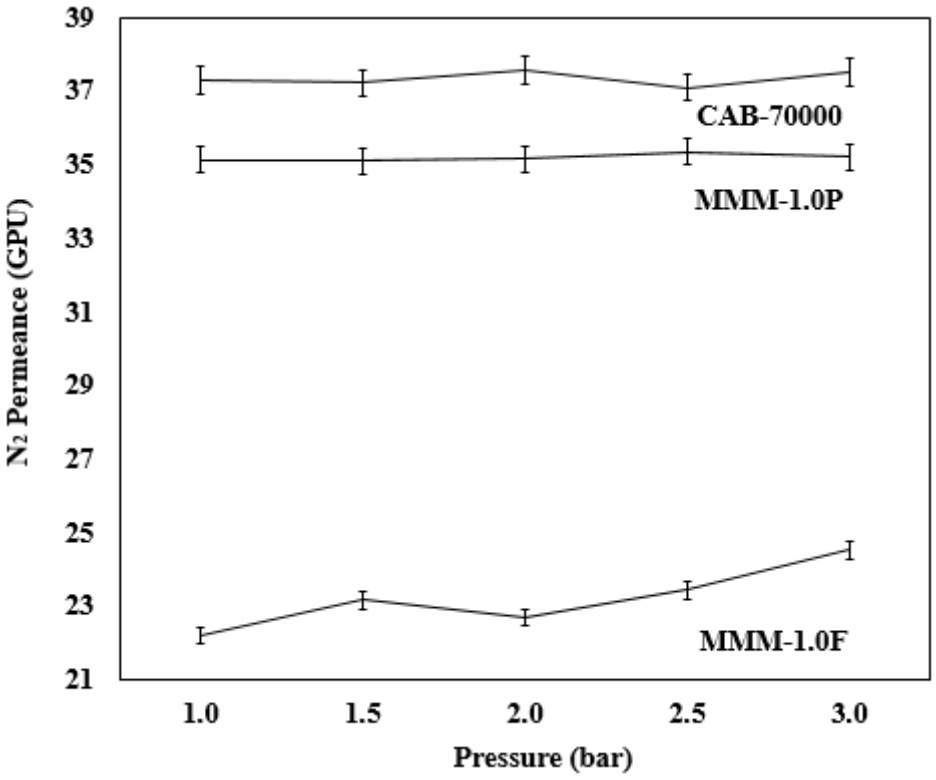

Figure 4.30 N_2 permeance comparison between neat (CAB-70000), pristine mixed matrix membrane (MMM-1.0P), and functionalized mixed matrix membrane (MMM-1.0F) at 1.0 wt% loadings membrane fabricated at casting thickness of 250 µm and 5 min solvent evaporation time

The results of N_2 permeance was further explained with the contact angle analysis for membranes CAB-70000, MMM-1.0P and MMM-1.0F as displayed in **Figure 4.32**. The incorporation of MWCNTs-F into the CAB polymer matrix reduce the contact angle value from 96.4˚ ± 0.1˚ (CAB-70000) to 72.9˚ ± 0.2˚ (MMM-1.0F). The resulting phenomena can be explained due to the usage of β-CD as the functionalisation agent of MWCNTs (Rahimpour et al., 2012). The β-CD has been described to have a hydrophobic inner wall and hydrophilic outer surface that enhances the solubility of MWCNTs due to their complex formation (Singh et al., 2010, Polarz et al., 2001). By incorporating MWCNTs-F into CAB polymer matrix, the membrane surface hydrophilicity is enhanced due to the presence of the extra hydroxyl and carboxyl groups originating from β-CD and MWCNTs, respectively (Del Valle. 2004, Ahmad et al., 2013). As discussed previously in **Figure 4.29**, these polar functional groups (C=O and O-H) can react with non-polar CO_2 and favour less N_2 gas (Shan et al., 2012). Since polar and non-polar are opposite charges, hence opposite charges tend to attract, while alike charges repel each other. Therefore, allowing the interaction between polar and non-polar gases within the membrane. The schematic diagram is illustrated in **Figure 4.31** to demonstrate the interaction between polar functional group with non-polar gases. Therefore, the N_2 permeance reduced with lower hydrophilicity yield from MMM-1.0F, and subsequently enhance the selectivity performance of the MMM.

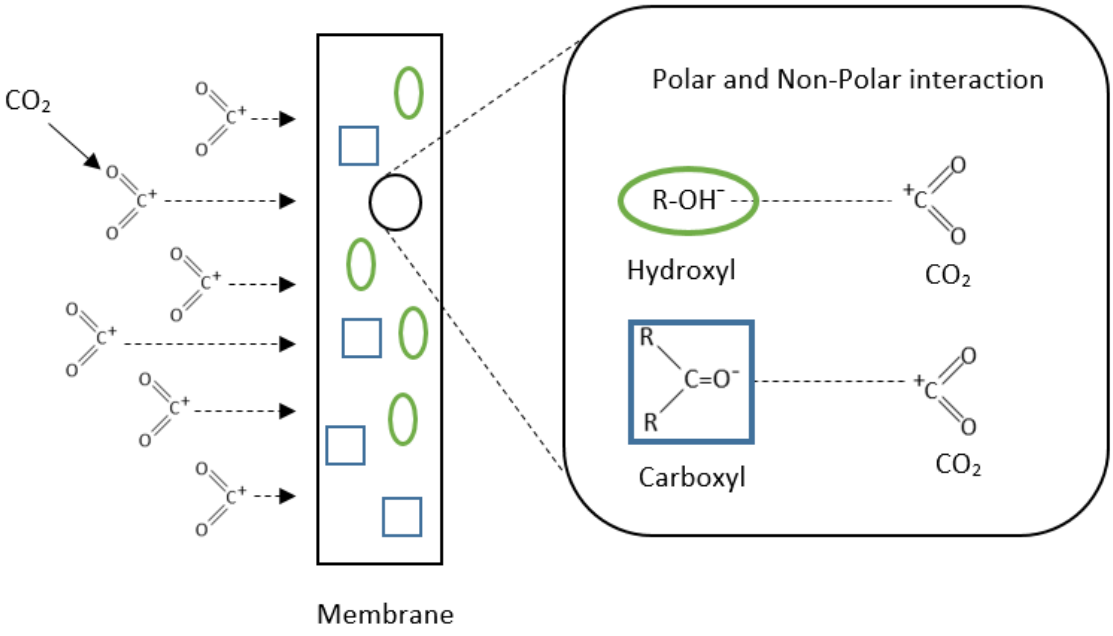

Figure 4.31 Schematic diagram of non-polar group interact with polar group

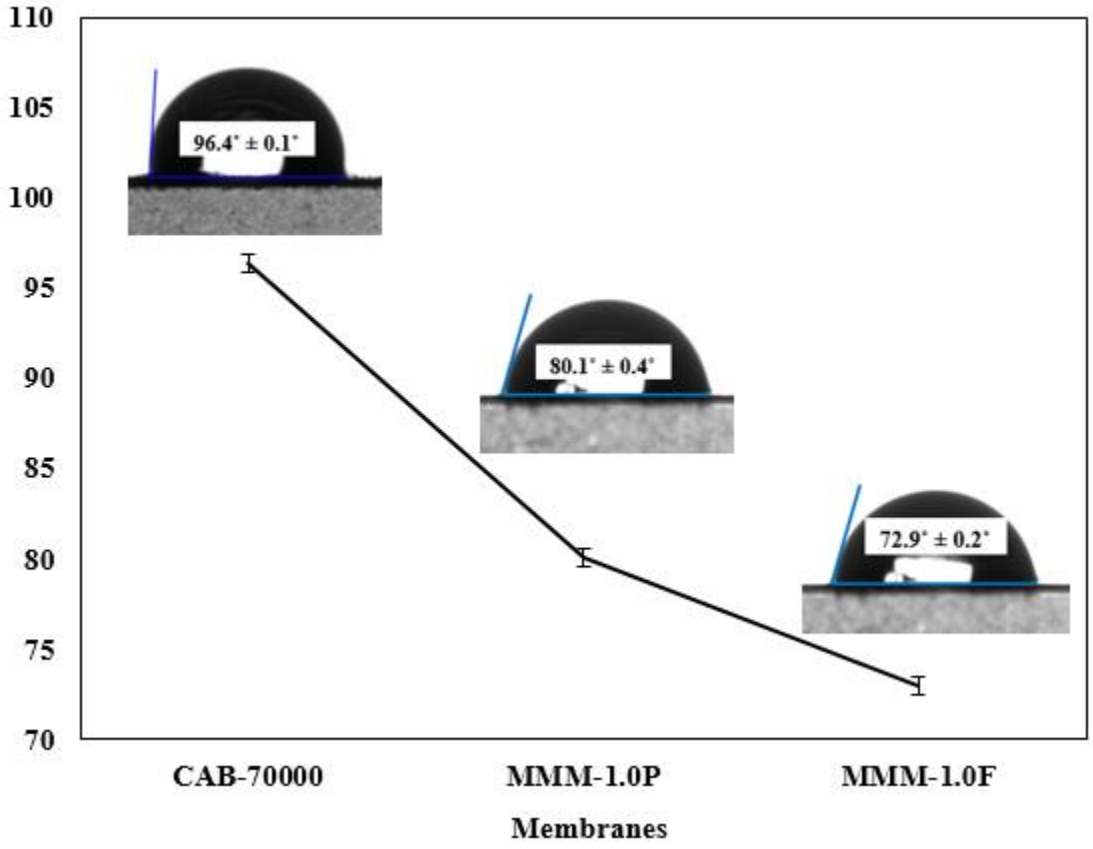

Figure 4.32 Contact angle analysis for neat membrane (CAB-70000), pristine MMM (MMM-1.0P), and functionalized MMM (MMM-1.0F) at casting thickness

of 250 µm and 5 min solvent evaporation time with CAB polymer matrix (*Mn*=70000)

The CO_2/N_2 separation performance of CAB-70000 and MMM-1.0P were summarized in **Figure 4.33**. As shown in **Figure 4.33**, the CAB-70000 and MMM-1.0P were able to achieve a selectivity of 6.12 ± 0.09 and 4.29 ± 0.38, respectively. The decrement in the selectivity of MMM-1.0P was mainly attributed by the not well distributed MWCNTs-P within the CAB matrix, because based on the hydrophobic nature of MWCNTs, which favour the formation of bundle forms instead of individual tubes, hence, the MWCNTs-P tend to interact with itself than the polymer matrix (Ismail et al., 2011). Thus, this prevent the MWCNTs-P to disperse homogenously within the polymer matrix. Consequently, the impermeable clusters formed by the bundle MWCNTs-P can interrupt the gas permeance, causing the low selectivity results for MMM-1.0P (Ahmad et al., 2014, Trotta et al., 2011). Meanwhile, by interpreting **Figure 4.33**, the ideal selectivity achieved for MMM-1.0P and MMM-1.0F was 4.29 ± 0.38 and 12.57 ± 1.19, respectively. The major reason for the increment in the selectivity for MMM-1.0F was because of the integration of MWCNTs-F into the CAB matrix, which provides more sites for physical and chemical adsorption through the nano-channel within MMM-1.0F. Furthermore, the functionalisation agent β-CD played a crucial role due to the abundant polar functional hydroxyl (O-H) group present, which interact well with the non-polar gas CO_2 (Shan et al., 2012, Bae and Snurr, 2011). Therefore, the CO_2 permeance and CO_2/N_2 selectivity of the MMM-1.0F improved.

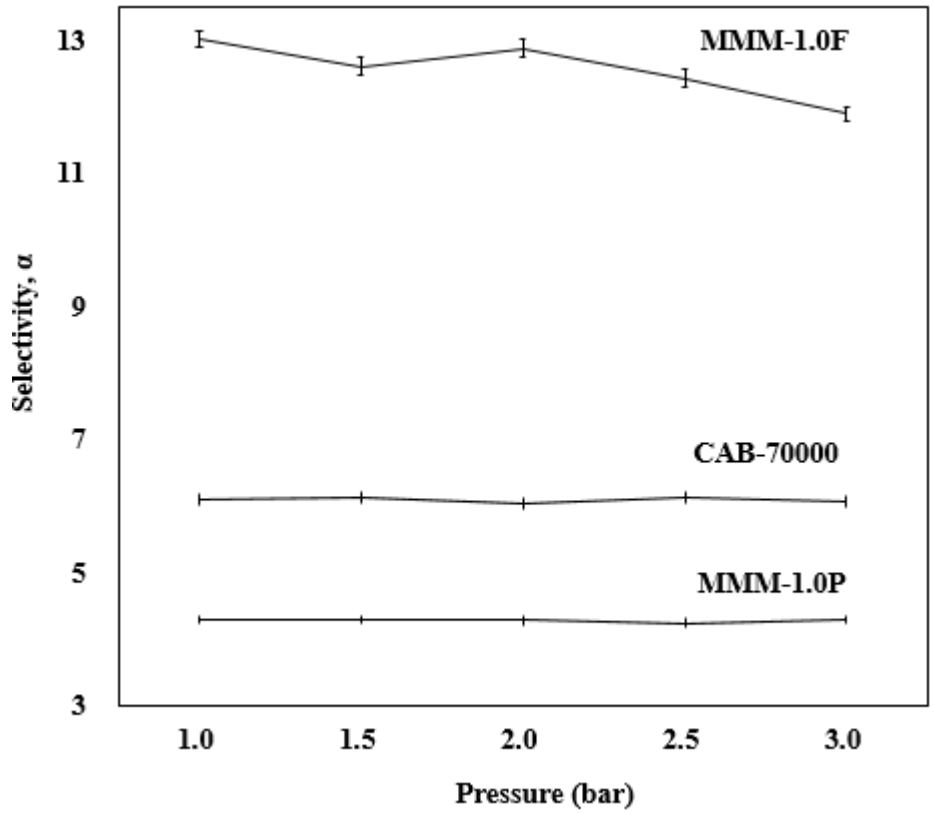

Figure 4.33 Ideal selectivity of CO_2/N_2 for neat membrane (CAB-70000), pristine mixed matrix membrane (MMM-1.0P), and functionalized mixed matrix membrane (MMM-1.0F) at 1.0 wt% loadings membrane fabricated at casting thickness of 250 µm and 5 min solvent evaporation time

4.2.2 X-ray diffraction (XRD) analysis

Since the incorporation of MWCNTs in CAB matrix can have significant impact on the efficiency of the membrane selectivity performance. The dispersion and crystalline properties of CAB-70000, MMM-1.0P, and MMM-1.0F were analysed using the scattering methods of X-rays. Based on the scattering or diffraction curve obtained, this method reveals the semi-quantitative information of the material is usually referring as X-ray diffraction (XRD) (Richards and Charles 2010). For XRD analysis, the intensity counts is usually measured as a function of the scattering angle (2θ), due to no energy differences between the incoming and outgoing protons (Richards and Charles 2010).

The XRD patterns with scattering angle values of the membranes are illustrated in **Figure 4.33**, while the inter-planar distance (*d*-spacing) were tabulated in **Table 4.2**. The CAB-70000 demonstrated a semi-crystalline curve, consisting both amorphous and crystalline phases. The broad and strong peaks are indicated starting at 30.37° (d=3.03), 33.73° (d=2.80), and 46.31° (d=1.99) of 2θ, were attributed by the CAB polymer chains. When the MWCNTs-P was integrated into the CAB matrix, the MMM-1.0P peaks shifted to a lower values starting at 29.53° (d=2.94), 31.97° (d=2.66), and 45.43° (d=1.96) of 2θ, the decrement of the crystalline peaks correspond to the crystalline phases of MWCNTs-P, demonstrating the successful incorporation of MWCNTs-P into the CAB matrix. Subsequently, for MMM-1.0F with the incorporation of MWCNTs-F, sharp crystalline peaks were found at 20.03° (d=4.43), and 23.76° (d=3.75), followed by a board peak at 38.03° (d=2.37). Consequently, the crystalline peaks shift to a higher value when MWCNTs-F were integrated into CAB matrix as compared to MMM-1.0P. These shifts indicate an increase in the segmental spacing of MMM-1.0F, which is important to create more free volume cavities for solution diffusion (Wang et al., 2014). Meanwhile, the enhancement of crystalline peaks at 20.03° (d=4.43), 23.76° (d=3.75), and 38.03° (d=2.37) for MMM-1.0F also indicate the successful grafting of MWCNTs-F into the CAB matrix (Isanejad and Mohammadi 2018).

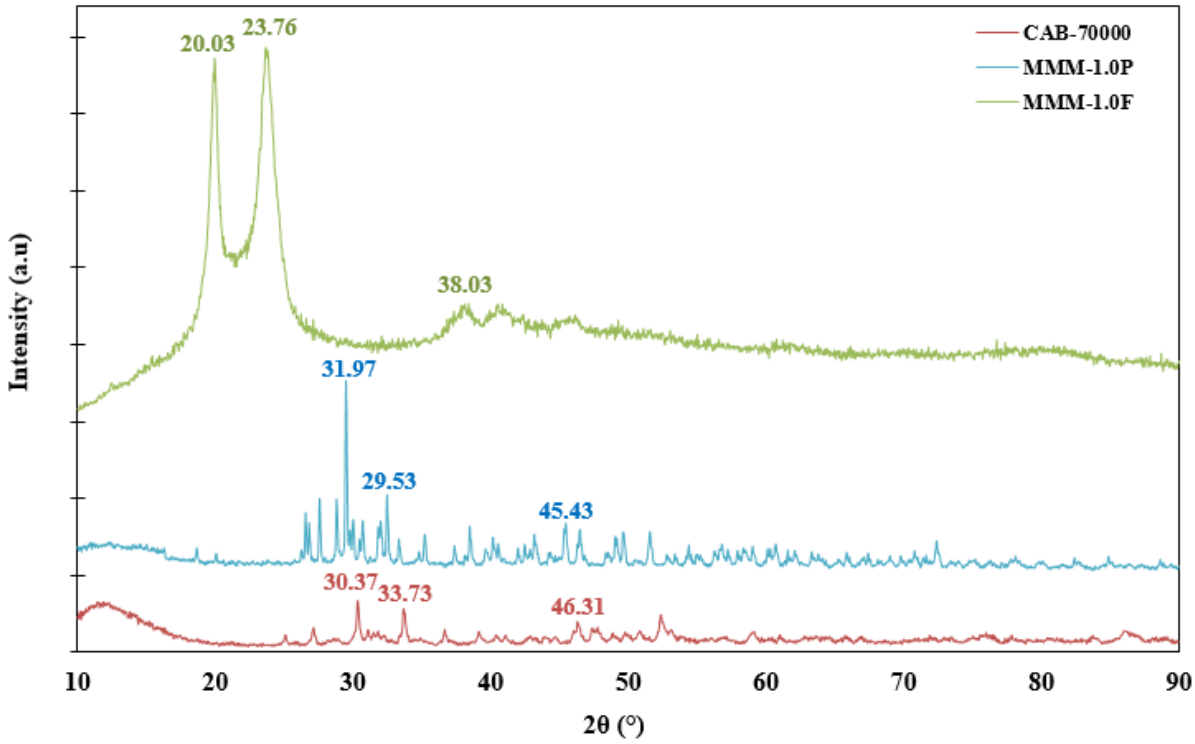

Figure 4.34 XRD patterns for neat membrane (CAB-70000), pristine MMM (MMM-1.0P) at 1.0 wt% loadings of MWCNTs-P, and functionalized MMM (MMM-1.0F) at 1.0 wt% loadings of MWCNTs-F fabricated at casting thickness of 250 µm and 5 min solvent evaporation time

Table 4.2 Scattering angles (2θ) of the main diffraction peaks for CAB-70000, MMM-1.0P, and MMM-1.0F with corresponding inter-planar distances (*d*-spacing)

	CAB-70000		MMM-1.0P		MMM-1.0F	
Peaks	2θ (°)	*d*-spacing	2θ (°)	*d*-spacing	2θ (°)	*d*-spacing
1	30.37	3.03	29.53	2.94	20.03	4.43
2	33.73	2.80	31.97	2.66	23.76	3.75
3	46.31	1.99	45.43	1.96	38.03	2.37

4.3 Effect of MWCNTs-F loading concentration

Based on the permeance and selectivity performance improvement of MMM-1.0F in CO_2/N_2, this study was continued with the investigation on the effect of loadings of MWCNTs-F in the range of 0.7 wt %, 0.8 wt%, and 0.9 wt %. These loadings ranges are selected, because according to Ismail et al. (2011), when low loadings of MWCNTs was incorporated into the MMM, it can prevent the nanotubes of MWCNTs to agglomerate due to the buildup attraction

force contributed by Van-Der Waals. The surface and cross sectional morphology of the MMMs are illustrated in **Figure 4.35.**

From **Figure 4.35a** and **c**, MMM-0.7F and MMM-0.8F shown to have smooth surface with dense cross sectional structure, indicating that the MWCNTs-F integrated into the CAB matrix are well dispersed within the MMM. In fact, this surface morphology is important to carry out the gas separation. By further increasing the content of MWCNTs-F to 0.9 wt% (MMM-0.9F), smooth surface with some clusters was observed in **Figure 4.35e**. The formation of cluster was due to the high amount of MWCNTs-F incorporated, which favour the particle-particle interactions and lead to the strong adhesion between MWCNTs and formation of clusters.

Notably, the membrane thickness decreased from 9.21 ± 1.01 μm (MMM-0.7F) to 8.68 ± 0.76 μm (MMM-0.8F) when higher loading of MWCNTs-F was incorporated. This was correspond to the interaction between polymer-chain segments between the MWCNTs-F and CAB matrix that had changed the original CAB polymer chain packing. As a result, creating more adsorption sites on the polymer chains that reduce the mobility of CAB molecular segments (Wang et al., 2014). Thus, creating high packing density for the CAB polymer when high loading of MWCNTs-F was integrated, and eventually reduce the membrane thickness of MMM-0.8F. However, for MMM-0.9F when higher loading of MWCNTs-F was integrated into the CAB matrix, the membrane thickness increased from 8.68 ± 0.76 μm (MMM-0.8F) to 10.79 ± 3.22 μm (MMM-0.9F). This contradiction result for MMM-.09F may arise due to the effect of poor adhesion between the MWCNTs-F surface with the CAB polymer chain, because when higher loading of MWCNTs-F was incorporated, the MWCNTs-F prefer the nanotubes-

nanotubes interaction with the filler itself instead of the polymer due to the Van-Der Waals attraction force is stronger than the nanotubes-polymer interaction, this lead to high repulsive force between the polymer and fillers (Ismail et al., 2011). Thus, the membrane thickness for MMM-0.9F increased.

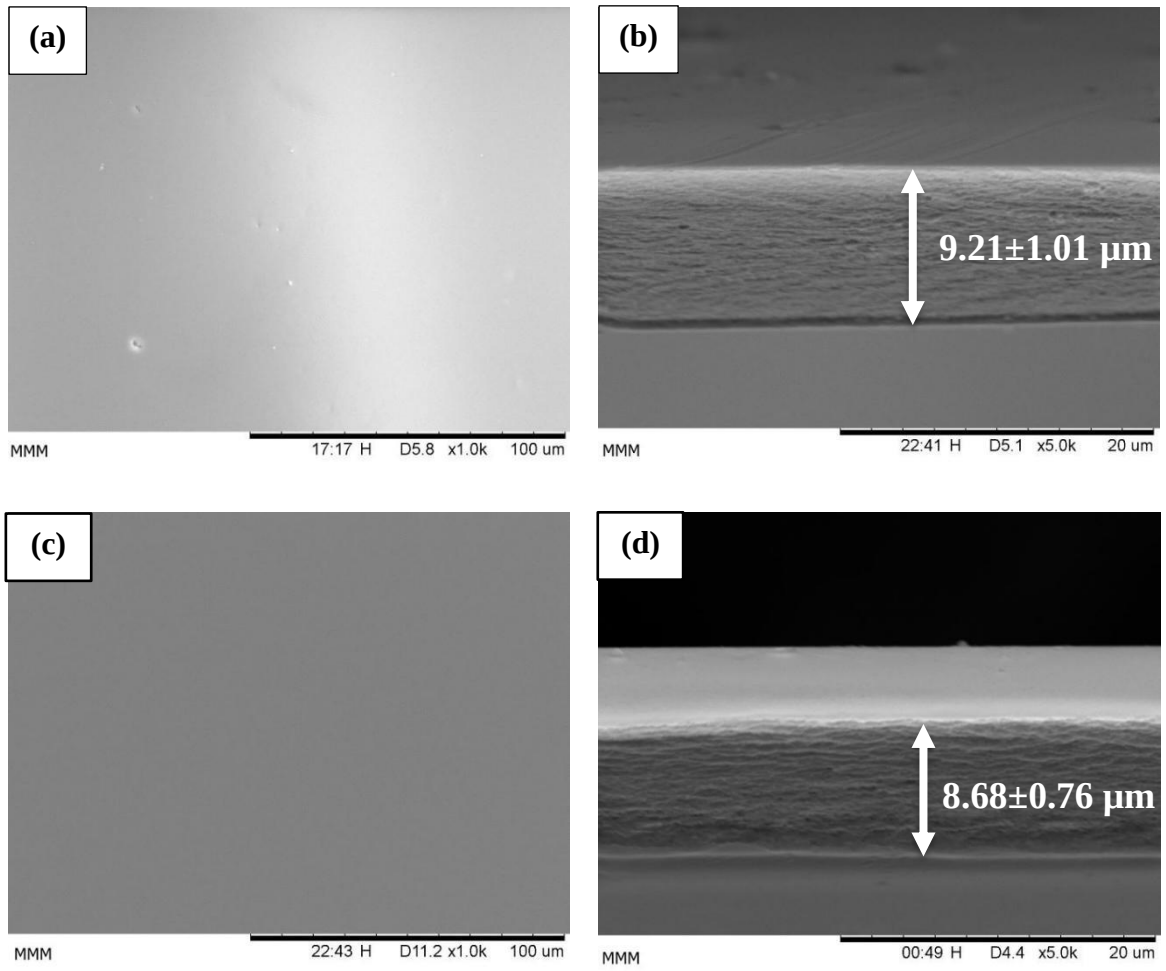

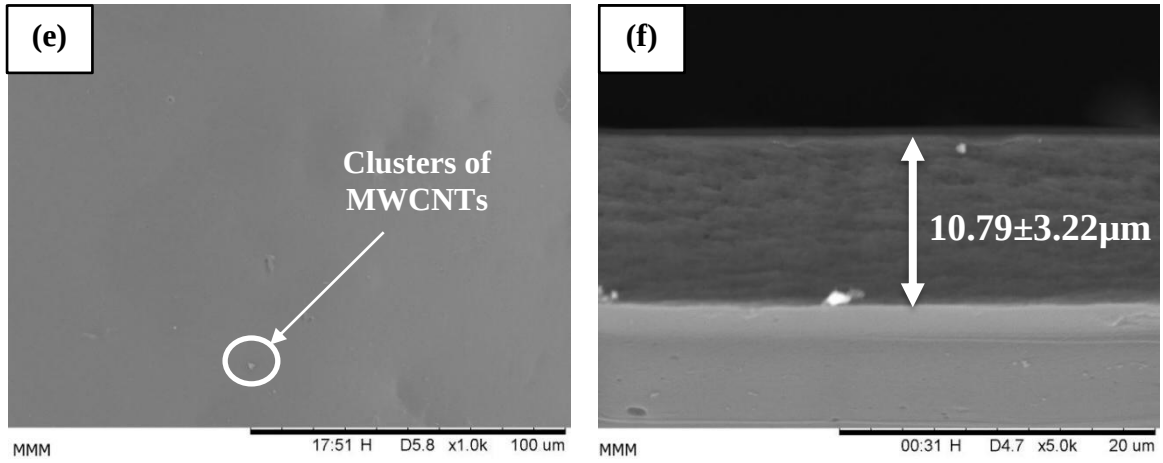

Figure 4.35 Surface and cross-sectional SEM of MMMs synthesised at different MWCNTs-F loadings concentration of (a-b) 0.7 wt% (MMM-0.7F), (c-d) 0.8 wt% (MMM-0.8F), and (e-f) 0.9 wt% (MMM-0.9F) at casting thickness of 250 µm and 5 min solvent evaporation time with CAB polymer matrix (*Mn* of 70000)

The permeance rates of CO_2 at different concentration loadings of MWCNTs-F are depicted in **Figure 4.36**. As shown in **Figure 4.36**, CO_2 permeance increased as the MWCNTs loading increased from 0.7 wt% (324.15 ± 1.88 GPU) to 0.8 wt% (377.62 ± 1.20 GPU), this was subsequently due to higher loading of MWCNTs incorporated into the MMM-0.8F that give more high diffusivity nanotubes tunnels within the MMM, hence improved the mass transport efficiency of MMM-0.8F (Kim et al., 2006). However, increasing the MWCNTs-F loadings from 0.8 wt% (377.62 ± 1.20 GPU) to 0.9 wt% (275.04 ± 1.13 GPU) the CO_2 permeance reduced, this result was attributed by the thick dense structure of MMM-0.9F when the MWCNTs-F content increases, they tend to combine together to form MWCNTs agglomerates due to the strong intermolecular force, implying that the MWCNTs-F interact strongly with themselves than the CAB matrix. When agglomeration occurred within membrane, this lead to the increase of membrane surface area based on the formation of MWCNTs-F bundle. This thick structure of membrane is not prefer, as it would definitely restrict the gas permeation of the membrane (Sanip et al., 2011).

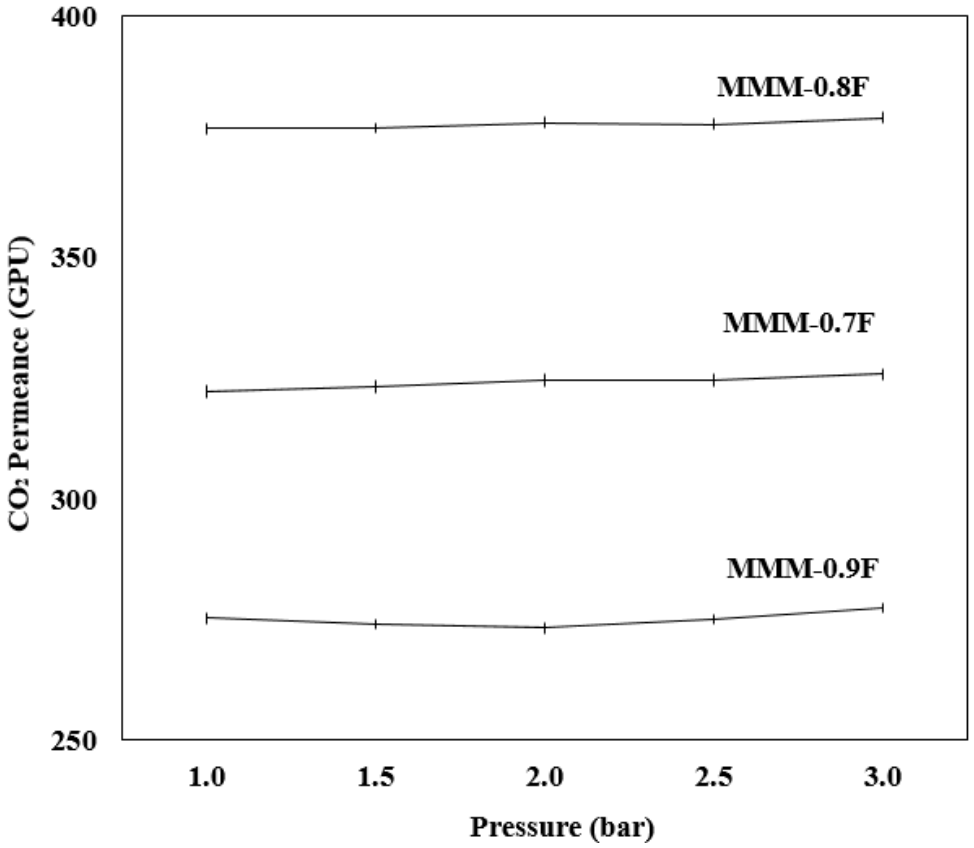

Figure 4.36 CO_2 permeance of MMMs synthesised at different MWCNTs-F loadings concentration of 0.7 wt% (MMM-0.7F), 0.8 wt% (MMM-0.8F), and 0.9 wt% (MMM-0.9F) at casting thickness of 250 µm and 5 min solvent evaporation time with CAB polymer matrix (*Mn* of 70000)

The relationship between the CO_2 permeance and membrane thickness for the fabricated MMMs are summarized in **Figure. 4.37**. Based on **Figure 4.37**, the CO_2 permeance of MMM increased when the membrane thickness was thin, with respect to the amount of MWCNTs-F incorporated. The thickness of the membrane played a crucial role in determining the CO_2 permeance of the membrane. As thick membrane usually induces greater mass transfer resistant within the membrane. Thus, thin membrane is usually more preferable in this case. The MMM-0.8F (377.62 ± 1.20 GPU) achieved the highest CO_2 permeance based on thin membrane thickness (8.68 ± 0.76 µm) demonstrated, followed by MMM-0.7F (324.15 ± 1.88 GPU) with a membrane thickness of 9.21 ± 1.01 µm, then MMM-0.9F (275.04 ± 1.13 GPU) with the lowest CO_2 permeance due to the thick membrane (10.79 ± 3.22 µm) morphology presented.

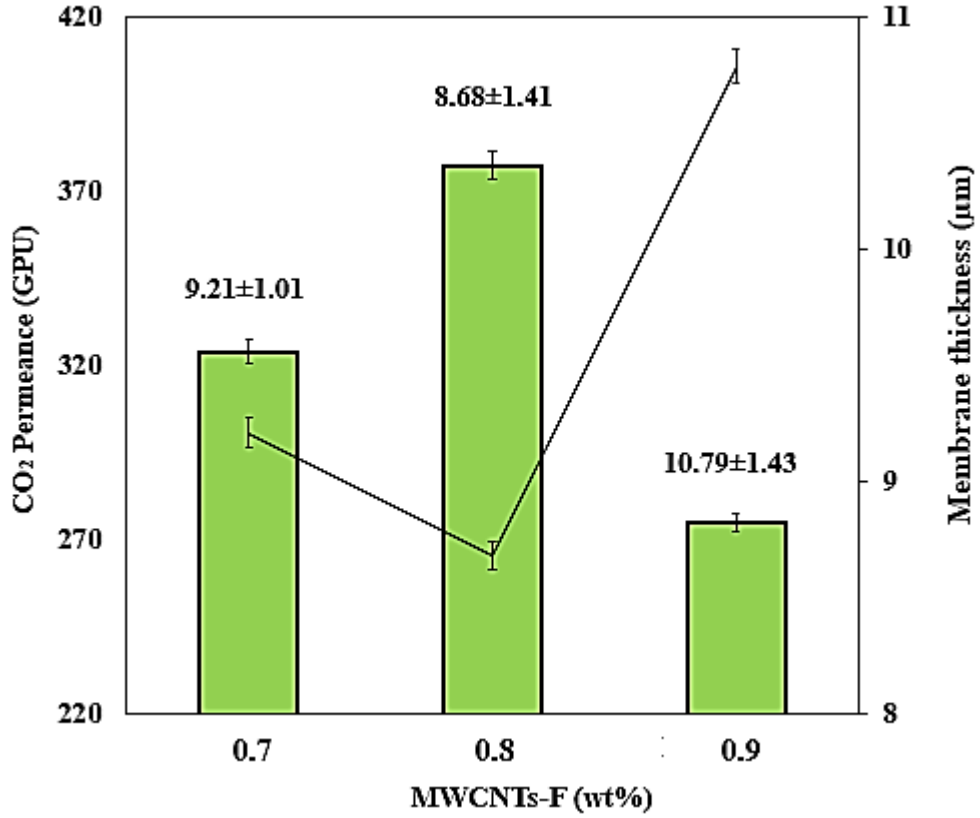

Figure 4.37 CO_2 permeance from MMMs synthesised at different MWCNTs-F loadings concentration of 0.7 wt% (MMM-0.7F), 0.8 wt% (MMM-0.8F), and 0.9 wt% (MMM-0.9F) versus thickness of the membrane at casting thickness of 250 µm and 5 min solvent evaporation time with CAB polymer matrix (*Mn* of 70000)

Consequently, the contact angle analysis was conducted to support the CO_2 permeance yield, based on the hydrophilicity of the membrane. According to **Figure 4.38**, the contact angle reduced when higher loading of MWCNTs-F was incorporated into MMM-0.7F (77.7˚ ± 0.5˚), MMM-0.8F (74.6˚ ± 0.4˚), and MMM-0.9F (73.4˚ ± 0.1˚). The reduction in contact angle can be explained with the addition of β-CD as the functionalisation agent of MWCNTs (Rahimpour et al., 2012). β-CD has been described to have a hydrophilic outer surface that enhances the solubility of MWCNTs due to their complex formation (Ahmad et al., 2013). By incorporating MWCNTs-F into CAB matrix, the membrane surface hydrophilicity is enhanced due to the presence of the extra hydroxyl and carboxyl groups originating from β-CD and MWCNTs,

respectively (Del Valle. 2004, Ahmad et al., 2013). Hence, the contact angle for MMM-0.8F from MMM-0.7F when higher loading of MWCNTs-F was incorporated into the MMM, indicating that MMM-0.8F is more hydrophilic than MMM-0.7F.

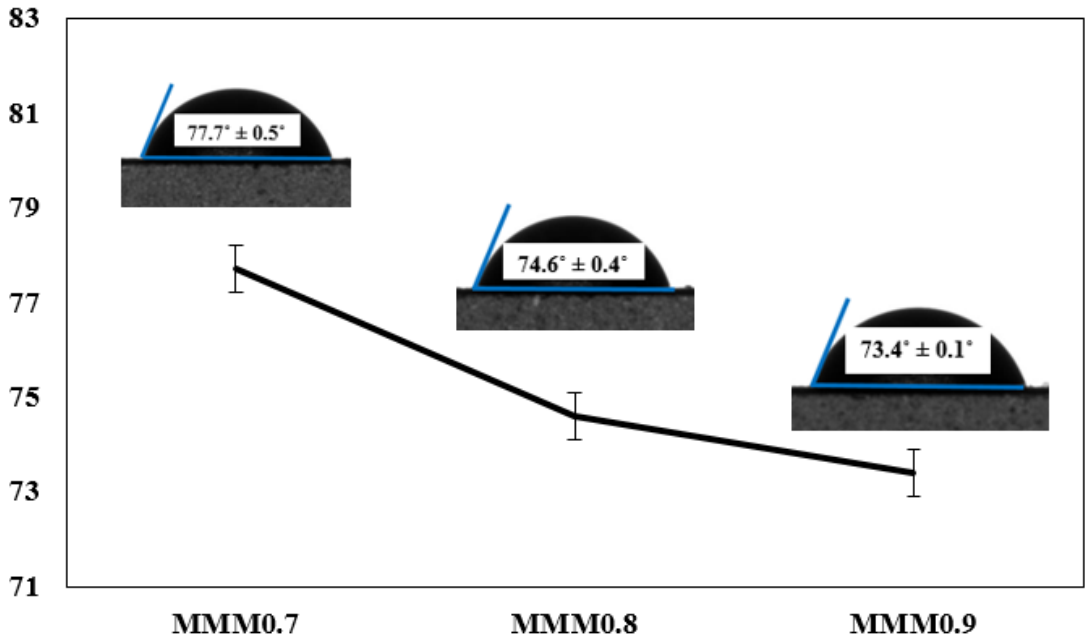

Figure 4.38 Contact angle of MMMs synthesised at different MWCNTs-F loadings concentration of (a) 0.7 wt% (MMM-0.7F), (b) 0.8 wt% (MMM-0.8F), and (c) 0.9 wt% (MMM-0.9F) at casting thickness of 250 µm and 5 min solvent evaporation time with CAB polymer matrix (*Mn* of 70000)

As the hydrophilicity increases due to the increased loadings of MWCNts-F incorporated into the polymer matrix, the strength of dipole-quadrupole interaction also increases, resulting the MMM-0.8F have stronger affinity towards CO_2 molecules (Lin and Park 2011). Therefore, contributing to the high CO_2 permeance result of MMM-0.8F. However, for MMM-0.9F when the loading of MWCNTs-F increases further, the CO_2 permeance decreased while it is supposed to have high CO_2 permeance due to low hydrophilicity presented. This contradict result of MMM-0.9F was subsequently caused by the thick dense membrane presented in **Figure 4.35f**, which induce high flow resistant for the membrane. Since, solution diffusion is the main transport mechanisms for dense membrane, therefore the thickness of the membrane is the

dominant factor over the hydrophilicity of the membrane that can affect the CO_2 permeance for the MMMs.

The N_2 permeance rates at different loadings of MWCNTs-F are summarized in **Figure 4.39**. The N_2 permeance increased as the MWCNTs loading increased from 0.7 wt% (27.44 ± 0.12 GPU) to 0.8 wt% (28.68 ± 0.19 GPU). This results can be explained by the thin thickness (8.68 ± 0.76 μm) of the membrane presented in **Figure 4.35d** which permit greater mass transfer of N_2 through MMM-0.8F. Subsequently, the N_2 permeance decreased when the loading of MWCNTs-F increased from 0.8 wt% (28.68 ± 0.19 GPU) to 0.9 wt% (25.32 ± 0.10 GPU). This reduction in the N_2 permeance correlates to the incorporation of MWCNTs-F into the CAB polymer matrix, which favours less polar gas permeance such as N_2. This phenomena can be explained with the Attenuated Total Reflectance Fourier Transform Infrared Spectroscopy (ATR-FTIR) spectra as presented in **Figure 4.40**.

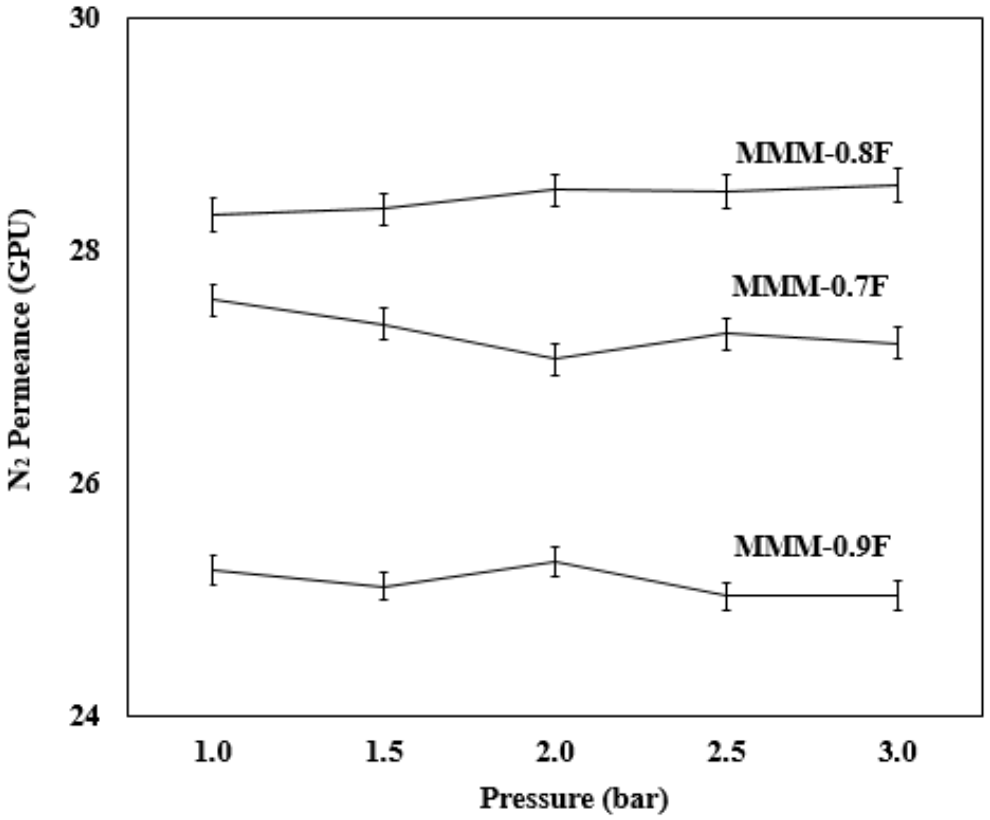

Figure 4.39 N_2 permeance of MMMs synthesised at different MWCNTs-F loadings concentration of 0.7 wt% (MMM-0.7F), 0.8 wt% (MMM-0.8F), and 0.9 wt% (MMM-0.9F) at casting thickness of 250 µm and 5 min solvent evaporation time with CAB polymer matrix (*Mn* of 70000)

The organic functional groups of MMM-0.7F, MMM-0.8F, and MMM-0.9F were described in **Figure 4.40**. The transmittance peak around 2965 cm^{-1} correspond to the C-H stretching (Lavorgna et al., 2013). Meanwhile, the peak at around 1736 cm^{-1} was attributed by the carbonyl group vibration of carboxylic acid (C=O) groups, and the peak at 1159 cm^{-1} represents the stretching of acrylate groups (acrylic C-O bond) (Suttiwijitpukdee et al., 2011). Furthermore, the peak at 1038 cm^{-1} was referred to as the C-O-C stretching (Lou et al., 2014). Additionally, the board peak at 1366 cm^{-1} was the -OH group (Del Valle 2004). The N_2 molecules are capable to interact weakly with the C=O groups through the π-electron system as stated by Blatchford et al. (2003). Therefore, when higher loading of MWCNTs-F was incorporated into MMM-0.9F, the intensity of C=O stretching is the highest as shown in **Figure**

4.40. Hence, the intermolecular force between the C=O groups and N_2 strengthen up within the membrane. As a result, more N_2 molecules are being captured within the membrane, and causes tougher permeation of N_2 molecules through the membrane (Blatchford et al., 2003). Thus, the permeance of N_2 for MMM-0.9F was the lowest compared to MMM-0.7F and MMM-0.8F.

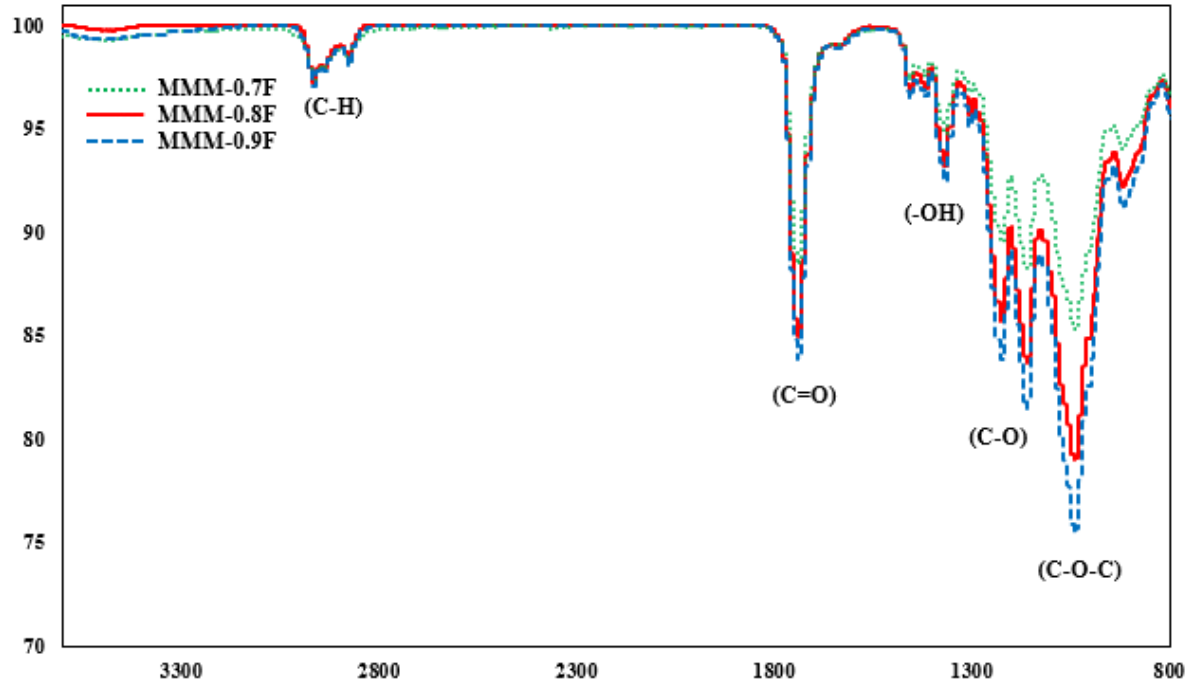

Figure 4.40 ATR-FTIR of MMMs synthesised at different MWCNTs-F loadings concentration of 0.7 wt% (MMM-0.7F), 0.8 wt% (MMM-0.8F), and 0.9 wt% (MMM-0.9F) at casting thickness of 250 µm and 5 min solvent evaporation time with CAB polymer matrix (*Mn* of 70000)

The selectivity performance for different loadings concentration of MWCNTs-F was summarized in **Figure 4.41**. Based on the selectivity performance illustrated in **Figure 4.41**, MMM-0.8F (13.17 ± 1.39) demonstrates the best selectivity results as compared to MMM-0.7F (11.81 ± 1.99) and MMM-0.9F (10.87 ± 1.24), this was contributed by the thin dense (8.68 ± 0.76 µm) morphology of the membrane yield, and also due to higher loading of MWCNTs-F incorporated into the MMM which increased the affinity towards CO_2 permeance based on the nano-channel consist within the membrane. Meanwhile, MMM-0.7F demonstrated lower

selectivity performance (11.81 ± 1.99) due to less MWCNTs-F applied, which limit higher solubility of gas within the MMM. Nevertheless, even with higher loading of MWCNTs-F were incorporated into MMM-0.9F, the low selectivity performance (10.87 ± 1.24) was subsequently caused by the thick dense membrane morphology, that restrict the transport of gas molecules within the MMM-0.9F.

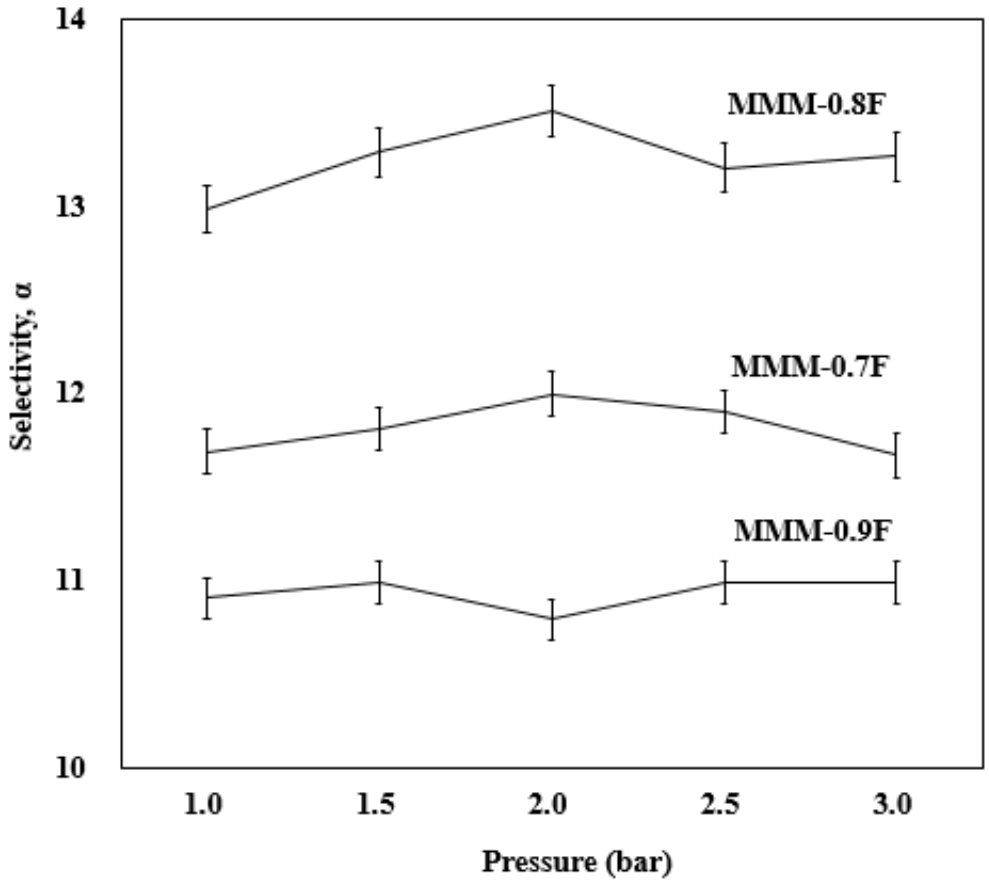

Figure 4.41 Ideal selectivity of MMMs synthesised at different MWCNTs-F loadings concentration of 0.7 wt% (MMM-0.7F), 0.8 wt% (MMM-0.8F), and 0.9 wt% (MMM-0.9F) at casting thickness of 250 µm and 5 min solvent evaporation time with CAB polymer matrix (*Mn* of 70000)

In addition, the selectivity performance obtained from the MMMs were supported with the crystal structure and intermolecular distances between the intersegmental chains using XRD analysis, as illustrated in **Figure 4.42**. The diffraction peaks (2θ) and inter-laminar distances

(*d*-spacing) observed for the MMM-0.7F, MMM-0.8F, and MMM-0.9F from the XRD results are tabulated in **Table 4.3**. The MMMs shown similar diffraction peaks at 20.03°, 23.76°, and 38.03° indicating identical MWCNTs-F were incorporated for each of the MMM. In addition, the intensity of the characteristics peaks of MMMs increases with the loadings of MWCNTs-F (Lee et al., 2006). This phenomenon was attributed to the disturbance of the inter-chain hydrogen bonding between the MWCNTs segments in the CAB matrix originated from the –OH group of β-CD, resulting in the increase of crystalline region in MMMs as indicated in **Figure 4.42** (Xiang et al., 2016). Meanwhile, the slight decreased of *d*-spacing values of the MMMs at each of the diffraction peaks was due to the suppression caused by higher loading of fillers incorporated, which disturbed the arrangement of specific sites of the organic polymer chains (Lee et al., 2006).

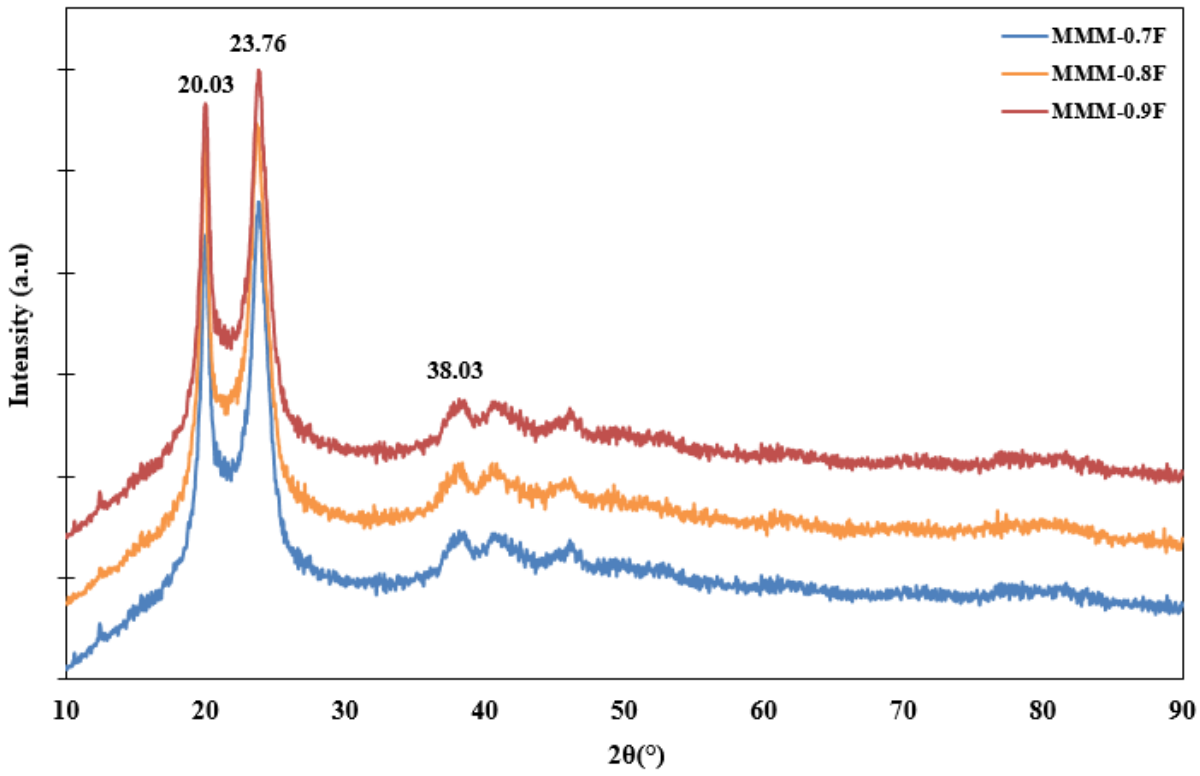

Figure 4.42 XRD patterns of (a) MMM with MWCNTs-F at loading of 0.7 wt % (MMM-0.7F), (b) MMM with MWCNTs-F at loading of 0.8 wt % (MMM-0.8F), and (c) MMM with MWCNTs-F at loading of 0.9 wt % (MMM-0.9F) fabricated at casting thickness of 250 µm and 5 min solvent evaporation time

Table 4.3 Scattering angles (2θ) of the main diffraction peaks for MMM-0.7F, MMM-0.8F, and MMM-0.9F with corresponding inter-planar distances (*d*-spacing)

	MMM-0.7F		MMM-0.8F		MMM-0.9F	
Peaks	2θ (°)	*d*-spacing	2θ (°)	*d*-spacing	2θ (°)	*d*-spacing
1	20.03	4.47	20.03	4.25	20.03	4.43
2	23.76	3.87	23.76	3.84	23.76	3.75
3	38.03	2.43	38.03	2.42	38.03	2.37

Moreover, thermal properties of MMMs were studied by Differential scanning Calorimetry (DSC) analysis to characterize the MMM morphology and permeation properties. Since, the crystallization properties of membrane is a significant parameter that affects the gas transport properties, due to the fact that the crystallized region can acts as impermeable barrier for gas permeation (Zhang et al., 2019). The glass transition temperature (T_g) of MMMs are tabulated in **Table 4.4**. By increasing the loadings of MWCNTs-F from 0.7 to 0.8 wt%, the T_g value increased to higher temperature from 140.56 (MMM-0.7F) to 142.63°C (MMM-0.8F). This increment of T_g for MMM-0.7F to MMM0.8F demonstrated the changes of chain mobility and the dynamics of polymer chains in the membrane structure. This phenomena can be explained by the incorporation of addition MWCNTs-F that leads to the increases of phase separation for MMM-0.8F, due to more vigorous interaction between MWCNTs-F with the ether groups in the soft segment of CAB matrix that causes the decreases of chain mobility in the soft segment (Molki et al., 2018). The decreased of chain mobility is usually accompanied by the increased of physical linkage between the hard and soft segments of the membrane, which in turn limits the movement of polymer chains and resulted higher T_g in the soft segment (Fakhar et al., 2019). The increment of T_g also indicate the good interaction between the dispersed (MWCNTs-F) and continuous phases (CAB matrix) of MMM-0.8F (Benes and Vankelecom 2019). However, increasing the loadings of MWCNTs-F further to 0.9 wt%, the T_g decreased from 142.63 (MMM-0.8F) to 132.60 °C (MMM-0.9F). The decrease of T_g is subsequently due to the formation of hydrogen bonding between the MWCNTs-F and soft

segment of polymer matrix, since the MWCNTs-F is mainly consists of hydroxyl group, and this can counteracts the phase separation leading to high chain mobility (Molki et al., 2018). Consequently, due to the high chain mobility it decreased the phase separation of polymer matrix, and leads to high crystallinity in the soft segment of MMM-0.9F. As a results, the dispersion of MWCNTs-F in MMM-0.9F is deprived due to the low mobility of MWCNTs-F within the polymer matrix (Fakhar et al., 2019).

Table 4.4 Glass transition temperature of MMM at different loadings of MWCNTs-F

Membrane	Tg (°C)
MMM-0.7F	140.56
MMM-0.8F	142.63
MMM-0.9F	132.60

4.3.1 Robeson's Chart

As the membranes are exposed to trade-off between selectivity and permeability, the Robeson's trade-off chart was used to provide guidance in evaluating the practicability of membrane as well as to assess membrane separation performance (Robeson, 2008). As shown in **Figure 4.43**, the best MMMs was MMM-0.8F with a CO_2 permeance of 3776 ± 1.20 Barrer and a selectivity of 13.17 ± 1.39. As revealed in **Figure 4.43**, the separation performances of MMM-0.8F synthesised in this present work are quite far from the Robeson's trade-off curve. Meanwhile, comparing the separation performance of MMM-0.8F with other research works, the selectivity performance of the current membrane is relatively lower than the others (Sun et al., 2017, Ahmad et al., 2014, Cong et al., 2007). Therefore, there is a need to further improve the current MMM-0.8F selectivity performance for achieving excellent gas separation performance.

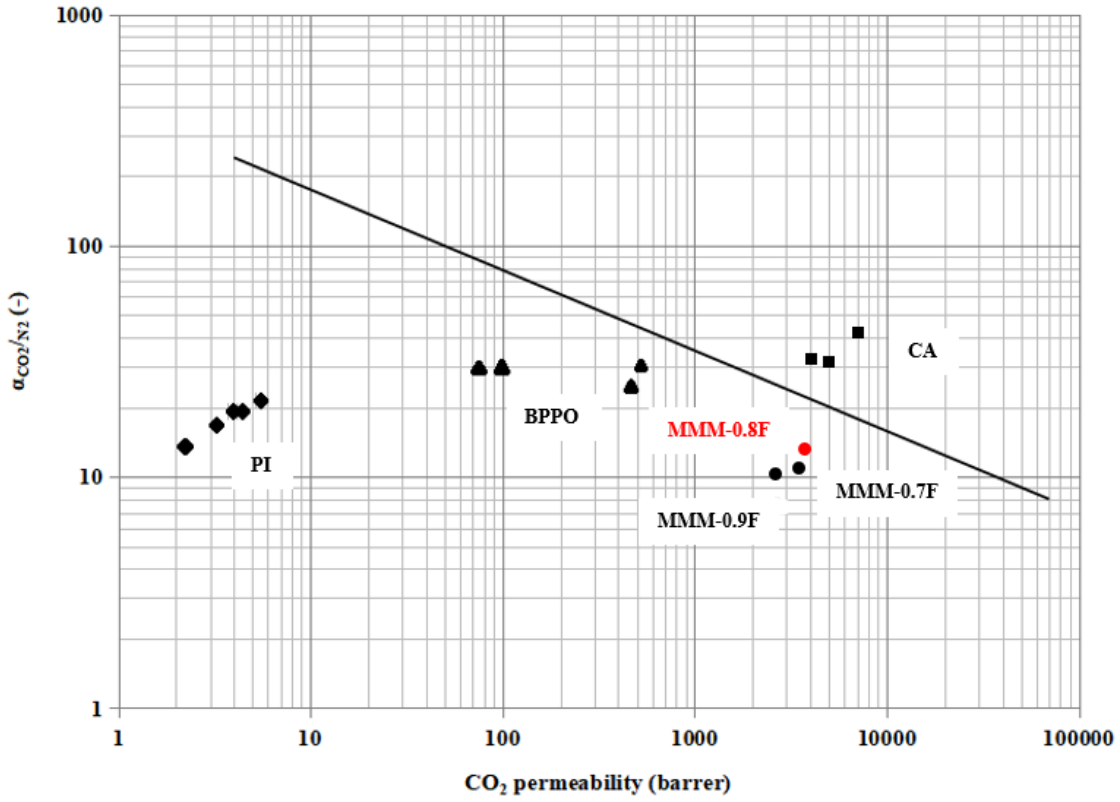

Figure 4.43 CO_2/N_2 separation performance on Robeson's 2008 upper bound chart (Robeson 2008) for MMM synthesised at different loadings of MWCNTs-F, 0.7 wt% (MMM-0.7F), 0.8 wt% (MMM-0.8F), and 0.9 wt% (MMM-0.9F) at casting thickness of 250 µm and 5 min solvent evaporation time

4.4 Effect of molecular weight combination on blend mixed matrix membrane

Based on the moderate separation performance demonstrated by MMM-0.8F. The improvement of MMM-0.8F selectivity towards a higher value is necessary to achieve better CO_2/N_2 separation performance. For this reason, blend MMM is synthesize with different molecular weight (*Mn*) of CAB polymers to enhance the CO_2 permeance and separation performance of the MMM-0.8F. The blend MMMs were synthesised based on the CAB polymers *Mn* combination of 70000:12000 (M1), 70000:30000 (M2), and 70000:65000 (M3) with a constant 0.8wt% loading of MWCNTs-F for all blend MMMs. Due to the different of combination in *Mn*, the functional groups composition of the blend MMM can affect the

membrane morphology and also the gas permeance, based on the enhance functional groups properties that would effectively facilitate CO_2 sorption in the membrane.

The blend MMMs M1 and M2 demonstrated a smooth surface in **Figure 4.44a** and **c**, which is in contrast to M3 (**Figure 4.44e**). The smooth surface of blend MMMs M1 and M2 was subsequently a result of blending lower molecular weight CAB polymer in the blend MMMs, which give the blend MMM lower chain mobility and eventually allow the formation of smooth and uniform surface due to the flexibility of polymer chain packing interaction (Kim et al., 2007; Ma et al., 2007). Nevertheless, based on the combination of CAB polymers in M1 and M2, also proved to improve the polymer-particle interactions due to the lower *Mn* applied which improve the flexibility movement of CAB polymer chain due to lower chain mobility originated from the CAB polymer chains (Wang et al., 2014). Therefore, a smooth and defect free surface was formed. Meanwhile, M3 (**Figure 4.44f**) demonstrated a thick membrane (9.80 ± 3.75 μm) morphology, as compared to the M2 (8.45 ± 1.32 μm) and M1 (8.34 ± 1.02 μm). The thick membrane thickness of M3 was because of the high *Mn* CAB polymer blend combination used in the membrane synthesis, this causes greater polymer chain packing within the blend MMM due to the high chain mobility (Sahoo et al., 2010). When M3 has high chain mobility, it inhibits movement of the polymer chain and favour the attachment of polymer chains within the MMM (Wang et al., 2014). Consequently, resulting the thick membrane (9.80 ± 3.75 μm) structure for M3.

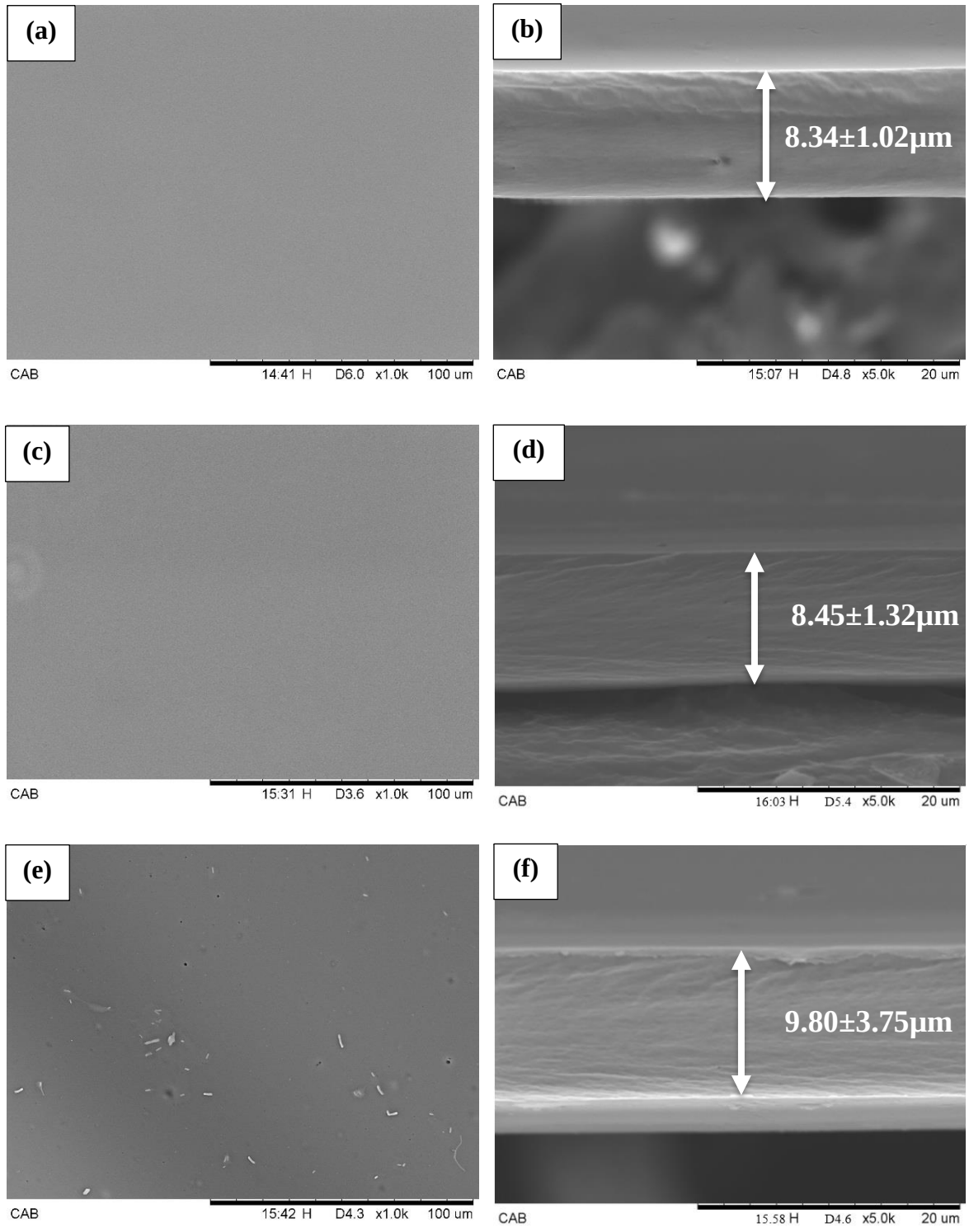

Figure 4.44 Surface and cross-sectional SEM of blend MMMs synthesised at different molecular weight CAB combinations, (a-b) 70000:12000 (M1), (c-d) 70000:30000 (M2), and (e-f) 70000:65000 (M3) with MWCNTs-F loadings of 0.8 wt%, at casting thickness of 250 µm and 5 min solvent evaporation time

In addition, the blend MMMs were further described with the characterisation of XRD. The XRD pattern of the M1 (*Mn* of 70000:12000), M2 (*Mn* of 70000:30000), and M3 (*Mn* of 70000:65000) are represented in **Figure 4.45** with the diffraction peaks tabulated in **Table 4.5**. The intensity curve for blend MMM (M2) shows slightly higher peaks than M1 and M3. This was due to the incorporation of additional CAB polymer (*Mn* of 30000) into the polymer matrix, which increases the crystallinity of CAB phases (Wang et al., 2014). Meanwhile, the decrease of intensity peaks for M3 also indicating that highly disordered nanotubes are structurally developed into high crystalline nanotubes (Kim et al., 2005). The *d*-spacing reduced from M3> M2> M1 when lower *Mn* blend combination was used as shown in **Table 4.5**, this decrement was due to the incorporation of blending low *Mn* CAB polymer, that decreased the crystallinity peaks based on the lower intensity of the CAB functional groups. Moreover, the shifts of *d*-spacing to lower values also indicate the decrease in intersegmental spacing which is anticipated to create more adsorption sites between the polymer chains and enhance the permeance of the blend MMM (Xiang et al., 2016, Isanejad and Mohammadi 2018).

Moreover, the T_g of blend MMMs were studied to explain the blend MMMs characterisation structure. The T_g results of blend MMMs were tabulated in **Table 4.6**. Based on the T_g value of M1 (163.44°C) and M2 (181.27°C), the increment of T_g for M2 was mainly contributed by the restrictions of polymer chains movement attributed by favourable interfacial interaction between CAB polymer blend (*Mn* of 30000:70000). In other words, when higher *Mn* of CAB polymer (*Mn* of 30000) was blend in M2 as compared to M1 (*Mn* of 12000), it restricts the rotation of polymer chains and increase the chain rigidity of the blend MMM, which as a result affects the characteristics of continuous phase of the blend MMM (Ranjbaran et al., 2015). Based on the former studies, the increase of T_g for M2 also indicate the well dispersed

of MWCNTs-F within the CAB matrix, due to the reduction in polymer chain when high *Mn* of CAB polymer was blended it can effectively reduce the crystallinity of polymer, which is crucial for the gas separation (Zhang et al., 2019, Moon et al., 2008). In contrast, when highest *Mn* of CAB polymer was blended for M3 (*Mn* of 65000:70000), the T_g reduce from M2 (181.27°C) and M2 (131.97°C). M3 present low T_g, indicating high chain mobility of the soft segment and decreased of phase separation that is accompanied by the increment of physical linkage between the soft and hard segment within the CAB matrix (Molki et al., 2018). With the increased of physical linkage for M3, this also means the presence of less compatible soft and hard domains, where the soft domains cause an inhibiting effect on the hard domains that can hinder the solubility coefficient of M3 as illustrated in **Figure 4.52** (Fakhar et al., 2019).

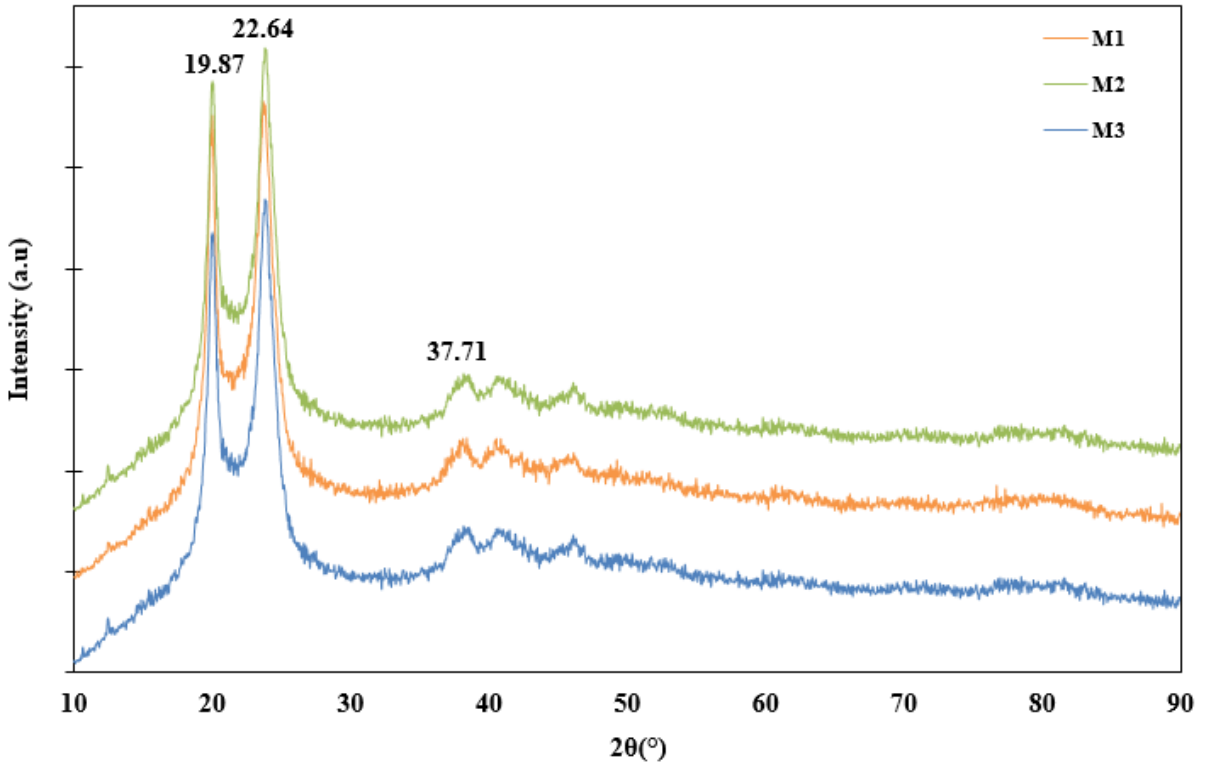

Figure 4.45 XRD curve of blend MMMs with CAB polymer molecular weight combinations of, (a) 70000:12000 (M1), (b) 70000:30000 (M2), and (c) 70000:65000 (M3) with MWCNTs-F loadings of 0.8 wt%, at casting thickness of 250 µm and 5 min solvent evaporation time

Table 4.5 Scattering angles (2θ) of the main diffraction peaks for M1, M2, and M3 with corresponding inter-planar distances (*d*-spacing)

	M1		M2		M3	
Peaks	2θ (°)	*d*-spacing	2θ (°)	*d*-spacing	2θ (°)	*d*-spacing
1	19.87	3.15	19.87	3.25	19.87	3.43
2	22.64	2.54	22.64	2.44	22.64	2.75
3	37.71	1.33	37.71	1.20	37.71	1.40

Table 4.6 Glass transition temperature (T_g) of blend MMMs

Membrane	Tg (°C)
M1	163.44
M2	181.27
M3	131.97

As shown in **Figure 4.46**, the CO_2 permeance of blend MMMs reduced from 369.56 ± 2.87 GPU (M1) to 341.15 ± 1.19 GPU (M2), and 252.63 ± 1.32 GPU (M3) with respect to each CAB polymers blend combination. Subsequently, M1 (8.45 ± 1.32 μm) and M2 (8.34 ± 1.02 μm) are able to achieve high CO_2 permeance due to the close thin membrane thickness obtained, and M3 has the lowest CO_2 permeance due to the thicker membrane (9.80 ± 3.75 μm) thickness presented. Apart from the membrane thickness, the membrane composition is another factor that can affect the CO_2 permeance result, such as blend MMMs M1 and M2 are able to attain higher CO_2 permeance than M3 was because of the low acetyl groups content present within CAB polymers. Whereby, the order of acetyl groups content range from M3 (40-46%)>M1 (28-34%)>M2 (24-30%), respectively. One of the critical factor which affect the performance of membranes is closely related to the content of acetyl functional groups, whereby lower acetyl group content would reduce the slow degradation of densely packed entanglements, consequently improve the CO_2 permeance and sorption ability of the membrane (Wong et al., 2018, Fakhar et al., 2018). Therefore, M1 and M2 are able to achieve high CO_2 permeance, while M3 has the lowest CO_2 permeance due to the highest content of acetyl group present

within the blend MMMs. Therefore, based on the concentration of acetyl functional groups, this also explained the contrasting result of the blend MMMs M1 (8.34 ± 1.02 μm) and M2 (8.45 ± 1.32 μm) that are having similar membrane thickness, but different CO_2 permeance.

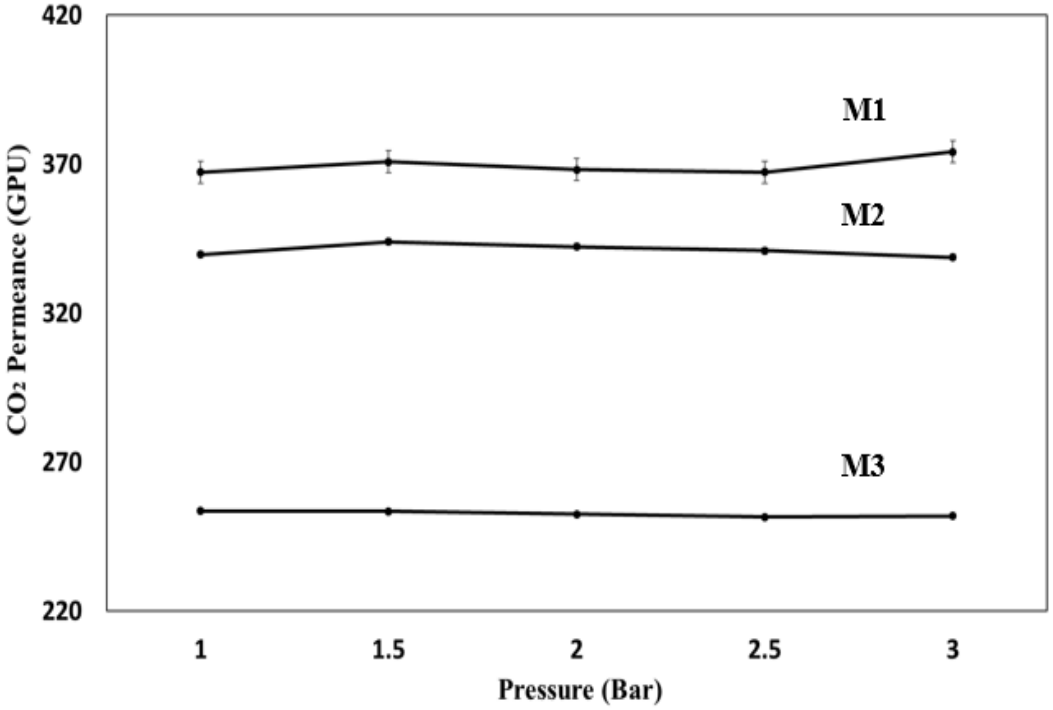

Figure 4.46 CO_2 permeance of blend MMMs synthesised at different molecular weight CAB composition, 70000:12000 (M1), 70000:30000 (M2), and 70000:65000 (M3) with MWCNTs-F loadings of 0.8 wt%, at casting thickness of 250 μm and 5 min solvent evaporation time

Consequently, the ATR FTIR analysis was carried out to describe the interaction between different *Mn* functional groups intensities based on CAB polymer combination. The prepared blend MMMs ATR-FTIR spectrum is portrayed in **Figure 4.47**. For the absorptive band at 1739 and 1035 cm^{-1} are assigned to C=O and C-O-C stretching vibrations, respectively (Xiang et al., 2016). Whereas, the characteristics peaks at 2957 and 1366 cm^{-1} are attributed by the C-H and –OH group, respectively (Wang et al., 2014). The intensity of butyryl functional group of blend MMMs were arranged in the descending order M2 (71-79 wt%)> M1 (65-74 wt%)> M3 (51.5-58 wt%).

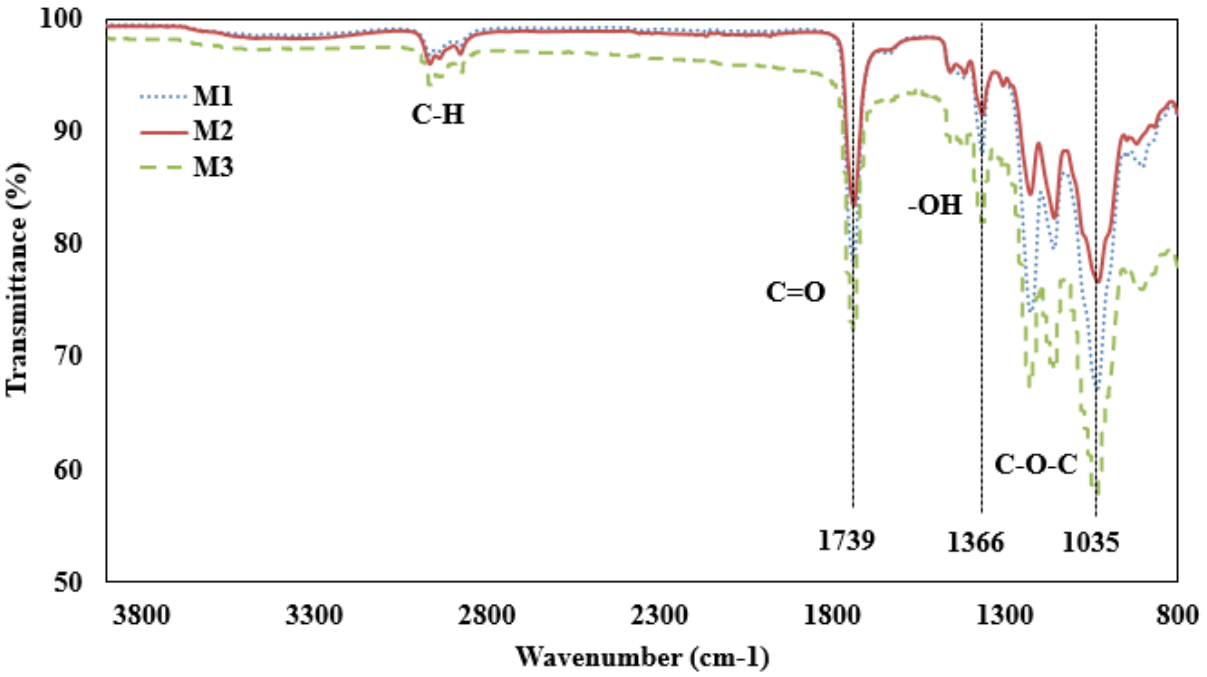

Figure 4.47 ATR FTIR spectra analysis for blend MMMs synthesised at different molecular weight CAB composition, 70000:12000 (M1), 70000:30000 (M2), and 70000:65000 (M3) with MWCNTs-F loadings of 0.8 wt%, at casting thickness of 250 µm and 5 min solvent evaporation time

As shown in **Figure 4.47**, the peak intensity of absorptive band at 1739 cm^{-1} (C=O) and 1035 cm^{-1} (C-O-C) was the lowest for M3, this was attributed by the low butyryl functional group content (51.5-58 wt%) found for M3 when high *Mn* CAB polymers combination (*Mn* of 70000:65000) was used for M3 (Xing et al., 2013). Consequently, the absorptive band at 1739 cm^{-1} (C=O) and 1035 cm^{-1} (C-O-C) increased for M1 (65-74 wt%) and M2 (71-79 wt%) was due to the higher butyryl functional group content found from the CAB polymers combination of M1 (*Mn* of 70000:12000) and M2 (*Mn* of 70000:30000) (Xing et al., 2013). Meanwhile, the frequency of vibration band at 2957 (C-H) and 1366 cm^{-1} (–OH) are the highest for M2 was correspond to the low acetyl functional group content (24-30 wt%) exist within the blend MMM (Sobral et al., 2008). Followed by M1 with an acetyl content of 28-34 wt%, and M3 with an acetyl content of 40-46 wt% (Sobral et al., 2008). The shift of frequency intensity for C-H and –OH group was corresponding to the formation of hydrogen bond between the acetyl group and

hydroxyl group due to the reaction of oxidation-reduction during the mixing dope solution (Xiang et al., 2016).

The N_2 permeance for blend MMMs are illustrated in **Figure 4.48**. The N_2 permeance for M1, M2, and M3 were 23.14 ± 2.14, 20.35 ± 1.71, and 18.23 ± 0.08GPU, respectively. The N_2 permeance of M2 decreased when higher *Mn* of CAB polymer was blended with CAB-70000. The reduction of N_2 permeance for M2 is correlated to the high intensity of carboxyl group (C=O) contents presented M2 and M3 which favour the absorption of CO_2 and reject N_2 (Sakakura et al., 2007). As the C=O group can act as non-ionic CO_2 carriers through covalently connected to cellulose chains and ease CO_2 transport, as a result it hinders the N_2 permeance (Zhang et al., 2018). Moreover, the functional groups of C=O can provide more CO_2 adsorption sites and thus, increasing the affinity toward CO_2, while permit less N_2 permeance due to low C=O content contained (Zhang et al., 2018, Shan et al., 2012).

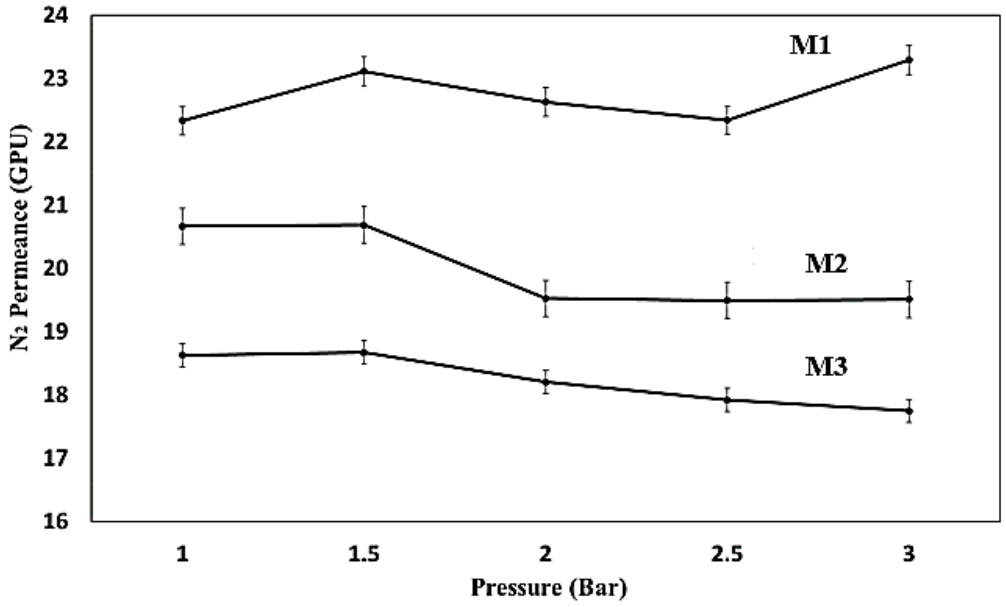

Figure 4.48 N_2 permeance of blend MMMs synthesised at different molecular weight CAB composition, 70000:12000 (M1), 70000:30000 (M2), and 70000:65000 (M3) with MWCNTs-F loadings of 0.8 wt%, at casting thickness of 250 µm and 5 min solvent evaporation time

Contact angle analysis was conducted to further explain the phenomena of N_2 permeance. The contact angle for M1 (67.7˚ ± 0.5˚), M2 (64.6˚ ± 0.4˚), and M3 (70.4˚ ± 0.1˚) was presented in **Figure 4.49**. The reduction of contact angle for M1 (*Mn* of 70000:12000) to M2 (*Mn* of 70000:30000) was due to the polymers combination with higher carboxyl groups content as illustrated in **Figure 4.49**, which make the membrane more hydrophilic (Rahimpour et al., 2012). This can be explained by incorporating higher carboxyl group content polymer into M2, the membrane surface hydrophilicity is enhanced due to the end group of –COOH in CAB polymer do not form hydrogen bond between polymer chains, thus the membrane become more hydrophilic in nature when less hydrogen bond was formed (Wang et al., 2014, Del Valle. 2004, Ahmad et al., 2013).

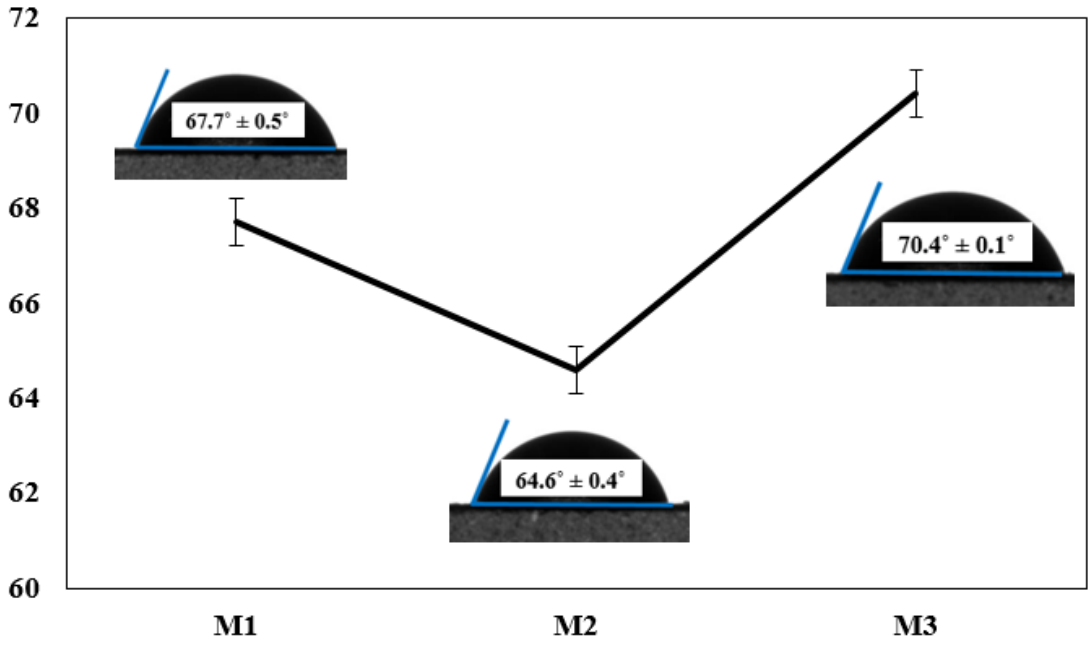

Figure 4.49 Contact angle of blend MMMs synthesised at different molecular weight CAB composition, (a) 70000:12000 (M1), (b) 70000:30000 (M2), and (c) 70000:65000 (M3) with MWCNTs-F loadings of 0.8 wt%, at casting thickness of 250 µm and 5 min solvent evaporation time

Meanwhile, blending lower carboxyl group content polymer into M3 (*Mn* of 70000:65000) polymer matrix, the membrane surface hydrophilicity is reduced due to the lower presence of the carboxyl groups originating from CAB polymer. Polar functional groups such as carboxyl group, tend to have high affinity towards non-polar gas compound CO_2 instead of polar gas N_2 (Shan et al., 2012). Therefore, the N_2 permeance reduced when lower carboxyl content CAB polymer (*Mn* of 12000 and *Mn* of 65000) was blended into M1 and M3.

The selectivity performance the blend MMMs are summarized in **Figure 4.50**. According to **Figure 4.50**, M2 demonstrated the highest selectivity (17.09 ± 1.29) followed by M1 (16.25 ± 2.97) then M3 (13.86 ± 1.40). The high selectivity performance yield for M1 and M2, correspond to the adding of low *Mn* CAB polymers *Mn* of 12000 (M1) and CAB 30000 (M2) into M1 (16.25 ± 2.97) and M2 (17.09 ± 1.29) which greatly improved the CO_2 permeance. As mentioned previously, lower acetyl group content would reduce the slow loosening of densely packed entanglements, therefore ensure the smooth sorption of gas molecules within the blend MMM. Thus, the permeance and solubility coefficients of the blend MMM is enhanced (Wong et al., 2018, Fakhar et al., 2018). Consequently, M3 (13.86 ± 1.40) has the lowest selectivity, due to the increased of electrostatic interactions between the polymer chains when high *Mn* polymer (*Mn* of 65000) was substituted within the ionic domains and leading to a lower CO_2 permeance caused by the stacking of polymer chains that disrupt the permeance of gas molecules within the blend MMM (Dai et al., 2018). The slight reduction of selectivity performance for M2 to M1 was caused by the insignificant increment of CO_2 permeance due to the increased of contact angle by 0.3° (**Figure 4.49**) that caused a small reduction in the CO_2-philic groups of M1. Therefore, M1 is able to hold the CO_2 molecules stronger within the blend MMM, and result the small reduction of CO_2 permeance as indicated in **Figure 4.46**.

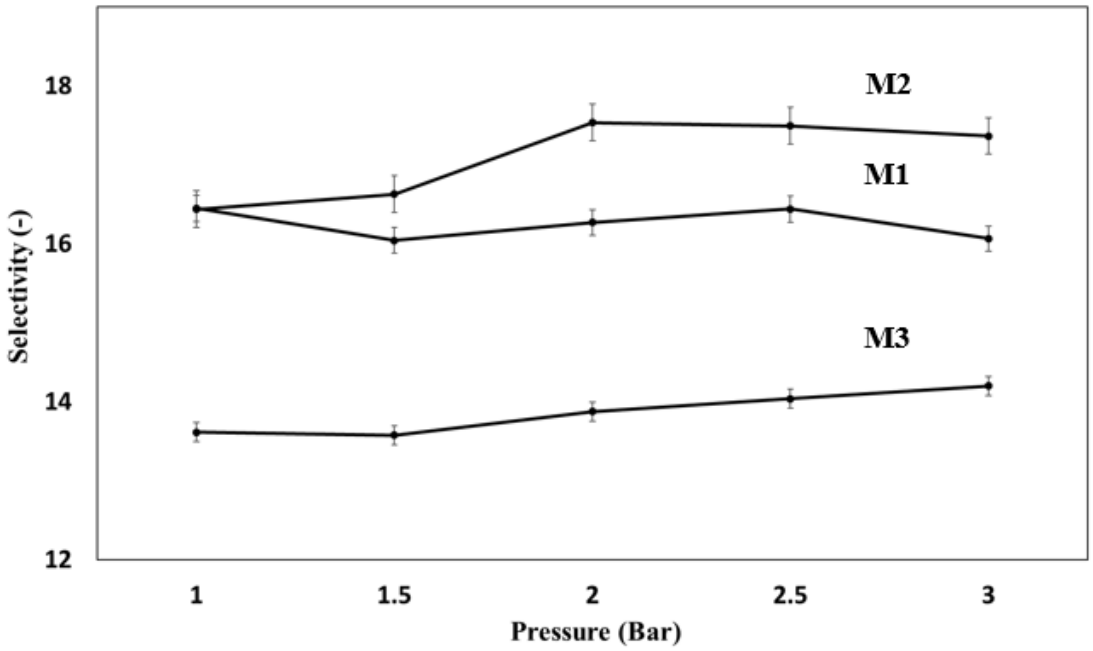

Figure 4.50 Ideal selectivity of blend MMMs synthesised at different molecular weight CAB composition, 70000:12000 (M1), 70000:30000 (M2), and 70000:65000 (M3) with MWCNTs-F loadings of 0.8 wt%, at casting thickness of 250 µm and 5 min solvent evaporation time

4.5 Kinetic sorption study on blend mixed matrix membranes

The transport phenomenon of gases through blend MMMs were studied with the evaluation of kinetic coefficient of the membranes, since the transport mechanism for dense membrane is governed by solution diffusion mechanism (Wang et al., 2014). Whereby, the two important parameters were determined in the kinetic sorption study were the solubility and diffusion rates through the dense blend MMM. According to the solution-diffusion model, the solution coefficient of the membrane was governed by the condensability of gas molecules, while the diffusion coefficient is mainly influenced by kinetic diameter of gas molecules (Wang et al., 2014).

As illustrated in **Figure 4.51**, was the CO_2 kinetic sorption curve for blend MMMs. It was observed that the M1 acquired the shortest time (2.01 $sec^{0.5}$/µm) to reach the equilibrium time

of CO_2 sorption, followed by M2 (2.25 $sec^{0.5}/\mu m$), and then M3 (2.39 $sec^{0.5}/\mu m$). The resulting pattern of the kinetic sorption curve was subsequently a results of the interaction between the acetyl functional groups with the non-polar CO_2 penetrant. The order of acetyl groups for the synthesised blend MMMs were M3 (40-46 wt%)>M1 (30-34 wt%)>M2 (24-30 wt%). As M1 (30-34 wt%) and M2 (24-30 wt%) contained lower acetyl functional groups compared to M3 (40-46 wt %) within the polymer matrix, this allowed more intra and intermolecular interactions to occur within the blend MMM, hence, enhance the CO_2 sorption capacity of the blend MMM allowing more CO_2 molecules to pass through the blend MMM (Kunthadong et al., 2015).

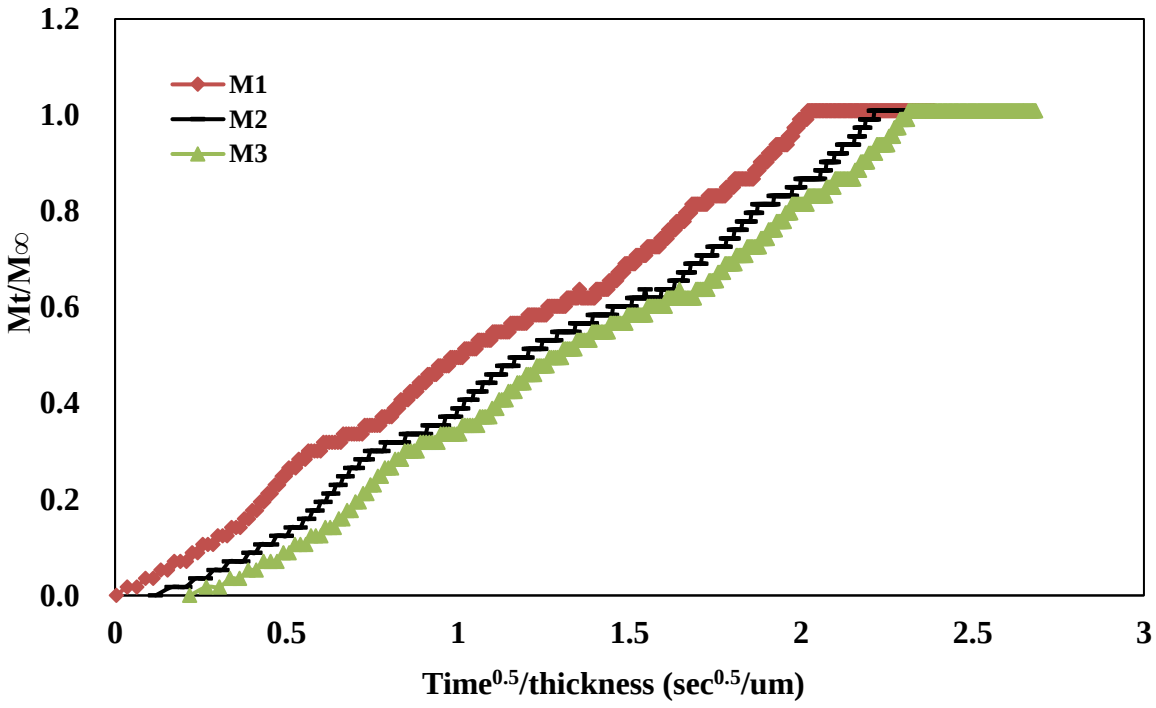

Figure 4.51 CO_2 kinetic sorption curve for blend MMMs synthesised at different molecular weight CAB composition, 70000:12000 (M1), 70000:30000 (M2), and 70000:65000 (M3) with MWCNTs-F loadings of 0.8 wt%, at casting thickness of 250 µm and 5 min solvent evaporation time

In addition, M2 has the highest butyryl group composition (71-79 wt %), followed by M1 (65-74 wt%), then M3 (51.5-58 wt%) presented within the blend MMMs. The butyryl group is able to improve and expand the capacity of CAB chain and leads to high CO_2 permeance due to the increased of mass transfer efficiency (Basu et al., 2010). Meanwhile, M3 took the longest duration (2.39 $sec^{0.5}/\mu m$) to reach the CO_2 equilibrium time, this was subsequently a result attributed by the high acetyl (40-46 wt%) and low butyryl (65-74 wt%) contents presented within the blend MMMs itself that limit the capacity of the membrane chain spacing and leads to low CO_2 sorption caused by lower mass transfer efficiency (Kunthadong et al., 2015, Basu et al., 2010, Wang et al., 2014).

As presented in **Table 4.7**, was the results of CO_2 diffusivity coefficient for blend MMMs with different CAB polymer combinations. The CO_2 diffusivity coefficient achieved for M1 was $4.0x10^{-11}$ cm^2/s, while for M2 was $4.5x10^{-11}$ cm^2/s, and M3 was $7.0x10^{-11}$ cm^2/s. Based on the tabulated data in **Table 3.11**, the blend polymers *Mn* combination are expected to be the main factor that regulate the CO_2 sorption coefficients (Wang et al., 2014). For blend MMM fabricated with high *Mn* CAB, this caused the decrease of chain spacing that can effectively inhibit the solution diffusion ability due to the decrement of mass transfer efficiency, hence reducing the CO_2 sorption (Wang et al., 2014). Since M3 (*Mn* of 70000:65000) has the highest molecular weight CAB combination, the diffusivity was the highest, then followed by M2 (*Mn* of 70000:30000), and lastly M1 (*Mn* of 70000:12000). The diffusivity coefficient corresponds to the lower amorphous fraction and shorter chain spacing along by the incorporation of high molecular weight CAB render the higher diffusivity coefficient for M3 (*Mn* of 65000) (Wang et al., 2014).

Table 4.7 CO_2 diffusivity coefficient of blend MMMs with different CAB polymer combinations

Sample	CAB combination (*Mn*)	CO_2 diffusivity coefficient (cm^2/s)
M1	70000:12000	4.0×10^{-11}
M2	70000:30000	4.5×10^{-11}
M3	70000:65000	7.0×10^{-11}

The CO_2 solubility coefficients were determined to evaluate the efficiency of CO_2 transport through the blend MMMs synthesised as represented in **Figure 4.52**. Based on **Figure 4.52**, M1 was able to achieved a CO_2 solubility coefficient of $9.24\times10^{12}\pm1.24$ cm^3 (STP)/cm^4cmHg. Subsequently, M2 with a CO_2 solubility coefficient of $7.58\times10^{12}\pm1.01$ cm^3 (STP)/cm^4cmHg, then followed by M3 with CO_2 solubility coefficient of $3.61\times10^{12}\pm0.71$ cm^3 (STP)/cm^4cmHg. According to the results in **Figure 4.52**, M1 has the highest solubility rate as compared to M2 and M3, was mainly because of the low molecular weight CAB combination within the polymer matrix that are capable to expanding the CO_2 permeate capacity due to larger chain spacing and high amorphous fraction that favour the affinity towards CO_2 in membrane hence significantly enhanced the CO_2 solubility coefficient (Bondar et al., 1999). It can be concluded that the relationship of the diffusivity coefficients and solubility coefficients is inversely proportional, because when high molecular weight CAB was incorporated into the MMM, M3 with lower amorphous fraction and packed chain spacing render higher diffusivity coefficient as tabulated in **Table 4.7**, while the decreased of amorphous fraction yield lower solubility coefficient for M3 (Wang et al., 2014). This results were similar to the trends found by several researchers, whereby the relationship between the permeability and diffusivity reduced when the membrane demonstrated high membrane solubility coefficient (Kim 2007). Therefore, it can be concluded that the CO_2 solubility coefficient is the main governing factor in the solution diffusion mechanisms for the blend MMM in term of CO_2 permeance and CO_2/N_2 selectivity.

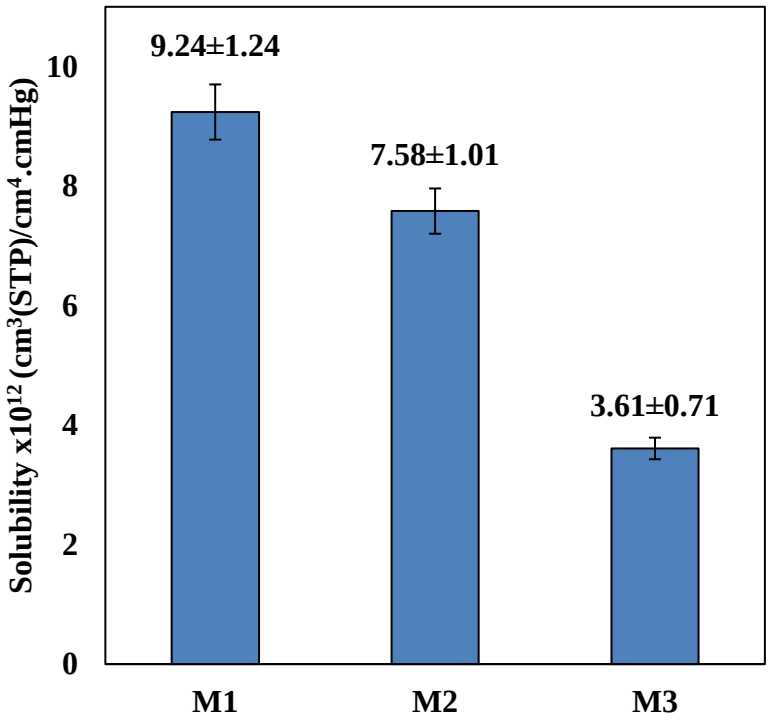

Figure 4.52 CO_2 solubility coefficient for blend MMMs synthesised at different molecular weight CAB composition, 70000:12000 (M1), 70000:30000 (M2), and 70000:65000 (M3) with MWCNTs-F loadings of 0.8 wt%, at casting thickness of 250 µm and 5 min solvent evaporation time

4.7 Robeson's Chart

Furthermore, the selectivity performance achieved from the blend MMM (M2) was then compared with the literature results to evaluate the performance of the blend MMMs fabricated in this present study. The best blend MMM (M2) shown average performance as compared to other literature blend MMMs as illustrated in **Figure 4.53** (Castro-Munoz et al., 2019, Dong et al., 2016). In this study, the main challenge is to synthesize a novel blend MMM by incorporating two different *Mn* CAB polymers with filler MWCNTs-F within the polymer matrix. It can be seen that the selectivity of M2 is much closer to the Robeson's upper bound in this work. In the current work, the excellent CO_2/N_2 selectivity can be achieved by blend the CAB *Mn* of 70000:30000 (2:1) with 0.8 wt% of MWCNTs-F.

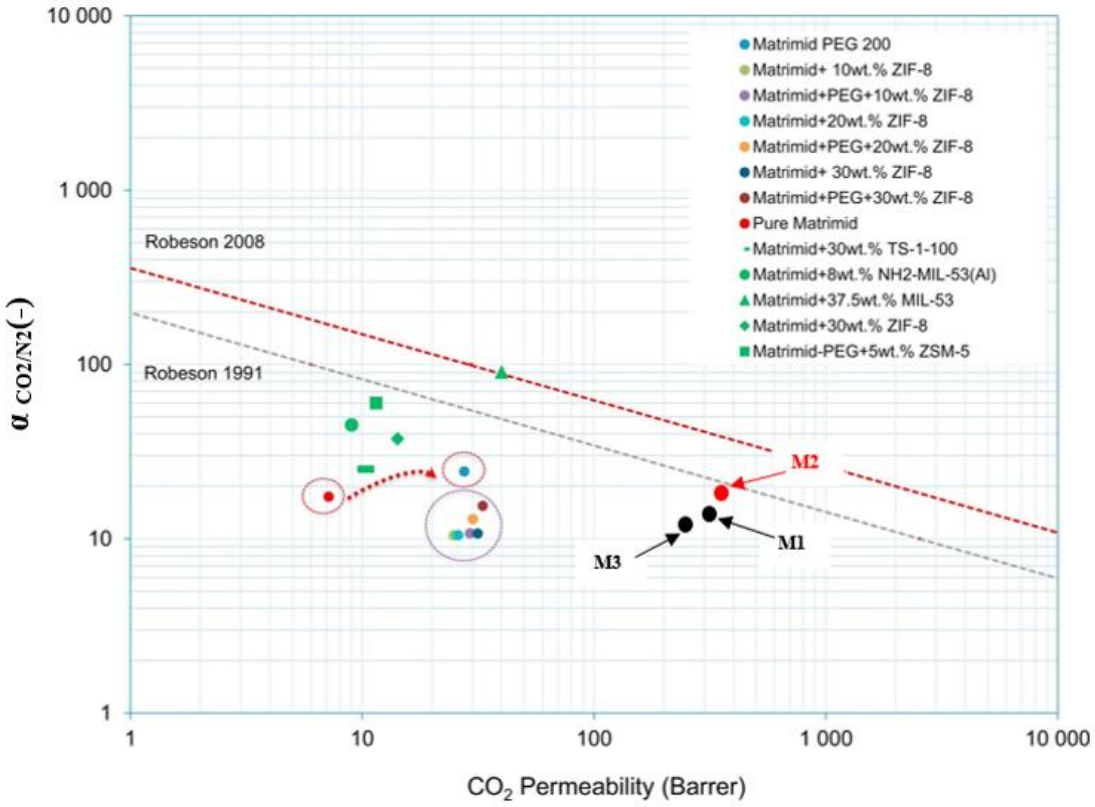

Figure 4.53 CO_2/N_2 separation performance on Robeson's 2008 upper bound chart (Robeson 2008) for blend MMMs synthesised at different molecular weight CAB composition, 70000:12000 (M1), 70000:30000 (M2), and 70000:65000 (M3) with MWCNTs-F loadings of 0.8 wt%, at casting thickness of 250 µm and 5 min solvent evaporation time

4.8 Binary gas permeation study

Binary gas permeation study was further carried out to evaluate the effect polymer combination on the mass transport between two penetrant gas molecules, which are the gas permeance and selectivity of the blend MMM (Wang et al., 2014). The mass transport of the blend MMM was evaluated with several CO_2 feed compositions. The selected CO_2 feed compositions were 20 vol%, 40 vol%, 50 vol%, 60 vol%, and 80 vol% as showed in **Figure 4.54**. In order to determine that the M2 is the best membrane, the binary gas permeation results was compared with M1 and M3. According to **Figure 4.54**, when the CO_2 feed composition increased from 20 vol% to 80 vol%, the CO_2 permeance increased from 26.44 ± 0.51 to 87.95 ± 2.43 GPU for M1, 26.40 ± 0.28 to 89.74 ± 2.66 GPU for M2, and 26.44 ± 0.46 to 87.96 ±

2.51 GPU for M3. This trend of increment for CO_2 permeance of CO_2/N_2 binary gas mixtures was attributed by the increase of feed concentration in CO_2 gas molecules of the binary gas mixture. Hence, increasing the CO_2 permeance within the blend MMMs. In addition, the blend MMMs mass transport mechanism main transport mechanism is solution diffusion. For solution diffusion mechanism, the solution coefficient mainly depends on the condensability of the penetrants gas molecules dissolve into membrane material according to the concentration gradient (Wang et al., 2014).

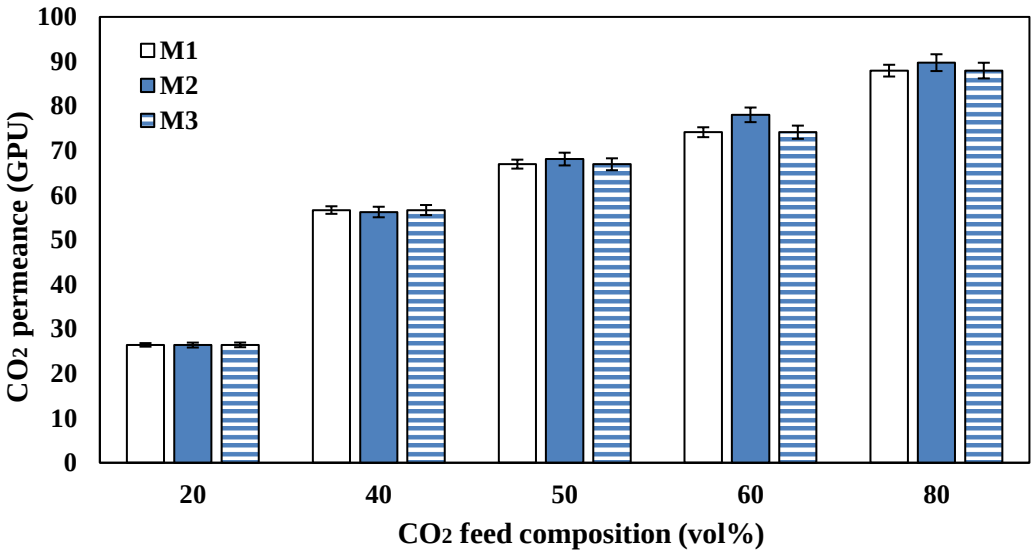

Figure 4.54 CO_2 permeance of binary CO_2/N_2 composition for blend MMMs synthesised at different molecular weight CAB composition, 70000:12000 (M1), 70000:30000 (M2), and 70000:65000 (M3) with MWCNTs-F loadings of 0.8 wt%, at casting thickness of 250 µm and 5 min solvent evaporation time

Meanwhile, **Figure 4.55** illustrated the N_2 feed composition at 20 vol%, 40 vol%, 50 vol%, 60 vol%, and 80 vol% for the CO_2/N_2 binary gas mixture. When the N_2 feed composition increased from 20 vol% to 80 vol%, the N_2 permeance also increased from 3.72 ± 0.71 to 12.55 ± 1.40 GPU for M1, 4.40 ± 0.24 to 12.82 ± 1.51 GPU for M2, and 4.99 ± 0.13 to 17.6 ± 2.12 for M3. The increased of N_2 permeance for the blend MMMs was due to the permeance increase of CO_2 within the membrane structure. Furthermore, lower permeance values were obtained for

N_2 permeance this was due to the coupling effect of CO_2 that restrict the passage of N_2 within the membrane (Perez et al., 2009). Eventually, when higher CO_2 and lower N_2 binary gas mixture was used, the coupling effect favour more of the CO_2 penetrant to dissolve through the membrane while retaining more of the N_2 molecules in the feed (Perez et al., 2009). The coupling effect is the sorption competitive due to two or more different gas molecules that exist within the membrane (Perez et al., 2009).

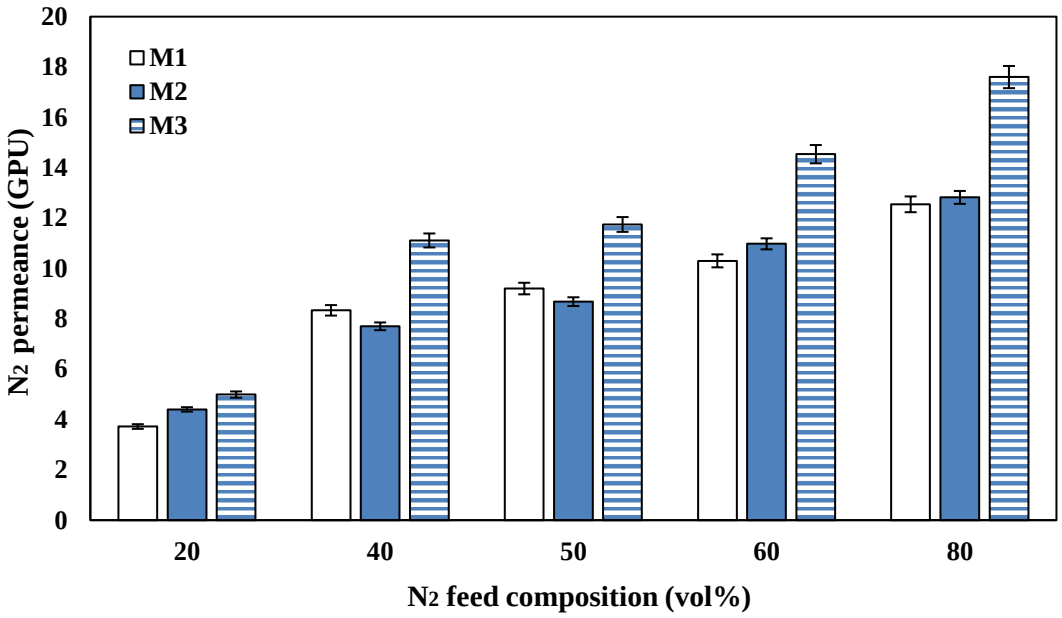

Figure 4.55 N_2 permeance of binary CO_2/N_2 composition for blend MMMs synthesised at different molecular weight CAB composition, 70000:12000 (M1), 70000:30000 (M2), and 70000:65000 (M3) with MWCNTs-F loadings of 0.8 wt%, at casting thickness of 250 µm and 5 min solvent evaporation time

The binary gas selectivity performance of the synthesised blend MMMs were then evaluated at a ratio of 50/50 vol% (CO_2/N_2). This binary gas ratio was utilized in this performance evaluation as it should reflect the real separation performance when the blend MMM is expose to the industrial condition at the feed ratio of 0.5:0.5 for CO_2/N_2 (Castro-Munoz et al., 2019, Chua et al., 2011, Zhang et al., 2016). According to **Figure 4.56**, the composition selectivity achieved for M1 is 7.28 ± 1.65, M2 with 7.85 ± 1.48, and M3 with 5.70 ± 1.18. By comparing the composition selectivity with the ideal selectivity (**Figure 4.50**) for

each blend MMM, the selectivity of binary gas mixture was lower than that of the pure single gas ideal selectivity. This was attributed by the reduction in CO_2 permeance due to the competitive permeation between the penetrant gases both N_2 and CO_2 within the polymer matrix, according to the principle of solution-diffusion mechanism (Wang et al., 2018). The lower selectivity achieved from the binary gas permeation as compared to ideal selectivity was identical with the literatures (Wang et al., 2014, Cakal et al., 2012). This was because of the overall selectivity for binary gas composition was pretentious by the penetrate molecules, mixed gas phase contrasts, and gas polarization (Amooghin et al., 2018).

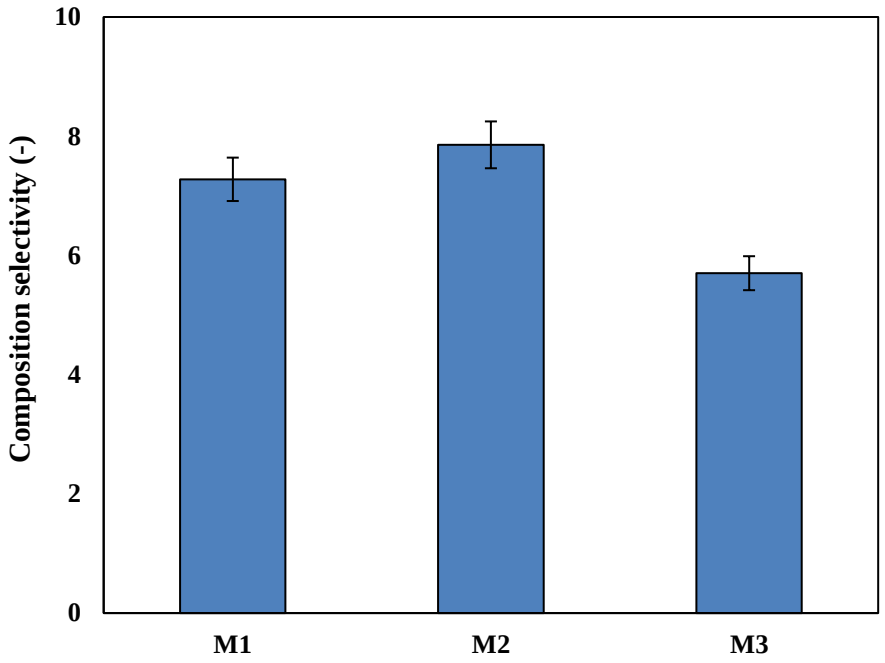

Figure 4.56 Blend MMMs selectivity with feed composition of 50:50 (CO_2/N_2) synthesised at different molecular weight CAB composition, 70000:12000 (M1), 70000:30000 (M2), and 70000:65000 (M3) with MWCNTs-F loadings of 0.8 wt%, at casting thickness of 250 µm and 5 min solvent evaporation time

The binary gas permeation of the blend MMMs in this present study was then compared with the published works, as tabulated in **Table 4.8**. It was found out that both the CO_2 permeance (67.12 ± 0.34 GPU) and binary gas selectivity (7.85 ± 1.48) of the M2 in the present

work was higher than the research work of others (Zhang et al., 2016, Wang et al., 2014). The results of M2 further proved that the newly synthesised membrane have strong interaction and was compatible with the polymer combination used according to industrial condition mention which is at the feed ratio of 50/50 vol% (Zhang et al., 2016). Hence, the findings of this present work can provide the opportunity to be applied in the industrial for the CO_2 separation targeted towards flue gas combustion and emission.

Table 4.8 Comparison of blend MMMs binary gas permeation with other published works

Sample	Fillers	CO_2/N_2 ratio	P (CO_2)	Selectivity	Conditions	Ref
CAB	MWCNTs-F					
M1	0.8 wt%	1.0/0	3695.6 ± 2.87[a]	16.25 ± 2.97	1-3x10^5 Pa, 250µm	Present work
		0.5/0.5	671.2 ± 0.34[a]	7.28 ± 1.65		
M2		1.0/0	3411.5 ± 1.19[a]	17.09 ± 1.29		
		0.5/0.5	671.2 ± 0.34[a]	7.85 ± 1.48		
M3		1.0/0	2526.3 ± 1.32[a]	13.86 ± 1.40		
		0.5/0.5	671.2 ± 0.34[a]	5.70 ± 1.18		
Pebax	CNTs	0.5	56.7 [a]	7.0	70-90 µm, 2 atm, 25°C	(Zhang et al., 2016)
PEG (*Mn*)	MWCNTs					
400	0.0 wt%	0.5	3.45[a]	1.70	80-100 µm, 2 atm, 25°C	(Wang et al., 2014)
600			3.56[a]	1.68		
2000			0.98[a]	2.17		
20000			0.96[a]	2.74		
400	2.0 wt%	0.5	3.65[a]	1.55		
600			3.64 [a]	1.68		
2000			1.11 [a]	2.13		
20000			1.02 [a]	2.27		

CAB- cellulose acetate butyrate, PEG- poly (ethylene glycol), MWCNTs-multi-walled carbon nanotubes

[a] Barrer. N/A- not available.

CHAPTER FIVE

CONCLUSIONS AND FUTURE RESEARCH DIRECTIONS

5.1 Conclusion

In this research study, the primary aim was to synthesise a blend mixed matrix membrane (MMM) to achieve high CO_2/N_2 gas separation. Referring to the first objective of this research study, the work focused on synthesising a polymeric CAB membrane. The results demonstrated that each of the membrane fabrication parameters, which included membrane polymer concentration, casting thickness and solvent evaporation time played a crucial role in determining the CAB polymer matrix's morphology and physical structure, which eventually affected the membrane separation performances. Thereafter, the neat polymeric CAB membrane was investigated based on the effects of solvent exchange drying method utilising both solvents, which were isopropyl alcohol and n-hexane. The outcome of the results demonstrated that solvent exchange duration of 30 minutes for solvent exchange between isopropyl alcohol and n-hexane was the best duration for high CO_2/N_2 separation. The CAB membrane designated as CAB-30H (4 wt % CAB polymer concentration, 250 µm casting thickness, 5 minutes solvent evaporation time and 30 minutes solvent-exchange duration method) offered a dense and smoother surface membrane morphology. Eventually, this contributed to the high permeance rates (CO_2: 227.95 ± 0.39 GPU, N_2: 37.28 ± 0.54 GPU) and a separation selectivity of 6.12 ± 0.09. In addition, the effect of CAB molecular weight (*Mn*) was determined using the preparation method of CAB-30H to synthesise the polymeric CAB membrane at different *Mn* for the evaluation of CO_2/N_2 separation performance. According to the experimental and characterisation results, membrane synthesised at *Mn* of 70000 (CAB-70000) presented the highest separation results compared to CAB-12000 and CAB-65000. In this study, CAB-70000 was able to achieve good CO_2 permeance (CO_2: 227.95 ± 0.39 GPU)

and selectivity results (6.12 ± 0.09). This was mainly due to the high molecular weight CAB polymer applied, which favoured the formation of defect-free and dense membrane morphology during membrane fabrication. Hence, the casting formula for CAB-70000 was selected to further develop MMM by incorporating the functionalised-MWCNTs (MWCNTs-F) with the CAB polymer matrix.

During the development of the MMM, it was first incorporated with pristine-MWCNTs (MWCNTs-P) and MWCNTs-F into the CAB polymeric matrix to investigate the compatibility between the CAB polymer with MWCNTs-P and MWCNTs-F. The results illustrated that MMM incorporated with MWCNTs-F (MMM-1.0F) demonstrated better CO_2 permeance (291.64 ± 1.02 GPU) and a selectivity of 12.57 ± 1.19. This was subsequently due to less formation of clusters and that the hydroxyl (-OH) functional group originating from β-CD, interacted well with non-polar gas (CO_2). Furthermore, experimental work was carried out on finding the optimal loadings of MWCNTS-F integrated into the CAB polymer matrix. At a loading of 0.8 wt% MWCNTs-F, the MMM (MMM-0.8F) displayed the best separation ability with CO_2 permeance of 377.62 ± 1.20 GPU and selectivity of 13.17 ± 1.39. This behaviour was the result of the high diffusivity of MWNCTs tunnels within the polymer matrix and the enhanced compatibility of MWCNTs-F within the polymer chain phase, which favoured the smooth transport of CO_2 penetrant. Hence, the optimal value for the loading of MWCNTs-F was ascertained to be 0.8 wt%. Thus, the interaction between the MWCNTs-F and CAB polymer matrix played a significant role and was one of the key aspects considered when synthesising high performance MMMs for CO_2/N_2 separation.

The development of MMM was then brought forward to advance the synthesisation of blend MMM. This study also revealed that the best combination for blend MMM was designated as M2 (*Mn* combination of 70000:30000 (ratio: 2:1 wt%)). The high CO_2 permeance (341.15 ± 1.19 GPU) and selectivity (17.09 ± 1.29) for M2 were attributed by the low acetyl content and high carboxyl groups present within the blend MMM. When low acetyl content polymer combination was applied, it reduced the densely packed entanglement within the structure of blend MMM and therefore, enhanced the solubility coefficients of M2. On the other hand, the high carboxyl group contents of M2 acting as non-ionic CO_2 carried through covalently connecting with the cellulose chains and easing the CO_2 transport. Additionally, polar functional groups such as the carboxyl group tended to have high affinity towards non-polar CO_2. In return this improved the CO_2 permeance and enhanced the selectivity of the blend MMM.

With reference to the the kinetic sorption study conducted on the blend MMMs, the combinations of blend MMMs with different *Mn* demonstrated significant impact on the CO_2 solubility and diffusivity parameters. Based on the results, the optimal blend MMM (M2) was the second to reach the equilibrium time of CO_2 sorption uptake (2.25 $sec^{0.5}/\mu m$) after M1. This trend of results was contributed by low amorphous fraction and shorter chain spacing along with the incorporation of low molecular weight CAB polymers (*Mn* of 30000). Additionally, M2 achieved a CO_2 diffusivity coefficient of $4.5x10^{-11}$ cm^2/s and a solubility coefficient of $7.58x10^{12}$ ± 1.01 cm^3 (STP)/cm^4cmHg, respectively. It was determined that the diffusivity coefficient relationship was inversely proportional to solubility coefficient due to the decreased amorphous fraction rendering lower solubility coefficient when high molecular weight CAB

polymer was applied in blend MMM. Consequently, it can be concludes that the main governing factor for the blend membranes is the solubility coefficient instead of the diffusivity factor.

Lastly, the binary gas permeation study was conducted at various CO_2 and N_2 feed compositions (20, 40, 50, 60 and 80 vol%) with blend MMMs synthesised in this research study at different molecular weight CAB combinations. The trend of increment for CO_2 and N_2 permeance was contributed by increasing the feed concentration through the blend MMM. In this study, the best composition selectivity was found at a feed composition ratio of 50 vol%, which equalled to CO_2/N_2 ratio of 1:1. This is closely related to industrial conditions. Therefore, the best blend MMM (M2) synthesised in this present study is expected to meet the industrial requirement and is feasible to apply in flue gas combustion application targeting CO_2/N_2 separation.

5.2 Future work and recommendations

In support of future improvements in CO_2/N_2 separation of blend CAB/MWCNTs-F MMM, the following suggestions are recommended to advance the present work:

1. In this present study, the flat sheet blend MMM was synthesised with the incorporation of MWCNTs-F through the wet phase inversion method. The fabrication procedure should be environmental friendly and economical to achieve high reproducibility and low production costs.
2. This study focuses on improving the CO_2/N_2 separation performance of blend CAB with MWCNTs-F. It is proposed that the Rhodeftal (polymer) can be added into the blend, as it is a proven high performance polymer. It was reported that the CO_2/N_2 results increases with the content of Rhodeftal. This is subsequently contributed by the

strong inter-molecular interactions, which cause the increment in chain packing of the polymer.

3. It was suggested that the sweep gas can be used as an option to increase the driving force for CO_2 permeation. Since sweep gas can enhance the separation performance of the membrane specifically for post-combustion application with no extra energy consumption. Subsequently, a systematic economic analysis can be conducted simulating post-combustion industry to compare this concept with the membrane concept without the sweep gas in term of energy efficiency.
4. It is highly recommended that the current blend MMM should be synthesised using the cross-linking method. This method provides higher gas transportation and higher overall gas separation performance. Cross-linking agents may come from PDMS (polydimethylsiloxane) and PAN (polyacrylonitrile) as they possess extremely impressive gas permeability due to the presence of highly contorted ladder-like structures in their polymer backbone.

REFERENCES

Aaron, D. and Tsouris, C., 2005. Separation of CO_2 from flue gas: a review. *Separation Science and Technology*, *40*(1-3), pp.321-348.

Abdul Mannan, H., Yih, T.M., Nasir, R., Muhktar, H. and Mohshim, D.F., 2019. Fabrication and characterization of polyetherimide/polyvinyl acetate polymer blend membranes for CO_2/CH_4 separation. *Polymer Engineering & Science*, *59*(S1), pp.E293-E301.

Abedini, R., Mosayebi, A. and Mokhtari, M. 2018. Improved CO_2 separation of azide cross-linked PMP mixed matrix membrane embedded by nano-CuBTC metal organic framework. Process Safety Environment Protection.

Adewole, J.K., Ahmad, A.L., Ismail, S., Leo, C.P. and Sultan, A.S., 2015. Comparative studies on the effects of casting solvent on physico-chemical and gas transport properties of dense polysulfone membrane used for CO_2/CH_4 separation. *Journal of Applied Polymer Science*, *132*(27).

Adhikari, A.K. and Lin, K.S., 2016. Improving CO_2 adsorption capacities and CO_2/N_2 separation efficiencies of MOF-74 (Ni, Co) by doping palladium-containing activated carbon. *Chemical Engineering Journal*, *284*, pp.1348-1360.

Afzali, A., Maghsoodlou, S. and Noroozi, B., 2018. Nanoporous Polymer/Carbon Nanotube Membrane Filtration: The "How-To" Guide to Computational Methods. In *Analytical Chemistry from Laboratory to Process Line* (pp. 99-150). Apple Academic Press.

Ahmad, A., Jawad, Z., Low, S. and Zein, S. 2014. A cellulose acetate/multi-walled carbon nanotube mixed matrix membrane for CO_2/N_2 separation. Journal Membrane Science. 451**,** 55-66.

Ahmad, A., Jawad, Z., Low, S. and Zein, S. 2013. The Functionalization of Beta-Cyclodextrins on Multi Walled Carbon Nanotubes: Effects of the Dispersant and Non Aqueous Media. Current Nanoscience. 9, 93-102.

Ali, I., Bamaga, O., Gzara, L., Bassyouni, M., Abdel-Aziz, M., Soliman, M., Drioli, E. and Albeirutty, M., 2018. Assessment of blend PVDF membranes, and the effect of polymer concentration and blend composition. *Membranes*, *8*(1), p.13.

Andrew, W. 2018. Greenhouse Gas Emissions. https://www.epa.gov/ghgemissions/global-greenhouse-gas-emissions-data. Accessed on 20 December, 2018.

Aroon, M. A., Ismail, A. F. and Matsuura, T. 2013. Beta-cyclodextrin functionalized MWCNT: A potential nano-membrane material for mixed matrix gas separation membranes development. Separation Purification Technology. 115**,** 39-50.

Aroon, M. A., Ismail, A. F., Matsuura, T. and Montazer-Rahmati, M. M. 2010a. Performance studies of mixed matrix membranes for gas separation: A review. Separation Purification Technology. 75**,** 229-242.

Aroon, M. A., Ismail, A. F., Montazer-Rahmati, M. and Matsuura, T. 2010b. Effect of raw multi-wall carbon nanotubes on morphology and separation properties of polyimide membranes. Separation Purification Technology. 45**,** 2287-2297.

Aroon, M. A., Ismail, A. F., Montazer-Rahmati, M. M. and Matsuura, T. 2010c. Effect of chitosan as a functionalization agent on the performance and separation properties of polyimide/multi-walled carbon nanotubes mixed matrix flat sheet membranes. Journal Membrane Science. 364**,** 309-317.

Aroon, M.A., Ismail, A.F., Montazer-Rahmati, M.M. and Matsuura, T., 2010d. Morphology and permeation properties of polysulfone membranes for gas separation: Effects of non-solvent additives and co-solvent. *Separation and Purification Technology*, *72*(2), pp.194-202.

Asgarkhani, M.A.H., Mousavi, S.M. and Saljoughi, E., 2013. Cellulose acetate butyrate membrane containing TiO 2 nanoparticle: preparation, characterization and permeation study. *Korean Journal of Chemical Engineering*, *30*(9), pp.1819-1824.

Awasthi, M.K., Duan, Y., Zhao, J., Ren, X., Awasthi, S.K., Liu, T., Chen, H., Pandey, A., Varjani, S. and Zhang, Z., 2019. Greenhouse Gases Emission Mitigation and Utilization in Composting and Waste Management Industry: Potentials and Challenges. In *CO2 Separation, Purification and Conversion to Chemicals and Fuels* (pp. 19-37). Springer, Singapore.

Bae, Y. S. and Snurr, R. Q. 2011. Development and evaluation of porous materials for carbon dioxide separation and capture. Angew Chemie Int. Edi. 50, 11586-11596.

Baker, R. W. 2002. Future directions of membrane gas separation technology. Industrial & Engineering Chemistry Research. 41**,** 1393-1411.

Baker, R.W., Wijmans, J.G. and Huang, Y., 2010. Permeability, permeance and selectivity: A preferred way of reporting pervaporation performance data. *Journal of Membrane Science*, *348*(1-2), pp.346-352.

Baker, R.W., 2012. *Membrane technology and applications*. John Wiley & Sons.

Bakeri, G., Ismail, A.F., Shariaty-Niassar, M. and Matsuura, T., 2010. Effect of polymer concentration on the structure and performance of polyetherimide hollow fiber membranes. *Journal of membrane science*, *363*(1-2), pp.103-111.

Banuri, T., Prates, F.F., Martino, D., Murthy, I.K., Park, J., Zenghelis, D.A. and Kosko, M., 2019. Drivers of Environmental Change-Global Environment Outlook (GEO-6): Healthy Planet, Healthy People Chapter 2. *Global Environment Outlook (GEO-6): Healthy Planet, Healthy People*.

Barsotti, E., Tan, S.P., Saraji, S., Piri, M. and Chen, J.H., 2016. A review on capillary condensation in nanoporous media: Implications for hydrocarbon recovery from tight reservoirs. *Fuel*, *184*, pp.344-361.

Basu, S., Cano-Odena, A. and Vankelecom, I.F., 2011. MOF-containing mixed-matrix membranes for CO_2/CH_4 and CO_2/N_2 binary gas mixture separations. *Separation and Purification Technology*, *81*(1), pp.31-40.

Benes, I.N.E. and Vankelecom, I., 2019. Composite membranes for gas separation.

Bhown, A.S. and Freeman, B.C., 2011. Analysis and status of post-combustion carbon dioxide capture technologies. *Environmental science & technology*, *45*(20), pp.8624-8632.

Bitter, J.G.A., 2012. *Transport mechanisms in membrane separation processes*. Springer Science & Business Media.

Blatchford, M.A., Raveendran, P. and Wallen, S.L., 2003. Spectroscopic Studies of Model Carbonyl Compounds in CO_2: Evidence for Cooperative C−H Interactions. *The Journal of Physical Chemistry A*, *107*(48), pp.10311-10323.

Bouma, R., Vercauteren, F., van Os, P., Goetheer, E., Berstad, D. and Anantharaman, R., 2017. Membrane-assisted CO_2 liquefaction: performance modelling of CO_2 capture from flue gas in cement production. *Energy Procedia*, 114, pp.72-80

Bozorg, M., Addis, B., Piccialli, V., Ramírez-Santos, Á.A., Castel, C., Pinnau, I. and Favre, E., 2019. Polymeric membrane materials for nitrogen production from air: a process synthesis study. *Chemical Engineering Science*.

Bugoi, R., Constantinescu, B., Pantos, E. and Popovici, D., 2008. Investigation of Neolithic ceramic pigments using synchrotron radiation X-ray diffraction. *Powder Diffraction*, *23*(3), pp.195-199.

Castro-Munoz, R., Fila, V., Martin-Gil, V. and Muller, C., 2019. Enhanced CO_2 permeability in Matrimid® 5218 mixed matrix membranes for separating binary CO_2/CH_4 mixtures. *Separation and Purification Technology*, *210*, pp.553-562.

Cha, W.C. and Jawad, Z.A., 2019. The influence of cellulose acetate butyrate membrane structure on CO_2/N_2 separation: effect of casting thickness and solvent exchange time. *Chemical Engineering Communications*, pp.1-19.

Chen, Y. and Ho, W.W., 2016. High-molecular-weight polyvinylamine/piperazine glycinate membranes for CO_2 capture from flue gas. *Journal of Membrane Science*, *514*, pp.376-384.

Chen, J., Dyer, M. J. and Yu, M. F. 2001. Cyclodextrin-Mediated Soft Cutting of Single-Walled Carbon Nanotubes. Journal American Chemical Society.

Chen, Jennifer Chih-Yi. 2002. "Evaluation of Polymeric Membranes for Gas Separation Processes: Poly (ether-b-amide) (PEBAXR 2533) Block Copolymer." Chemical Engineering University of Waterloo. Waterloo, Ontario, Canada.

Chen, J., Zhang, J.M., Feng, Y., He, J.S. and Zhang, J., 2014. Effect of molecular structure on the gas permeability of cellulose aliphatate esters. Chinese Journal of Polymer Science, 32(1), pp.1-8.

Cheng, G., Wang, T., Zhao, Q., Ma, X. and Zhang, L. 2006. Preparation of cellulose acetate butyrate and poly (ethylene glycol) copolymer to blend with poly (3-hydroxybutyrate). Journal Applied Polymer Science. 100(2), pp.1471-1478.

Chua, M.L., Shao, L., Low, B.T., Xiao, Y. and Chung, T.S., 2011. Polyetheramine–polyhedral oligomeric silsesquioxane organic–inorganic hybrid membranes for CO_2/H_2 and CO_2/N_2 separation. *Journal of membrane science*, *385*, pp.40-48.

Chung, T.S., 1996. A review of microporous composite polymeric membrane technology for air-separation. *Polymers and Polymer Composites*, *4*(4), pp.269-282.

Cong, H., Zhang, J., Radosz, M., and Shen, Y. 2007. Carbon nanotube composite membranes of brominated poly (2, 6-diphenyl-1, 4-phenylene oxide) for gas separation. Journal Membrane Science. 294(1), 178-185.

Dai, Z., Aboukeila, H., Ansaloni, L., Deng, J., Baschetti, M.G. and Deng, L. 2018. Nafion/PEG hybrid membrane for CO_2 separation: Effect of PEG on membrane micro-structure and performance. Separation and Purification Technology, *214*, pp.67-77.

Daraei, P., Madaeni, S.S., Ghaemi, N., Khadivi, M.A., Astinchap, B. and Moradian, R. 2013. Enhancing antifouling capability of PES membrane via mixing with various types of polymer modified multi-walled carbon nanotube. *Journal of membrane science*, *444*, pp.184-191.

Del Valle, E.M. 2004. Cyclodextrins and their uses: a review. Process Biochemistry. 39(9), 1033-1046.

Deng, W., Wei, G., Zhao, J.X. and Zeng, T., 2019. Anthropogenic effects on tropical oceanic climate change and variability: An insight from the South China Sea over the past 2000 years. *Quaternary Science Reviews*, *206*, pp.56-64.

Dilshad, M.R., Islam, A., Hamidullah, U., Jamshaid, F., Ahmad, A., Butt, M.T.Z. and Ijaz, A., 2019. Effect of alumina on the performance and characterization of cross-linked PVA/PEG 600 blended membranes for CO_2/N_2 separation. *Separation and Purification Technology*, *210*, pp.627-635.

Dinda, Srikanta. 2013. "Development of solid adsorbent for carbon dioxide capture from flue gas." *Separation and Purification Technology* 109: 64-71.

Dong, X., Liu, Q. and Huang, A., 2016. Highly permselective MIL-68 (Al)/matrimid mixed matrix membranes for CO_2/CH_4 separation. *Journal of Applied Polymer Science*, *133*(22).

Dorosti, F., Omidkhah, M.R., Pedram, M.Z. and Moghadam, F., 2011. Fabrication and characterization of polysulfone/polyimide–zeolite mixed matrix membrane for gas separation. *Chemical Engineering Journal*, *171*(3), pp.1469-1476.

Ebneyamini, A., Azimi, H., Tezel, F.H. and Thibault, J., 2017. Modelling of mixed matrix membranes: Validation of the resistance-based model. Journal of Membrane Science, 543, pp.361-369.

EIA 2018. https://www.eia.gov/outlooks/ieo/International Energy Outlook 2018. Accessed on 20 December, 2018.

Erinosho, T.O., Collins, D.M., Wilkinson, A.J., Todd, R.I. and Dunne, F.P.E., 2016. Assessment of X-ray diffraction and crystal plasticity lattice strain evolutions under biaxial loading. International Journal of Plasticity, 83, pp.1-18.

Estahbanati, E.G., Omidkhah, M. and Amooghin, A.E., 2017. Preparation and characterization of novel Ionic liquid/Pebax membranes for efficient CO_2/light gases separation. *Journal of Industrial and Engineering Chemistry*, *51*, pp.77-89.

Fakhar, A., Sadeghi, M., Dinari, M. and Lammertink, R., 2019. Association of hard segments in gas separation through polyurethane membranes with aromatic bulky chain extenders. *Journal of membrane science*, *574*, pp.136-146.

Feller, S. E., Brown, C. A., Nizza, D. T. and Gawrisch, K. 2002. Nuclear Overhauser Enhancement Spectroscopy Cross-Relaxation Rates and Ethanol Distribution across Membranes. Biophysical journal. 82, 1396-140.

Feng, S., Ren, J., Zhao, D., Li, H., Hua, K., Li, X. and Deng, M., 2019. Effect of poly (ethylene glycol) molecular weight on CO_2/N_2 separation performance of poly (amide-12-b-ethylene oxide)/poly (ethylene glycol) blend membranes. *Journal of Energy Chemistry*, *28*, pp.39-45.

Feng, Y., Zhang, J. M., Zhang, J. and Chang, J. 2015. Gas Separation Properties of Cellulose Acetate Butyrate/MWCNTs Mixed Matrix Membranes. Acta Polymerica Sinica, 1396-1401.

Freeman, B.D., 1999. Basis of permeability/selectivity tradeoff relations in polymeric gas separation membranes. *Macromolecules*, *32*(2), pp.375-380.

Freeman, B., Yampolskii, Y. and Pinnau, I. eds., 2006. *Materials science of membranes for gas and vapor separation*. John Wiley & Sons.

Friess, K., Hynek, V., Šípek, M., Kujawski, W.M., Vopička, O., Zgažar, M. and Kujawski, M.W., 2011. Permeation and sorption properties of poly (ether-block-amide) membranes filled by two types of zeolites. *Separation and purification technology*, *80*(3), pp.418-427.

Ge, L., Zhu, Z. and Rudolph, V. 2011. Enhanced gas permeability by fabricating functionalized multi-walled carbon nanotubes and polyethersulfone nanocomposite membrane. Separation Purification Technology. 78(1), pp.76-82.

Ghadimi, A., Mohammadi, T. and Kasiri, N., 2014. A novel chemical surface modification for the fabrication of PEBA/SiO2 nanocomposite membranes to separate CO_2 from syngas and natural gas streams. *Industrial & Engineering Chemistry Research*, *53*(44), pp.17476-17486.

Goh, P. S., Ismail, A. F., Sanip, S. M., NG, B. C. and Aziz, M. 2011. Recent advances of inorganic fillers in mixed matrix membrane for gas separation. Separation Purification Technology. 81**,** 243-264.

Göttlicher, G. and Pruschek, R., 1997. Comparison of CO_2 removal systems for fossil-fuelled power plant processes. *Energy Conversion and Management*, *38*, pp.S173-S178.

Hacarlioglu, P., Toppare, L. and Yilmaz, L. 2003. Effect of preparation parameters on performance of dense homogeneous polycarbonate gas separation membranes. *Journal of applied polymer science*, *90*(3), pp.776-785.

Hake, J.F., Bansal, N. and Kleemann, M. eds. 2019. *Strategies and technologies for greenhouse gas mitigation: an Indo-German contribution to global efforts*. Routledge.

Hamad, F., Khulbe, K.C. and Matsuura, T., 2005. Comparison of gas separation performance and morphology of homogeneous and composite PPO membranes. *Journal of membrane science*, *256*(1-2), pp.29-37.

Hashimoto, K., 2019. Current Situation of Energy Consumption and Carbon Dioxide Emissions of Our World. In *Global Carbon Dioxide Recycling* (pp. 25-31). Springer, Singapore.

Hilal, N., Ismail, A.F., Matsuura, T. and Oatley-Radcliffe, D. eds., 2017. *Membrane Characterization*. Elsevier.

Hosseini, S.S., Peng, N. and Chung, T.S. 2010. Gas separation membranes developed through integration of polymer blending and dual-layer hollow fiber spinning process for hydrogen and natural gas enrichments. *Journal of Membrane Science*, *349*(1-2), pp.156-166.

Ho, K.C., Teow, Y.H., Ang, W.L. and Mohammad, A.W. 2017. Novel GO/OMWCNTs mixed-matrix membrane with enhanced antifouling property for palm oil mill effluent treatment. *Separation and Purification Technology*, *177*, pp.337-349.

Ho, W. and Sirkar, K. 2012. *Membrane handbook*. Springer Science & Business Media.

Isanejad, M. and Mohammadi, T., 2018. Effect of amine modification on morphology and performance of poly (ether-block-amide)/fumed silica nanocomposite membranes for CO_2/CH_4 separation. *Materials Chemistry and Physics*, *205*, pp.303-314.

Ismail, A. F., Goh, P. S., Sanip, S. M. and Aziz, M. 2009. Transport and separation properties of carbon nanotube-mixed matrix membrane. *Separation Purification Technology*. 70, 12-26.

Ismail, A. F., Rahim, N. H., Mustafa, A., Matsuura, T., Ng, B. C., Abdullah, S., and Hashemifard, S. A. 2011. Gas separation performance of polyethersulfone/multi-walled carbon nanotubes mixed matrix membranes. *Separation Purification Technology*. 80(1), 20-31.

Jami'an, W.N.R., Hasbullah, H., Mohamed, F., Rani, A.R.A., Saman, M.F.K., Yusof, N. and Ibrahim, N., 2015. Effect of solvent evaporation time on CO2/CH4 gas performance for poly (lactic) acid membranes. In *Advanced Materials Research* (Vol. 1113, pp. 660-666). Trans Tech Publications.

Jawad, Z., Ahmad, A., Low, S., and Zein, S. 2015a. Incorporation of Inorganic Carbon Nanotubes Fillers into the CA Polymeric Matrix for Improvement in CO_2/N_2 Separation. *Current Nanoscience*. 11(1), 69-79.

Jawad, Z. A., Ahmad, A. L., Low, S. C., Chew, T. L. and Zein, S. H. S. 2015b. Influence of solvent exchange time on mixed matrix membrane separation performance for CO_2/N_2 and a kinetic sorption study. *Journal Membrane Science*. 476, 590-601.

Joseph, R.M., Merrick, M.M., Liu, R., Fraser, A.C., Moon, J.D., Choudhury, S.R., Lesko, J., Freeman, B.D. and Riffle, J.S., 2018. Synthesis and characterization of polybenzimidazole membranes for gas separation with improved gas permeability: A grafting and blending approach. *Journal of membrane science*, *564*, pp.587-597.

Kentish, S.E., Scholes, C.A. and Stevens, G.W., 2008. Carbon dioxide separation through polymeric membrane systems for flue gas applications. Recent Patents on Chemical Engineering, 1(1), pp.52-66.

Khanna, N., Fridley, D., Zhou, N., Karali, N., Zhang, J. and Feng, W., 2019. Energy and CO_2 implications of decarbonization strategies for China beyond efficiency: Modeling 2050 maximum renewable resources and accelerated electrification impacts. *Applied Energy*, *242*, pp.12-26.

Khan, A.L., Li, X., Ilyas, A., Raza, M.T. and Vankelecom, I.F. 2016. Novel sulfonated and fluorinated PEEK membranes for CO2 separation. *Separation and Purification Technology*, *167*, pp.1-5.

Kim, H.S., Mun, J., Lee, W.H. and Park, Y.D., 2018. Ultrasonication-Mediated Self-Assembly in Polythiophene Films via Control of Residual Solvent Evaporation. *Macromolecular Research*, *26*(2), pp.139-144.

Kim, Y.A., Hayashi, T., Endo, M., Kaburagi, Y., Tsukada, T., Shan, J., Osato, K. and Tsuruoka, S., 2005. Synthesis and structural characterization of thin multi-walled carbon nanotubes with a partially facetted cross section by a floating reactant method. *Carbon*, *43*(11), pp.2243-2250.

Kim, Y.K., Park, H.B. and Lee, Y.M., 2005. Gas separation properties of carbon molecular sieve membranes derived from polyimide/polyvinylpyrrolidone blends: effect of the molecular weight of polyvinylpyrrolidone. *Journal of membrane science*, *251*(1-2), pp.159-167.

Kinoshita, Y., Wakimoto, K., Gibbons, A.H., Isfahani, A.P., Kusuda, H., Sivaniah, E. and Ghalei, B. 2017. Enhanced PIM-1 membrane gas separation selectivity through efficient dispersion of functionalized POSS fillers. *Journal of Membrane Science*, *539*, pp.178-186.

Kobayashi, S. and Müllen, K., 2015. *Encyclopedia of Polymeric Nanomaterials-With 2021 Figures and 146 Tables*. Springer.

Koros, W.J. and Fleming, G.K., 1993. Membrane-based gas separation. *Journal of membrane science*, *83*(1), pp.1-80.

Koros, W.J., Fleming, G.K., Jordan, S.M., Kim, T.H. and Hoehn, H.H., 1988. Polymeric membrane materials for solution-diffusion based permeation separations. *Progress in Polymer Science*. 13(4), pp.339-401.

Kreyszig, E., 2008. Advanced engineering mathematics. *Integration*, *9*, p.4.

Krol, J.J., Boerrigter, M. and Koops, G.H., 2001. Polyimide hollow fiber gas separation membranes: preparation and the suppression of plasticization in propane/propylene environments. *Journal of Membrane Science*, *184*(2), pp.275-286.

Kunthadong, P., Molloy, R., Worajittiphon, P., Leejarkpai, T., Kaabbuathong, N. and Punyodom, W. 2015. Biodegradable Plasticized Blends of Poly(L-lactide) and Cellulose Acetate Butyrate: From Blend Preparation to Biodegradability in Real Composting Conditions. *Journal of Polymer and the Environment.* 23**,** 107-113.

Lavorgna, M., et al. 2013. Silanization and silica enrichment of multiwalled carbon nanotubes: Synergistic effects on the thermal-mechanical properties of epoxy nanocomposites. *European Polymer Journal*. 49(2): 428-438.

Lee, J.H., Kim, S.K. and Kim, N.H., 2006. Effects of the addition of multi-walled carbon nanotubes on the positive temperature coefficient characteristics of carbon-black-filled high-density polyethylene nanocomposites. *Scripta Materialia*, *55*(12), pp.1119-1122.

Lewis, J., 2018. Gas Separation Membranes: Polymeric and Inorganic by AF Ismail, KC Khulbe, and T. Matsuura. *Chemical Engineering Education*, *52*(3), p.223.

Li, F., Newman, P., Pawson, S. and Perlwitz, J., 2018. Effects of greenhouse gas increase and stratospheric ozone depletion on stratospheric mean age of air in 1960–2010. *Journal of Geophysical Research: Atmospheres*, *123*(4), pp.2098-2110.

Li, H., Song, Z., Zhang, X., Huang, Y., Li, S., Mao, Y., Ploehn, H.J., Bao, Y. and Yu, M., 2013. Ultrathin, molecular-sieving graphene oxide membranes for selective hydrogen separation. *Science*, *342*(6154), pp.95-98.

Li, J.F., Xu, Z.L., Yang, H., Yu, L.Y. and Liu, M., 2009. Effect of TiO_2 nanoparticles on the surface morphology and performance of microporous PES membrane. *Applied Surface Science*, *255*(9), pp.4725-4732.

Li, Q., Zhou, C., Ji, Z., Gao, D., Han, B., Xia, K., Gao, Q. and Wu, J. 2018. Insight into the high-efficient functionalization of carbon nanotubes by advanced oxidation using peroxomonosulfate. *Microporous and Mesoporous Materials*. 260, 24-29.

Li, S., Jiang, X., Yang, X., Bai, Y. and Shao, L. 2019. Nanoporous framework "reservoir" maximizing low-molecular-weight enhancer impregnation into CO_2-philic membranes for highly-efficient CO_2 capture. *Journal of membrane science*, *570*, pp.278-285.

Lin, K.Y.A. and Park, A.H.A. 2011. Effects of bonding types and functional groups on CO_2 capture using novel multiphase systems of liquid-like nanoparticle organic hybrid materials. *Environmental science & technology*, *45*(15), pp.6633-6639.

Liu, L., Chakma, A. and Feng, X., 2004. A novel method of preparing ultrathin poly (ether block amide) membranes. *Journal of Membrane Science*, *235*(1-2), pp.43-52.

Loeb, S., Titelman, L., Korngold, E. and Freiman, J., 1997. Effect of porous support fabric on osmosis through a Loeb-Sourirajan type asymmetric membrane. *Journal of Membrane Science*, *129*(2), pp.243-249.

Loloei, M., Moghadassi, A., Omidkhah, M. and Amooghin, A.E., 2015. Improved CO_2 separation performance of Matrimid® 5218 membrane by addition of low molecular weight polyethylene glycol. *Greenhouse Gases: Science and Technology*, *5*(5), pp.530-544.

Lou, Y., Liu, G., Liu, S., Shen, J. and Jin, W., 2014. A facile way to prepare ceramic-supported graphene oxide composite membrane via silane-graft modification. *Applied surface science*, 307, pp.631-637.

Luo, S., Stevens, K.A., Park, J.S., Moon, J.D., Liu, Q., Freeman, B.D. and Guo, R. 2016. Highly CO_2-selective gas separation membranes based on segmented copolymers of poly

(ethylene oxide) reinforced with pentiptycene-containing polyimide hard segments. *ACS applied materials & interfaces*, *8*(3), pp.2306-2317.

Madzarevic, Z.P., Shahid, S., Nijmeijer, K. and Dingemans, T.J., 2019. The role of ortho-, meta-and para-substitutions in the main-chain structure of poly (etherimide) s and the effects on CO_2/CH_4 gas separation performance. *Separation and Purification Technology*, 210, pp.242-250.

Manimaran, D., Jawad, Z.A. and Leng, C.T., 2019. Effect of Solvent Evaporation Time and Casting Thickness on the Separation Performance of Cellulose Acetate Butyrate Blend Membrane. *Journal of Applied Membrane Science & Technology*, *23*(2).

Martin-Gil, V., López, A., Hrabanek, P., Mallada, R., Vankelecom, I.F.J. and Fila, V., 2017. Study of different titanosilicate (TS-1 and ETS-10) as fillers for Mixed Matrix Membranes for CO2/CH4 gas separation applications. *Journal of Membrane Science*, *523*, pp.24-35.

Matthews, H.D., Zickfeld, K., Knutti, R. and Allen, M.R., 2018. Focus on cumulative emissions, global carbon budgets and the implications for climate mitigation targets. *Environmental Research Letters*, *13*(1), p.010201.

Merkel, T.C., Freeman, B.D., Spontak, R.J., He, Z., Pinnau, I., Meakin, P. and Hill, A.J., 2002. Ultrapermeable, reverse-selective nanocomposite membranes. *Science*, *296*(5567), pp.519-522.

Moaddeb, M. and Koros, W.J., 1997. Gas transport properties of thin polymeric membranes in the presence of silicon dioxide particles. *Journal of membrane science*, *125*(1), pp.143-163.

Moghadassi, A.R., Rajabi, Z., Hosseini, S.M. and Mohammadi, M., 2013. Preparation and characterization of polycarbonate-blend-raw/functionalized multi-walled carbon nano tubes mixed matrix membrane for CO_2 separation. *Separation Science and Technology*, *48*(8), pp.1261-1271.

Molki, B., Aframehr, W.M., Bagheri, R. and Salimi, J., 2018. Mixed matrix membranes of polyurethane with nickel oxide nanoparticles for CO_2 gas separation. *Journal of membrane science*, *549*, pp.588-601.

Moon, K.S., Lin, W., Jiang, H., Ko, H., Zhu, L. and Wong, C.P., 2008, May. Surface treatment of MWCNT array and its polymer composites for TIM application. In *2008 58th Electronic Components and Technology Conference* (pp. 234-237). IEEE.

Moore, T. T., Mahajan, R., Vu, D. Q. and Koros, W. J. 2004. Hybrid membrane materials comprising organic polymers with rigid dispersed phases. AIChE. Journal. 50**,** 311-321.

Mulder, J. 2012. *Basic principles of membrane technology*: Springer Science & Business Media.

Nour, M., Berean, K., Balendhran, S., Ou, J.Z., Du Plessis, J., McSweeney, C., Bhaskaran, M., Sriram, S. and Kalantar-zadeh, K., 2013. CNT/PDMS composite membranes for H_2 and CH_4 gas separation. *International Journal of Hydrogen Energy*, *38*(25), pp.10494-10501.

Noy, A., Park, H.G., Fornasiero, F., Holt, J.K., Grigoropoulos, C.P. and Bakajin, O., 2007. Nanofluidics in carbon nanotubes. *Nano today*, *2*(6), pp.22-29.

Pabby, A.K., Rizvi, S.S. and Requena, A.M.S. 2008. *Handbook of membrane separations: chemical, pharmaceutical, food, and biotechnological applications*. CRC press.

Pan, W.L., Pan, W., Liu, S., Tsai, S.B., Hu, C. and Tu, H., 2019. China's provincial energy-related carbon emissions-economy nexus: A two-stage framework based on decoupling analysis and panel vector autoregression. *Energy Science & Engineering*.

Pandey, P. and Chauhan, R.S., 2001. Membranes for gas separation. *Progress in polymer science*, *26*(6), pp.853-893.

Patel, N.P. and Spontak, R.J., 2004. Mesoblends of polyether block copolymers with poly (ethylene glycol). *Macromolecules*, *37*(4), pp.1394-1402.

Pearce, W., Niederer, S., Özkula, S.M. and Sánchez Querubín, N., 2019. The social media life of climate change: Platforms, publics, and future imaginaries. *Wiley Interdisciplinary Reviews: Climate Change*, *10*(2), p.e569.

Pengilley, C., 2016. *Membranes for gas separation* (Doctoral dissertation, University of Bath).

Polarz, S, Bernd S, Lyudmila B, and Markus A. 2001. "From Cyclodextrin Assemblies to Porous Materials by Silica Templating." *A*ngewandte. Chem. Int. Ed. 40 (23): 4417-4421.

Rahimpour, A., Jahanshahi, M., Khalili, S., Mollahosseini, A., Zirepour, A. and Rajaeian, B., 2012. Novel functionalized carbon nanotubes for improving the surface properties and performance of polyethersulfone (PES) membrane. *Desalination*, 286, pp.99-107.

Ranjbaran, F., Omidkhah, M.R. and Amooghin, A.E., 2015. The novel Elvaloy4170/functionalized multi-walled carbon nanotubes mixed matrix membranes:

Fabrication, characterization and gas separation study. *Journal of the Taiwan Institute of Chemical Engineers*, *49*, pp.220-228.

Ren, X., Kanezashi, M., Nagasawa, H. and Tsuru, T., 2015. Plasma-assisted multi-layered coating towards improved gas permeation properties for organosilica membranes. *Rsc Advances*, *5*(74), pp.59837-59844.

Rezakazemi, M., Amooghin, A.E., Montazer-Rahmati, M.M., Ismail, A.F. and Matsuura, T., 2014. State-of-the-art membrane based CO_2 separation using mixed matrix membranes (MMMs): an overview on current status and future directions. *Progress in Polymer Science*, *39*(5), pp.817-861.

Robeson, L. M. 2008. The upper bound revisited. *Journal Membrane Science*. 320, 390-400.

Robeson, L.M. 1991. Correlation of separation factor versus permeability for polymeric membranes. *Journal of membrane science*, *62*(2), pp.165-185.

Ruysschaert, J.M. and Raussens, V., 2018. ATR-FTIR Analysis of Amyloid Proteins. *In Peptide Self-Assembly* (pp. 69-81). Humana Press, New York, NY.

Sadeghi, M., Semsarzadeh, M.A. and Moadel, H., 2009. Enhancement of the gas separation properties of polybenzimidazole (PBI) membrane by incorporation of silica nano particles. *Journal of Membrane Science*, *331*(1-2), pp.21-30.

Safarpour, M., Vatanpour, V. and Khataee, A., 2016. Preparation and characterization of graphene oxide/TiO2 blended PES nanofiltration membrane with improved antifouling and separation performance. *Desalination*, *393*, pp.65-78.

Sahoo, N.G., Rana, S., Cho, J.W., Li, L. and Chan, S.H., 2010. Polymer nanocomposites based on functionalized carbon nanotubes. *Progress in polymer science*, 35(7), pp.837-867.

Sanip, S. M., Ismail, A. F., Goh, P. S., Soga, T., Tanemura, M., and Yasuhiko, H. 2011. Gas separation properties of functionalized carbon nanotubes mixed matrix membranes. *Separation and Purification Technology*. 78(2), 208-213.

Sanyal, O., Zhang, C., Wenz, G.B., Fu, S., Bhuwania, N., Xu, L., Rungta, M. and Koros, W.J., 2018. Next generation membranes - using tailored carbon. *Carbon*, *127*, pp.688-698.

Sáez, A.E. and Baygents, J.C., 2014. *Environmental transport phenomena*. CRC Press.

Shahid, S. and Nijmeijer, K., 2017. Matrimid®/polysulfone blend mixed matrix membranes containing ZIF-8 nanoparticles for high pressure stability in natural gas separation. *Separation and Purification Technology*, *189*, pp.90-100.

Shan, M., Xue, Q., Jing, N., Ling, C., Zhang, T., Yan, Z. and Zheng, J. 2012. Influence of chemical functionalization on the CO_2/N_2 separation performance of porous graphene membranes. *Nanoscale*, 4, 5477-5482.

Shindo R., Nagai K. (2013) Gas Separation Membranes. Encyclopedia of Polymeric Nanomaterials. Springer, Berlin, Heidelberg.

Shirvani, H., Maghami, S., Pournaghshband Isfahani, A. and Sadeghi, M., 2019. Influence of Blend Composition and Silica Nanoparticles on the Morphology and Gas Separation Performance of PU/PVA Blend Membranes. *Membranes*, *9*(7), p.82.

Shojaie, S.S., Krantz, W.B. and Greenberg, A.R., 1994. Dense Polymer Film and Membrane Formation via the dry-cast process Part II. Model validation and morphological studies. *Journal of Membrane Science*, 94(1), pp.281-298.

Singh, R., Bharti, N., Madan, J. and Hiremath, S.N., 2010. Characterization of cyclodextrin inclusion complexes a review. Journal Pharmaceutical Science Technology. 2(3), pp.171-183.

Songolzadeh, M., Soleimani, M., Takht Ravanchi, M. and Songolzadeh, R., 2014. Carbon dioxide separation from flue gases: a technological review emphasizing reduction in greenhouse gas emissions. *The Scientific World Journal*, *2014*.

Sridhar, S., Bee, S. and Bhargava, S.K., 2014. Membrane-based gas separation: principle, applications and future potential. *Chem. Eng. Dig*, pp.1-25.

Sun, H., Wang, T., Xu, Y., Gao, W., Li, P., and Niu, Q. J. 2017. Fabrication of polyimide and functionalized multi-walled carbon nanotubes mixed matrix membranes by in-situ polymerization for CO_2 separation. *Separation and Purification Technology*. 177(Supplement C), 327-336.

Suttiwijitpukdee, N., Sato, H., Zhang, J., Hashimoto, T., and Ozaki, Y. 2011. Intermolecular interactions and crystallization behaviors of biodegradable polymer blends between poly (3-hydroxybutyrate) and cellulose acetate butyrate studied by DSC, FT-IR, and WAXD. *Polymer*. 52(2), 461-471.

Takamura, Y., Aoki, J., Uchida, S. and Narita, S., 2001. Application of high-pressure swing adsorption process for improvement of CO_2 recovery system from flue gas. *The Canadian Journal of Chemical Engineering*, *79*(5), pp.812-816.

Tan, P.C., Jawad, Z.A., Ooi, B.S., Ahmad, A.L. and Low, S.C., 2016. Correlation between polymer packing and gas transport properties for CO_2/N_2 separation in glassy

fluorinated polyimide membrane. *Journal of Engineering Science and Technology*, *11*(7), pp.935-946.

Tong, H.M., Kowalczyk, S., Saraf. R., and Chou, N. 2010. Characterization of Polymers. Momentum Press. New York.

Tripathi, A.D., Mishra, R., Maurya, K.K., Singh, R.B. and Wilson, D.W., 2019. Estimates for World Population and Global Food Availability for Global Health. In *The Role of Functional Food Security in Global Health* (pp. 3-24). Academic Press.

Trotta, F., Cavalli, R., Martina, K., Biasizzo, M., Vitillo, J., Bordiga, S., Vavia, P. and Ansari, K., 2011. Cyclodextrin nanosponges as effective gas carriers. *Journal of inclusion phenomena and macrocyclic chemistry*, 71(1-2), pp.189-194.

Tsai, C.H., Shih, C.J., Chou, Y.R., Chi, W.F., Huang, W.C. and Yu, Y.H., 2018. Preparation of reduced graphene oxide/macrocyclic manganese complex composite materials as counter electrodes in dye-sensitized solar cells. *Organic Electronics*, *52*, pp.51-60.

Vatanpour, V., Madaeni, S.S., Moradian, R., Zinadini, S. and Astinchap, B., 2012. Novel antibifouling nanofiltration polyethersulfone membrane fabricated from embedding TiO2 coated multiwalled carbon nanotubes. *Separation and purification technology*, 90, pp.69-82.

Venturi, S., Tassi, F., Magi, F., Cabassi, J., Ricci, A., Capecchiacci, F., Caponi, C., Nisi, B. and Vaselli, O., 2019. Carbon isotopic signature of interstitial soil gases reveals the potential role of ecosystems in mitigating geogenic greenhouse gas emissions: Case studies from hydrothermal systems in Italy. *Science of the Total Environment*, *655*, pp.887-898.

Visakh, P.M., Markovic, G. and Pasquini, D. eds., 2016. *Recent Developments in Polymer Macro, Micro and Nano Blends: Preparation and Characterisation*. Woodhead Publishing.

Wang, D., Li, K. and Teo, W.K., 2000. Highly permeable polyethersulfone hollow fiber gas separation membranes prepared using water as non-solvent additive. *Journal of Membrane Science*, *176*(2), pp.147-158.

Wang, D., Teo, W.K. and Li, K., 2002. Preparation and characterization of high-flux polysulfone hollow fibre gas separation membranes. *Journal of Membrane Science*, 204(1-2), pp.247-256.

Wang, S., Liu, Y., Huang, S., Wu, H., Li, Y., Tian, Z. and Jiang, Z., 2014. Pebax–PEG–MWCNT hybrid membranes with enhanced CO_2 capture properties. *Journal of membrane science*, *460*, pp.62-70.

Wind, J. D., Sirard, S. M., Paul, D. R., Green, P. F., Johnston, K. P. and Koros, W. J. 2003. Carbon dioxide-induced plasticization of polyimide membranes: pseudo-equilibrium relationships of diffusion, sorption, and swelling. *Macromolecules*. 36, 6433-6441.

Wissinger, R.G. and Paulaitis, M.E., 1987. Swelling and sorption in polymer–CO_2 mixtures at elevated pressures. *Journal of Polymer Science Part B: Polymer Physics*, 25(12), pp.2497-2510.

Wu, K., Li, X., Wang, C., Yu, W. and Chen, Z., 2015. Model for surface diffusion of adsorbed gas in nanopores of shale gas reservoirs. *Industrial & Engineering Chemistry Research*, *54*(12), pp.3225-3236.

Xiang, L., Pan, Y., Zeng, G., Jiang, J., Chen, J. and Wang, C. 2016. Preparation of poly (ether-block-amide)/attapulgite mixed matrix membranes for CO_2/N_2 separation. *Journal of Membrane Science*, *500*, pp.66-75.

Xin, Q., Gao, Y., Wu, X., Li, C., Liu, T., Shi, Y., Li, Y., Jiang, Z., Wu, H. and Cao, X. 2015. Incorporating one-dimensional aminated titania nanotubes into sulfonated poly (ether ether ketone) membrane to construct CO_2 facilitated transport pathways for enhanced CO_2 separation. *Journal Membrane Science*. 488, 13-29.

Yamasaki, A., 2003. An overview of CO_2 mitigation options for global warming emphasizing CO_2 sequestration options. *Journal of Chemical Engineering of Japan*, 36(4), pp.361-375.

Yang, H., Xu, Z., Fan, M., Gupta, R., Slimane, R. B., Bland, A. E. and Wright, I. 2008. Progress in carbon dioxide separation and capture: A review. *Journal of Environment Science. 20, 14-27*.

Yang, J., Lin, Y., Wang, J., Lai, M., Li, J., Liu, J., Tong, X. and Cheng, H. 2005. Morphology, thermal stability, and dynamic mechanical properties of atactic polypropylene/carbon nanotube composites. *Journal of Applied Polymer Science*, *98*(3), pp.1087-1091.

Yildirim, Y. and Hughes, R. 2003. An Experimental Study of CO_2 Separation Using a Silica Based Composite Membrane. *Process Safety Environment Protection*. 81, 257-261.

Zarshenas, K., Raisi, A. and Aroujalian, A. 2016. Mixed matrix membrane of nano-zeolite NaX/poly (ether-block-amide) for gas separation applications. *Journal of Membrane Science*, *510*, pp.270-283.

Zhang, B., Fu, J., Zhang, Q., Yi, C. and Yang, B., 2019. Study on CO_2 facilitated separation of mixed matrix membranes containing surface modified MWCNTs. *Journal of Applied Polymer Science*, *136*(33), p.47848.

Zhang, H., Guo, R., Hou, J., Wei, Z. and Li, X., 2016. Mixed-matrix membranes containing carbon nanotubes composite with hydrogel for efficient CO_2 separation. *ACS applied materials & interfaces*, 8(42), pp.29044-29051.

Zhang, T. and Tremblay, P.L., 2019. Possible Industrial Applications for Microbial Electrosynthesis From Carbon Dioxide. In *Microbial Electrochemical Technology* (pp. 825-842). Elsevier.

Zhang, X., Luo, L. and Skitmore, M., 2015. Household carbon emission research: an analytical review of measurement, influencing factors and mitigation prospects. *Journal of Cleaner Production*, *103*, pp.873-883.

Zhang, Y., Sunarso, J., Liu, S. and Wang, R., 2013. Current status and development of membranes for CO_2/CH_4 separation: A review. *International Journal of Greenhouse Gas Control*, *12*, pp.84-107.

Zhang, Z. E., Y.F, Y., L., Z. and S.X, J. 2014. Hollow fiber membrane contactor absorption of CO_2 from the flue gas: review and perspective. *Glob. Nest. J*. 16, 355-374.

Zhao, J., Wang, Z., Wang, J. and Wang, S., 2012. High-performance membranes comprising polyaniline nanoparticles incorporated into polyvinylamine matrix for CO_2/N_2 separation. *Journal of membrane science*, *403*, pp.203-215.

Zhao, Y., Jung, B.T., Ansaloni, L. and Ho, W.W., 2014. Multiwalled carbon nanotube mixed matrix membranes containing amines for high pressure CO_2/H_2 separation. *Journal of membrane science*, *459*, pp.233-243.

Zinadini, S., Zinatizadeh, A.A., Rahimi, M., Vatanpour, V. and Zangeneh, H., 2014. Preparation of a novel antifouling mixed matrix PES membrane by embedding graphene oxide nanoplates. *Journal of Membrane Science*, *453*, pp.292-301.

Ziyarati, M.T., Bahramifar, N., Baghmisheh, G. and Younesi, H., 2019. Greenhouse gas emission estimation of flaring in a gas processing plant: Technique development. *Process Safety and Environmental Protection*, *123*, pp.289-298.

Every reasonable effort has been made to acknowledge the owners of copyright materials. I would be pleased to hear from any copyright owner who has been omitted or incorrectly acknowledged.

Appendix A- Sample calculation for single gas permeation

Specification:

Drying method: 1hr Isopropyl alcohol + 1hr hexane

Polymer concentration: 4 wt% CAB

Evaporation time: 5 minutes

Permeation cell effective area: 3 cm

Membrane permeation cell area (A=π/4*D): 7.0695 cm^2 = 0.00070695 m^2

Pressure difference across the membrane permeation cell = 1 bar = 101325 Pa

Temperature = 25°C = 298.15K

Sample calculation from excel:

Pressure (bar)	Bubble Flow Meter Volume (ml)	Time (s)	Single N_2 Flow (mol/s)	Single N_2 Flux (mol/m2.s)	Single N_2 Permeance (mol/m2.s.Pa)	Single Gas Permeance (GPU)
1	1	14.25	2.86851E-06	0.0041	4.00E-08	120.1359
1	1	14.25	2.86851E-06	0.0041	4.00E-08	120.1359
1	1	14.21	2.87659E-06	0.0041	4.02E-08	120.4741
1	1	14.22	2.87457E-06	0.0041	4.01E-08	120.3894
Average					**4.01E-08**	**120.2838**
					STDV	0.1743
					Sqrt	2.0000
					Std Error	0.0871

Pressure (bar)	Bubble Flow Meter Volume (ml)	Time (s)	Single N_2 Flow (mol/s)	Single N_2 Flux (mol/m2.s)	Single N_2 Permeance (mol/m2.s.Pa)	Single Gas Permeance (GPU)
1.5	1	9.72	4.20538E-06	0.0059	3.91E-08	117.4168
1.5	1	9.57	4.2713E-06	0.0060	3.98E-08	119.2572
1.5	1	9.70	4.21405E-06	0.0060	3.92E-08	117.6589
1.5	1	9.72	4.20538E-06	0.0059	3.91E-08	117.4168
Average					**3.93E-08**	**117.9374**
					STDV	0.8872
					Sqrt	2
					Std Error	0.4436

Pressure (bar)	Bubble Flow Meter Volume (ml)	Time (s)	Single N_2 Flow (mol/s)	Single N_2 Flux (mol/m2.s)	Single N_2 Permeance (mol/m2.s.Pa)	Single Gas Permeance (GPU)
2	1	7.08	5.77349E-06	0.0082	4.03E-08	120.8995
2	1	7.10	5.75723E-06	0.0081	4.02E-08	120.5589
2	1	7.10	5.75723E-06	0.0081	4.02E-08	120.5589
2	1	7.08	5.77349E-06	0.0082	4.03E-08	120.8995
Average					**4.02E-08**	**120.7292**
					STDV	0.1966
					Sqrt	2
					Std Error	0.0983

Pressure (bar)	Bubble Flow Meter Volume (ml)	Time (s)	Single N_2 Flow (mol/s)	Single N_2 Flux (mol/m2.s)	Single N_2 Permeance (mol/m2.s.Pa)	Single Gas Permeance (GPU)
2.5	1	5.66	7.22196E-06	0.0102	4.03E-08	120.9849
2.5	1	5.50	7.43206E-06	0.0105	4.15E-08	124.5045
2.5	1	5.53	7.39174E-06	0.0105	4.13E-08	123.8291
2.5	1	5.53	7.39174E-06	0.0105	4.13E-08	123.8291
Average					**4.11E-08**	**123.2869**
					STDV	1.5673
					Sqrt	2
					Std Error	0.7837

Pressure (bar)	Bubble Flow Meter Volume (ml)	Time (s)	Single N_2 Flow (mol/s)	Single N_2 Flux (mol/m2.s)	Single N_2 Permeance (mol/m2.s.Pa)	Single Gas Permeance (GPU)
3	1	4.59	8.90552E-06	0.0126	4.14E-08	124.3237
3	1	4.52	9.04343E-06	0.0128	4.21E-08	126.2490
3	1	4.55	8.98381E-06	0.0127	4.18E-08	125.4166
3	1	4.53	9.02347E-06	0.0128	4.20E-08	125.9703
Average					**4.18E-08**	**125.4899**
					STDV	0.8510
					Sqrt	2
					Std Error	0.4255

Pressure (bar)	Bubble Flow Meter Volume (ml)	Time (s)	Single CO_2 Flow (mol/s)	Single CO_2 Flux (mol/m2.s)	Single CO_2 Permeance (mol/m2.s.Pa)	Single Gas Permeance (GPU)
1	1	4.25	9.61796E-06	0.0136	1.34E-07	402.8087
1	1	4.25	9.61796E-06	0.0136	1.34E-07	402.8087
1	1	4.25	9.61796E-06	0.0136	1.34E-07	402.8087
1	1	4.21	9.70934E-06	0.0137	1.36E-07	406.6358
Average					**1.35E-07**	**403.7654**
					STDV	1.9136
					Sqrt	2
					Std Error	0.9568

Pressure (bar)	Bubble Flow Meter Volume (ml)	Time (s)	Single CO_2 Flow (mol/s)	Single CO_2 Flux (mol/m2.s)	Single CO_2 Permeance (mol/m2.s.Pa)	Single Gas Permeance (GPU)
1.5	1	2.83	1.44439E-05	0.0204	1.34E-07	403.2831
1.5	1	2.88	1.41932E-05	0.0201	1.32E-07	396.2817
1.5	1	2.86	1.42924E-05	0.0202	1.33E-07	399.0529
1.5	1	2.88	1.41932E-05	0.0201	1.32E-07	396.2817
Average					**1.33E-07**	**398.7248**
					STDV	3.3077
					Sqrt	2
					Std Error	1.6539

Pressure (bar)	Bubble Flow Meter Volume (ml)	Time (s)	Single CO_2 Flow (mol/s)	Single CO_2 Flux (mol/m2.s)	Single CO_2 Permeance (mol/m2.s.Pa)	Single Gas Permeance (GPU)
2	1	2.15	1.90122E-05	0.0269	1.33E-07	398.1248
2	1	2.18	1.87506E-05	0.0265	1.31E-07	392.6460
2	1	2.11	1.93727E-05	0.0274	1.35E-07	405.6722
2	1	2.17	1.8837E-05	0.0266	1.31E-07	394.4555
Average					**1.33E-07**	**397.7246**
					STDV	5.7678
					Sqrt	2
					Std Error	2.8839

Pressure (bar)	Bubble Flow Meter Volume (ml)	Time (s)	Single CO_2 Flow (mol/s)	Single CO_2 Flux (mol/m2.s)	Single CO_2 Permeance (mol/m2.s.Pa)	Single Gas Permeance (GPU)
2.5	1	1.75	2.33579E-05	0.0330	1.30E-07	391.2998
2.5	1	1.70	2.40449E-05	0.0340	1.34E-07	402.8087
2.5	1	1.73	2.36279E-05	0.0334	1.32E-07	395.8235
2.5	1	1.73	2.36279E-05	0.0334	1.32E-07	395.8235
Average					**1.32E-07**	**396.4389**
					STDV	4.7519
					Sqrt	2
					Std Error	2.3759

Pressure (bar)	Bubble Flow Meter Volume (ml)	Time (s)	Single CO_2 Flow (mol/s)	Single CO_2 Flux (mol/m2.s)	Single CO_2 Permeance (mol/m2.s.Pa)	Single Gas Permeance (GPU)
3	1	1.45	2.81906E-05	0.0399	1.31E-07	393.5487
3	1	1.44	2.83863E-05	0.0402	1.32E-07	396.2817
3	1	1.46	2.79975E-05	0.0396	1.30E-07	390.8531
3	1	1.42	2.87861E-05	0.0407	1.34E-07	401.8631
Average					**1.32E-07**	**395.6366**
					STDV	4.7055
					Sqrt	2
					Std Error	2.3528

Pressure (bar)	N_2 Gas Permeance (GPU)	CO_2 Gas Permeance (GPU)	Selectivity (PCO_2/PN_2)
1	120.28	403.77	3.36
1.5	117.94	398.72	3.38
2	120.73	397.72	3.29
2.5	123.29	396.44	3.22
3	125.49	395.64	3.15
Average	121.55	398.46	3.28
STDV	2.91	3.19	0.10
Sqrt	2.24	2.24	2.24
Std Error	1.30	1.43	0.04

Appendix B- GC Calibration Curve for CO_2 and N_2

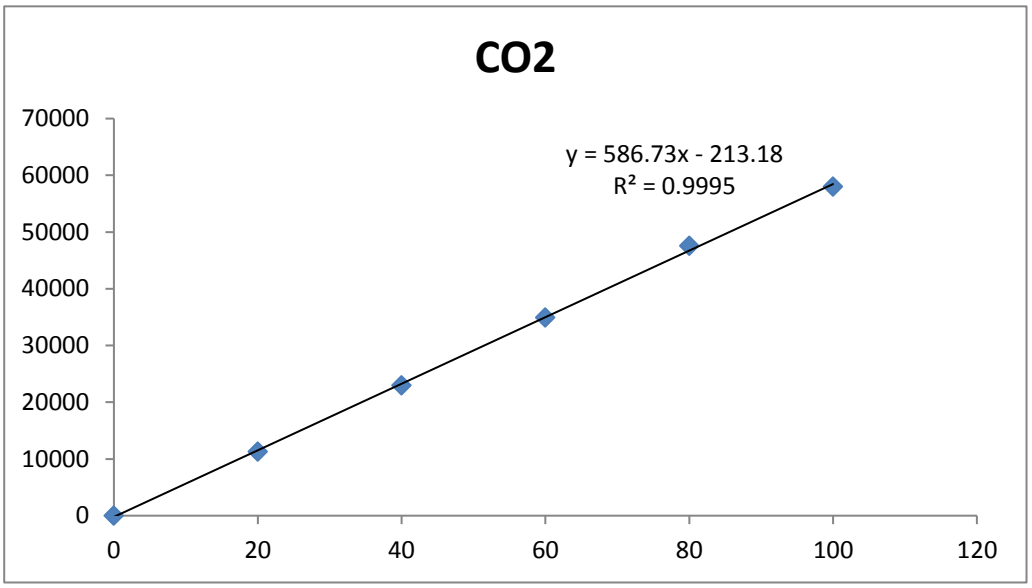

Figure A. Calibration curve for CO_2

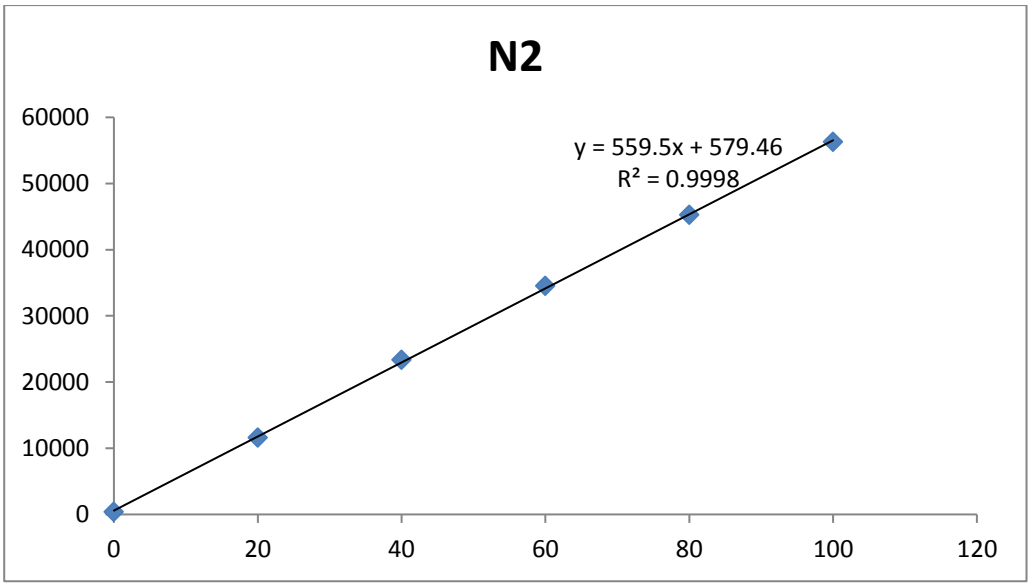

Figure B. Calibration curve for N_2

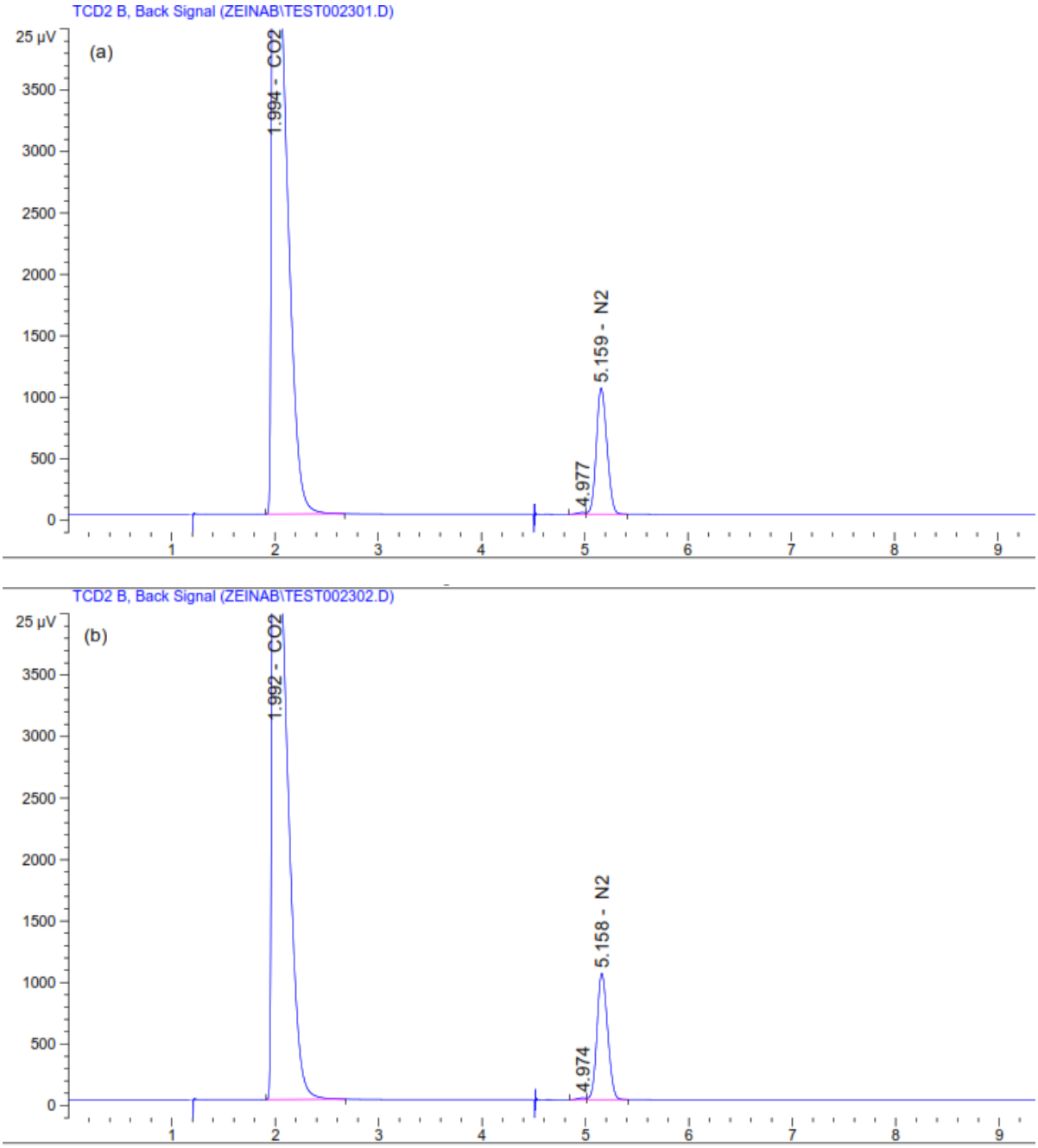

Figure C. Binary gas permeation chromatogram of CO_2/N_2 at 50:50 vol% (a) permeate stream, (b) retentate stream

Appendix C- Sample calculation for binary gas permeation for Blend MMM

Drying method: 0.5hr Isopropyl alcohol + 0.5hr hexane

Polymer concentration: 2 .67 wt% of CAB (*Mn* of 70000) + 1.33 wt% of CAB (*Mn* of 30000)

Evaporation time: 5 minutes

Permeation cell effective area: 3 cm

Membrane permeation cell area (A=π/4*D): 7.0695 cm^2 = 0.00070695 m^2

Pressure difference across the membrane permeation cell = 1 bar = 101325 Pa

Temperature = 25°C = 298.15K

	N_2/CO_2	GC	x (fraction)	Feed (Fraction)	Permeance
1	y (80n2 20co2)	4.40E+04	0.776222	0.8	0.970277
2	y (60n2 40co2)	3.33E+04	0.584175	0.6	0.973625
3	y (50n2 50co2)	1.55E+04	0.266981	0.5	0.533962
4	y (40n2 60co2)	2.24E+04	0.390359	0.4	0.975898
5	y (20n2 80co2)	1.11E+04	0.18834	0.2	0.941698

	N_2/CO_2	GC	x	Feed	Permeance
1	y (80n2 20co2)	1.43E+04	0.247743	0.2	1.238717
2	y (60n2 40co2)	2.22E+04	0.38156	0.4	0.953899
3	y (50n2 50co2)	4.60E+04	0.788309	0.5	1.576618
4	y (40n2 60co2)	4.28E+04	0.732676	0.6	1.221127
5	y (20n2 80co2)	5.79E+04	0.990048	0.8	1.23756

	N_2/CO_2	N_2	CO_2	Selectivity
1	y (80n2 20co2)	0.970277	1.238717	1.276663
2	y (60n2 40co2)	0.973625	0.953899	0.979739
3	y (50n2 50co2)	0.533962	1.576618	2.952676
4	y (40n2 60co2)	0.975898	1.221127	1.251285
5	y (20n2 80co2)	0.941698	1.23756	1.314179

Appendix D- Thermograms of MMMs and blend MMMs

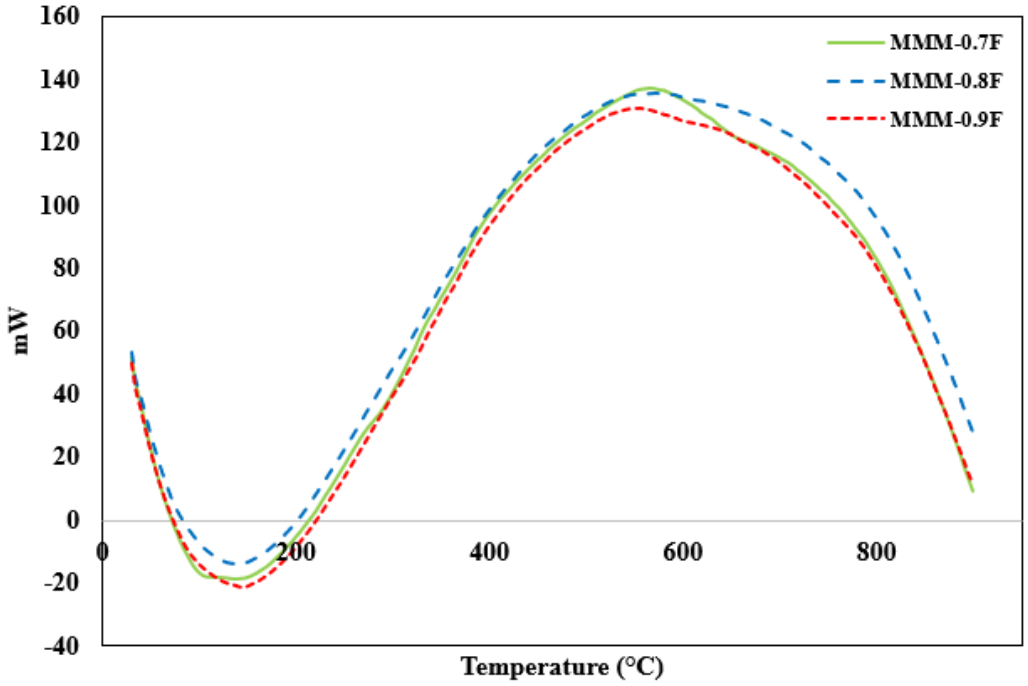

Figure D. DSC curves for MMM at different loadings of MWCNTs-F

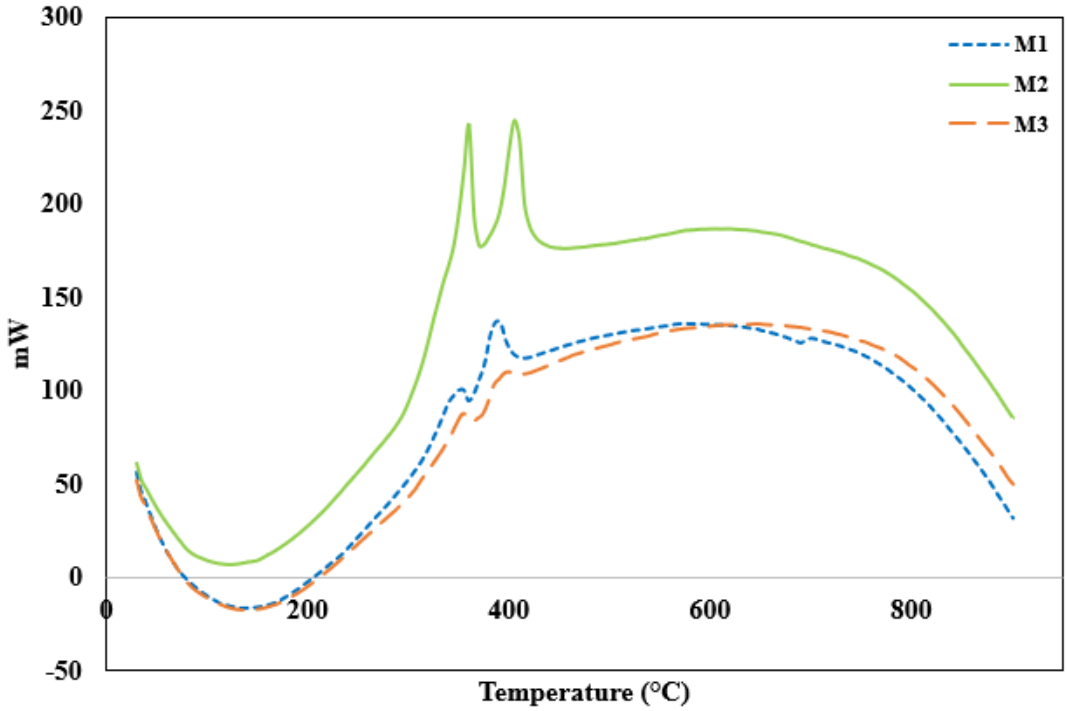

Figure E. DSC curves for blend MMMs with MWCNTs-F loadings of 0.8 wt%

Appendix E- Design of permeation cell

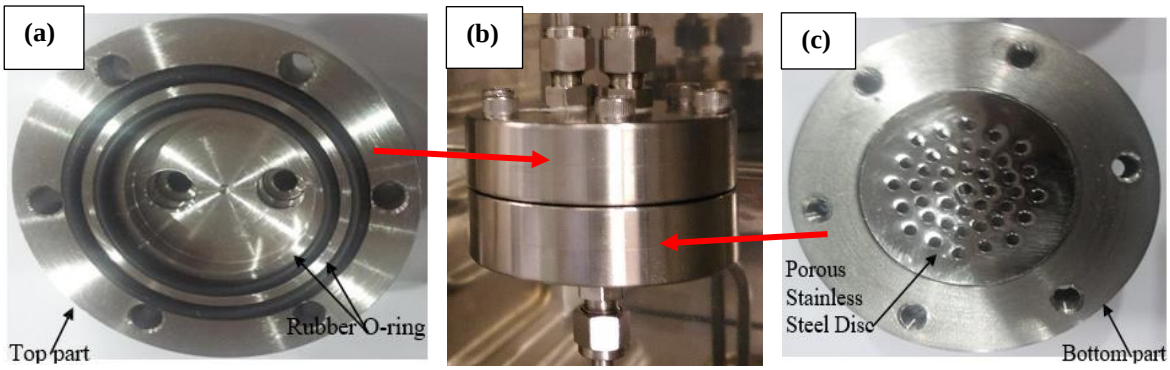

Figure F. Photograph of actual gas permeation cell a) top part of permeation cell internal design, b) full gas permeation cell, and c) bottom part of permeation cell internal design